# Confinement induced transition between wave-like cellular migration modes

Vanni Petrolli

Communauté
UNIVERSITÉ Grenoble Alpes

# THÈSE

Pour obtenir le grade de

**DOCTEUR DE LA COMMUNAUTE UNIVERSITE GRENOBLE ALPES**

Spécialité : Physique pour les Sciences du Vivant

Arrêté ministériel : 25 mai 2016

Présentée par


## Vanni PETROLLI

Thèse dirigée par **Giovanni CAPPELLO,** Chercheur, CNRS
et codirigée par **Martial BALLAND,** Maître de Conférences, UGA

préparée au sein du **Laboratoire Interdisciplinaire de Physique**
dans **l'École Doctorale Physique**


# Confinement induced transition between wave-like migration modes.

Thèse soutenue publiquement le **6 novembre 2019**,
devant le jury composé de :

**Monsieur Johannes GEISELMANN**
Professeur, Université Grenoble Alpes, Laboratoire Interdisciplinaire de Physique, CNRS, Grenoble, Président

**Madame Sara A. WICKSTROM**
Associate Professor, Helsinki Institute of Life Science, Biomedicum, University of Helsinki, Helsinki, Rapportrice

**Monsieur Xavier TREPAT**
Associate Professor, Institució Catalana de Recerca i Estudis Avançats (ICREA), Barcelona, Rapporteur

**Monsieur Eric BERTIN**
Directeur de Recherche, Laboratoire Interdisciplinaire de Physique, CNRS, Grenoble, Examinateur

**Madame Isabelle BONNET**
Maître de Conférences, Laboratoire Physico-Chimie Curie, Institut Curie - Sorbonne Universités, UPMC  CNRS, Paris, Examinatrice

**Monsieur Kevin PAINTER**
Professeur, School of Mathematical and Computer Sciences, Heriot-Watt University, Edinburgh, Examinateur

# Abstract

The ability of organisms to spontaneously generate order relies on the intricate interplay of mechanical and bio-chemical signals. If the general consensus is that chemical signaling governs the behavior of cells, an increasing amount of evidence points towards the impact of mechanical factors into differentiation, proliferation, motility and cancer progression. In this context, several studies recently highlighted the existence of long-range mechanical excitations (i.e. waves) at the supra-cellular level.

Here, we investigate the origins of those velocity waves in tissues and their correlation with the presence of boundaries. Practically, we confine epithelial cell monolayers to quasi-one dimensional geometries, to force the almost ubiquitous establishment of tissue-level waves. By tuning the length of the tissues, we uncover the existence of a phase transition between global and multi-nodal oscillations, and prove that in the latter regime, wavelength and period are independent of the confinement length. Together, these results demonstrate the intrinsic origin of tissue oscillations, which could provide cells with a mechanism to accurately measure distances at the supra-cellular level and ultimately lead to spatial patterning. Numerical simulations based on a Self-propelled Voronoi model reproduce the phase transition we measured experimentally and help in guiding our preliminary investigations on the origin of these wave-like phenomena, and their potential role for the spontaneous appearance of hair follicles in mouse skin explants.



# Résumé

La capacité des cellules à générer spontanément de l'ordre a l'échelle supra cellulaire repose sur l'interaction de signaux mécaniques et biochimiques. Si le consensus général est que la signalisation chimique est le régulateur principal du comportement cellulaire, il est aujourd'hui bien établi que l'impact des facteurs mécaniques est primordial sur des processus fondamentaux de la physiologie cellulaire tel que la différenciation, la prolifération, la motilité et qu'une dérégulation des paramètres mécaniques du microenvironnement des cellules sont impliqués dans un grand nombre de pathologies allant du cancer aux myopathies. Dans ce contexte, plusieurs études ont récemment mis en évidence l'existence d'ondes mécaniques se propageant à l'échelle supra-cellulaire.

Nous étudions dans le cadre de cette thèse l'origine de ces ondes de vitesse dans les tissus et discutons leur origine biologique. En pratique, nous confinons des monocouches de cellules épithéliales à des géométries quasi unidimensionnelles, pour forcer l'établissement presque omniprésent d'ondes au niveau tissulaire. En accordant la longueur des tissus, nous découvrons l'existence d'une transition de phase entre les oscillations globales et multi-nodales, et prouvons que dans ce dernier régime, longueur d'onde et période sont indépendantes de la longueur de confinement. Ces résultats démontrent que l'origine de ces oscillations est intrinsèque au système biologique, ce mécanisme apparait comme un candidat pertinent permettant aux cellules de mesurer avec précision des distances au niveau supra-cellulaire et potentiellement de structurer spatialement un tissu. Des simulations numériques basées sur un modèle de type Self-propelled Voronoi reproduisent la transition de phase que nous avons observé expérimentalement et aident à guider nos recherches sur l'origine de ces phénomènes ondulatoires et leur rôle potentiel dans l'apparition spontanée des follicules pileux dans les explants cutanés des souris.

# Contents

# List of Figures

# Thesis aim, hypothesis and outline

The aim of this thesis is to study the effect of geometrical constraint on the heterogeneity of multicellular systems.

The idea stems from the observation of patterns in biology, from the stripes of a zebra to the spiral arrangement of leafs on *Aloe polyphylla*, from the feather array on birds to the the villi in our stomach. All these structures begin as local differences in the behavior of cells during the development of the organism, and later give rise to the intricate shapes we observe. How these patterns originate from a homogeneous state, although not the central concern of this work, is an extremely fascinating question, the answer of which has, at least in part, been provided by Alan Turing in his 1952 paper. He explained how periodic biochemical patterns can spontaneously arise from a nearly homogeneous state, providing the framework for the successful study of many of these natural phenomena. While researching this, we noticed that in some cases Turing's theories have to be expanded to implement mechanical actors. Some of the necessary components to generate patterns can in fact be related to the mechanical interaction of cells with each other and their surroundings. This sparked an idea in our mind. Could we take a homogeneous biological system and generate differences in the local behavior of cells only by playing with the geometrical and mechanical properties of the confinement? In other words, venturing a hazardous comparison of cells and people, can we change the behavior of our guests simply by changing the shape of the room?

Our idea was to follow a bottom-up approach: since working with *in vivo* conditions means navigating an extremely entangled network of bio-chemical and mechanical inputs, we decided to tackle the problem by reducing complexity to the extreme. We would concentrate on the most simplified setup that would allow us to uncouple all these signals, while still inducing a cellular response. We would then, in my time or with successive works, build new hypotheses and experiments to move towards more realistic conditions. We chose to work on small 2-dimensional epithelial cell colonies that we confined to specific shapes. The design of said shapes was chosen to accommodate enough cells to be considered a model for a compact tissue, while ensuring to

have sub-populations exposed to different mechanical environments in terms of cell geometry, number of neighbors and contact areas. We fabricated these tissues and then concentrated on understanding if cells were responding, and in which ways they were affected.

Chapter 1 introduces our project, what reasoning led us to follow certain tracks and the literature necessary to understand the work we present later. In chapter 2 we describe the techniques and protocols we utilized throughout our work in order to obtain the results reported in Chapter 3. Following our experimental path, this chapter is divided into 2 parts:

- Part 1 describes the results obtained during our first exploratory moment, when we investigated different possible readouts and our setup was not optimized. This first period helped us better understand the behavior of our tissues and gave us an overview of how cells were affected by our geometrical input. We found the presence of periodic oscillations in the velocity of cells most interesting.

- The second part of the chapter describes how we adjusted our approach to focus on the periodic oscillations we had previously observed. We decided to try to find a configuration that would allow us to generate reproducible velocity pattern and, for this reason, we changed the shape of tissues and developed new analysis protocols, which are all detailed here rather than in chapter 2. This second part of our work absorbed by far the majority of our time, but it culminated in the discovery of extremely reproducible long-range oscillations in the velocity of cells. These oscillations loosely resemble standing waves, with cells first accumulating at specific positions, and then dispersing over time.

During my third and last year, we had to choose how to invest the small amount of time remaining in my PhD. Two roads lay ahead, we could either concentrate on obtaining a more thorough characterization of the waves we observed, or try to find a possible biological counterpart to these oscillations. The first option was, in a way, safer and more certain to yield sound results. What I chose, on the other hand, meant fishing in the vast realm of biology for a proof that our waves play a part in the biochemistry of cellular development. I took this choice because I found it more interesting, and I deemed the possible outcome worth the higher degree of uncertainty. My choice meant quickly exploring a number of paths with little time to reach definitive conclusions. I describe all these attempts and their outcomes in chapter 4. I decided to keep this separated to stress the preliminary nature of these results, not to diminish their importance. These are the first small steps towards a more realistic system, the beginning of the

“upwards” motion in our bottom-up approach. I believe they will prove useful to direct future investigations, and they allow me to discuss my project and build future perspectives relying on concrete work. These features are reported in chapter 5, together with a discussion of our results and a comparison with what is present in literature.

# 1. Introduction

## 1.1 The origin of our project

### 1.1.1 Patterning in biology

Throughout history our greatest minds have been drawn towards the presence of patterns in Nature. On very different scales, and in biology as much as in geology and physics, patterns are omnipresent in our natural environment. Regularly arranged sand dunes form spontaneously in the desert, just like the scarcity of water and nutrients gives rise to patchy vegetation in semiarid areas [1]. Moving to smaller scales, the competition between predator and prey leads to peculiar structures in the distribution of populations [2]. Many animals, such as mammals, fishes and insects, possess the ability to coordinate their motion on a long-range, giving rise to spectacular phenomena [3]. On the single organism scale, we recognize regularly arranged stripes on the fur of a zebra, spots on tigers and feathers on chickens. We can trace these displays back to the behavior of cells during the growth of organisms, and in doing so we discover, yet again, the presence of periodic arrangement of villi in our stomach or the precise occurrence of denticles in the *Drosophila Melanogaster* embryo [4].

If the beauty of these natural phenomena is reason enough to catch our attention, in a world where the laws of physics describe a continuous decline into disorder, their reproducible occurrence is somehow even more striking. And in no other realm the presence of reproducible spatial organization is as abundant and diverse as in biology. This is because, while in many cases spontaneous patterning is rare, in biology it is the norm: every organism begins its life as a single cell, a fertilized egg, and ends it as an extremely complex entity, with a specific hierarchy of shapes, structures and functions. The process through which tissues and organs acquire their shape is called *morphogenesis*. Its inherent complexity, thousands of processes happen under strict spatio-temporal control, is complemented by an almost absolute reproducibility. And for these reasons, the scientific community has devoted much attention to its understanding.

There are presently 2 main points of views on the occurrence of patterns in biology. One supposes that a pre-existing pattern can impose order on a homogeneous system, like information from the mother aiding the appearance of form in the growing embryo. This idea of relying on external cues to shape an organism has proven right in some cases [4], while being inapt for many others. The second idea is self-organization, defined as the emergence of a "pattern at the global level of a system solely from numerous interactions among the lower-level components of the system. Moreover, the rules specifying interactions among the system's components are executed using only local information, without reference to the global pattern" [5]. This second point of view was put forwards by Alan Turing in his seminal paper in 1952 [6], where he formulated the basis for his reaction-diffusion systems. Simplistically, the model is based on 2 antagonizing signals: an activator, with low spatial range, enhancing both itself and an inhibitor, which is the second signal, characterized by a longer spatial range. The presence of these two actors alone suffices to explain how, only based on local interactions, a global chemical pattern can be generated from a homogeneous system. Turing also suggests that this pre-pattern can develop into complex structures if these actors have a biological function, i.e they are "morphogens". He coined this term to indicate any general entity diffusing through biological matter able to "persuade it to develop along different lines" [6].

Although for many years after its publication this theory lacked experimental proof, the idea was extremely influential. The notion that bio-chemistry could be responsible for controlling much of the events in morphogenesis married well with the recent discoveries of DNA and the molecular revolution in biology. DNA slowly conquered the main stage and when it came to understanding a biological process, genes were to be held responsible. From this point of view, patterning is simply explained as cells blindly following the behavior dictated by morphogens, which act as a "molecular blueprint". Research concentrated on understanding how such blueprint came to be. Our knowledge of the inner workings of DNA transcription/translation grew together with our technical ability to observe molecular processes within the cell. And as the molecular landscape was slowly discovered, mathematical applications of the reaction-diffusion model became more numerous [7–10].

### 1.1.2 The role of the environment

If, on the one hand, the role of genes in controlling patterning and morphogenesis is undisputed, on the other we cannot help but realize that a piece of the puzzle is missing. Turing himself admits that self-organization generates patterns, not form. Talking about

the stripes of a zebra, he said: “Well, stripes are easy, but what about the horse part?”.

Organisms are in fact extremely complex, and their functionality strongly depends on their 3D conformation. A biochemical pattern is a first step towards the final product, it creates a coordinate system if we want, but a series of mechanical deformations need to take place in order to give the embryo, and later the organs, their finals shape [11]. These deformations cannot be comprehensively addressed without considering the interaction of cells with their environment.

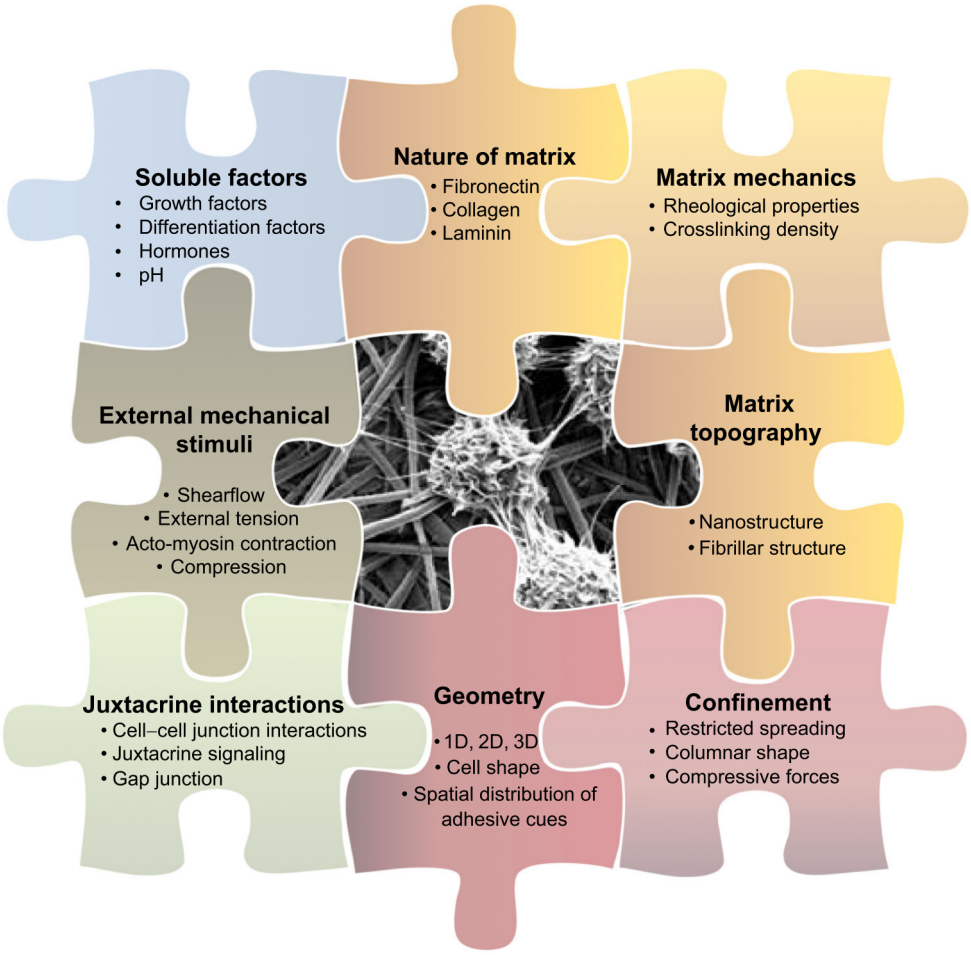


Figure 1.1: Schematic representation of the biophysical parameters involved in cellular environmental sensing. Adapted from [12].

I have so far referred to Turing’s theory as a purely chemical theory. To be fair, in his paper, he mentions the possible integration of mechanical actors in pattern formation, but he limits his studies to the chemical sphere because “...the interdependence of the chemical and mechanical data adds enormously to the difficulty” [6]. The idea of considering mechanical inputs was already present, but the awareness of their importance only emerged recently, together with the development of tools and techniques to observe and measure such interactions [13–17]. This allowed us to re-position ourselves and contextualize the DNA-centric point of view, to realize that cell behavior,

just like organ development and morphogenesis, is inherently correlated to the environment. And we cannot understand how Nature generates form and function without considering the entirety of its communication channels.

I mentioned mechanical cues as an example, but the reality is that cells are in constant dialogue with the matter surrounding them. The term "environmental sensing" describes how wide the range of this communication is: classical biochemical signals, such as soluble factors, nutrients, oxygen and the composition of the extracellular matrix (ECM) are now flanked by more biophysical aspects like the density and mechanical properties of the ECM, geometrical confinement and mechanical tension (see Figure 1.1). All these factors work together to stimulate or inhibit cellular response on disparate time and length-scales. The communication is strictly bi-directional, cells internalize external cues, integrate them in their signaling cascades and change the way they act on the surrounding material. I also want to stress that there is strong crosstalk between these actors *in vivo*, creating an extremely intertwined network of signals, as I will explain later.

The awareness of a signaling network extending beyond bio-chemical factors, in turn, influenced how we look at the emergence of patterns in morphogenesis. If, initially, the actors in reaction-diffusion models were strictly bio-chemical, the appearance of new pieces in the "puzzle" changed this notion. New theories were formulated, where both the roles of local activator and long-range inhibitor could be occupied by players of different nature, mostly mechanical [18–23], and, more recently, practical examples of such influence on organ morphogenesis have been found [24–28] (see [11, 29, 30] for reviews).

### 1.1.3 Our idea - one piece of the puzzle at a time

It was while researching morphogenesis and the recent changes in the scientific approach that we formulated the idea for my project. Morphogenesis is, in fact, far from being the major concern of this work, but it has been in the back of our minds throughout. When I started my project, the idea of the mechanical environment playing a role in cell fate was well on its way. We chose to look for a (extremely) simplified setup able to induce local differences in cell behavior solely by changing the mechanical properties (i.e. the mechanical boundary conditions) of the substrate. We wanted to see if we could generate patterning only playing with the contour. We were well aware that our bottom-up approach lead us far from those *in vivo* conditions typical of morphogenesis, and that our possible results would not be immediately relevant in that context, but we kept the idea of steering our research back towards such relevance. Our fascination

with morphogenesis is the reason for many of the choices we took and many of the results presented later on, and that is why I wanted to briefly introduce it here.

Before getting back to our question, and how we chose to answer it, there are several basic concepts one needs to be familiar with in order to fully understand this work. We will concentrate on the vast literature on how cells interact mechanically with their environment, and how, in turn, this environment affects cell behavior. This field is broadly referred to as *mechanobiology*, and reviewing the enormous body of work produced in the last century is not the scope of this text. I will briefly touch all fundamental concepts, referring as much as possible to relevant review papers for further information. I devote more time to those areas which are of particular relevance for our work and to understand our results.

## 1.2 *In vivo* vs *In vitro*: compromising to understand

As the following chapters will elucidate, cells are at the center of a complex network of signals. They sense the characteristics of the environment through their cytoskeleton, integrate such inputs in the genetic machinery and elicit specific functions on their own body and on the surrounding material. The heterogeneity of this bi-directional communication is at the root of the robustness and reproducibility of life, yet it is cause for a great deal of complexity when it comes to studying *in vivo* phenomena. Even though techniques to quantify mechanical interactions *in vivo* have been developed [14, 31, 32], reaching precise measurements and definitive cause-effect relations in such environments remains extremely challenging. For this reason, many *in vitro* systems have been developed to mimic biological phenomena while simplifying the experimental approach. Most of the work and knowledge I will present are obtained with such exploits.

I will now introduce the basic concepts behinds the role of mechanics in biology. Just as the morphogenesis of an organism, attention will first be focused on the single cell, and how it senses and communicates with its surroundings. I will then approach a larger scale, and review the literature concerning how cells interact with one another, and what phenomena this communication gives rise to.

## 1.3 The mechanical machinery of single cells

We started as a single cell, through cell division and differentiation we became an embryo, and later obtained form thanks to coordinated migration and forces exertion. All

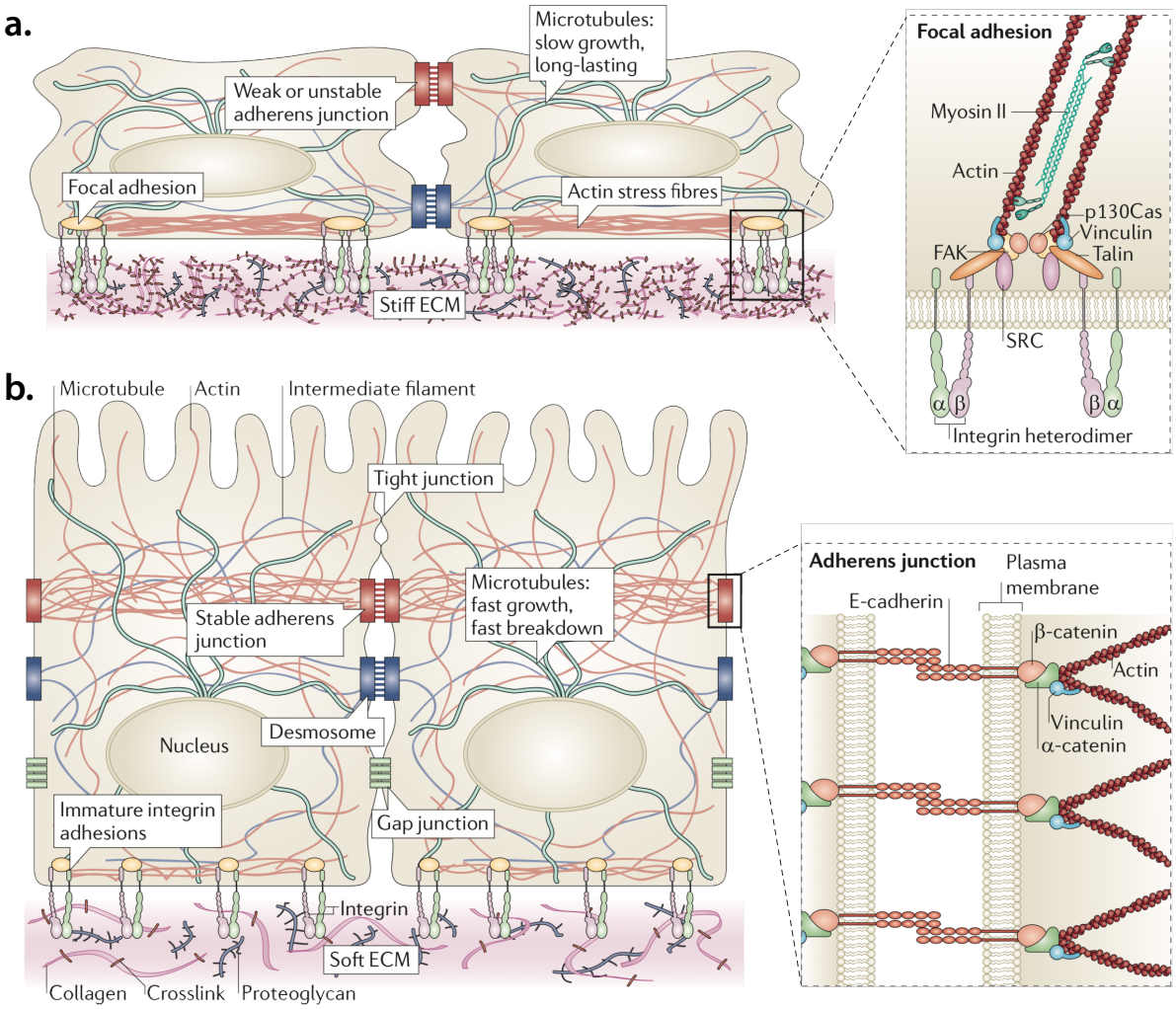


Figure 1.2: Summary of mechanical sensing in cells. Mechanical integrity, intra-cellular organization and force generation are all functions provided by the cystoskeleton, a dynamic protein network spanning the whole internal body of the cell. Cells are then in contact with the surrounding matter, mainly constituted by ECM, a fibrous network of macromolecules, and other cells (in tissues). The interaction with these two elements happens through focal adhesions and cell-cell adhesions, respectively. **a.**) Focal adhesions are multi-protein complexes. Integrins are membrane spanning proteins that, with the help of adaptor proteins, bind the ECM to the actin cytoskeleton. FAs probe the physical properties of the ECM thanks to specialized mechanosensitive proteins such as talin and integrins. These proteins change conformation, recruit other actors and activate specific signaling pathways (*inset*). **b.**) Cells in tissues maintain their mechanical integrity thanks to cell-cell junctions, subdivided into gap-junctions, desmosomes and adherens junctions. The actin cytoskeleton of neighboring cells is connected through adherens junctions. The two cells are mechanically linked by cadherins, which recruit other proteins to create extended complexes (*inset*). Many components of these complexes are sensitive to the tensile stress and can activate downstream signaling pathways. All junction types are interconnected thanks to the cytoskeleton and the nucleus, creating a active mechanical network not only able to relay forces, but to integrate and respond to physical cues. One such example is the remodeling of cell shape depending on ECM stiffness. Adapted from [33].

these processes, together with diseases and healing, are inherently connected to the way cells interact with the environment that surrounds them, and how they push and pull on it.

### 1.3.1 The contractile machinery: the cytoskeleton

To maintain their mechanical integrity and carry out their tasks, cells need to spatially organize their contents, communicate with their environment, and generate forces to change shape and move. All three functions are performed by the cytoskeleton, a fibrous networks that spans the whole body of the cell. It is constituted of 3 main polymeric macromolecules: actin filaments, microtubules and intermediate filaments (see Figure 1.2). These components are made of monomeric sub-units, which polymerize into long fibers. The stability and morphology of such fibers is controlled by a series of regulatory proteins, which continuously remodel the cytoskeleton to adapt cell shape and force generating ability (see [34] for review). Here, I will focus on actin filaments, the major player when it comes to cell contractility and motility.

Actin is present in the cell as a monomeric protein (G-actin) which progressively polymerizes to create filaments (F-actin). Since actin is polar, the polymerization happens in a specific direction: actin is recruited at the (+) end, and shed at the (-) end, in a dynamic process called *treadmilling*. By coordinating the polymerization of multiple actin filaments the cell can generate protrusive forces and help pushing the plasma membrane in specific directions. Actin is also responsible for contractile forces: actin fibers in non-muscle cells are intercalated with myosin II, a motor protein that binds two different actin filaments with its head and tail. Thanks to its ATPase activity, myosin can take a step along one of the actin filament, effectively sliding it against the other in an anti-parallel manner, thus producing a force. The long fibers arising from the combination of actin bundles and Myosin II are called stress fibers (SF).

Cells need to dynamically control the forces they exert and their location, and this is done by different classes of regulatory proteins: nucleation-promoting proteins (Arp2/3, profilin) begin filament formation; capping proteins stop filament growth; polymerases stimulate filament growth; depolymerizing factors (ADF/cofilin) promote the disassembly of filaments; crosslinkers (e.g., $\alpha$-actinin, fascin, filamin) branch the network and stabilizing factors reinforce the fibers (see [34–38] for review). These proteins affect both the structure of the cytoskeleton and the type of forces it is exerting (i.e. protrusive vs contractile force).

### 1.3.2 Substrate sensing: the ECM and focal adhesions

Most cells in the body are anchored to a network of macromolecules called the Extra Cellular Matrix (ECM). As one of the main interfaces between cells and their environment, the ECM acts as a scaffold and provides mechanical support. It is also responsible for controlling the influx of nutrients and the presentation of signals to the cell membrane [39], and as such its role is ubiquitous, from cell growth and differentiation to tissue homeostasis and cancer development (for a review see [40]). The major components of the ECM are collagens, elastins, proteoglycans, fibronectin and laminin, which determine its properties in terms of both composition and molecular organization (e.g. cross-linking degree) (see Figure 1.2) [33].

The interaction of cells with the ECM is primarily controlled by a family of membrane spanning proteins called integrins. When integrins bind their substrates, ECM proteins like fibronectin, collagen and laminin, they change conformation and start clustering. Integrins are in fact heterodimers, and the specific combination of $\alpha$ and $\beta$ sub-units defines the affinity to the specific ECM protein, activating different molecular pathways. Integrins are also activated by mechanical stimulation [41], which begins the process of clustering and gives rise to macromolecular complexes called focal adhesion (FA). The formation and stability of FA is a highly dynamical process, which revolves around the interaction of many proteins, each with specific conformation and properties (see Figure 1.2a). Briefly, integrins bind the ECM and start recruiting the protein talin. When subjected to tensile forces, talin unfolds to expose binding sites for a second protein, vinculin, which will, in turn, recruit more adaptor proteins such as focal adhesion kinase (FAK) and paxillin. This extended talin-vinculin complex ultimately stabilizes the linkage between integrins and F-actin, and helps recruiting myosin II into the stress fibers [36, 42]. The connection between FA and the cytoskeleton is a crucial part of the focal adhesion maturation process. The force exerted by stress fibers is directly transmitted to FAs, and this increase in tension leads to additional clustering and expansion in complex size and stability. A decrease in force will cause an opposite result. This is not a unidirectional relationship: focal adhesions affect force generation as much as they depend on it. Many members of the FA complex, such as integrins and downstream effectors of FAK, are involved in the Rho pathway [43, 44], which has been shown to control multiple aspects of cellular mechanics, such as actin polymerization, stabilization and myosin activity. This complex inter-dependence is at the core of the mechano-sensing properties of the cell, as we shall explain soon. In reality, the machinery is much more

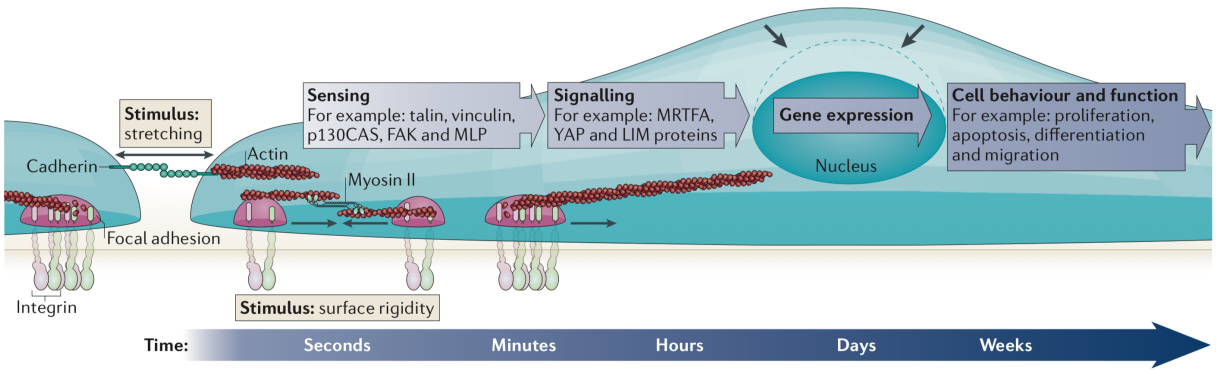


Figure 1.3: Factors playing a role in mechanotransduction, typical targets and the relative timescale of the response. Adapted from [45].

complex, with many more actors and signaling interconnections (reviewed in [45–48]).

### 1.3.3 Mechanotransduction at the focal adhesions

Focal adhesions allow cells to "feel" and probe their environment, while the cytoskeleton exerts forces that deform the ECM and the substrate. These phenomena paint a picture where mechanical signals are “read” by the cells, integrated into their machinery and even “written” and transmitted to the ECM and, as we shall see later, to other cells down the line. I would thus like to devote some time to explaining each of these phenomena and their biological consequences.

In this context, the capacity of cells to “read” is called *mechanosensing*, defined as “the ability of a cell to sense mechanical cues of its micro-environment, including not only all components of force, stress and strain but also substrate rigidity, topography and adhesiveness” [46]. Such inputs are then transduced into bio-chemical signals, which elicit a biological response and modify cellular behavior in what is termed *mechanotransduction* [49].

For mechanotransduction to happen, cells need to physically interact with their surroundings. Even though we have mainly concentrated on integrins, there are other mechanosensitive proteins active at the membrane, such as stretch-activated ion channels [50, 51] and G protein coupled-receptors [52]. The diversity in mechanosensitive molecules is then mirrored in the astonishing number of bio-molecular signaling cascades affected, and the complexity of their crosstalk [46]. For a matter of clarity and simplicity, I will here mainly concentrate on aspects of mechanotransduction that are relevant for this work.

Mechanostransduction begins with the ECM (see Figure 1.3). Cells are sensitive to the nanostructure, composition and rigidity of the ECM. These factors are highly regulated *in vivo*, where they play important roles on the correct development of organisms

[53]. The importance of such regulation is exemplified by the role of ECM in many pathologies [54, 55], such as cancer progression [56, 57].

Mechanical signals from the ECM are relayed inside the membrane by FAs. Focal adhesions are extremely heterogeneous, a variety controlled by the mechanical conditions of the environment in terms of spacing and density of adhesion sites [58]. FAs are also reinforced when subjected to external load and weakened when unloaded [48, 59], a process that proceeds until the cell is at equilibrium with the substrate. A cell can in fact "only generate as much force as can be counterbalanced by the substrate" [60]. Cell also actively try to maintain this constant level of tension against external perturbations, a phenomenon called *mechanical homeostasis* [61].

Homeostasis requires the interaction of FAs and the cytoskeleton, highlighting what is effectively the second messenger for mechanical signals. By pulling on focal adhesions, forces propagate from the ECM through the cell body, and vice versa. This bidirectional communication acts on many signaling cascades, one of the most important being the Rho/ROCK pathway. Members of the FAs complexes indirectly influence the activity of adaptor proteins, which in turn change the conformation of the cytoskeleton. For effective mechanotransduction, FAs and stress fibers need to cooperate to stabilize each other.

To elicit a biological response, mechanical signals ultimately need to be relayed to the nucleus, where they affect DNA transcription and protein expression. The nucleus is in fact the third messenger, and its response to mechanical changes happens through two major channels: shuttling proteins and direct mechanical linkage. Upon a tension increase or change, one of the downstream effects of mechanosensitive complexes at the cell membrane is inducing structural transformation to certain proteins and their successive shuttling to the nucleus. The first such proteins discovered was $\beta$-catenin, a member of the adherens junction complex (subsection 1.4.1). Other significant examples are Yes-associated protein (YAP), and WW Domain-Containing Transcription Regulator Protein 1 (WWTR1/TAZ), whose nuclear shuttling, involved in the Hippo [63] and Rho pathways [64], has been associated to substrate stiffness [65] and topology [66], cell–cell interaction [67], cell spreading and density [68**?** ] (see Figure 1.4). Once in the nucleus, YAP interacts with transcription factors to activate several genetic programs, involved first in cytoskeletal and ECM reorganization [68], then in differenciation, proliferation, cancer [69] and organogenesis [70] (reviewed in [62, 71]).

Mechanical signals can also reach the nucleus by the direct physical link existing between the cytoskeleton and the nuclear membrane, which has its own mechanosensitive apparatus [72]. This connection is secured by a protein complex called the Linker of

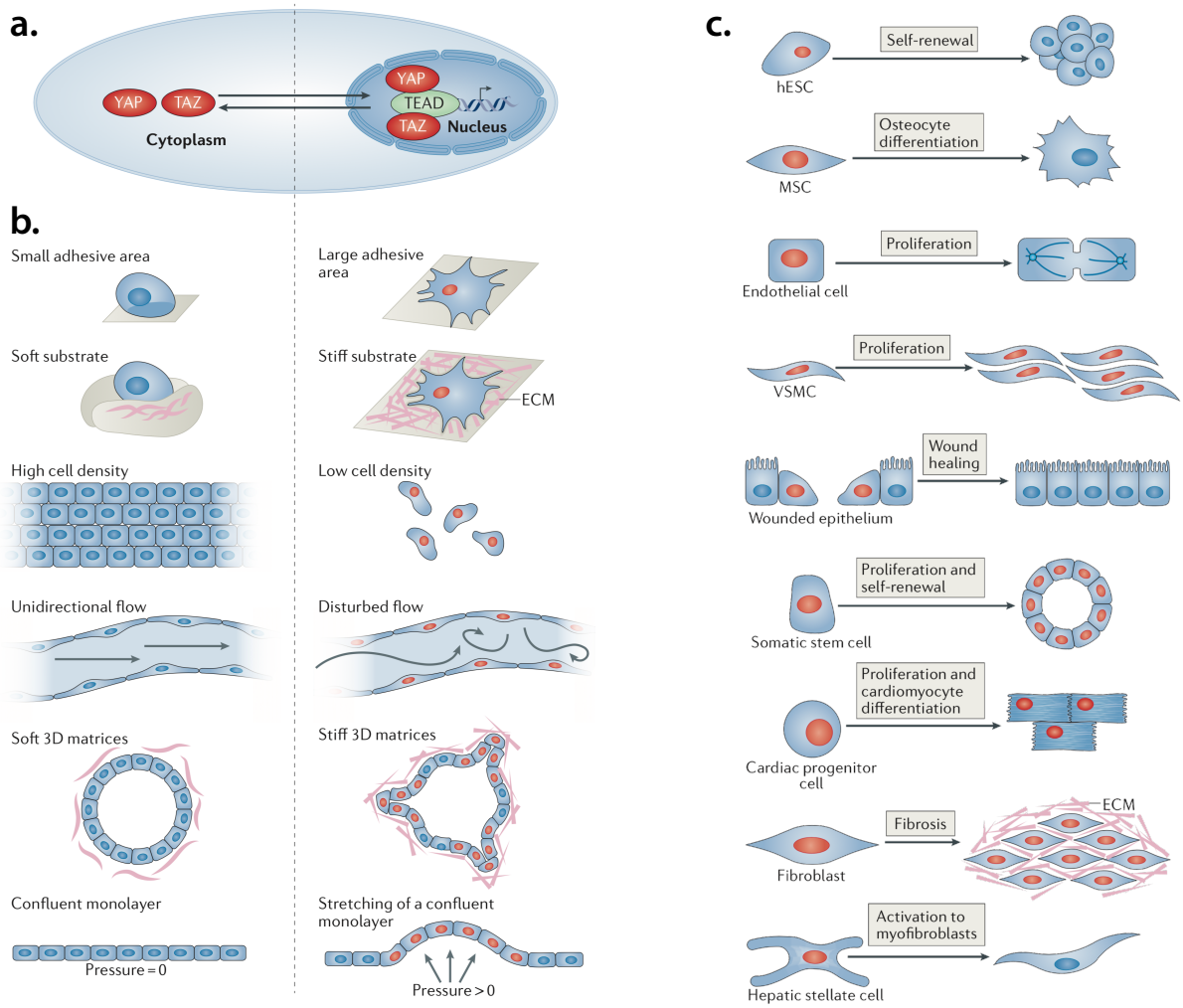


Figure 1.4: Schematic representation of mechanotransduction through YAP/TAZ. **a.**) When YAP and TAZ are mechanically activated (*red*), they translocate to the nucleus where they regulate gene expression. **b.**) Several mechanical circumstances affect the subcellular localization of YAP and TAZ, in both single cell and multicellular environments. Situations where YAP/TAZ are inhibited and remain in the cytoplasm are reported on the left, conditions that activate YAP/TAZ and cause their translocation are on the right. **c.**) The accumulation of YAP/TAZ in the nucleus (*red*) has several downstream biological consequences, which depend on the specific cell type and tissue. Altogether, these examples illustrate the range of biological functions regulated by mechanical signaling through mechanotransduction. [hESC: human embryonic stem cell; VSMC: vascular smooth muscle cell]. Adapted from [62].

Nucleoskeleton and Cytoskeleton (LINC) [73], which plays a role in the nuclear shape response to substrate rigidity and chromatin reorganization [46, 74]. Interestingly, LINC and shuttling proteins participate in the same pathways, creating, once more, an entangled signaling network. The LINC complex, for example, is involved in the shuttling of YAP [75].

The full range of cellular functions controlled or affected by mechanosensitive signaling is still unknown, but it is somehow recapitulated in Figure 1.4, describing all documented cases of a mechanical response through YAP translocation. Another significant

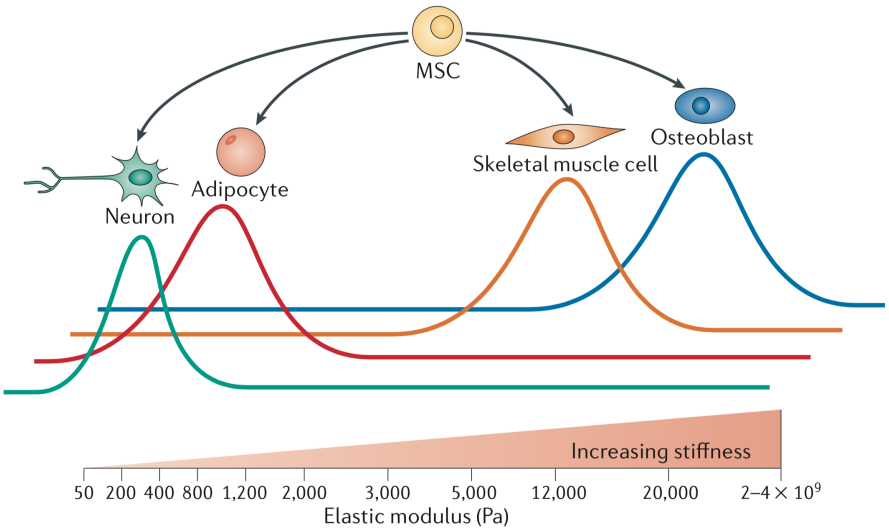


Figure 1.5: Schematic illustration of cell differentiation based on ECM stiffness. *In vivo*, cells are surrounded by tissues whose rigidity varies from extremely soft (like the brain or adipose tissue) to extremely stiff (the bone). All cells are sensitive to substrate rigidity, which acts as a signal to guide their behavior. An archetypal example of such mechanotransduction is the differentiation of mesenchymal stem cells: by tuning the mechanical properties of artificial substrates to mimic specific tissues we can drive the differentiation of MSCs towards cells belonging to that tissue. Plotted lines represent the relative differentiation, the peak its maximum. Adapted from [71].

example is the differentiation path taken by stem cells cultured on substrates/dishes of different stiffness and topology [76]. Mesenchymal stem cells (MSCs) show preferential differentiation towards osteoblasts when cultured on bone-like dishes (stiffness $\sim$ 40 kPa) and towards myoblasts when the substrate has muscle-like characteristics (stiffness $\sim$ 10 kPa) [77] (see Figure 1.5). Interestingly, it has also been demonstrated that changes in cell shape alone can direct stem cell fate [78]. On a more general level, both the geometry and surface topology of the spreading area affect proliferation [79] and direct cell differentiation [80**?** ].

Finally, one of the most evident examples of the effect of substrate sensitivity has to do with cell migration: many cells display preferential migration towards stiffer areas.

### 1.3.4 Single cell migration and durotaxis

Cell migration is a fundamental process for the development and maintenance of viability in organisms, both at the single and multicellular scale. Many processes require cells to migrate and carry out specific tasks at specific location, the archetypal example being the immune response to pathogens. Even though there are several modes, we focus here on cell migration on 2D substrates.

Cell migration relies on drastic and dynamic changes in the architecture of cytoskeleton and FAs machinery. Single cells generally migrate in response to an external signal,

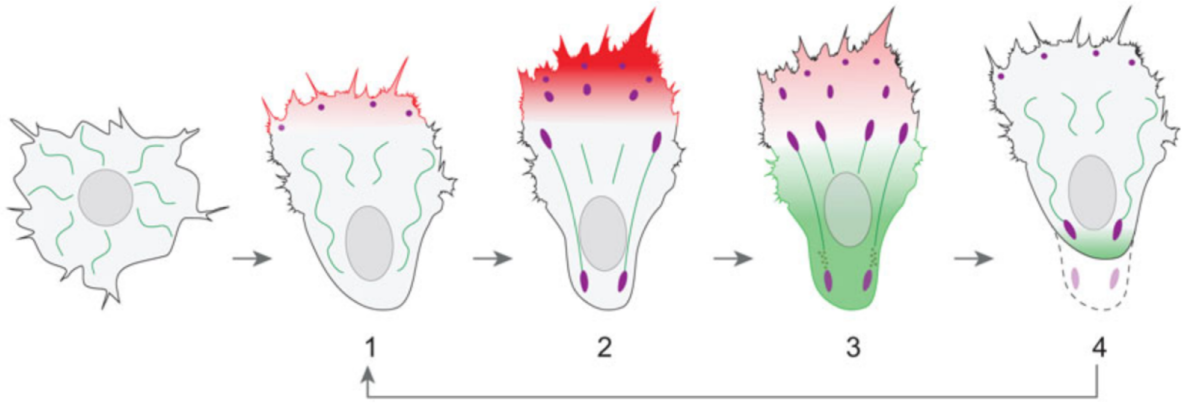


Figure 1.6: Schematic representation of single cell migration on 2D substrates. Protrusive actin-polymerzation activity is highlighted in *red*, contractile myosin II activity is in *green* and FAs in *purple*. Cell migration happens in 4 schematic steps: (1) cells break their symmetry and polarize their cytoskeleton; (2) the membrane at the leading edge is extended by actin polymerization, followed by a maturation of focal adhesions; (3) contractile activity in the rear of the cells helps translocating the cell body and (4) retracting the rear of the cell. Adapted from [81].

being it mechanical or chemical. To move in a direction, cells need to polarize and define a leading edge, the one pointing in the direction of movement, and a trailing edge (see Figure 1.6). Migration is then achieved in 3 schematic steps [82]. The cytoskeleton is re-arranged to favor actin polymerization at the leading edge, which causes a forwards movement of the membrane thanks to protrusive forces. Cells extend two main types of protrusions: filopodia and lamellipodia. Interestingly, the shape of the protrusion is governed by the specific regulatory protein recruited. Filopodia are rich in fascin, promoting straight and parallel actin polymerization, while lamellipodia are characterized by Arp2/3, favoring branched polymerization and a more disc-shaped membrane advancement [38]. This protrusion is associated with a maturation of the focal adhesions, which in turn leads to a stabilization of the polarization of the cytoskeleton [83]. As this happens, the cell body is slowly pushed forwards. If the leading edge is characterized by actin polymerization, the retracting edge displays high RhoA signaling and stronger myosin II activity. This enhanced contractile force propels the cell forward and helps the disassembly of focal adhesions and the retraction of the cell rear [84].

The characteristics of cell motility, together with the peculiar mechanical sensing happening at the focal adhesion (see subsection 1.3.3), explains the propensity of cells to move to regions of higher substrate stiffness. This phenomenon is termed *durotaxis* [85], and a simple mechanical explanation, neglecting many biological details [86], is as follows [87]. Since cells generate higher tractions on stiffer substrates [88], and FAs are reinforced under mechanical stress [48, 59], it results that adhesions become

stronger and more stable on stiffer substrates [83, 89–91]. FAs are responsible for the friction between the cell and the substrate and their stability is directly correlated with the detachment of the rear. The net result is that cells migrate slower on stiffer substrates [92]. Considering that most cells migrate as a random-walk, we have a complete picture: cell migration is fast until a region of higher stiffness is reached, where it slows down. This amounts to an overall movement towards rigid areas (for reviews see [93]).

## 1.4 Multicellular systems

The feedback mechanisms described above, linking cellular behavior and the conformation of the nearest ECM, might seem to have consequences only at the local scale. The range of force sensing, for single cells, was calculated to be in the range of several microns [94]. To understand how these concepts produce global behavioral patterns, which ultimately lead to morphogenesis and complex shapes, we need to consider how cells communicate on a "long-range". I want to stress again that, even though soluble factors certainly play a role in cellular communication, I will here tackle this subject from a mechanical point of view.

As mentioned above, the ECM has an important function in cell behavior. Due to its fibrillar and intertwined nature, the forces one cell exerts on the ECM can be directly relayed and felt by others. The active remodeling of matrix plays an equally important role. Another, more direct way to transmit mechanical information is by making direct contact to other cells. This "tethering" activity is performed by junctions, which connect cells on a large scale, creating epithelia.

### 1.4.1 Cell-Cell junctions and epithelia

Epithelial cells are a highly specialized cell type, which, thanks to its strong cell-cell adhesions, forms cohesive sheets, called epithelia. Their primary function is lining all surfaces of our body and organs (e.g. the skin, blood vessels, guts), acting as a physical barrier and providing protection against pathogens, light and chemical attacks. In their role as a barrier, epithelia are also required to absorb and secrete substances (e.g. in the gut and kidneys). To achieve both mechanical strength and selective permeation, epithelial cells need to be be tightly bound to each other, while retaining sufficient fluidity to allow for chemical transport and a dynamic response to deformations, growth and damage. Moreover, to efficiently carry out their barrier function, cells need to distinguish between the two surfaces (i.e. what is "inside" and what is "outside") and polarize

accordingly [95]. This is done by accurately rearranging their internal organelles and junctions to define an apico-basal polarity. The part of the cell in contact with the external surface (the lumen) defines the apical membrane, whereas the part of the cell in contact with the ECM is the basal membrane (Figure 1.2b). This compartmentalization of the cell, just like the mechanical stability of the tissue, is aided by the presence of specialized junctions.

There are four main types of cell-cell junctions (see Figure 1.2): tight junctions, adherens junctions (AJs), desmosomes and gap junctions [96]. Tight junctions are located close to the apical membrane, their role being the regulation of ion diffusion and segregating apical and basal membrane proteins. Gap junctions, situated next to the basal lamina, create a "tunnel" across the membranes of adjacent cells and allow direct cell-cell communication and diffusion of molecules. Desmosomes and AJs connect the cytoskeleton on neighboring cells. The difference lays mostly in the type of filament concerned. Desmosomes connect intermediate filaments, creating highly adhesive structures, mainly present in tissues where mechanical stability is prioritized [97, 98]. They are less dynamic than AJ, and even though their activity has been recently correlated to that of actin [99], they are of smaller interest here.

Adherens junctions connect actin filaments and stress fibers across two membranes. Just like FAs, they are extended protein complexes, whose major actors are cadherins. E-cadherins, the most relevant member of the family, of different cells engage in calcium-dependent dimerization, which creates the first link. This is followed by the recruitment of additional proteins that create the adherens complex, which links the membrane to F-actin and stress fibers for each cell (see Figure 1.2). Briefly, the intracellular domain of E-cadherin recruits $\beta$-catenin and $\alpha$-catenin, which in turn bind F-actin. Upon force application, $\alpha$-catenin changes conformation exposing a binding site for vinculin and ultimately recruiting additional F-actin. Another member of the complex is P20-catenin, responsible for controlling cadherin stability and interacting with the Rho pathway. This force-sensitive reinforcement of AJs is extremely important for many of the coordinated behavior typical of epithelia (for reviews see [100–103])

Aside from the junctions, another strategy to achieve functional diversity in epithelia is changing the 3D conformation of the tissue: the gut is lined by a single layer of epithelial cell, which adopt a columnar shape to maximize surface area and molecule exchange; in contrast, the skin is made of a stratified epithelium, with multiple cell layer providing better protection and water retention [104].

### 1.4.2 Adherens Junctions in mechanotransduction

Adherens junctions play a fundamental role in mechanical sensing and in cell coordination. The observation that the structure of AJ reinforces in response to the force and the substrate stiffness provided the first evidence of an active behavior [105, 106]. We have already mentioned $\alpha$-catenin and cadherins, but many other proteins within the AJ complex were discovered to be activated upon mechanical stimulation.

One such protein is $\beta$-catenin. Under normal conditions $\beta$-catenin is continuously degraded in the cytosol. When Wnt binds a surface receptor, this degradation is stopped and $\beta$-catenin is allowed to accumulate and eventually enter the nucleus [107]. Mechanical strains, or their absence, have been shown to achieve similar effects by releasing $\beta$-catenin from the junction [108, 109]. Once in the nucleus, $\beta$-catenin acts as a transcriptional co-activator, ultimately controlling cell cycle [110] and many developmental gene expression programs (for reviews see [99, 107]). Interestingly, both the Wnt/$\beta$-cat and Hippo pathways are activated upon tissue stretch [109, 110], suggesting that YAP and $\beta$-cat might cooperate to promote cell proliferation (see Figure 1.4).

The role of mediator between the contractile machinery of a cell and the rest of the epithelia makes AJs extremely important for all phenomena involving tissue homeostasis, defined as the maintenance of an internal steady state within a defined tissue [111]. AJs participate in controlling proliferation, differentiation, cell death, extrusion and migration (see Figure 1.4, for reviews see [106, 112–115]).

### 1.4.3 Crosstalk between cell-cell and cell-substrate adhesion

Mechanotransduction is key for tissue homeostasis. Cells read mechanical inputs through FAs and cell-cell junctions, and as such, we cannot examine collective phenomena without considering both junctions and how they dialogue. Even though FAs and AJs are spatially separated, their functions are strongly interdependent. Both cadherins and integrins are physically connected to the cytoskeleton, and both directly affect the actin cytoskeleton and are affected by its reinforcement. Moreover, many of the downstream signaling molecules, such as FAK, vinculin and Rac, are shared [116, 117], in what resembles a global collective network rather than single cascades (see Figure 1.7). Since the interaction between adhesion sites is highly dependent on the context, in terms of cell type, density, ECM characteristics, and the typical timing of the stimulation, we are far from having a clear picture of it. Strengthening of integrin complexes seems to weaken cell-cell binding through FAK activation [118], and vice versa [119]. On the other hand, several studies have suggested that, through the Rho pathway and

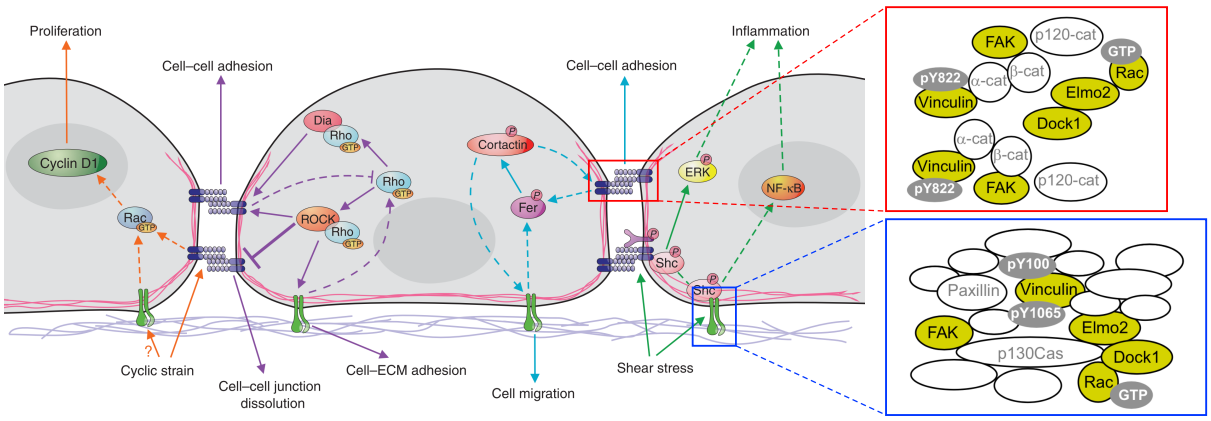


Figure 1.7: Focal adhesions and adherens junctions signaling pathways. **Left**) Schematic representation of the signaling pathways activated by focal adhesions (*light green*) and adherens junctions (*dark blue*), and their crosstalk. One of the main effectors is the Rho/ROCK pathway (*purple arrows*). Rho affects several cytoskeletal properties, among which the actin-organizing protein cortactin (*blue arrows*). Adapted from [116]. **Right**) Molecular components involved in signaling for focal adhesions (*blue*) and adherens junctions (*red*). Signaling molecules in common are highlighted in yellow, white circles represent components that are associated with only one junction. Adapted from [117].

ROCK activation, increased tension at focal adhesions could stimulate cadherins complex maturation [116, 120]. The presence of specific integrins is also necessary for the recruitment of E-cadherin and p120-catenin at AJs, confirming this second idea [121] (for reviews see [112, 116, 117]).

Despite this extremely complicated crosstalk, the integration of signals originating at cell-substrate and cell-cell junctions extends to every aspect of cell physiology, and is at the very basis of all emergent behavior in systems with more than one cell.

### 1.4.4 Mechanotransduction at the global scale and emergent properties

In the general context, those properties that do not depend on the individual parts, but rather on their relationships to one another are termed *emergent properties*, also described as “the whole is greater than the sum of its parts”. Most of the patterning necessary for life to occur (see subsection 1.1.1), being it cell differentiation, motion, or any other peculiar cellular activity, is an emergent behavior. We have already seen the means through which cells communicate with each other and their surrounding environment, and we shall now concentrate on what supra-cellular organization and phenomena this dialogue creates. This idea is easily conveyed by considering how cell-generated forces and mechanotransduction “team up” to reach a global effect (see Figure 1.8). The contractile stress generated by single cells, adapted to the local envi-

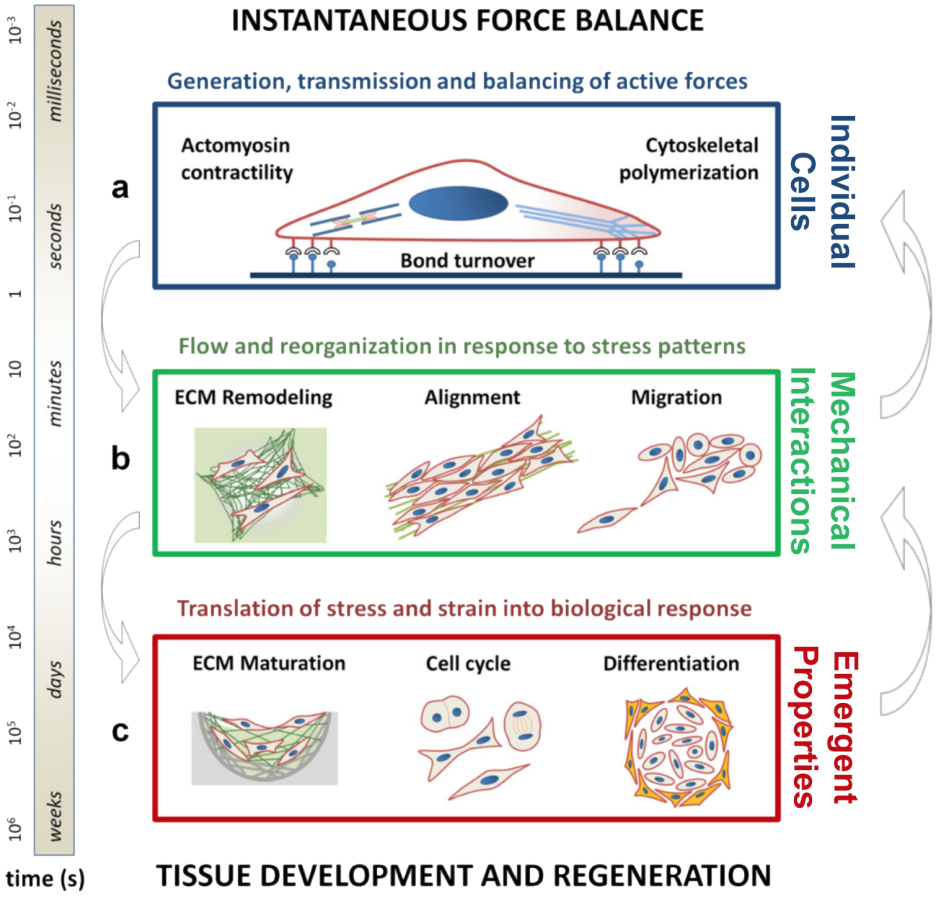


Figure 1.8: From the homeostasis of individual cells to emergent properties at the tissue scale. Instantaneous mechanical balance at short timescales is linked to characteristic events happening during morphogenesis and organism growth at longer timescales. These mechanisms are bidirectionally related by feedback loops (*grey arrows*). **a.**) Individual cells generate and sense forces through the reorganization of focal adhesions and the contractility of the cytoskeleton. **b.**) Line stresses are transmitted between cells and the ECM, creating collective responses such as ECM remodeling (*left*), cell alignment (*center*), and cell migration (*right*). These processes are slower than cytoskeletal organization, but are both dependent on it and able to affect it in different manners. **c.**) Heterogeneities in mechanical stresses are sensed by cells, which undergo different processes such as ECM maturation (*left*), proliferation (*center*) or differentiation (*right*). Since complex signaling pathways are required, these changes take place on longer timescales, in the order of several days. Adapted from [60].

ronment, is relayed on a supra-cellular scale and summed to that of the neighbors. This stress is ultimately balanced at a 2D level, in what Foolen et al. define as a 2D "cell sheet tension" [60]. Such stress buildup has 2 outcomes, at very different scales: (i) the geometry and relative strength of this surface tension affect the shape and curvature of tissues [122, 123], so that when tension is stronger than adhesive forces a layer can detach from the substrates to generate 3D structures [124, 125]; (ii) on a smaller scale, geometrical considerations and constraints imposed by the environment affect the local distribution of stresses, which in turn influence single cell [126–128]. The literature on the matter is far too vast and detailed to be fully addressed here, but some of the

common physical principles and their relative timescales are summarized in Figure 1.8 and in [60, 111, 114, 129, 130]. The importance of these emergent properties, and, more generally, mechanostransduction at all levels is highlighted by the high number of pathologies that arise when mechanical signals are missing or not correctly interpreted [46, 131, 132].

Emergent properties arise when working in multicellular environments, the simplest of which is small 2-dimensional tissues. In this context, cell ensembles spontaneously give rise to patterns of proliferation [126], differentiation [78, 127, 133] and, in some cases, 3D conformation [128, 134]. More specifically, for what concerns this work, the most important such behaviors are related to the collective migration of cells, and the emergent properties related to their response to external confinement or the lack thereof.

## 1.5 Collective cell migration

Many contexts in the physiology of organisms require multiple cells to act in unison, displaying long-range cooperation. One emerging aspect from this interaction is collective cell migration (CCM), the coordinated movement of multicellular arrangements of cells, happening for both cohorts of unicellular organisms and within multicellular ones [135]. Large scale coordination requires communication between cells, and, as we have already seen, this happens through two intertwined channels: bio-chemical signaling and cell-cell contacts. Even though CCM is generally characterized by the maintenance of cell-cell adhesions and their integrity, it has also been observed in cells that retained cell contacts only transiently, indicating that communication via soluble factors alone is an alternative for long scale coordination [136].

CCM is responsible for many physiological phenomena, and it is particularly prevalent in morphogenesis, where it regulates the formation of complex tissues and organs [11, 81, 103, 137]. Collective migration is also responsible for wound closure and tissue homeostasis, and it is once more invoked when normal cell behavior is compromised, leading to the development of cancer and the formation of metastasis [103, 137, 138]. This latter example is, unfortunately, one of the major incentives to strive for a full understanding of this phenomenon.

The most evident advantage of supra-cellular coordination is the higher efficiency of migration. If, on one side single cells have a higher instant velocity, they also move in a random-walk manner. Cell-cell contacts increase the overall persistence, creating a more efficient system, which can also generate and sense bio-chemical and mechanical

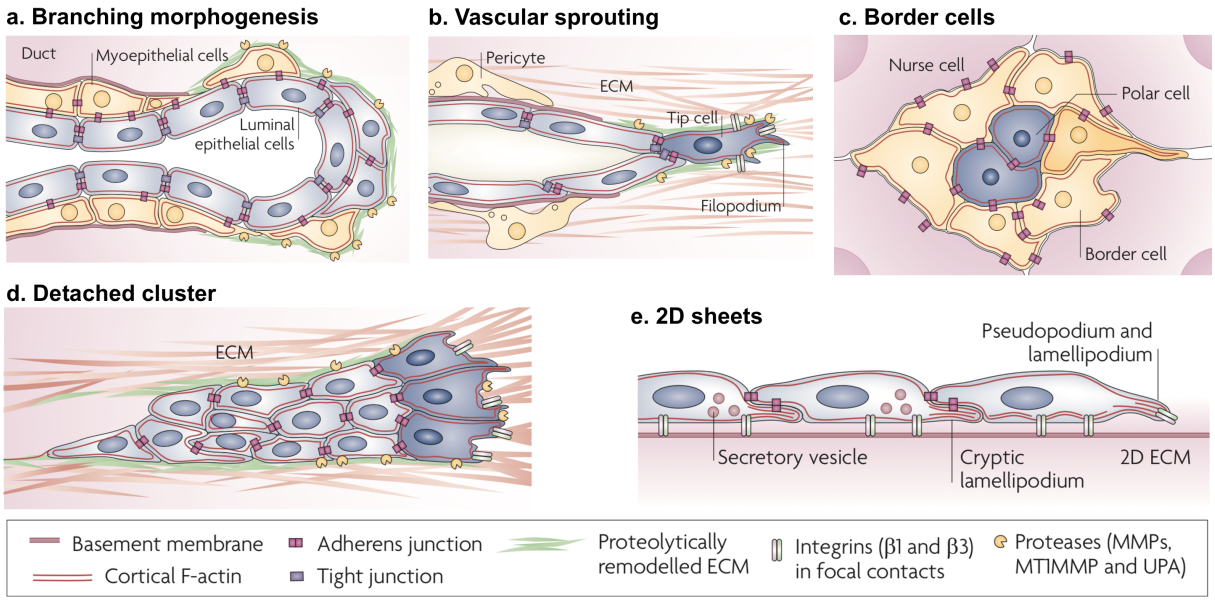


Figure 1.9: Examples of collective cell migration *in vivo* and the role of cell adhesion proteins and ECM. **a.**) Branching morphogenesis during the mammary gland development. **b.**) Vascular sprouting in the angiogenesis. **c.**) Border cell clustering in Drosophila melanogaster. **d.**) Migration as a cell cluster for the development of the lateral line in zebrafish and in cancer metastasis. **e.**) Collective migration of an intact monolayer across a 2D surface functionalized with ECM. Adapted from [137].

gradients on scales bigger than that of single entities [84].

The term collective migration encompasses a wide range of phenomena: it can happen as sheets on a 2D surface or as clusters and sprouts through a 3D matrix. The specifics depend on the characteristics of the environment, as well as the type and stability of inter-cellular junctions [139]. A more detailed treatment of CCM *in vivo* can be found in [84, 103, 137, 140, 141]. In Figure 1.9 we summarize the main migratory phenotypes by providing some notable examples, such as mammary branching morphogenesis (*a*) [142]; vascular sprouting during angiogenesis (*b*) [143]; dorsal closure [144] and border cell migration (*c*) during the morphogenesis of Drosophila melanogaster [145]; and finally migration of cell clusters in lateral line in zebrafish [146], neural crest formation [147] and cancer invasion (*d*) [138, 148].

### 1.5.1 CCM in planar geometry

The vast majority of the research on collective cell migration *in vitro* is done on epithelial cells plated on flat surfaces. Planar surfaces are extremely easy to work with, and many techniques for the quantification of displacements, forces and bio-molecular signals are readily available (see chapter 2). Moreover, although CCM refers to many forms and shapes of collective behavior, 2D migration recapitulates many of the general mechanisms characteristic of *in vivo* conditions [144, 149].

The most popular model for such studies is Madin-Darby Canine Kidney (MDCK) cells, due to their strong apicobasal polarity and robust cadherin expression. Second in line are human mammary epithelial cells (MCF-10A), often utilized thanks to the readily available tumorigenic counterparts.

Experiments are generally performed on glass or soft polymeric substrates, previously functionalized with ECM proteins in order to promote cell adhesion. The recent development of easy and high-throughput techniques to accurately control protein deposition guarantees almost complete control over the geometry and size of cell confinement (see section 2.2). Another possibility is that of releasing such confinement and present tissues with free surface. This was originally done by physically scratching a confluent monolayer to mimic the wound healing process [150]. The damages inflicted to the cells, together with the lack of precision, stimulated the development of more sophisticated techniques, chief among which the removal of a previously installed PDMS or polymeric barrier (model wound assay) [151–153]. Accurate control over the geometry of the barrier allows for great versatility and reproducibility. Better and more continuous temporal control can also be achieved by using light to locally release the confining properties of the substrate [154].

The advantage of using soft gels as culture surface, rather than glass, is the possibility to utilize small fluorescent beads to track the displacement of the substrate in response to cellular-exerted forces. This makes the calculation of the force field possible and, with adequate assumptions, the deduction of the stress field within the cell monolayer [155].

Combinations of the techniques briefly introduced here and in chapter 2 enabled the precise study of collective cell migration in engineered micro-environments. Before diving into how cell ensembles respond to the presence of boundaries or free space, it is useful to consider the role of cell density. Crowding is in fact a fundamental aspect of CCM, one that should be kept in the back of one's mind when considering cell behavior at multicellular scale.

### 1.5.2 The role of cell density, proliferation and jamming

It is well known that cells on 2D substrates do not proliferate indefinitely, but rather divide until all available space is filled, a state defined as *confluence*. Normal cells will then slow down their cell cycle to keep density approximately constant. This behavior corresponds to stable homeostatic situations in epithelia [156], and is generally lost in cancerous tissues [157]. The transition between freely proliferating cells and dense epithelia is usually referred to as *contact inhibition*, a generic term that includes 2 aspects

of cell behavior: a decrease of cell motility, and a reduction of mitotic rate upon contact with other cells [157]. These two phenomena are strongly correlated. I will use the results obtained by recent studies on MDCK cells as examples to elucidate the general trends in epithelia [155, 158–161].

#### 1.5.2.1 Contact inhibition of Proliferation

The proliferation of cells follows 3 phases. As long as the environment provides enough space, mitotic activity proceeds constantly without a decrease of the average cell area. The tissue expand until a full monolayer is formed. At this point cells are forced to accommodate their increasing numbers with a gradual reduction of the average projected area and an expansion in the vertical direction. The density increases, albeit with a progressively slower rate due to the inhibition of cell proliferation, which is approximately proportional to the area and level of crowding [162]. When the area falls below a certain threshold ($\sim$ 150 $\mu$m$^2$ [159], corresponding to $\sim$ 6 $\times 10^5$ cell/$c$m$^2$ [158]), mitosis is arrested and a steady state is reached (see Figure 1.10b). Interestingly, it has been shown that the rate of cell extrusion correlates with local density as well [163].

#### 1.5.2.2 Contact inhibition of Locomotion

This trend in cell density also correlates with the motile behavior of cell. The average velocity, often measured as the root-mean-square velocity, remains approximately constant until confluence is reached, after which it decreases to a steady value ($\sim$ 4 $\mu$m/h) over approximately 30 hours [128, 158–160, 163, 164]. If cell velocity is a useful parameter to describe the transition between motile and quasi-static monolayers, it fails to quantify how cooperative the migration of adjacent cells is. This is better expressed by the velocity correlation length, which represents the distance over which cells move in a correlated fashion, i.e. the size of the cell patches moving in the same direction [159, 160], or the radius of a swirl [161, 165] (see Figure 1.12). As cells become more dense and slow their movement down, the correlation length increases progressively to approximately 10 cells lengths or 150 $\mu$m [158–160, 165, 166]. Eventually, when the movement of cells is at its minimum, displacements are confined to the local environment and the correlation length drops to the single cell value. Interestingly, the correlation length depends on many factors, such as substrate rigidity (described in the next paragraph), the cell type [158, 167], contractility [168] and cell-cell adhesion [155, 160, 169]. With density, there is also an increase of extrusion events, which are generally associated with a net movement towards the site. Rather than extending with crowding, this process becomes more local and involves a smaller cluster at high cell

density [163].

#### 1.5.2.3 Substrate rigidity and velocity-traction alignment

The coordination of cell velocity has also been studied together with the displacement of a soft substrate underneath the tissue. As explained later (see subsection 2.3.7), this is a proxy for the traction exerted on the surface by moving cells. Angelini and colleagues found that the displacement correlation length follows a similar trend to that of the velocity correlation, with a linear increase with cell density from $\sim$ 100 $\mu$m to $\sim$ 150 $\mu$m [161]. This trend displays a strong dependence on substrate rigidity: on soft gels, the correlation length increases with cell density, whereas on glass substrates, with seemingly infinite rigidity, the opposite trend has been recorded [161]. Interestingly, another work, carried out on widely different wound healing essays, is in direct contrast with these findings: the authors report that the correlation length increases with gel rigidity [170], suggesting that glass should induce coordination over the longest distances. Even though these works contradict each other, they both hint at the role of mechanical coupling through the substrate in creating coordinated motion. These results beg the question of how such coordination happens, and if cell exerted forces align with the direction of cell motion.

What we know is that traction forces decrease with density [163], but the rest is still a matter of debate. The evidence that velocity direction lags substrate displacement indicates that cells use mechanical information to guide collective movement [161], a position further corroborated by theoretical models [171]. Notbohm and colleagues, on the other hand, found no alignment between directions of traction and velocity [172]. Peculiar cases are the presence of boundaries (where velocity and forces display anti-correlation [173]) and free expansion (cell near the edge pull themselves outwards [172, 174]), as we shall see later (see subsection 1.5.5).

#### 1.5.2.4 Glassy materials and jamming

One might think that, while density increases and cells slow down, the monolayer velocity would be homogeneous. This is far from the case, as tissues are characterized by clusters of cells with faster and coordinated velocity, referred to as *dynamic heterogeneities* [164, 175]. Their average size is estimated around 20 cells, and it increases with cell density [164]. This interesting behavior is reminiscent of the transition between fluid-like and solid-like phases in glassy materials [164, 175, 176], a comparison that could be useful in understanding how, only based on local interactions, complicated dynamics spontaneously arise in tissues.

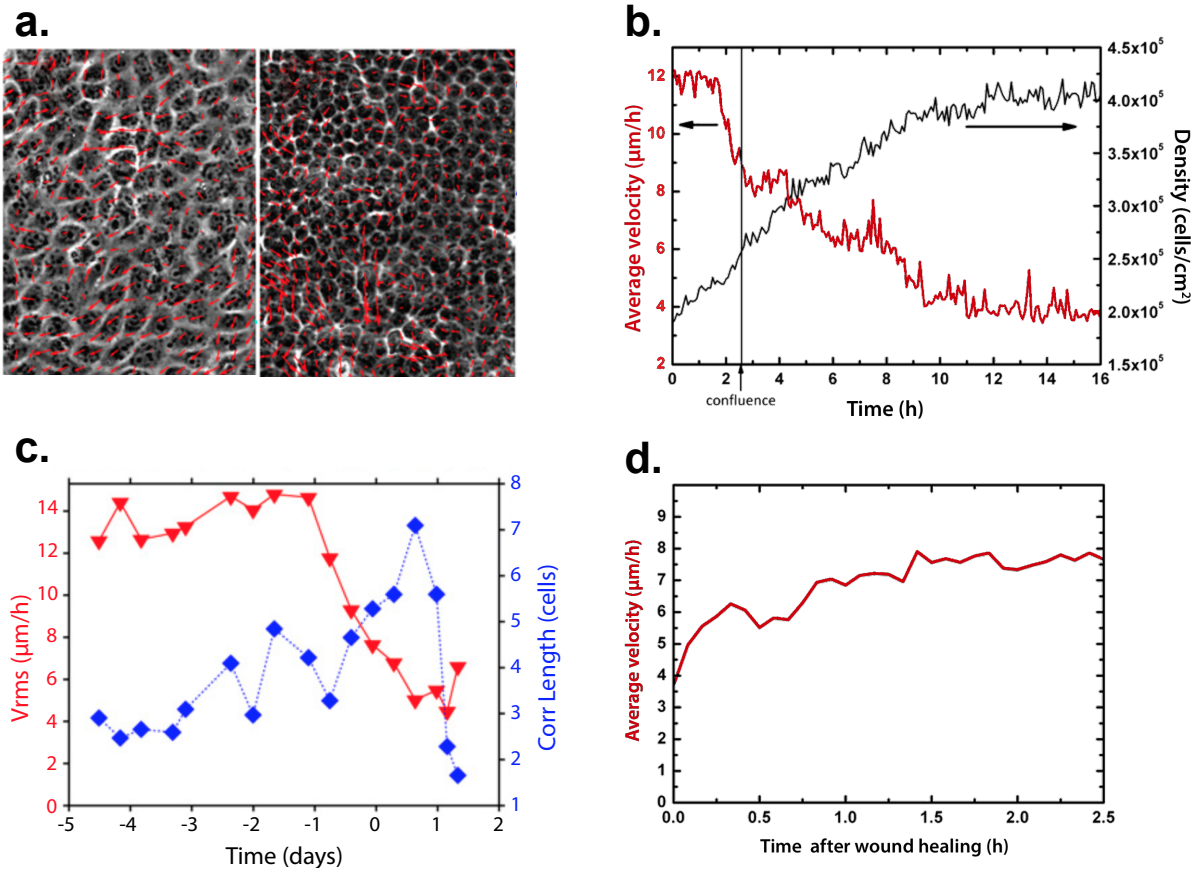


Figure 1.10: In MDCK cells monolayers, the average velocity and velocity-correlation-length depend on cell density. When density is relatively low (**a.** *left*), cell motility is enhanced. As proliferation continues, crowding increases and migration is slowly impeded (**a.** *right*). This process can be measured as a function of time (**b.**). Such decrease in cell velocity is associated with a more cooperative migration, as quantified by the velocity-correlation-length (**c.**). After jamming, free space is sufficient to trigger cell migration as shown by an increase in average velocity after a wound healing experiment (**d.**). **a.** and **c.** are adapted from [159]; **b.** and **d.** are adapted from [158].

Liquid behavior is characterized by an amorphous distribution of particles and a lack of long-range order. Upon solidification, like water turning into ice, matter undergoes a strong structural reorganization that leads to long-rage order. When this process is not accompanied by such rearrangement, as in amorphous materials, we refer to it as a *jamming transition*, and disorder remains a key characteristic of this new solid state, called glassy solid [177]. Jamming happens, for example, in particle suspensions: as the volume fraction increases, the motion of each particle is progressively more constrained by the presence of neighbors [176]. As such, the state of the system can be described by the extent of this confinement, or cage. At low densities, particles are free to diffuse because the amount of neighbors to be displaced in the process is limited. This also means that cellular rearrangements face a small energy barrier, and are thus relatively easy to accomplish. As crowding increases, so does the strength of the

caging effect and the height of the energy barrier. In order to move, a particle must now rearrange the contacts and positions of its neighbors, which involves the coordinated displacement of all particles located within a certain surrounding area. For the same reason, position exchanges become increasingly expensive as well. The amount of particles to be relocated for any of the two processes, i.e. the size of the surrounding area affected, represents the spatial extent of the correlation of motion, and it increases with the density of particles.

A confluent tissue, where each cell is surrounded by neighbors, constitutes a comparable system. As crowding begins, cells only coordinate motion locally. Dynamic instabilities begin to appear at a small scale, but as caging grows in importance, more and more cells become involved until, eventually, the entire tissue moves as one (i.e. the velocity correlation length increases). As the presence of boundaries hinders such motion, the system slows down and ultimately freezes in place, with a global decrease in velocity as the tissue becomes jammed.

This physical framework is well suited to describe the fundamental features of the behavior of cells in 2D monolayers. As such, it recapitulates, in one unified model, multiple phenomena dependent on cell density that were previously considered separately [156]. The parameters controlling glassy materials (volume exclusion, deformability and adhesive interactions) are those included in the models developed in recent years to understand cellular behavior (see Figure 1.11). The one difference is in that, contrarily to the particles in glassy materials, cells display an active behavior that needs to be taken into account (for reviews see [178, 179]).

Figure 1.11 presents an adaptation of the classical three-axes jamming diagram for glasses to the case of cell biology. In this case, cell motility plays the role of the temperature and adhesion that of stresses. Although many other axes could be envisioned [156], this graph is useful to interpret the effect that specific chemicals, such as EGTA disrupting cadherin junctions or ErbB2 over-expression promoting cell division [155], could have on the system. A similar graph has also been drawn for the specific case of a vertex model [180], which will be introduced later (see subsection 3.2.8).

The validity of a jamming transition to interpret cell behavior is of general consent, it has been proposed and utilized with different cell types [181, 182] and *in vivo* [183, 184]. For the sake of simplicity, the physical picture presented so far attributes jamming mainly to caging and mechanical constraints. There is however a debate on whether such mechanism is the sole responsible, and whether cell density is, in itself, the only pertinent parameter [185, 186], with works pointing towards the role of inhibition of locomotion [187] and maturation of cell-cell junctions [160].

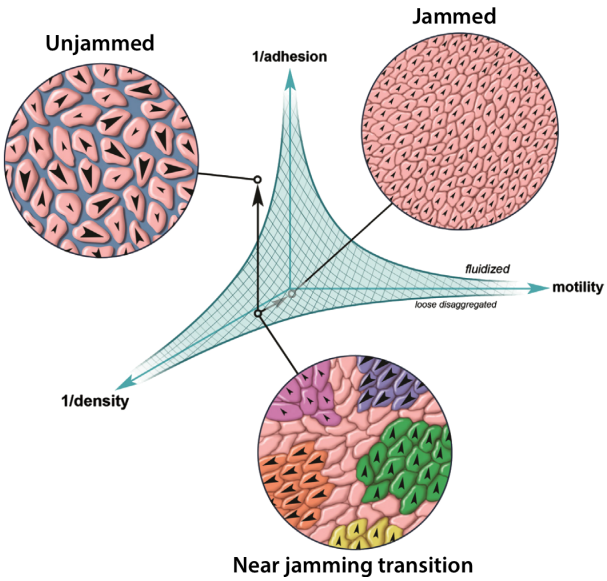


Figure 1.11: Hypothetical phase diagram of jamming in cell monolayers. The blue surface separates situations of jammed and unjammed tissues depending on cell density, adhesion and motility. Crowding and cell interactions are represented as the reciprocal of cell density and adhesion, respectively, so that points close to the origin correspond to solid tissues, points above the surface to fluid tissues. Black arrows represent transitions between different states, which are schematically portrayed in the round insets. Black arrowheads represent the velocity and direction of the migration of cells, whose area is color coded to represent clusters that move in a coordinated manner. Adapted from [156].

Notwithstanding some details, this framework will be a useful tool throughout this work to contextualize the different cellular behavior we will consider.

#### 1.5.2.5 Reawakening of cellular motility

To carry out all their physiological functions, tissues need to integrate characteristics of the fluid and jammed regime. It has been suggested that such a versatility is achieved by resting in a mechanical state close to the glassy transition. This lets cells readily respond to environmental changes by switching between these two regimes, "freezing" in homeostatic conditions, and renewing migration when necessary [175]. Unjamming is, in fact, a very important property of tissues. We described how an increases in density causes a monolayer to solidify, but a decrease of the same parameters induces the opposite effect. This is generally achieved by releasing a constraint, as in wound healing essays, and providing more space for cells to move into [152, 158, 188], even though biochemical strategies exist as well [189]. This fluidizes those cells at the edges of the tissue, which begin moving outwards [152, 158]. Since cells cannot stretch indefinitely, tissue expansion is not sufficient to fill the new space alone. At the edge, cell area increases (i.e. density drops) and this causes a reawakening of mitotic activity [190] and cell motility, effectively moving back (towards the left) in the graph in Figure 1.10b.

This process continues until all space is filled, and both mitosis and motility are once more inhibited. Motility reawakening elucidates a very important characteristic of collective migration and its guidance, the subjects of the next few paragraphs: it only happens at intermediate densities. The effect of mechanical inputs on CCM is generally studied in 2 manners: a reservoir of cells at confluence is suddenly allowed to diffuse into specifically tailored space [158, 174, 191–195], or experimental observations are narrowed to the window of time between full surface coverage and cell jamming [128, 165, 172].

### 1.5.3 Collective migration dynamics during wound healing

We can distinguish 2 scenarios when it comes to CCM on planar geometry. In wound healing and motion over "large" spaces, the dynamics of the tissue are largely driven by the crawling motion of the single cell. This autonomous behavior is then coordinated at the supra-cellular level. Conversely, closure of small gaps or migration over non-adherent surface relies mainly on cell-cell adhesion and activity of the cytoskeleton [113, 196]. Even though both dynamics generally happen concomitantly, I will mainly concentrate on those cases where autonomous cell motility is the bigger player.

The most exemplary situation is a wound healing experiment, a condition that teaches us that the presence of a free surface is stimulus enough to trigger cell migration. In response to the wound, the tissue polarizes, displays enhanced motility and slowly invades the newly available space. We can define this area as the leading edge (the front of the migrating cluster), and the bulk of the tissue as the rear. Overall, the edge advances at $\sim$ 30 $\mu$m/h [174, 197, 198], a velocity dependent on cell division [174, 195]. The major characteristics of the migration of expanding tissues are summarized in Figure 1.12. It is worth pointing out that single cells exhibit random-walk behavior when they migrate on planar substrates [199], and the presence of the confinement imposed by neighbors and cell-cell junctions is at the root of the different behaviors we see in Figure 1.12.

Three phenomena are noteworthy: (i) although the net result is an overall motion into the free space, not all cells move in such direction, and their displacement can follow any orientation, albeit with some degree of local correlation; (ii) the tissue generally migrates as a continuum and no single cell escapes its front edge; (iii) the shape of the advancing edge is not linear, but rather irregular and jagged, and cell clusters, composed of 30 to 80 cells [152, 158, 178], appear to anticipate the rest of the monolayer in what is referred to as *finger-like protrusions* [152, 158, 200] (see Figure 1.13).

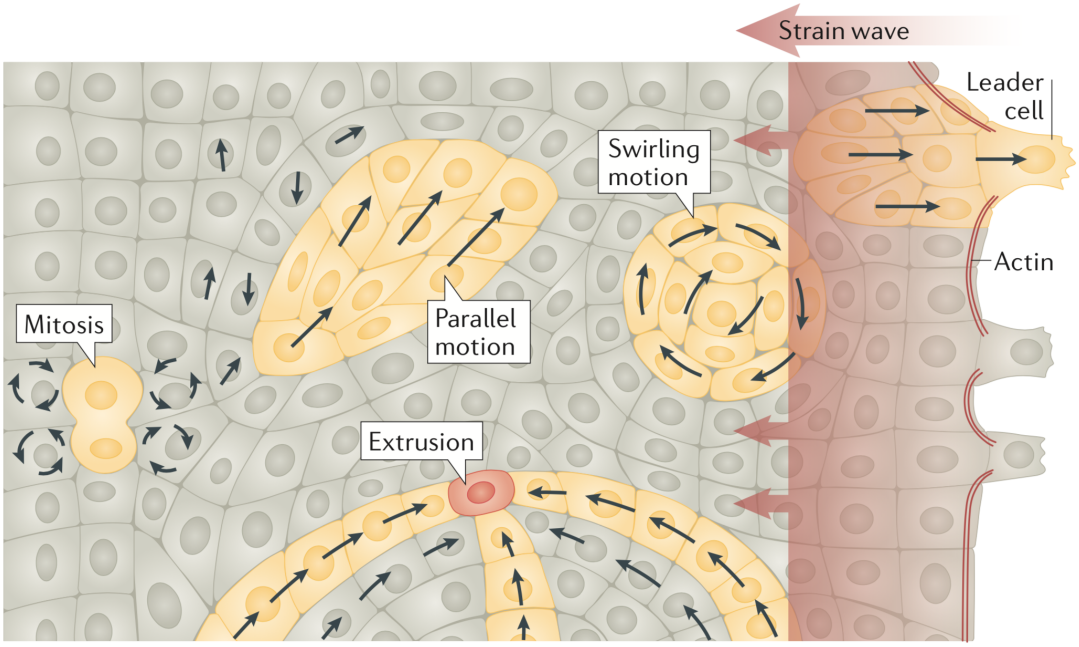


Figure 1.12: Representation of the local dynamics of collective movement. Black arrows represent the local velocity field. The front of the monolayer is characterized by the presence of finger-like protrusions and more spread cells. Strain (*red arrow*) and velocity (*red shaded area*) waves propagate from the edge inwards. The correlation of the movement of neighboring cells leads to the appearance of swirling motion and clusters of cells moving coherently. Events like mitosis and extrusion can alter the dynamics of the tissue, causing local or extended rearrangement, respectively. Adapted from [113].

Cells sitting at the tip of these fingers are generally larger, and their enhanced FA presence and protrusive activity led to the idea that CCM is directed by these *leader* cells, which drag the rest of the colony forwards. Cells located behind the leaders are unsurprisingly called *followers*. Here, the presence of cell–cell contacts thwarts the formation of classical protrusions. Although their name suggests a completely passive role, followers are necessary for efficient migration and the global polarization of cellular ensembles.

### 1.5.4 Global polarization

As seen for single cells (see subsection 1.3.4), polarization is an extremely important aspect of cell migration. The difference with collective movement is that, if the polarization of the front is somehow a straightforward consequence of free space, the specification of the rear needs to be communicated through the migrating monolayer. This process involves all communication channels we have introduced so far, but three aspects are of particular interest: cell–cell adhesions and force transmission at these points, supra-cellular organization of the cytoskeleton and long-range stress build-up. The two former will be briefly summarized here, whereas purely mechanical aspects are

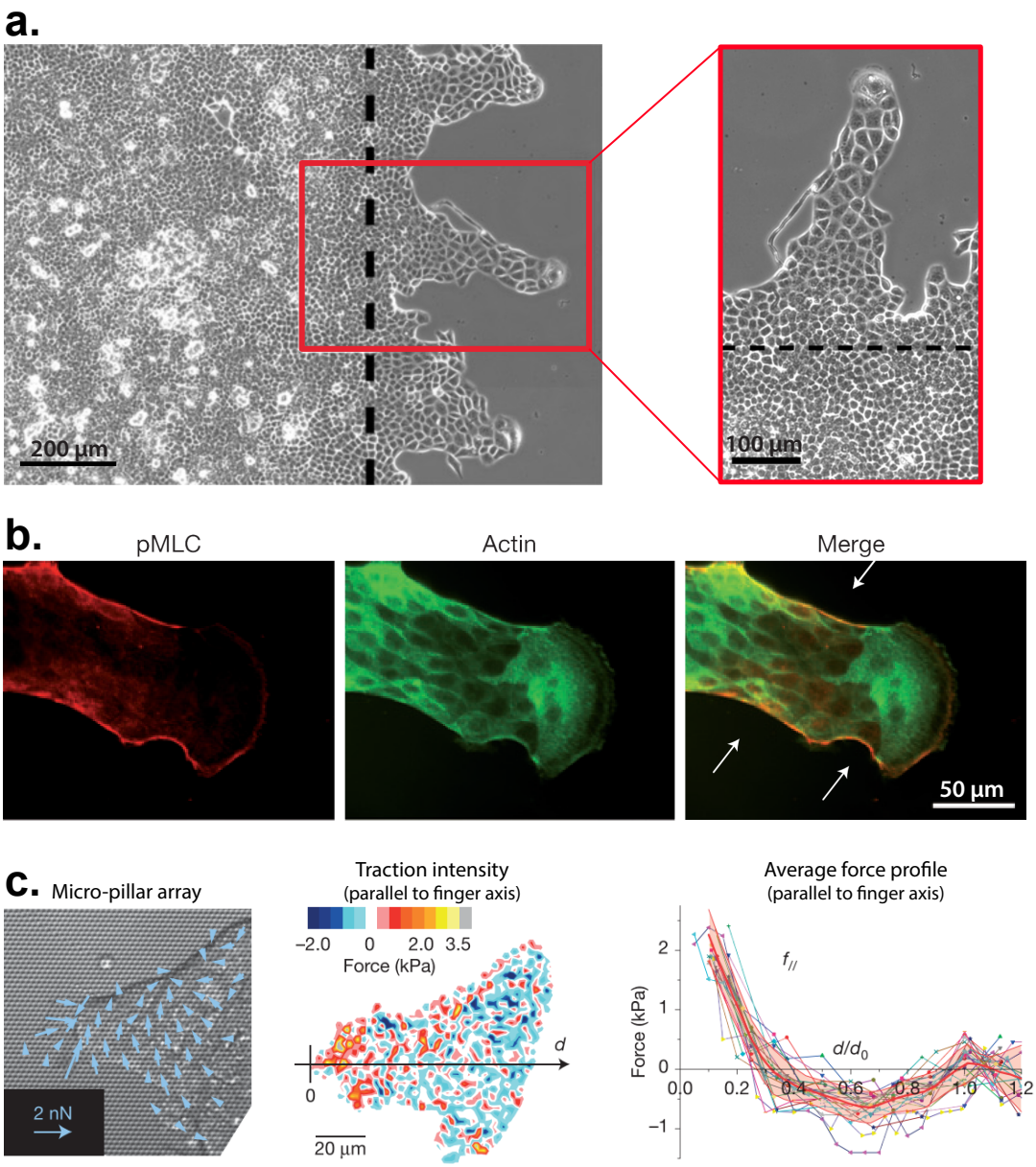


Figure 1.13: Finger-like protrusions during collective cell migration. **a.**) Finger-like protrusions appear during the invasion of free space by a MDCK monolayer on planar geometry. Adapted from [158]. **b.**) These structures are characterized by actomyosin cables spanning multiple cells, represented by the colocalization (*right*) of phosphorylated myosin light chain (pMLC) (*left*) and actin (*center*). **c.**) The traction forces exerted on the surface by finger-like structures are characterized thanks to micro-pillar arrays (*left*). The intensity of the projected component in the direction parallel to the finger axis is displayed in the *center*, and its average for 22 fingers on the *right*. Adapted from [200].

discussed later (see subsection 1.5.5).

At the front, FA sense the free space and activate Rac1, causing enhanced actin activity, the presence of protrusions (lamellipodia and filopodia) and cytoskeletal rearrangement (see subsection 1.3.4) [84, 113]. The local decrease of cell density [201] has also been shown to correlate to ERK activity [202], as discussed later (subsection 1.6.7). *In vivo*, surface receptors also activate in the presence of soluble factors. High levels of

RhoA at the back of the leader cell are then obtained thanks to the interaction with followers and the presence of cadherins under tension [84, 113], achieving the typical signature of single cell migration: Rac active at the front and Rho at the rear (see subsection 1.3.4). Interestingly, this bio-chemical profile is also present at the larger supra-cellular scale of the finger [200].

Leaders display a somehow mixed phenotype, the front loses apico-basal polarity to favor a more mesenchymal front-rear polarity and strong actin protrusions, whereas the back retains the cell-cell junctions characteristic of epithelial cells [84] (see Figure 1.14). The composition [203] and distribution [204] of these adherent junctions is then responsible for the extended polarization of follower cells. At their front, only during migration, a protein called Merlin is released from the cell-cell contact to induce differential Rac1 activation and long-range polarity [168]. Cadherin fingers are shown to participate in such process as well [205, 206].

Another important factor for global polarization is the supra-cellular organization of the cytoskeleton. Specifically, an acto-myosin cable spanning multiple cells is consistently present on the sides of protrusive fingers (see Figure 1.13b) [200, 207], and seems to have an extremely important role in directing cell migration and establishing the hierarchy in the finger. There is, in fact, higher probability of new leader formation at locations where the cable is damaged or discontinuous [158, 200], suggesting that peripheral actin might act as a confinement, "herding" the other cells in the forward direction. As we will see later (subsection 1.7.1), many are the phenomena that rely strongly on such supra-cellular organization.

This paints a picture where global polarization is achieved thanks to the interplay of signaling pathways and mechanical tensions, generated at the leading edge and transmitted through cell adhesions (for reviews see [84, 113]).

#### 1.5.4.1 Contact inhibition of locomotion

It has recently been suggested that contact inhibition of locomotion (CIL) [157] might explain how follower cells help collective movement by inducing stronger polarization in leaders. Even though CIL has already been presented in the context of jamming in epithelia (subsubsection 1.5.2.2), and the consequences are largely correlated, it assumes here a slightly different connotation. For cells migrating independently, CIL is the process whereby, upon collision, two migrating cells stop their motion and invert their polarization to move in opposite directions, substantially repelling each other. This implies that the cell-cell contacts define an area lacking membrane protrusions and enhance actin activity at the opposite end. If applied in the context of collective cell

migration, through CIL, the presence of followers forces leaders to migrate away from their contacts in a more consistent manner [84, 208]. This behavior has been observed in cells confined to small channels. Where CIL is classically expected to cause cells to move in opposite directions, Desai and colleagues observed the presence of small cell "trains" moving collectively in a persistent manner [209].

It is important to note that leader cells are not pre-determined, as before they take upon their role, they are indistinguishable from all their neighbors. It has been suggested that leaders might be formed as a consequence of the stronger and more extended cell alignment in the bulk towards the finger [158, 200]. The bi-directional interaction between leaders and followers is a key ingredient to understand collective cell migration and emergent behaviors in tissues (for reviews see [83, 84, 103, 113, 137, 140, 178, 210, 211]). To gain a better grasp and a more complete picture of CCM and global polarization, we need to consider the mechanical interaction between different cells and with the substrate.

### 1.5.5 Distribution of forces in collective migration

Forces generated by cells onto the substrate are measured through the deformation of the underlying material (see subsection 2.3.7). From these measurement, it emerges that the maximum amount of force is located at the edges of the tissue, in proximity of the leader cells [200]. The profile of the forces for a finger-like protrusion is reported in Figure 1.13c, and it clearly shows the presence of a maximum near the tip and a minimum in proximity of the intersection between the finger and the bulk of the tissue. Such profile is reminiscent of the force distribution in single migrating cells [212].

From a more distant point of view, considering the entirety of a monolayer, tractions follow a similar trend. The largest forces are localized at the front and perpendicular to the monolayer's edge. Cells far from the leading edge exert smaller forces on the substrate, although important tractions are generated up to several hundreds of micrometers inside the monolayer [155, 174, 213] (see Figure 1.14). This points towards an active force-generating role for follower-cells, corroborated by the presence of cryptic lamellipodia in the bulk of the tissue [214]. This argument is challenged by some evidence, obtained by observing the wrinkling of thin membranes, which places tractions only at the front [201]. In the bulk of the tissue, forces are extremely heterogeneous in magnitude and direction, with small hot spots and fluctuations [155, 174]. Whether traction forces and cell velocity align has been discussed in subsubsection 1.5.2.3.

Force transmission through the substrate, if easily measured, is only half of the phys-

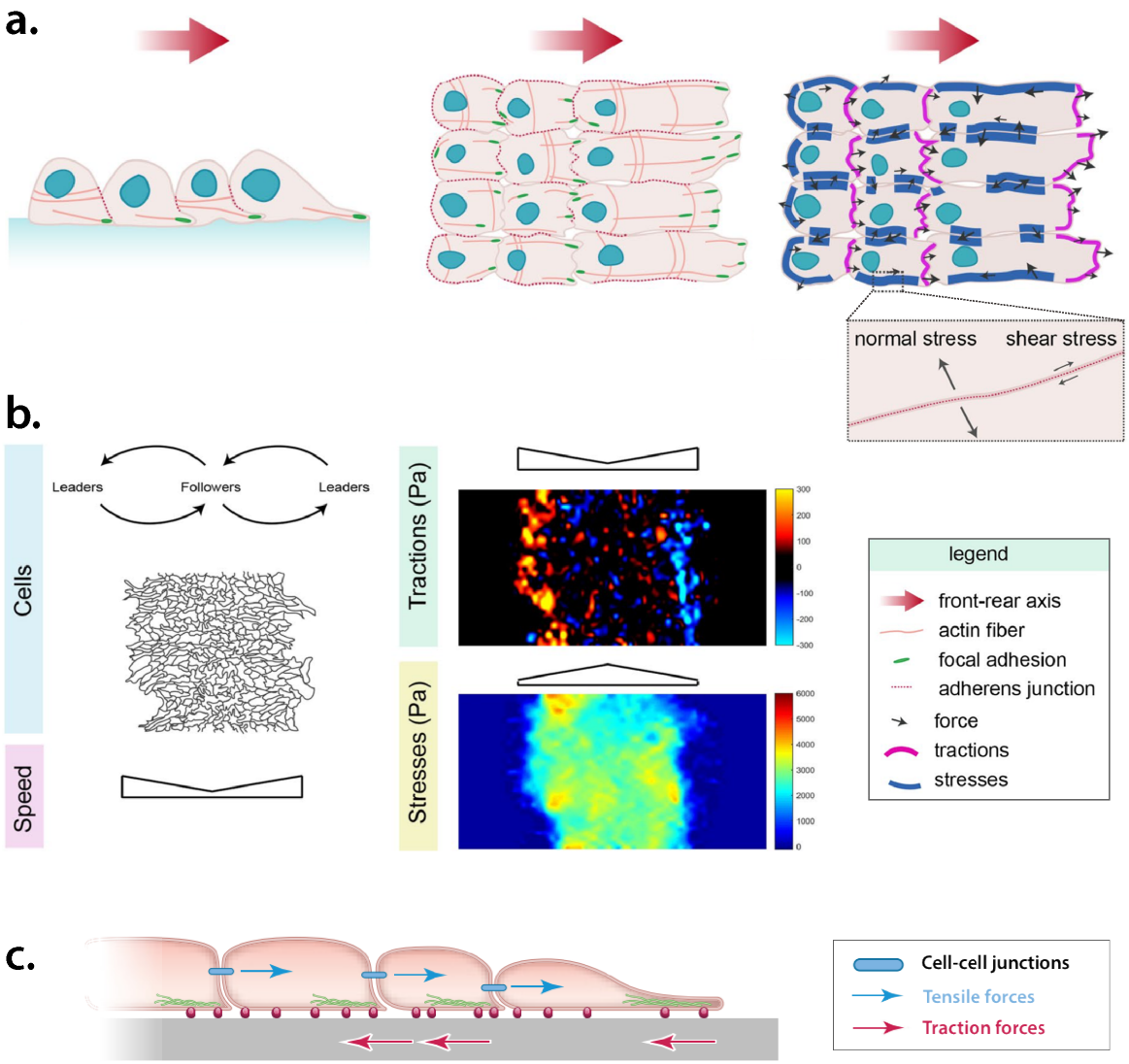


Figure 1.14: Distribution of tractions and stresses in a migrating monolayer. **a.**) Representation of the cytoskeletal organization during the collective migration of a monolayer, from a side (*left*) and top (*center*) view. Cells (light pink), moving towards the right (red arrow), display an asymmetric distribution of focal adhesions (green) and actin (pink lines), indicating global polarization. The general distribution of forces (*right*) displays high traction on the substrate (magenta) at the cell front and intercellular stresses located at cell–cell contacts (blue). The gray arrows represent possible forces and their directions. **b.**) Schematic representation of a wound healing experiment carried out as in [174, 213]. The speed of the monolayer and the average cell size are portrayed on the *left*, whereas the measured tractions and stresses, calculated with monolayer stress microscopy, are on the *right*. Adapted from [211]. **c.**) Illustration of the tug-of-war mechanism, relying on mechanical interaction of cells with the substrate (red) and with their neighbors (blue). The latter is responsible for the integration of local traction into long-range gradients of tension. Adapted from [210].

ical picture of collective cell migration. The other half is the transmission of tensions at cell-cell junctions, and it lies hidden within the monolayer. As a matter of fact, the direct measurement of these interactions is one of the big hurdles that mechanobiology will have to tackle in the coming years. One method to indirectly access this information is monolayer stress microscopy (MSM) [213, 215]. By applying Newton's laws and writing the force balance between cell–cell and cell-substrate interactions, the mechanical stress within the monolayer can be calculated as the integral of the traction forces over the tissue area. This mechanical stress accumulates from the edge towards the bulk of the tissue (see Figure 1.14) [213, 215], a trend also validated with the use FRET sensors [216]. Moreover, immediately after release of the confinement, forces and stresses are limited to a to thin boundary layer at the leading edge, to then propagate backwards into the monolayer with time [174].

These results describe a tissue where single cells engage in a global tug-of-war: a given cell within the monolayer feels the pulling force exerted at the front through its neighbors and, in turn, pulls on the substrate along the same direction, but opposite orientation. The balance of forces is ultimately satisfied when, through the junctions, the cell pulls on the neighbors immediately behind it (see Figure 1.14b), describing a mechanical signal which, traveling backwards through the colony, generates global forward migration. This integration of local forces along the tissue has the net result of a global state of tensile stress [155, 174, 176, 213, 217], believed to be an important ingredient to achieve global polarization in migrating tissues. Force transmission through cadherin junction is fundamental, as confirmed by the drop of stress accumulation upon adhesion disruption [155, 174]. Like substrate tractions, stresses are heterogeneous, with areas under compressive and areas under tensile stress. By rotating the system of reference, MSM also enables the calculation of the stress components along the direction perpendicular and parallel to a surface, defined as normal and shear stresses, respectively. The comparison of local stresses and cell velocity highlights a propensity of individual cells to "migrate along the local orientation of the maximal normal stress, or equivalently, minimal shear stress" [176], named *plithotaxis* [155] (see subsection 1.6.5). This is a first example of the guidance of cell migration in tissue, a subject treated in more detail in section 1.6. Another peculiarity of expanding monolayers is the presence of propagating mechanical waves of tissue strain rate and stress. Superimposed to the mechanical landscape we have just described, these waves originate at the edge, where forces are highest, and propagate backwards throughout the tissue at roughly twice the speed of the advancing front edge, in a manner which is dependent on contractility and cell-cell junctions [174]. Interestingly, similar deformation waves were observed in colliding

epithelia, and more generally at all repulsive interfaces [194] (see subsection 1.8.1). If considered together with the mechanotransducing apparatus (e.g. the protein merlin), physical waves might be responsible for carrying mechanical information from the leading edge to the bulk of the tissue and, ultimately, for large-scale polarization.

### 1.5.6 Elastic behavior of expanding tissues

Cell layers are generally considered as viscoelastic materials. Very briefly, over relatively short timescales the response is elastic [218], and its origin is thought to be related to the passive spring-like behavior of the cytoskeleton and intercellular adhesions [218]. On longer timescale ($\sim$ minutes), tissues behave as active materials, accommodating deformations by remodeling cell-cell junctions, cell-cell rearrangements [219] or division [220], processes that dissipate stress in a manner reminiscent of viscous materials.

A peculiarity of the mechanical waves observed by Serra-Picamal and colleagues is that stress and strain are in phase, describing what is effectively an elastic behavior, on timescales in the order of hours [174]. Normal physiological processes of the cell are in this very same range, suggesting that elasticity has an active origin [221]. Even though the assumption of elastic behavior is far from being universally accepted, other works seem to be pushing the idea forward. Similar mechanical oscillations also emerge in round discs, where Notbohm and colleagues observed, once again, that cell velocity and monolayer tension are in phase. Moreover, phases of outwards motion were associated with an average cell stretching and, contrarily, inward motion with compression, further implying an elastic relationship with a modulus of $113 \pm 28$ Pa [172]. Another measurement of this quantity was obtained by stretching a tissue between flexible poles, technique that enabled Harris and colleagues to estimate the elastic modulus at $20 \pm 2$ kPa for a MDCK cell monolayer [218]. A linear relationship between strain rate and stress was also observed in expanding tissues, with experiments that probed the long timescale, further suggesting that elasticity must have an active origin [221]. Interestingly, the stress buildup is independent of the substrate rigidity, therefore highlighting the role of cell-cell junctions. Without confinement, the traction forces exerted by cell colonies scale with their size, a linear relationship that agrees with the interpretation of the tissue as a (contractile) elastic layer coupled to the substrate [222].

In specific situations, such as the migration of monolayers over thin strips, tissues can extend over non adherent areas, called *epithelial bridges* [223] (see subsection 1.7.1). As cell-substrate interactions are inhibited outside of the strips, the structural integrity of such bridges is ensured thanks to adherens junctions and actin contractility, which self assemble into a supra-cellular actin-cable under strong tension. The behavior of epithe-

lial bridges in response to geometrical and mechanical perturbations is coherent with that of an elastic material. Interestingly, this is true for primary human keratinocytes, but not for MDCK cells, a discrepancy attributed to the more fluid nature of MDCK tissues [223].

Another peculiar instance of the mechanical response of tissues was reported by Latorre and colleagues. While studying the formation of 3D epithelial domes, they noticed that epithelial sheets could sustain massive deformations under constant tension thanks to the coexistence of super-stretched cells with barely stretched ones, in a behavior reminiscent of the super-elasticity of some alloys [224].

## 1.6 Collective cell guidance

The migration of single cells is guided by their interactions with the local environment: they migrate along a gradient of signal concentration (chemotaxis) [225], adhesion proteins (haptotaxis) [226] and ECM stiffness [85]. Similarly, cells moving collectively respond to the same mechanisms, with the additional guidance provided by the physical interactions with their neighbors. Cells in groups integrate these different inputs to coordinate their behavior at a global level. This guidance gives rise to very interesting phenomena, that we will introduce only briefly. Interestingly, many of the cases described below are characteristic of cell ensembles, and cannot be explained only based on the behavior of single cells, i.e. they are emergent properties. For reviews see [113, 176, 178, 227].

### 1.6.1 Chemotaxis

Chemotaxis is also present at the multicellular scale, although with dynamics that are far from the mere sum of single cells following a gradient. An example of such phenomenon is the directional migration of malignant lymphocytes responding to chemokine gradients [228]. If at low chemokine concentrations single cells move up the gradient, for high concentrations they are shown to move in the opposite direction, a behavior that is avoided when cell migrate collectively. The rapid exchange of leader cells is thought to be at the basis of such peculiar behavior, which can be explained thanks to a combination of the mechanism previously presented (see subsection 1.5.4) [228, 229].

### 1.6.2 Electrotaxis

Electrotaxis (also referred to as galvanotaxis) is defined as the "directional migration of cells relative to a direct-current electric field" [227], and its roots lie in the observation of endogenous electrical signals at the edge of wounded tissues. The response and magnitude of the alignment are cell-dependent [230, 231]. Just like in the case of collective chemotaxis, some cells invert the direction of motion depending on the strength of the electrical field and larger clusters respond in a more enhanced manner [232]. Electrotaxis is not fully explained, but it appears that electric fields apply forces on membrane components, changing their position and possibly activating their downstream signaling pathways [233]. Reviewed in [230, 231].

### 1.6.3 Haptotaxis

Haptotaxis describes the directed migration of cells along a gradient of ligand immobilized on the surface [227]. Migration towards both increasing and decreasing concentrations of adhesion sites has been observed, depending on cell type [234]. Haptotaxis combines principles of mechanical and chemical guidance in the same process, and as such is important *in vivo*, where leader cells sense the surrounding matrix and actively modify it to guide the behavior of the followers [227].

### 1.6.4 Durotaxis

As discussed throughout this work, cells are sensitive to the stiffness of the environment. Specifically, at the multicellular scale, cells on stiffer substrates increase their persistence, directionality, and velocity correlation distance [170]. When seeded on a stiffness gradient, tissues migrate faster over the rigid areas, with a net displacement of the center of mass in that direction [193]. There are two noteworthy differences with respect to isolated cells: (i) collective durotaxis is observed in cells types that do not display durotaxis in isolation; (ii) thanks to long-range stress transmission through adhesions, multicellular ensembles are also much more sensitive to shallow gradients than single entities [193, 235]. Even though the precise mechanism is still under debate, a possible explanation relies on the observation that the amplitude of traction forces on both sides (rigid and soft) of the tissue are equal. Due to the rigidity difference, the contraction at the softer edge is higher, causing the displacement mentioned above (summarized in [236]).

### 1.6.5 Plithotaxis

Plithotaxis is the propensity of individual cells to "migrate along the local orientation of the maximal normal stress, or equivalently, minimal shear stress" [173, 174, 176]. Unsurprisingly, this effect is suppressed upon calcium chelation or cadherin knockdown [155]. The contribution of plithotaxis to tissue expansion and the maintenance of organized hierarchy has been further analyzed in [237]. According to this model, in response to the presence of free space, those cells at the edges begin moving in a highly directional manner. These faster migrating (leader) cells pull on their neighbors in different fashions. (i) Follower cells experience a normal stress, which, in agreement with plithotaxis, leads to cell polarization and the alignment of the velocity with the stress direction. The authors observed areas of the tissue characterized by coordinated stress. Similarly to [174], such patches propagate in a wave-like manner inside the monolayer to achieve global polarization. Interestingly, the presence of a patch is followed by an area of velocity-coordination, validating their model and confirming that a stress can cause motion alignment. (ii) Leaders induce shear stress in adjacent cells, which activates their motility in a wave-like recursive manner. This evidence places plithotaxis in a key position to explain how leader cells, through the propagation of mechanical information (i.e. strain) at cell-cell junctions, lead to global polarization and global directed migration. As such, it has to be regarded as a major organizational cue in collective cell migration

### 1.6.6 Kenotaxis

A situation presenting a significant deviation form plithotactic behavior is that of an epithelial monolayer migrating towards an island where cells cannot adhere [173]. As one might expect, upon encountering the obstacle, the flow of cells divides around it and, ultimately, merges on the opposite side, surrounding the island. This flow involves complicated local cell dynamics, such as the presence of stagnation points (cell velocity drops to zero) where the flux splits and merges, and migration in a direction tangential to the island 90° away from said points. Despite this intricate velocity distribution, cells near the edge (within $\sim 50$ $\mu$m) display a "tendency to generate local tractions pulling systematically and cooperatively towards unfilled space" [173]. The authors call this kenotaxis, and it implies a strong deviation from the stress-velocity alignment typical of plithotaxis, which is nonetheless observed far from frustrated edges.

This phenomenon highlights the importance of boundaries, being them external (i.e.

a confinement) or internal (i.e. a non adhesive island) to the tissue. This is, once more, an example of mechanical guidance, which is the main subject of this work. Before devoting our attention to this matter, we need to consider a molecule whose activation shows striking similarities with the propagation of mechanical signals in tissues.

### 1.6.7 Cell guidance by Extracellular Signal-related Kinase (ERK)

As presented above, cell motility requires the cooperative regulation of many processes involving the cytoskeleton and its interactions with the environment. Even though we have been concentrating mainly on the mechanical hemisphere, each of these processes is, at one point of the cascade, controlled by the spatiotemporal activation of various intracellular signaling pathways. An increasing amount of evidence is pointing towards the role of extracellular signal-related kinase (ERK) as a key regulator of cellular activity, such as proliferation, differentiation, response to environmental signals, tumor progression and, most importantly, collective migration. The ubiquitous role of ERK is reviewed in [238–241], but here, it suffices to say that amongst its substrates are most of the molecules we mentioned for the regulation of the activity of the cytoskeleton (RhoA, ROCK, Rac, pMLC) [240]. ERK is particularly interesting when considering wound healing experiments, because it offers another insight into the guidance of collective migration. Upon the release of the monolayer, ERK activity increases at the edges, in proximity of the leader cells [202]. This local activation is concomitant with a decrease of cell density. A strong inverse correlation has, in fact, been demonstrated [198, 202].

More interestingly, ERK was shown to be activated in a wave-like manner, propagating from the wound edge to the rear of the sheet [198, 242, 243] (and *in vivo* in [244]) (see Figure 1.15). A more thorough analysis shows that ERK is activated in a "two wave" fashion: (i) for the first $\sim$ 3h, cells at the edge display synchronous oscillations that, eventually, lead to a back-propagating ERK-activation wave (*tidal wave*), whose traveling speed is $\sim 120\ \mu$m/h; (ii) behind this wavefront, randomly propagating secondary waves of ERK activity appear in a spontaneous manner (*spontaneous waves*). Interestingly, when reached by the ERK activity wavefront, cells systematically move in the opposite direction of the wave, i.e. towards the wound for the tidal wave and randomly for spontaneous wave (see Figure 1.15c) [198].

This directed migration underlines the importance of ERK oscillations in CCM, further confirmed by the strong mechanical response they elicit. Aoki and colleagues propose a model which recapitulates these phenomena [198] (see Figure 1.15b). As the wave approaches, ERK inhibits actomyosin contraction (MLC is dephosphorylated). The

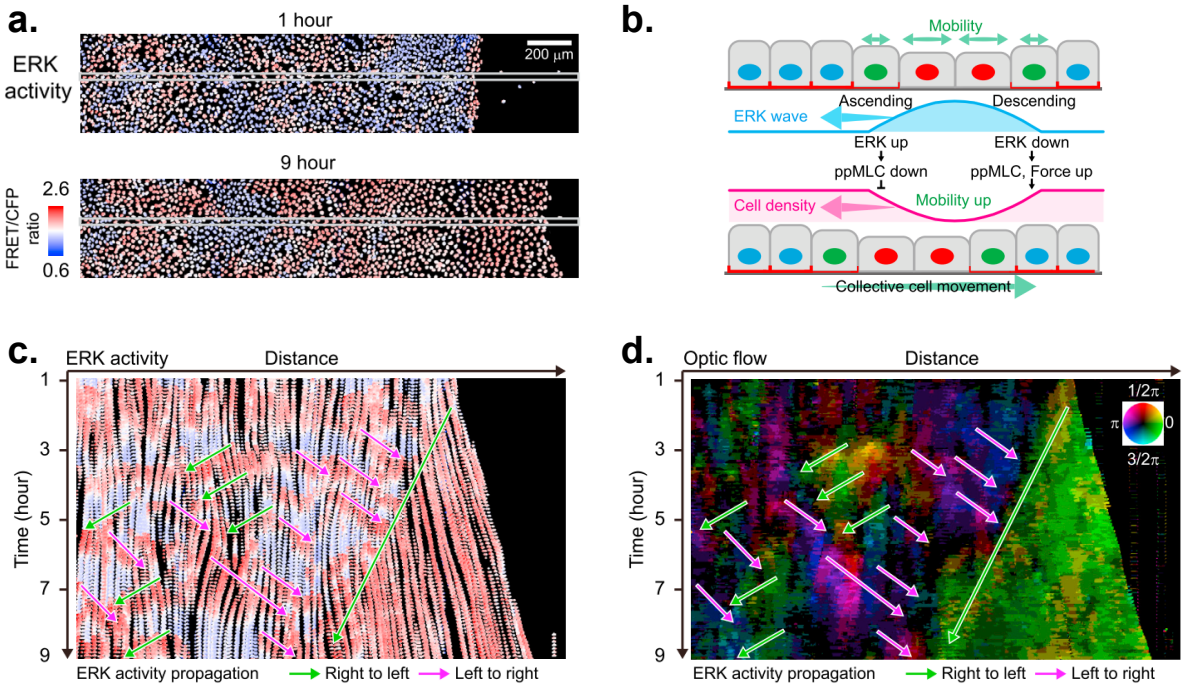


Figure 1.15: ERK-activation waves during wound healing. **a.**) ERK activity is visualized with a FRET biosensor localized at the nucleus. Red represents high ERK activity, blue low activity. Snapshots 1h (*top*) and 9h (*bottom*) after scratching are reported as examples. **c.**) The evolution of ERK activity in time (for cells located within the gray boxes in **a.**) is reported in the form of a kymograph. Magenta and green arrows represent the right-ward and left-ward activation waves, respectively. The longest arrow describes the tidal wave, whereas spontaneous waves are represented on the left of the figure. The same arrows are also present in (**d.**), reporting a kymograph of the orientation of cell migration calculated with optic flow. The color represents cell direction, according to the color-map in the top-right corner, and the brightness the velocity. **b.**) A schematic representation of the model recapitulating the effect of the ERK activity wave on collective migration. Adapted form [198].

cell relaxes and increases its spreading area, explaining the inverse correlation between ERK and cell density [198, 202]. The wave then propagates through the tissue because the sudden increase of ERK activation is passed onto adjacent cells through ligands at the surface [198, 245]. The initial cytoskeletal relaxation caused by the approach of the wave is somehow counteracted as it passes. The decrease of ERK activation, 6 minutes after the wave peak, induces strong actomyosin recruitment and MLC activation in the center of the cell. The tractions exerted by the cell spike, resulting in a net movement. Even though this motion is directed against the propagation of the wave, the specifics of this orientation are still unclear.

There is strong evidence pointing towards the importance of the ERK wave in guiding CCM. ERK activation is not necessary for wound healing, which proceeds in a mildly slower manner when ERK is inhibited, but its spatial distribution is. When extensively activated along the tissue, CCM is not wound-directed [202]. This suggests that ERK activation is not responsible for cell polarization (single cells do no polarize in response

to local activation [198]), but it is important for regulating overall cellular speed, ensuring correct leader cell placement and, overall, initiating the collective motion of large portions of the tissue, which ultimately leads to large-scale response[198, 202].

Interestingly, using an optogenetic construct, Aoki and colleagues were able to induce a wave-like cell motion by sweeping light over confined cells [198]. The optimal migratory response was reached by moving the beam at a speed of 120 $\mu$m/h, matching exactly the velocity of the activation wave during wound healing [198, 242, 243]. This number hints at a correlation of the tidal wave with other phenomena, strictly mechanical, observed in expanding monolayers. Deformation waves traveling at similar speeds ($117 \pm 16$ $\mu$m/h) backwards through the tissue are a common feature of repulsive interfaces [194]. Serra-Picamal and colleagues also observed wave-like crests of strain rate launched at the edge of monolayers, albeit with speeds closer to 60 $\mu$m/h [174]. To our knowledge, a direct association between these phenomena has not specifically been tested, but similarity in experimental setup and the agreement in orders of magnitude seem to suggest a common nature.

## 1.7 Effects of geometry on collective cell migration

The geometry of the space allowed for cells has consistently been utilized as a tool to probe collective migration and understand how it copes with external perturbations. Generally, this is done in two manners: by applying confining borders to CCM to highlight cell motion characteristics, or by changing the shape and adhesiveness of substrates to affect the closure of small close-contour wounds. Normally, this would be the natural order to follow in presenting these phenomena. In this work, being the former example more relevant, I will first briefly mention the closure of wounds, to then concentrate on the effect of borders on collective migration and how it leads to the emergence of wave-like mechanical excitation.

### 1.7.1 Role of geometry in wound closure

Experiments involving small wounds introduce the effect of curvature (reviewed in [246]), effect that was somehow ignored by "open wound" experiments where the edge is linear and quasi-infinite. We can distinguish 2 situations: newly created adhesive gaps, and the closure of small wounds over non-adhesive areas. Based on a vast amount of evidence present on adhesive wounds, gap closure is attributed to either the contraction of the supra-cellular actomyosin cable surrounding the gap, in what is called a *purse-string* manner (see Figure 1.16), or the crawling of cells on the substrate,

characterized by the presence of lamellipodia. Even though one of the two prevails in specific situations, like actomyosin contraction driving apoptotic cell extrusion [247], recent evidence support the concomitant presence of both mechanisms [248–250]. The specifics of their mutual interactions and the relative contributions have been clarified by applying mechanical and geometrical constraint. As a general rule, relatively large wounds ($r \gtrsim 100$ $\mu$m) are thought to be guided by protrusive activity because they exhibit an irregular edge with finger-like protrusions, while smaller wounds preserve their round shape throughout the process, index of purse-string contraction [248, 251]. Even though in both cases a supra-cellular actomyosin cable is assembled to surround the edge of the gap, in most cases wound closure is driven by protrusive activity, and purse-string contraction is only secondary [249–251]. As demonstrated by the example of cell extrusion, actomyosin takes over only when the radius of the gap becomes comparable to the size of single cells.

This paradigm is confirmed by the study of the tractions on the substrate. The distribution of forces at the edge of a wound resembles that of an expanding monolayer (Figure 1.14): (i) a first layer of outwards (i.e. away from the wound) pointing tractions associated with lamellipodial protrusions, followed by (ii) an outer layer of tractions pointing inwards, caused by force transmission from the actomyosin ring to the substrate [249]. Interestingly, these inwards-pointing tractions have a strong component parallel to the edge, which is thought to help wound closure by squeezing the substrate tangentially, to cause its deformation in the perpendicular direction, i.e. towards the center of the wound. The size of the wound is most probably felt in terms of the local curvature, which has been studied in detail by Ravasio and colleagues by designing wounds containing both convex and concave features [250] (see Figure 1.16c). They demonstrated, once more, the coupling between actomyosin cables and lamellipodia, albeit in curvature dependent manner. Convex areas are associated to strong lamellipodia activity, thin actin cable and tangential forces. Conversely, concave regions have a thicker actomyosin ring under higher tension, exerting forces parallel to the edge. They also demonstrated that, whereas lamellipodia-associated protrusive activity is almost independent of curvature and always promotes forwards movement, actomyosin-cable-contractility helps wound closure at concave regions, but actively fights it for convex areas.

The results presented thus far describe the contractility of actin bundles as marginal. The second scenario, that of wound closure over non-adhesive areas, finds a situation where crawling is impossible and actin contractility is the only actor.

The first such example is the migration of cells over thin strips separated by non-

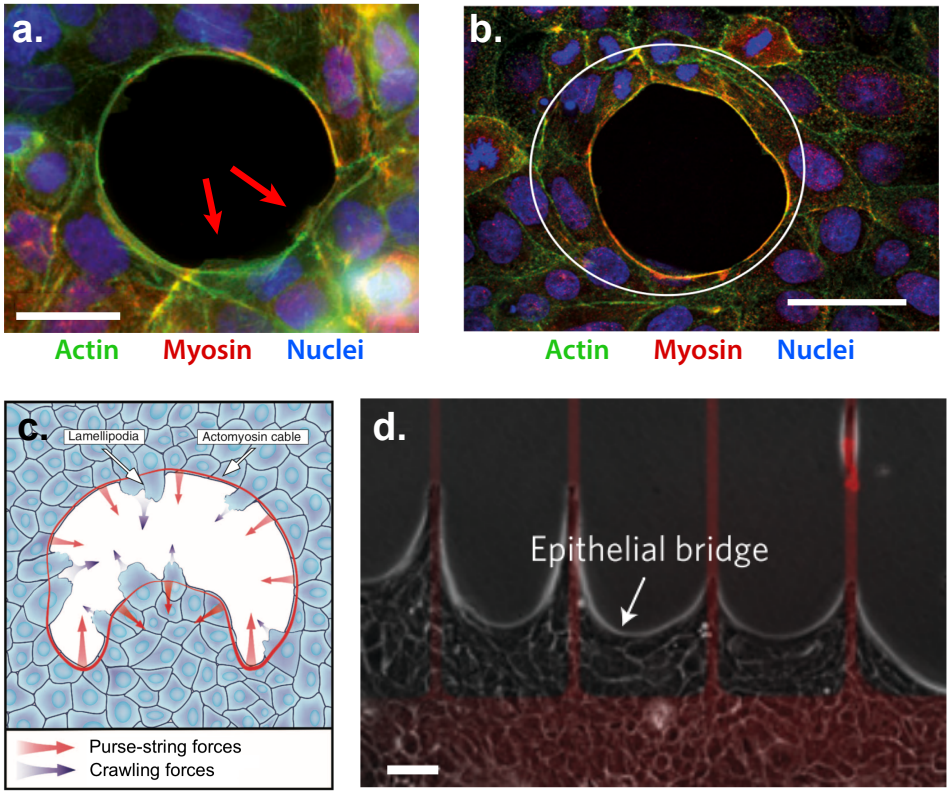


Figure 1.16: Examples of the effect of geometry on wound closure dynamics, in the case of MDCK cells on adhesive (**a.**) and non adhesive (**b.**) wounds. In both cases, a strong actomyosin cable (co-localization of actin and myosin) is assembled around the edge of the wound. When possible, crawling is the main driver for gap-closure, as shown by the presence of lamellipodia (red arrows). The interaction and relative importance of crawling and actomyosin contractility depend on the local curvature of the substrate (**c.**) and the availability of substrate adhesion sites. When the latter is hindered, contractile actin cables become the main driver of wound closure (**b.**) and keratinocytes can extend epithelial bridges over non adherent areas (**d.**). Scale bar is 50 $\mu$m. **a.** is adapted from [251]; **b.** is adapted from [252]; **c.** is adapted from [250] and **d.** is adapted from [223].

adhesive areas. In this situation, the tissue advances while maintaining cohesiveness through epithelial bridges, parts of the monolayer suspended over non adhesive areas (see Figure 1.16d). This is possible thanks to the assembly of actomyosin cables, whose shape and tensional state resemble the behavior of elastic materials (see subsection 1.5.6 [223]. Epithelia can also close over non adherent gaps (see Figure 1.16 b), a phenomena selectively guided by purse-string-like contractility of actin cables [196, 252]. Even though this process appears to be more inefficient and slow compared to cell crawling [196], it grants tissues the ability to migrate over non adherent patches, a conditions relevant *in vivo*. In this situation, different cell types manage to close gaps of different sizes, a phenomenon related to tissue fluidity and its hindrance of actin cable assembly. Specifically, this threshold is $\sim$ 60 $\mu$m for MDCK cells [252] and $\sim$ 150 $\mu$m for HaCaT keratinocytes [196]. Once again, curvature proves to be an

important parameter, with convex areas closing first due to the highest stability and forces exerted by actin bundles. Two noteworthy details emerge from these works: adherens junctions are fundamental for gap closure, which is surprisingly not affected by downregulation of desmosomes [196]; the edge of the tissue does not advance isotropically, but rather displays strong fluctuations, which are crucial to accelerate the closure [252].

### 1.7.2 Orientation at external boundaries

Collective cell migration has also been studied in the presence of externally imposed boundaries defining regions of space that cells can not invade. In general, cells show a tendency to align tangentially to a boundary between adherent and non-adherent substrates [253–256]. Drawing general conclusions is not trivial because the specifics of this alignment depend strongly on cell type and density.

Most of the works on cellular alignment have been carried out on spindle-shaped cells, a property that makes quantification much easier [253–255]. Fibroblasts are particularly interesting for the study of collective orientation, with and without external cues, because they develop weaker cell-cell adhesions and their interactions rely mainly on steric hindrance. This peculiarity means that the physics developed for liquid crystals is easily adapted to interpret the rise of collective ordering in cell colonies of this kind. Unfortunately, this also makes the knowledge obtained on these cell types harder to transfer on epithelial tissues. The results are nonetheless interesting.

Non-interacting fibroblasts have been shown to create patches of cells with common orientation [253] (see Figure 1.17a), whose size can be estimated by calculating the spatial orientational correlation length, a quantity that describes the distance to which information (about orientation) travels in a cell ensemble. The orientation correlation length, like those quantities introduced above (see subsection 1.5.2), depends on cell density, but it reaches a steady value around 500 $\mu$m. This is verified by forcing the orientation in a specific location, in this case the edge where cells are aligned tangentially, and measuring how far this instruction is propagated. Duclos and colleagues put cells on stripe patterns (two edges separated by a specific distance) and noticed that for width lower than 500 $\mu$m all cells were oriented parallel to the stripe [253, 254] (see Figure 1.17a). Unsurprisingly, the velocity of migration also orients with the edges, creating a shear flow, which is killed for widths lower than 50$\mu$m [254] (see Figure 1.17b).

Epithelial cells are different, because of their propensity to assume hexagonal shape and the presence of cell-cell junctions, but their behavior is somehow similar. In MDCK monolayers growing on 230 $\mu$m wide rings, all cells, including the ones in the center,

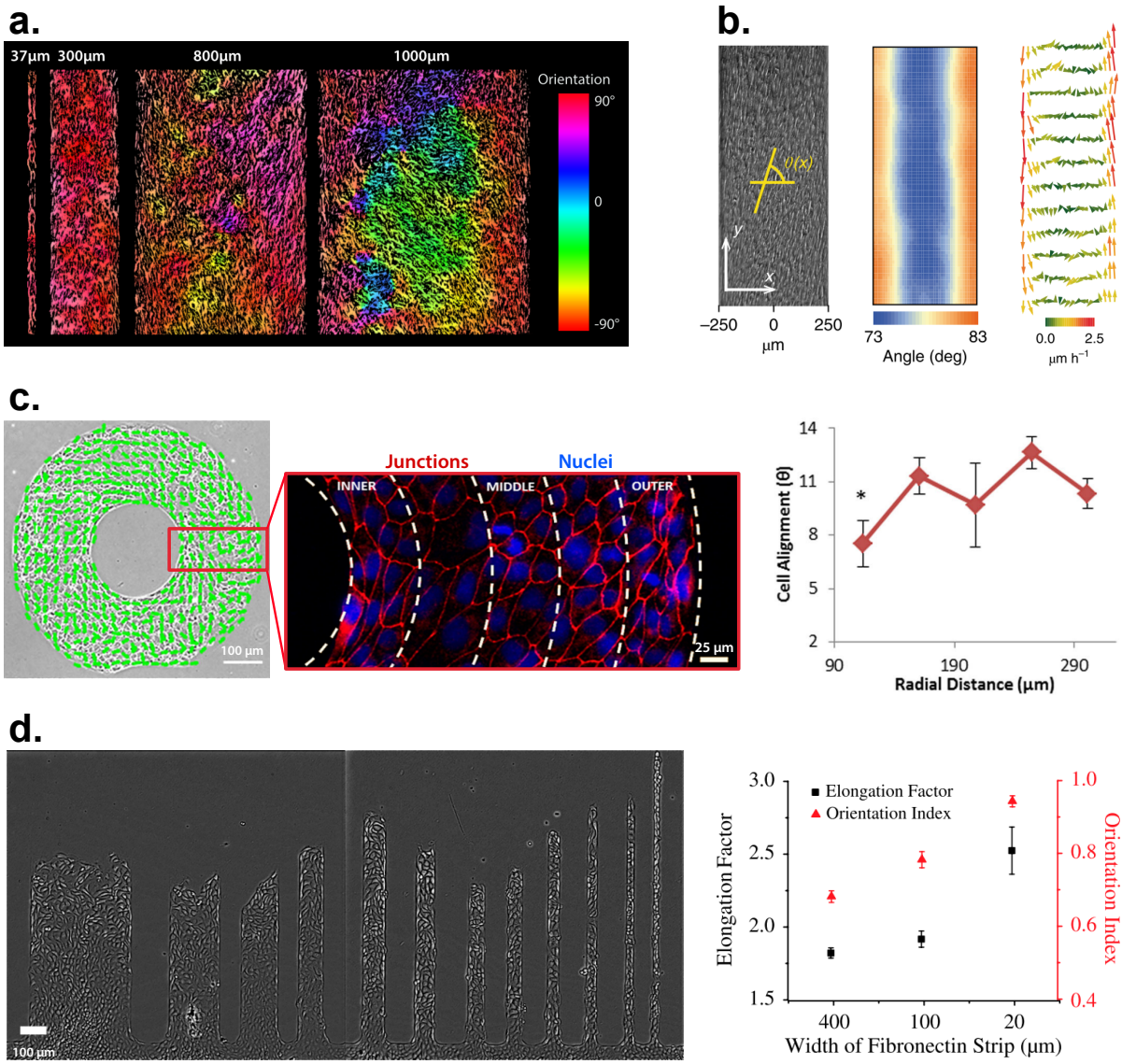


Figure 1.17: Cellular orientation in presence of external boundaries. **a.**) Orientation of NIH-3T3 fibroblasts confined on strips of different width (*left*). An angle of 0° represents orientation perpendicular to the stripe long edge. Adapted from [253]. **b.**) Brightfield image of RPE1 cells on 500 $\mu$m wide strips (*left*), average orientation along the channel (*middle*), and average velocity field (*right*). Adapted from [254]. **c.**) Brightfield image of MDCK cells confined on rings of external radius equal to 325 $\mu$m and internal radius equal to 90 $\mu$m (*left*). Staining of the junctions (*middle*) highlights cell orientation (*right*). Adapted from [256]. **d.**) MDCK monolayer migrating on adhesive strips of different widths (*left*) and the quantification of elongation ratio and orientation for 3 widths (*right*). Adapted from [257].

align within 15° of the tangential direction [256] (see Figure 1.17c). This is unsurprising because we know that cells coordinate their migration velocity over a well-defined correlation distance, $\sim$ 150 $\mu$m for MDCKs (see subsubsection 1.5.2.2), so we expect any forced orientation to propagate within the tissue for approximately the same length. If cells at the edges can only migrate parallelly to the border, then an overall orientation is to be expected. Similar results are obtained for MDCKs confined on strips of different widths, confirming that cell orientation increases with decreasing width, and becomes

global below $\sim$ 100 $\mu$m [257] (see Figure 1.17d).

### 1.7.3 Collective migration with confining borders

The tendency of cells to correlate their velocity over a specific distance is a hallmark of CCM, giving rise to many of the phenomena highlighted in Figure 1.12. The presence of boundaries, together with the preferential orientation they cause, enabled scientists to isolate and reproduce some of these behaviors.

When freely migrating in a 2D planar geometry, patches of cells spontaneously generate rotating swirls of different sizes, a behavior that can be replicated on round patterns (i.e. discs of different size). The most rudimentary form is 2 cells confined on small circular islands, situation in which the angular symmetry is spontaneously broken and cells are observed to rotate in a coordinated manner around the center of the pattern [199, 258]. On a much larger scale ($\sim$ 200 $\mu$m), MDCK tissues plated on similar round islands respond in the same manner [165] (see Figure 1.18a). On these patterns, cells exhibit different behaviors depending on density, adhesion strength and, most importantly, confinement size. Before reaching confluence, cell clusters move mostly in a disorganized manner, occasionally displaying collective rotation, although with extremely short persistence. Once confluence is reached, the tissues begin rotating in a "disc-like" synchronized and collective manner. As expected, the increase of density associated to cell division produces a slow decrease of the rotational speed, with average velocity values going from $\sim$ 25 $\mu$m/h to $\sim$ 8 $\mu$m/h, and an eventual jamming of the tissue. Interestingly, there seems to be a critical diameter ($\sim$ 250 $\mu$m) of the circular patterns above which global rotation is substituted by smaller vortices and transient coordinated flows. This is reasonable when viewed with the velocity correlation length ($\sim$ 150 $\mu$m, see subsubsection 1.5.2.2) in mind. For small circles, the whole area falls within this distance, and cells can cordinate their motion globally. When the diameter approaches twice the correlation length, cells at opposing sides of the colony behave "independently", and multiple swirls are formed. Since supra-cellular coordination depends on cell-cell junctions, it is unsurprising that MDCKs where cadherins are downregulated, as well as cancerous cell lines, cannot give rise to collective rotations. Interestingly, these collective motion have also been associated to counter rotating waves of ERK activation (see subsection 1.6.7), although with very different speeds [198] (see Figure 1.18b).

These experiments tell us that increasing the confinement length above the typical velocity correlation distance drives a transition between migration modes, and this is also verified on adhesive strips [257]. By creating a cell reservoir, and then releasing the

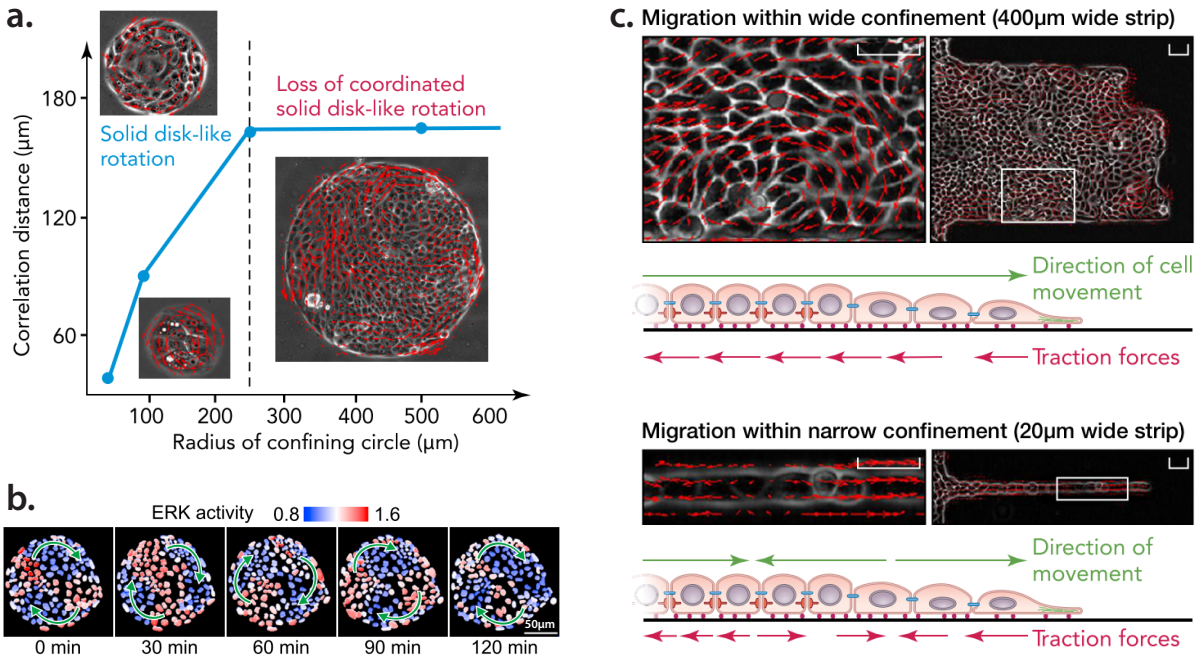


Figure 1.18: Collective cell migration in confined 2D environments. **a.**) Plot of the velocity correlation distance for MDCK cells plated on circular adhesive islands. The correlation increases with the radius as long as cells exhibit synchronized collective rotation. Above the critical distance (*vertical dashed line*), single separated swirls appear and the correlation remains constant. Adapted from [210]. **b.**) ERK activation wave rotating in a clockwise direction while cells rotate in a counter-clockwise manner on circular patterns. Adapted from [198]. **c.**). PIV measurements of MDCK cells migrating on wide channels (*top*) showing the presence of vortices. On more narrow channels (*bottom*) cells migrate in a contraction-relaxation manner. The schemes summarize the distributions of traction forces for both behaviors. Adapted from [210].

tissue onto a pre-patterned substrate, the authors confined the wound healing migration of MDCK tissues to strips of different widths (see Figure 1.17d and Figure 1.18c). As one might expect, wide channels allow the formation of vortices (diameter $\sim 300$ $\mu$m) and the presence of finger-like protrusions and leader cells, a behavior reminiscent of that of unconfined wounds. These vortices become less prominent when the migration of cells is confined to strips whose width is smaller than the velocity correlation length (100 to 200 $\mu$m). In this situation, cell velocity becomes, on average, oriented in the direction of the strip [257], and all monolayers below this confinement size advance with approximately constant speed ($\sim 20$ $\mu$m/h) [192]. In this regime, the velocity of cells follows a plug-flow-like distribution perpendicularly to the channel, and the overall flow is well described by a constant drift component and a diffusion-like contribution dependent on local cell density [192]. Vortices disappear altogether under the strongest confinement. In very narrow strips ($\sim 20$ $\mu$m), cells become more elongated, the velocity becomes strongly aligned in the direction of the strip, and the front of the tissue advances more rapidly. Moreover, PIV analysis shows that in highly confined geometries, MDCKs switch to a contraction-relaxation or “caterpillar-like” migration mode, whose

cycle spans more or less 100 $\mu$m [257] (see Figure 1.18c). Interestingly, the advance of monolayers in wide strips is associated to a monotonic increase in the stress component, in line with CCM in wound healing experiments (see subsection 1.5.5). Cells migrating by contraction-relaxation, on the other hand, exert on the substrate an alternation of positive and negative forces. Once more, Aoki and colleagues reproduced these experiment, and found periodic waves of ERK activity associated to the oscillation of MDCK cells in thin lines (width = 15 $\mu$m) [198]. Even though not specifically reported, the periodicity of these oscillations is $\sim$ 4 hours and 250 $\mu$m, values in agreement with the mechanical phenomena presented later (see section 1.8).

It is worth noting that a similar transition between migration modes is observed under tubular confinement, although the overall velocity of the front follows an opposite trend with the diameter [259].

## 1.8 Mechanical waves in 2 dimensional tissues

Another effect of confinement is that, in many situations, it highlights the emergence of wave-like phenomena, which we will refer to as mechanical waves. Chen and colleagues define them as "oscillations of mechanical parameters within the tissue – such as the tissue strain rate (a direct consequence of velocity patterns) and mechanical stress – in space and time, which can travel from one point to another, like ripples in water" [260] or sound waves through a medium.

The situations leading to the spontaneous appearance of mechanical waves can be subdivided into two major categories: expanding monolayers, being it freely or with the forceful migration through confined spaces [174, 194, 195, 257]; and fully confined environments (such as circles or rectangles) where cell migration is limited to local cell rearrangements [128, 163, 165, 172].

### 1.8.1 Waves in expanding monolayers

#### 1.8.1.1 Freely expanding

Before diving into confined situations, we will first consider the case of expanding monolayers [174]. This is a stereotypical example not only because, chronologically, it was the first one reporting the presence of mechanical waves, but also because it highlights the existence of both oscillations in velocity and in forces/stresses. As explained previously in subsection 1.5.5, when a confluent monolayer is offered free space, cells at the edge are the first ones to react: they polarize towards the wound and begin mi-

grating and exerting forces onto the substrate. This pattern is closely followed by the monolayer stress, which is initially limited to a boundary layer near the edge, and will eventually propagate backwards towards the bulk (see Figure 1.19a,b). This trend is not only typical of the initial moment, but it continues in a fluctuating manner throughout the expansion of the monolayer. By averaging their measurables over y (i.e. to obtain a measurement as a function of the distance from the edge, x), the authors of [174] obtained the kymographs in Figure 1.19d-f, which demonstrate in a clear way the presence of mechanical waves of velocity, stress and tissue strain-rate ($\dot{\varepsilon}_{xx}$). The behavior of the latter, calculated from the velocity ($\dot{\varepsilon}_{xx} = \partial v_x/\partial x$) is the most transparent: wave-like excitations originate from the edge, propagate backwards into the tissue, past the midline and towards the opposite edge at a speed of roughly 60 $\mu$m/h, in what the authors call "X-waves" [174]. If, normally, we would expect stress to rise monotonically from the edges towards the midline, X-waves modulate this behavior, so that monolayer stress in the center of the tissue oscillates with a periodicity of $\sim$ 5 hours (see Figure 1.19c). Interestingly, these fluctuations are in phase with those of cell area in a trend reminiscent of purely elastic behavior (see subsection 1.5.6). As one might expect by now, inhibition of both actin contractility and cell-cell adhesiveness arrested the oscillations.

#### 1.8.1.2 Colliding tissues

Surprisingly, mechanical waves are not only distinctive of expanding monolayers, but they have also been observed in situations where a migrating tissue meets an obstacle, being it another epithelium or a wall [194, 261]. When two repulsive tissues meet, they create an interface characterized by parallel cell alignment and strong tractions. As time proceeds, cell density increases and the tissue start jamming, a conditions necessary for the appearance of waves at boundaries. The mechanical dynamics are, once more, visualized as kymographs of the average components perpendicular to the boundary (Figure 1.19g-i). Cells at the interface exert forces pulling away from the edge, but as we move further within the tissue we notice nearly periodic oscillations in the direction of the forces (Figure 1.19i). Rather than homogenizing, this pattern seems to be stable in time, in what is a long-lived supracellular cooperative behavior. The periodicity is approximately 50 $\mu$m, a value comparable with those obtained for traveling oscillations in expanding monolayers [174, 213]. If these characteristics might have been expected based on previous works, a peculiarity of colliding epithelia is the presence of deformation/velocity waves propagating across the monolayer. The diagonal bands in Figure 1.19g,h represent velocity/strain-rate patches launched at the boundary and

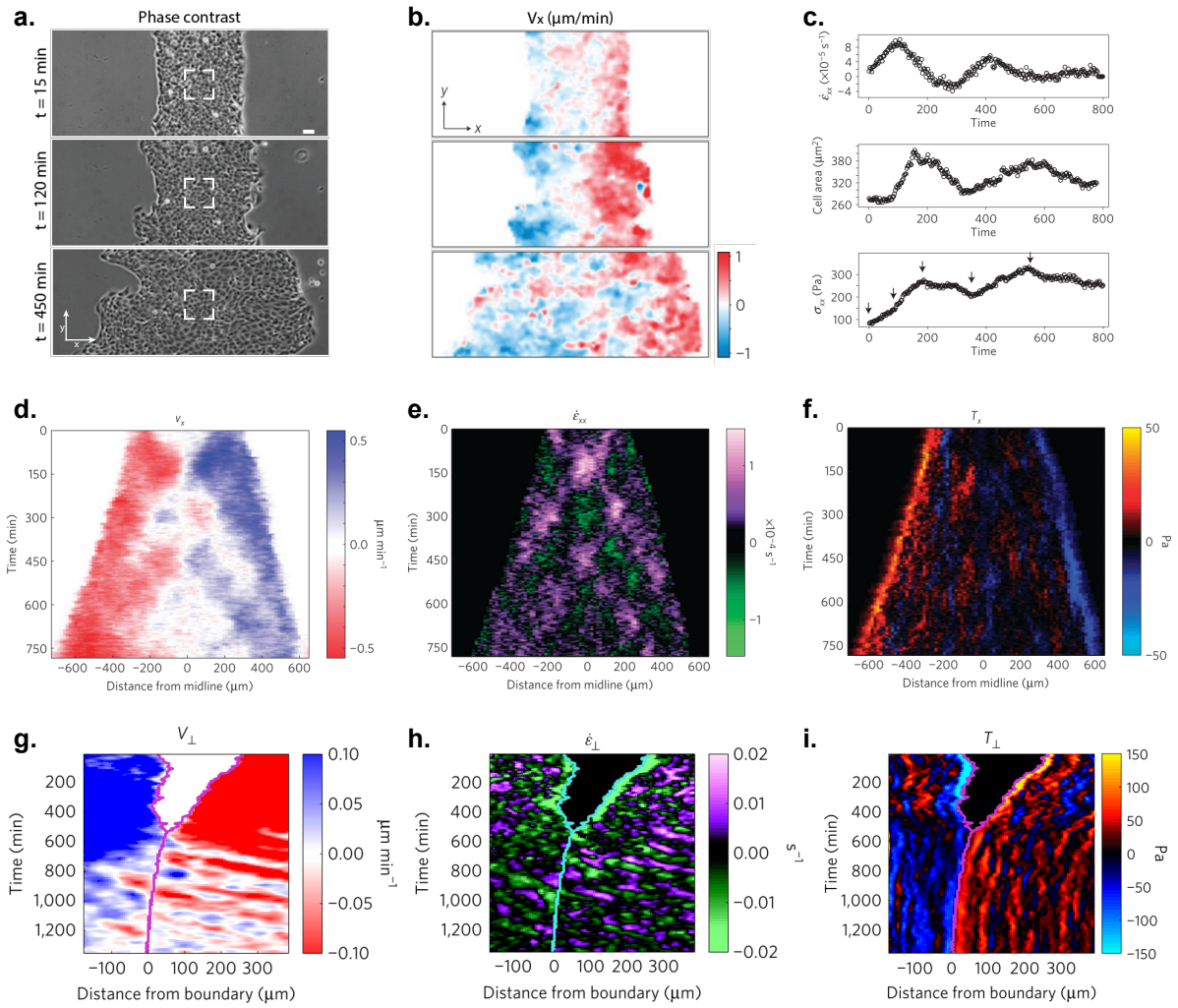


Figure 1.19: Mechanical waves in expanding monolayers and at repulsive interfaces. A confluent tissue is grown within a rectangular hole in a PDMS membrane, which is in turn resting on top of a collagen substrate. The membrane is lifted and the tissue starts invading the available space (**a.**), moving outwards with a velocity measured with PIV (**b.**). The mechanical behavior of the tissue is described by averaging the components in the x-direction over y (the tissue edge) to generate kymographs of x-velocity ($V_x$, **d.**), strain-rate ($\dot{\varepsilon}_{xx}$, **e.**) and $x$-tractions ($T_x$, **f.**). The average values of $\dot{\varepsilon}_{xx}$, cell area and monolayer stress component ($\sigma_{xx}$) at the monolayer midline (averaged over the white square in *a.*) are reported in (**c.**). Adapted from [174]. A similar analysis, for the case of 2 colliding repulsive monolayers, highlights the presence of oscillations in velocity ($V_x$, **g.**), strain-rate ($\dot{\varepsilon}_{xx}$, **h.**) and x-tractions ($T_x$, **i.**). Adapted from [194].

traveling backwards at a velocity of $\sim$ 120 $\mu$m/h, without attenuation. Interestingly, similar waves were also observed at the boundary with a repulsive wall and identical tissues, making velocity waves a generic feature of repulsive interfaces.

#### 1.8.1.3 Wound healing in confined channels

In a recent paper [195], Tlili and colleagues repeated wound healing experiments while forcing MDCK tissues to migrate along functionalized adhesive strips. Even though they do not report a strong effect of the confinement width, like in [257], the lack of swirling

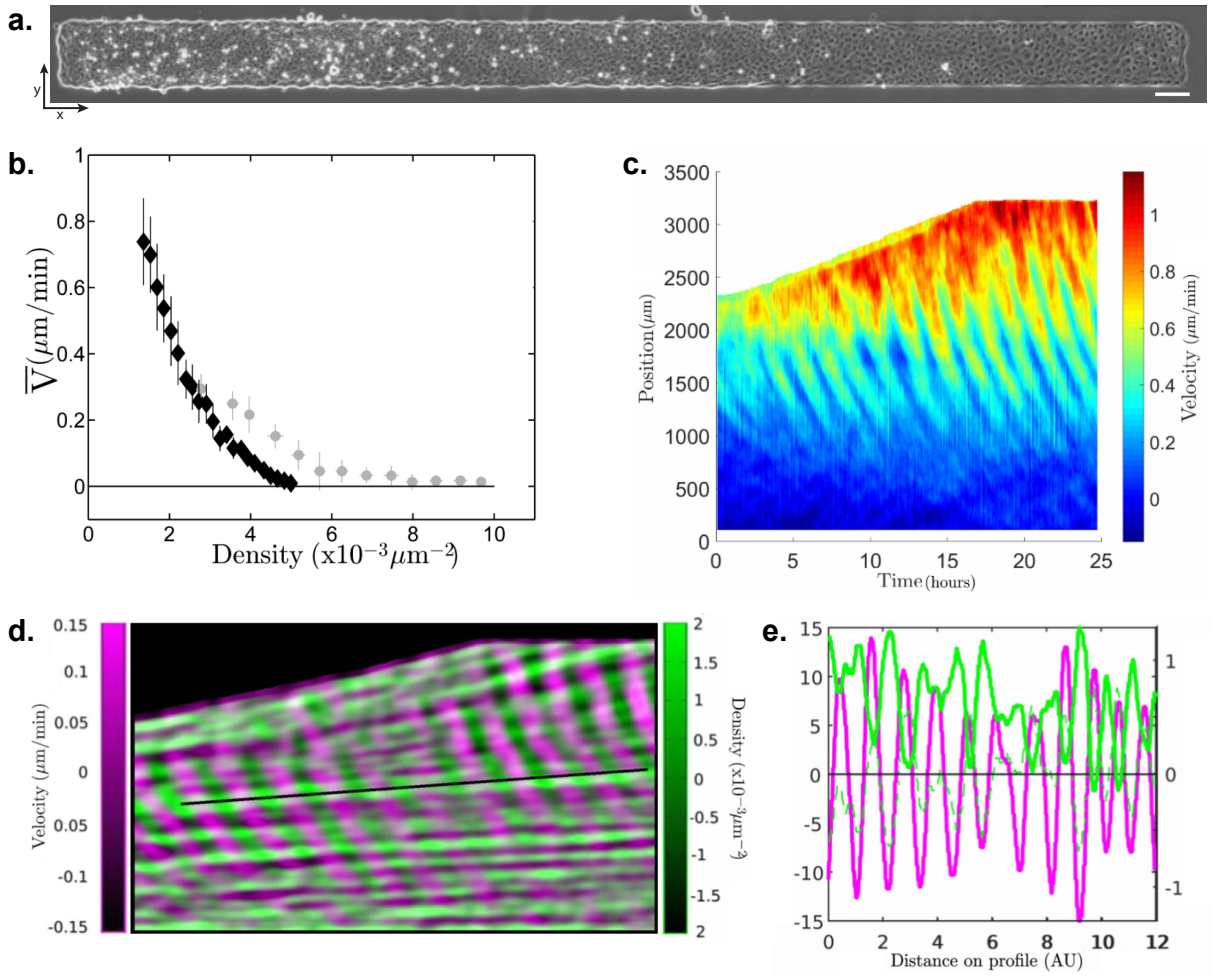


Figure 1.20: Mechanical waves in confined expanding monolayers. **a.**) Brightfield image of MDCK cells expanding in confined channels without proliferation (scalebar = 100 $\mu$m). **b.**) Graph reporting a negative correlation between cell density and average velocity for experiments where proliferation progressed normally (*gray circles*) or was inhibited (*black diamonds*). **c.**) Kymograph of the velocity of the expanding tissue in time (without proliferation). **d.**) Superimposed kymographs of small scale variations in local cell density (*green*) and velocity (*purple*). The space along $x$ is reported on the vertical axis (from 0 at the bottom to 3 $m$m at the top) and time on the horizontal axis (from 0 on the left to 25 hours on the right). The dark space in the top-left corner represents the area not yet invaded by the tissue. **e.**) Plots of density (*green*) and velocity (*purple*) along the black line in (*d*). The phase opposition between the quantities plotted is highlighted by inverting the sign of the density plot (*dashed green line*). Adapted from [195].

motion and globally directed, quasi-laminar flow place their experiments in the central region (see subsection 1.7.3), where migration is strongly guided, albeit without the presence of the contraction-relaxation phenotype. The authors inhibit cell division in order to disentangle the contribution of migration and proliferation, and they report faster advance of the leading edge ($\sim$ 40 $\mu$m/h) compared to similar examples where mitosis was unaffected. The first observation in such conditions is that, as the tissue spreads and cells in the back progressively join the forward migration, the average

velocity decreases from the front towards the bulk. Interestingly, the velocity is inversely proportional to local cell density (see Figure 1.20b), in a trend that does not depend on the distance from the leading edge.

On top of this average velocity profile, the authors observe multiple periods of backwards propagating velocity waves (see Figure 1.20c,d), essentially describing cells that slow down and accelerate with a period of $\sim$ 2 hours and a wavelength of $\sim$ 1 $m$m. The absence of cell division guarantees a better contrast and, thanks to the lack of jamming, longer observations ($\sim$ 20 h). If the nature of the waves is similar to those reported before, their phase velocity is much higher, around 600 $\mu$m/h. Moreover, the wave crests in Figure 1.20c are curved, evidence that the wave slows down near the bulk, where density is higher. There is, in fact, a strong link between velocity oscillations and inhomogeneities in cell numbers (see Figure 1.20d). The authors report steady fluctuations of density (period $\sim$ 200 $\mu$m) parallel to the edge, which seem to deform with the stretching of the tissue. More interestingly, density oscillations are present in the perpendicular direction, in a fashion that follows velocity waves in phase opposition (Figure 1.20d,e). The authors also demonstrate that lamellipodia inhibition slows or hinders the formation of waves altogether, confirming once more the fundamental role played by actin contractility in these phenomena.

Overall, these evidences describe backwards mechanical waves as a common feature of all the boundaries of migrating monolayers, being them with free space or repulsive walls. Here, we have concentrated on planar geometry, but similar back-propagating velocity waves have been reported under tubular confinement, traveling at comparable speeds [259]. Even though the values vary between reports, there is agreement on the general magnitude for the periodicity of these phenomena, in the order of hours and hundreds of micrometers.

An interesting correlation is that with waves of ERK activation (see subsection 1.6.7), which have been reproduced in three of the situations mentioned in this section: free expansion, swirling motion and contraction-relaxation migration [198]. Strikingly, the periodicity of ERK waves ($\sim$ 4 hours and 250 $\mu$m) agrees with the typical time and space of mechanical oscillations, a similarity which begs further experimental work.

A different kind of mechanical wave has also been reported in fully confined tissues, where collective motion only happens through neighbors exchange rather than directed expansion.

### 1.8.2 Breathing oscillations in fully confined space

Oscillatory movements have been observed in epithelia confined to round patterns of radii smaller than $\sim 300$ $\mu$m. Contrarily to the swirling motion presented earlier, these oscillations happen along the radial direction, displaying standing waves of highly coordinated outward and inward cell movement (Figure 1.21) [128, 163, 172]. The two phenomena, collective rotation and these "breathing " oscillations, are not mutually exclusive, but are rather superimposed and observed together. As one might expect, they are both only present at intermediate densities and the jamming transition characteristic of cell crowding brings them to a halt [128, 163]. Within this narrow time window, oscillations are present as modulation of the radial velocity, which is generally averaged over the angular coordinate for better visualization. When this is done (Figure 1.21b-*right*), we can appreciate that cells in the center of the disk and those at the far edge tend to be still, whereas the maximum of the radial velocity is at the mid-point between the two positions [128]. The amplitude of the cell displacements is the order of micrometers, and the period a few hours. Although this latter quantity is in general agreement with those for expanding monolayers, the period of breathing oscillations depends strongly on the radius of the round patch (Figure 1.21a-*right*). For what concerns the amplitude of the velocity fluctuations, it changes depending on the accounts, from $\sim 15$ $\mu$m/h [163] to less than 1 $\mu$m/h [172].

Surprisingly, even though radial motion is very limited, oscillations in cell velocity are accompanied by similar standing-waves in the radial component of the tractions on the substrate, with patterns of inwards and outwards pointing forces over time (Figure 1.21c) [172]. These oscillations only interest the central part of the tissue, as cells at the edges constantly pull themselves towards the exterior, in a manner coherent with kenotaxis. One might be tempted to assume that tractions and velocities are interdependent, an assumption carefully disproven by the authors, who demonstrate that no correlation between traction and velocities, nor their relative angles, exists. The study of stresses within the monolayer led to an interesting conclusion: tensions and cell area (i.e. strain) are in phase, implying that the tissue behaves elastically with no viscous contribution (see subsection 1.5.6).

Given the correlation between the presence of waves and ERK activation advanced recently (see subsection 1.6.7) [198], it is interesting to point out that breathing oscillation were suppressed upon ERK inhibition [172]. This is loosely in contrast with what is reported, admittedly in a very different situation, in [173], indicating that ERK activity has no significant role in kenotaxis.

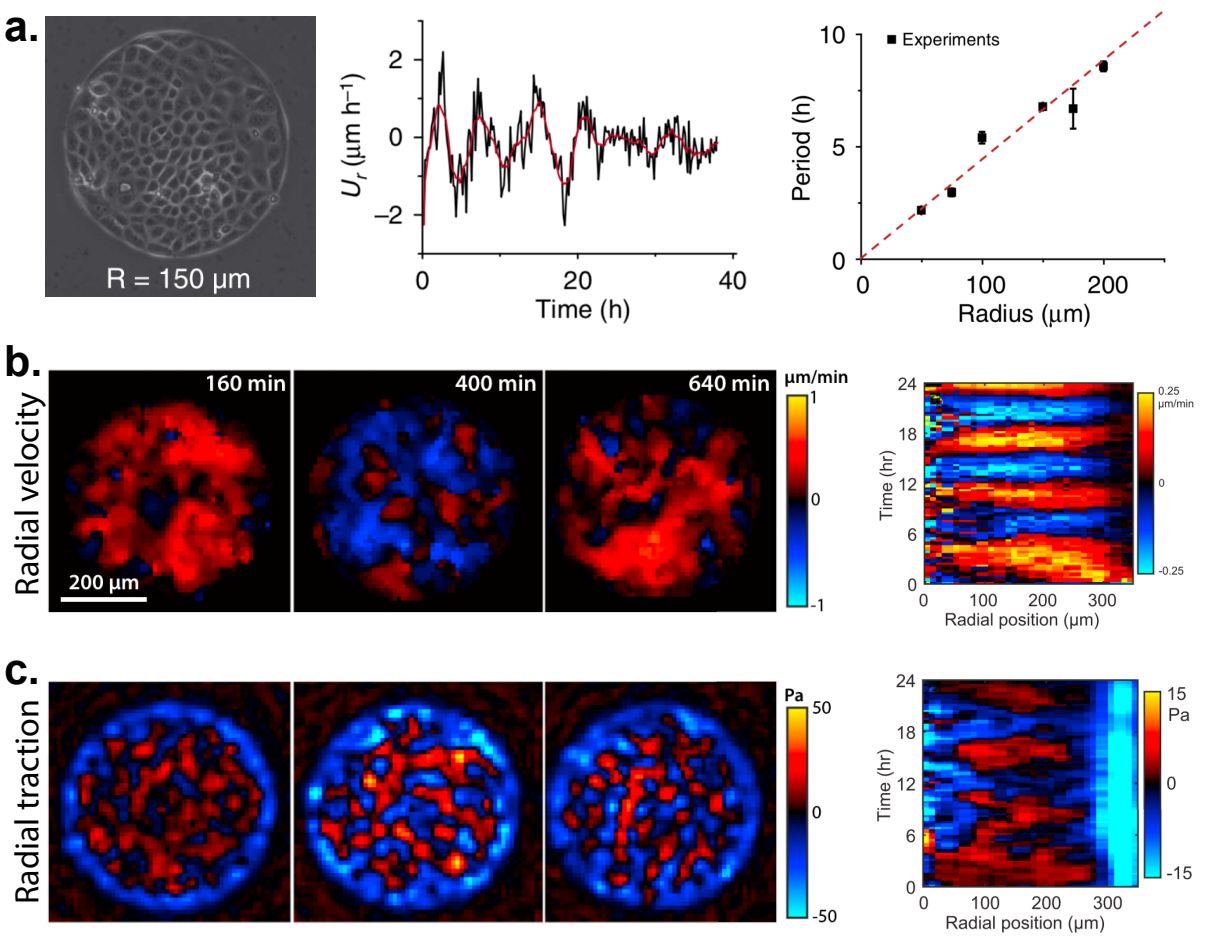


Figure 1.21: Breathing oscillations in epithelial tissues confined to round adhesive patterns. **a.**) A phase-contrast image of MDCK cells confined on a disk-like pattern (*left*) and the evolution of the average radial velocity in time (*center*). The typical time period for these oscillations can be quantified as a function of the radius of the tissue (*right*). Adapted from [128]. **b.**) Examples of the distribution of radial velocity over time for MDCK cells on patterns of radius equal to 350 $\mu$m. The velocity is averaged over the angular direction to yield a kymographs (*right*). **c.**) Cell-generated tractions on the substrate (*left*) for the examples in (*b*) are reported together with a kymograph of the average over the angular direction (*right*). Adapted from [172].

These breathing oscillations share many similarities with those mechanical waves present in expanding monolayers, like the strong dependence on cell-cell junctions and contractility, and might be explained by the same basic principles of force transmission and mechanotransducive coupling with polarization [172]. One big difference lies in that, whereas velocity waves in wound healing are propagating through the tissue, on circular patterns the phase difference between radial positions is insignificant.

### 1.8.3 Effective inertia at the cellular level

The propagation of mechanical waves is, from a physical point of view, not of any particular complexity. It can generally be explained as a continuous inter-conversion between potential and kinetic energy, damped by friction forces. In this scenario, the presence

of oscillations critically depends on the ratio between friction forces ("fighting" the oscillation) and the inertia (i.e. the mass, defining a timescale for the oscillation). When friction is negligible, the system is underdamped and waves can propagate indefinitely. Within tissues, on the other hand, being the mass of the cell extremely small, inertia is negligible compared to friction (i.e. the viscous drag of the liquid) [217], an overdamped situation where wave propagation is, in principle, impossible. In this case, to explain the presence of the mechanical waves we have just reviewed, an additional phenomenon must be present to play the role of "effective inertia" [194] and restore oscillatory behaviors. Even though the biological nature of this feedback is not clear yet, merlin seems like the most obvious candidate, theoretical works have taken this factor into account by introducing an additional term. Even though a full review of the models utilized to explain oscillations in tissues is beyond the scope of this work (see [178, 179, 262]), it is nonetheless interesting to quickly glance at the different solutions embraced in literature.

One example is that of Vicsek models [263], where the velocity of each cell is assumed to align to that of its neighbors [128]. This alignment happens on a typical timescale, a fundamental quantity for the appearance of coordinated motion [264], and is affected by rotational noise. The group of Marchetti introduces a feedback between the local strain and the rate of change in contractile tension. Simply put, larger cells will exert stronger contractile forces. This, together with the assumption of tissue elastic behavior, explains the presence of oscillations [172, 265]. Other possibilities are a dynamic response from the cytoskeleton, first reinforcing and then fluidizing in response to stretch [174], and a slow realignment of cell polarity to the local strain [195].

## 1.9 Concluding remarks

The presence of mechanical waves acquires new importance when viewed in light of the intricate relationship between bio-chemical signaling and mechanosensitive pathways. As highlighted throughout this introduction, cells are not only able to read the mechanical state of the surroundings, but also utilize this information to adjust their behavior and affect that of neighboring cells and their environment. Mechanical signals are, by all means, a major communication channel in biological systems. In this context, just like for humans, the presence of traveling waves make sense as a mean to exchange information over distances bigger than the immediate surroundings. This interpretation, even though extremely enticing, is still suffering from a general lack of documented

biological consequences. The obvious candidates for such role are those molecules involved in mechanotransduction, chief among which is YAP/TAZ (see subsection 1.3.3). This possibility has been recently explored by Peyret and colleagues [266], in a paper which focuses on the presence of oscillations in confined environments. Due to the overlap of the results presented in [266] with what we obtained and the almost striking contemporaneity between the publications, we will comment this paper in the discussion.

The idea of mechanical waves for long-distance communication brings us back to the original question behind this work, and, in all fairness, behind all studies of morphogenesis and development. What controls the appearance of patterns in biology? In other words, all events leading to complex structures and shapes require cells in different positions to behave differently, in terms of differentiation, proliferation and death [11]. For this to happen, those same cells need to somehow be aware of the state of the tissue and their particular location. How is this possible? The concept is summarized as *positional sensing* [176], and, as we now understand, happens through a bidirectional relationship between genetic and epigenetic factors, mechanical signals being a crucial player within this second category [130]. In 2D *in vitro* systems, the effect of mechanics on cell differentiation [77, 127, 133], proliferation [126, 191, 267], extrusion [128, 255] and migration [165, 210, 257] is well documented. In many of these cases, the specific setup prompts the emergence of a long-range mechanical landscape, used as a reference system. An example is that of cells plated on square patters, where the edges are under stronger stress compared to the inside [126]. Every single cell then feels the local state, and acts accordingly, in this particular case enhancing or reducing proliferation rate. The coordination offered by the mechanical reference system leads to the emergence of a global phenomenon, at a scale much larger than that of the single cell sphere of influence. The presence of standing/traveling mechanical waves fits well into this framework, serving for the both the local guidance and long-range behavioral coordination.

Throughout my work, we built a setup to reproduce periodic velocity waves in confined tissues, with the intent of understanding whether mechanical oscillations are intrinsically encoded in the activity of the cell, or if they are induced by the characteristics of the environment (i.e. the presence of external constraints). We then performed some experiments directed at finding a biological consequence to such velocity oscillations.

The matter of waves in epithelia is momentarily set aside, to be tackled later in chapter 3. Originally, we were fascinated by the concept of positional information and how a local mechanical parameter might be involved. For this reason, we set out to design and

build a protocol to control and continuously tune the local mechanical state of cells. We decided to rely on the geometrical control offered by 2D-substrate-patterning for our input, and on microscopy as well as immunostaining to characterize the biological response. Our experimental approach and the techniques used are detailed in the next chapter.

# 2. Materials and Methods

This chapter explains in detail all the materials, techniques and protocols utilized. The basic idea behind this project is, in an oversimplified manner, to study how several aspects of cellular behavior are affected by the local geometrical and mechanical properties of the confinement. We tackled the problem with a bottom-up approach: we chose to take many liberties when it came to seeking *in vivo* conditions, because this granted us a better control on the inputs of the system. As described in the introduction, in fact, cells in living organisms are constantly subjected to a variety of signals. Many of these come from the environment, which communicates with cells through hormones, nutrients, oxygen, inorganic molecules, elastic as well as plastic responses, geometry and many more. In principle, each and every property of the environment can be sensed and utilized by cells. To add to this complexity, we now know that these signals do not play compartmentalized roles, and that we are facing a extremely entangled network of inputs, where every actor influences and is influenced by many others. If the behavior of cells is still not fully characterized, it is because this overwhelming complexity often makes it impossible to distinguish inputs and outputs and build a logical connection.

Our approach is to try to reduce this complexity and force phenomena into simplicity, and this requires conditions that are not necessarily "natural". We use an epithelial cell type which mimics the tightly packed cell layers found *in vivo*. Even though this lacks the complexity of a full tissue, it allows us to work in a planar configuration, and to expose all cells to the same culture medium decoupling bio-chemical and mechanical signals. We welcome some limitations because we want to understand cell behavior in its simplest form. We would then, in my time or with successive works, use the knowledge acquired to formulate hypotheses and design new experiments to mimic more realistic conditions. At the same time, our idea is to try to find general rules. Given the amount and diversity of signaling in biology, simplification is our strategy to control the inputs and discern related outputs.

The experiments we designed have three main requisites: a model for living tissues; a mean to control the geometry of the space allowed for cell and thus tune the input

of the system; and finally a method to look at the response of the system in terms of cell movement, arrangements, forces and many more. The techniques developed or adapted from literature for these purposes are here presented. This chapter is divided into three main sections, describing how we chose to tackle each of the requisites mentioned above.

## 2.1 Tissue model and cell culture

The choice of the cell type is crucial for the scientific and biological significance of the project, and that is why we settled on Canis familiaris kidney normal (MDCK). These particular cells are widely used as models for epithelium, which is usually comprised of tightly packed cells organized into sheets. MDCKs have in fact the tendency to grow in arranged layers, which well suits the aim of this work. Moreover, the behavior of this cell type has been well documented on a number of recent papers. [159, 195, 213, 254, 257, 268].

Canis familiaris kidney normal (MDCK) cells expressing E-cadherins-EGFP (kindly provided by Isabelle Bonnet, Institut Curie, 26 rue d'Ulm 75248 PARIS, France) were cultured in Dulbecco's Modified Essential Medium (DMEM) containing 10% bovine fetal serum (BFS) and 1% Penicillin/Streptomycin (GIBCO, Invitrogen), at 37 °C and 5% $CO_2$. Cells were detached with trypsin (Gibco) and seeded at different densities on the micropatterned substrates. After $\sim$2 hours each sample was washed with PBS and previously warmed up medium to remove all unattached cells still floating in solution.

## 2.2 Controlling boundary conditions: micropatterning techniques

Having settled on a cellular model, the next step in designing our experiments was to find a method to confine tissue growth, and thus fix the boundary conditions of our system. The nature of this external input and how to deliver it are as important for the significance of the project as the choice of the cell type. These two factors should be integrated coherently in order to tailor the experimental setup to the question in mind.

In our case, we chose 2D micro-fabrication. With the exception of factors secreted by cells located within the tissue, our 2D approach allows us to uncouple bio-chemical from mechanical signals, placing us as close as possible to a situation where the only input comes from the geometrical confinement.

The techniques chosen allowed us to deposit extra-cellular matrix (ECM) proteins on patches of desired shape and size. These areas, called micro-patterns, sit on a glass slide coated with a polymer, chosen for its ability to avoid unspecific protein attachment. To spread on a substrate cells need the appropriate ECM proteins, and since these are only found on the micro-pattern area, cells are effectively contained. An additional advantage of one of the techniques chosen is the possibility to create micro-patterns on soft polyacrylamide gels. This material is biocompatible, stable and, most importantly, has an elastic modulus that can be easily tuned. It has, in fact, been shown that both spreading geometry and substrate rigidity play a role in many physiological processes [77, 78, 126, 191, 269, 270]. These techniques allow us to control both, while working on hundreds of identical tissues and increasing our statistics. We also chose 2D micro-fabrication for its simplicity and extremely robust reproducibility. Samples obtained with both techniques can be sterilized by immersing them in 70% EtOH for 1 minute prior to use. In our case this step was not necessary, but it was employed when working with epidermal stem cells.

We adopted 2 different techniques: Poly(N-isopropylacrylamide) (PNIPAM) patterning for extreme durability and long-term confinement, and Polyacrylamide (PAA) gel patterning to create soft environments and measure substrate displacements. The basic concepts behind both is to coat the surface of a glass slide with an appropriate polymeric layer able to avoid unspecific protein attachment. Selectively allowing proliferation is done by illuminating these glass slides with UV radiation through a lithographic mask. Where light reaches the surface, it burns the polymer and activates the glass. These areas are then covered by ECM proteins, creating a suitable environment for cell interaction. Patterned proteins can then be transferred on the surface of polyacrylamide gels. Both procedures follow this general guidelines, but each has advantages and drawbacks that make it suitable for different experiments and timescales.

### 2.2.1 Gel micropatterning

This is a description of the procedure based on the work done by Vignaud, Ennomani, and Théry, [271] with modifications done in the Motiv group.

All necessary steps are reported in Figure 2.1. Briefly, a glass coverslip (32 $m$m diameter), previously rinsed with water and isopropanol, is activated with $O_2$ plasma for 5 minutes (A). A poly-$_L$-lisine-PEG (pLL-PEG) drop (70 $\mu$l, 0.1 mg/ml in HEPES 10 mM) is sandwiched between the activated side of the coverslip and parafilm (B). After 30 min incubation, the glass coverslip is removed and gently washed with HEPES 10

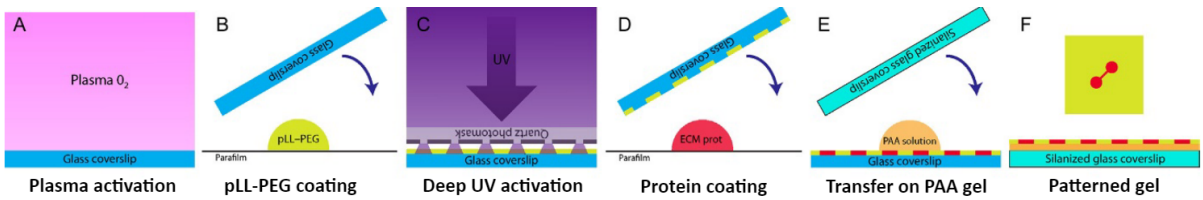


Figure 2.1: Schematic description of the fundamental steps for micropatterning glass coverslips and polyacrylamide gels. Adapted from [271].

mM. A drop (7 $\mu$l) of water is used to attach the pLL-PEG coated side of the coverslip to the chrome side of the photolithography mask, previously rinsed with water and isopropanol, and cleaned for 15 minutes with $O_2$ plasma. The mask and the coverslip are exposed to deep UV radiation for 5 minutes from the quartz side (C), burning the pLL-PEG at defined loci with minimum loss of resolution due to diffraction. The patterned coverslip is gently lifted off and washed with PBS solution. A drop (70 $\mu$l) of ECM protein (20 $\mu$g/mL fibronectin, 20 $\mu$g/mL fluorescently labeled fibrinogen in sodium bicarbonate 100 mM) is sandwiched between the patterned glass coverslip and parafilm and incubated for 30 min (D). Proteins only adsorb on the pLL-PEG free islands, creating patterns of adhesive shapes. To then transfer the proteins on top of soft gels, a solution of acrylamide and bisacrylamide is sandwiched between the patterned coverslip and a previously silanized one (E). To make future traction force microscopy possible, small fluorescent beads are added to the solution at this step. The monomer/cross-linker ratio directly controls the mesh size of the final hydrogel and, ultimately, the stiffness of the substrate [272]. By controlling the chemistry of this pre-mix solution we can tune the mechanical properties of the samples within a physiologically relevant range (1.2 to 100 kPa) [273, 274]. As the solution polymerizes, the protein pattern is transferred onto the newly formed hydrogel, which is later detached (F). The full protocol is reported in Appendix A

This technique has several advantages: the whole process is fast ($\sim$ 3 hours), low cost and extremely reproducibles. Moreover, polyacrylamide is optically transparent, inert to chemical degradation and efficient at preventing non specific cell attachment [271]. It is useful to keep in mind that, even when conserved in PBS at 4 °C, the mechanical properties of polyacrylamide gels changes with time [275]. This makes for a relatively short shelf life (gels were always used within 48h) which hinders the possibility of transporting and storing samples.

### 2.2.2 PNIPAM micropatterning

A different patterning technique, based on the use of Poly(N-isopropylacrylamide) (PNIPAM) polymer was also implemented. This was done because of the extreme robustness and confinement quality of the samples generated. If, on the one hand, the polymer is extremely stable in time, on the other the technique only allows for patterning on glass slides. It is then possible to transfer the protein on PAA gels, but the quality is generally poor. The technique was introduced by Bureau and Balland [276], and has been adapted in the Motiv group.

The fundamental steps of the procedure are reported in Figure 2.2. Briefly, a glass coverslip (32 $m$m diameter) is first rinsed with acetone and ethanol and then activated with $H_2O$ plasma for 6 minutes (A). The activated sample is then dipped for 1 minute in a 3-Aminopropyl-triethoxysilane (APTES) solution (APTES $5.4 \times 10^{-2}$ M, Triethylamine $1.8 \times 10^{-1}$ M in Toluene) and 1 minute in $\alpha$-Bromoisobutyryl bromide solution ($\alpha$-Bromoisobutyryl bromide $8.1 \times 10^{-2}$ M, Triethylamine $0.36$ M in dichloromethane). The aim of this first steps is to graft amino-terminated initiators on the surface for the subsequent atom-transfer radical polymerization (ATRP) (B). The functionalized coverslip is then flipped onto the photolithography mask, previously rinsed with $H_2O$ and ethanol. A drop (2 $\mu$l) of hexadecane is used to ensure tight attachment of the initiator-functionalized coverslip on the chrome side of the mask. The mask and the coverslip are then exposed to deep UV radiation for 2 minutes from the quartz side (C), degrading and inactivating the polymerization initiator present under the transparent parts of the photomask (D). Polymerization is later restricted to those areas that have not been exposed to UV light. The patterned coverslip is gently lifted off and washed with acetone and ethanol. For the polymerization step, the coverslip is first immersed for 30 minutes in a N-Isopropylacrylamide (NIPAM) monomer solution (NIPAM $4.4 \times 10^{-1}$ M, Copper(II) bromide $8.9 \times 10^{-4}$ M, Pentamethyldiethylenetriamine $1.2 \times 10^{-2}$ M, L-ascorbic acid $8.5 \times 10^{-3}$ M in $H_2O$), and then washed with Milli-Q water and ethanol. The coverslip obtained is covered by a patterned PNIPAM polymer brush layer, exposing polymer free islands (E). A drop (100 $\mu$l) of ECM protein is sandwiched between the patterned glass coverslip and parafilm and incubated for 30 min. Since PNIPAM avoids aspecific interactions, the proteins only adsorb on the polymer free islands, creating patterns of adhesive shapes.

Compared to pLL-PEG patterning, this procedure is more elaborated and requires

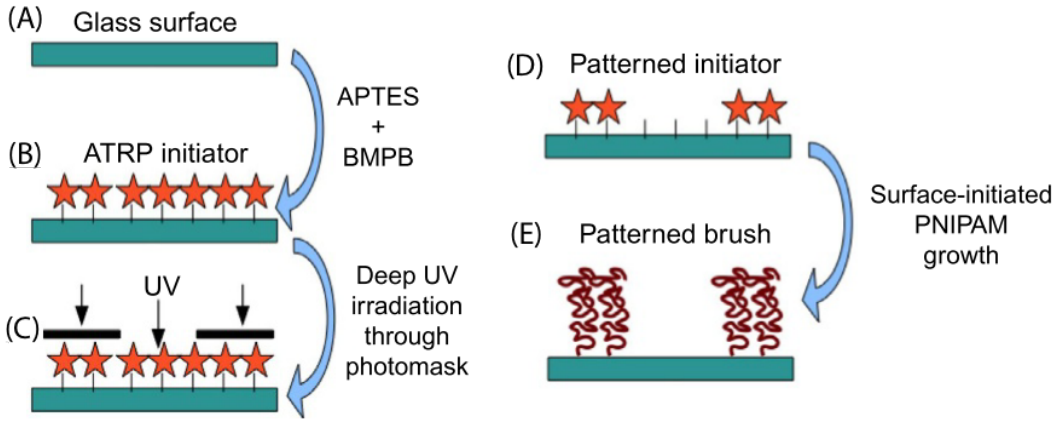


Figure 2.2: Schematic description of the fundamental steps for micropatterning glass coverslips with PNIPAM. Adapted from [276]

more complicated and time consuming chemical steps, but it offers the advantage of a stronger cell confinement over time. The high density of PNIPAM polymer chains makes up for a higher protein repulsion with respect to that of polyacrylamide gels, making it ideal for longer observations.

## 2.3 Observing cellular response: imaging and quantification

The last step in building our experimental setup was finding techniques that would allow us to observe and quantify the behavior of cells. The methods we chose are here presented, together with the motivation for adopting these specific solutions and the details of their implementation.

### 2.3.1 Image acquisition

Two different microscopic techniques were employed to image the samples, the characteristics of each making it suitable for a particular type of experiments.

#### 2.3.1.1 Optical microscopy

*Confocal Microscope*

A Leica TCS SP8 confocal microscope equipped with HC PL APO CS2 63x oil objective lens (NA 1.40) and HC PL APO CS2 40x oil objective lens (NA 1.30) was used to generate z-stacks and high resolution images when needed.

*Epifluorescence Microscope*

A Nikon Eclipse T*i*-E equipped with Plan Apo VC 60x oil objective (NA 1.40) and a Nikon CFI 40X air objective (NA 0.65) was used for Traction Force Microscopy and to obtain faster readouts and single images. In certain instances, when long time lapses required fluorescent imaging and wider field of view, this microscope was used with a Nikon CFI Plan Fluor DLL 10X objective (NA 0.30) and a $CO_2$/temperature control unit.

#### 2.3.1.2 Lensless microscopy

Performing continuous imaging of viable cells has multiple requirements. To proliferate normally cells need accurate control of $CO_2$ concentration, a constant temperature of 37 °C and extremely high humidity levels. Moreover, the particular experiments designed for this project required a wide field of view to image high number of shapes and allow for statistical analysis. These requirements are not easily met by classical microscopy, and, in the specific case of this work, the microscopes were a facility shared between numerous users, making it hard to use continuously more than one day. These reasons pushed us to search for alternative solution.

*Cytonote®*

Continuous live imaging over multiple days was performed using a Cytonote® lensless microscope produced by Iprasense. The working principle of the microscope is explained in detail in [277, 278]. Briefly, this microscope adopts an in-line holographic imaging setup (see Figure 2.3): a LED with small pinhole (150 $\mu$m diameter) acts as a point source, illuminating a sample positioned approximately 5 $c$m away with coherent light. Each cell in the petri dish scatters the incident light and the interference pattern thus produced is recorded by a small CMOS sensor, approximately 1 $m$m far from the plane of the object. Since the change in phase of the light scattered by each cell is lost, a recursive algorithm is used to predict this phase shift and then reconstruct the image of the sample, both in terms of absorption modulus and phase. The sensitivity of this system to cell thickness is exemplified by considering a cell division event. When a mitosis event begins, cells round up increasing their thickness in a process referred to as mitotic cell rounding (see Figure 2.3). This broader profile affects the length of the path traveled by light within the cell, and thus increases the final phase shift imposed. Once division is over, the two daughter cells spread again, canceling this effect. A picture was generally taken every 10 minutes, generating a time-lapse video that follows cell dynamics over time without affecting their normal behavior. The apparatus is extremely

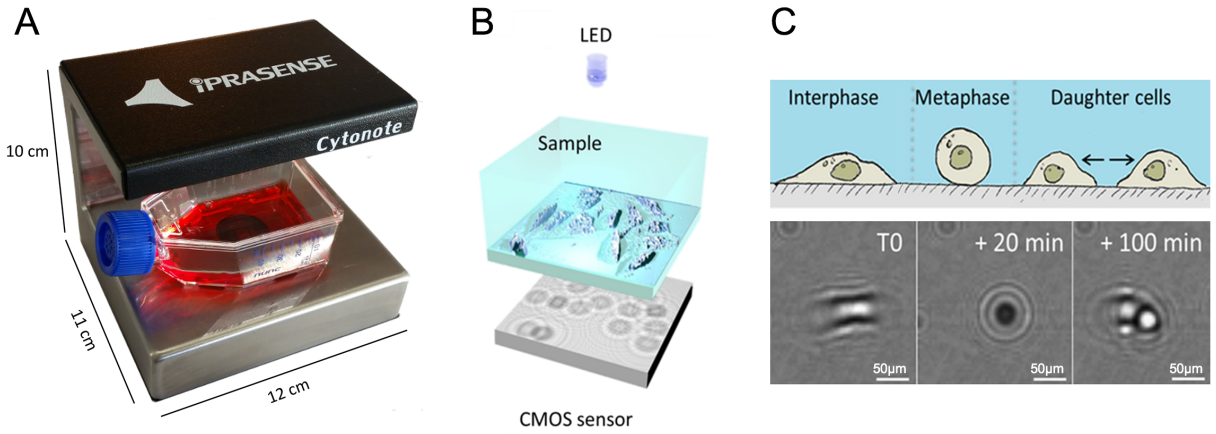


Figure 2.3: Picture of the Cytonote® lensless microscope (A) and schematic description of the components and working principle of the apparatus (B). An example of a cell division event recorded with this microscope is reported in C, together with a schematic drawing of the biological event (adapted from [277]).

small and it is designed to fit inside a cell culture incubator, removing the need of complex gas and temperature control systems built *ad hoc*. Moreover, since the field of view is only limited by the size of the CMOS sensor, the microscope gathers extremely large images ($6.5 \times 4.5$ $m$m$^2$), which allow for more statistics in terms of cell dynamics.

If, on the one hand, a wide field of view and great simplicity of use make this microscope a great tool for preliminary and exploratory experiments, on the other, the system is not specifically optimized for our experiments. The quality of the image reconstruction decreases with the density of cells, and in some cases it grows so low that it renders single cells indistinguishable. These problems hold especially true for the peculiar cell type, MDCK cells, which form strong cell-cell junctions and very tightly packed confluent layers. To remedy these issues while trying to retain the ease of use of this particular technique, we collaborated with the group of Cédric Allier at CEA-Leti to test a new prototype of lensless microscope.

*Home-built incubator microscope*

In order to improve the resolution of the images, a 10x objective was implemented in the design of the lensless microscope by the group of Cédric Allier [1]. The setup and a schematic drawing is shown in Figure 2.4. A blue LED (CREE, max 450 nm, FWHM 18 nm) source coupled with $400$ $\mu$m multimode fibre (Thorlabs) with a narrow band filter (Thorlabs FB450-10, max 450 nm, FWHM 10 nm) is used for illumination in transmission geometry. Semi-coherent light passes through the sample and is collected by 10x/0.25 NA Objective (Motic CCIS EF-N Plan, Achromat). A short tube lens (Thor-

[1] Cedric P. Allier, Commissariat á l'énergie atomique et aux énergies alternatives (CEA), LETI, MINATEC, 17 rue des martyrs, Grenoble cedex 9, 38054 France

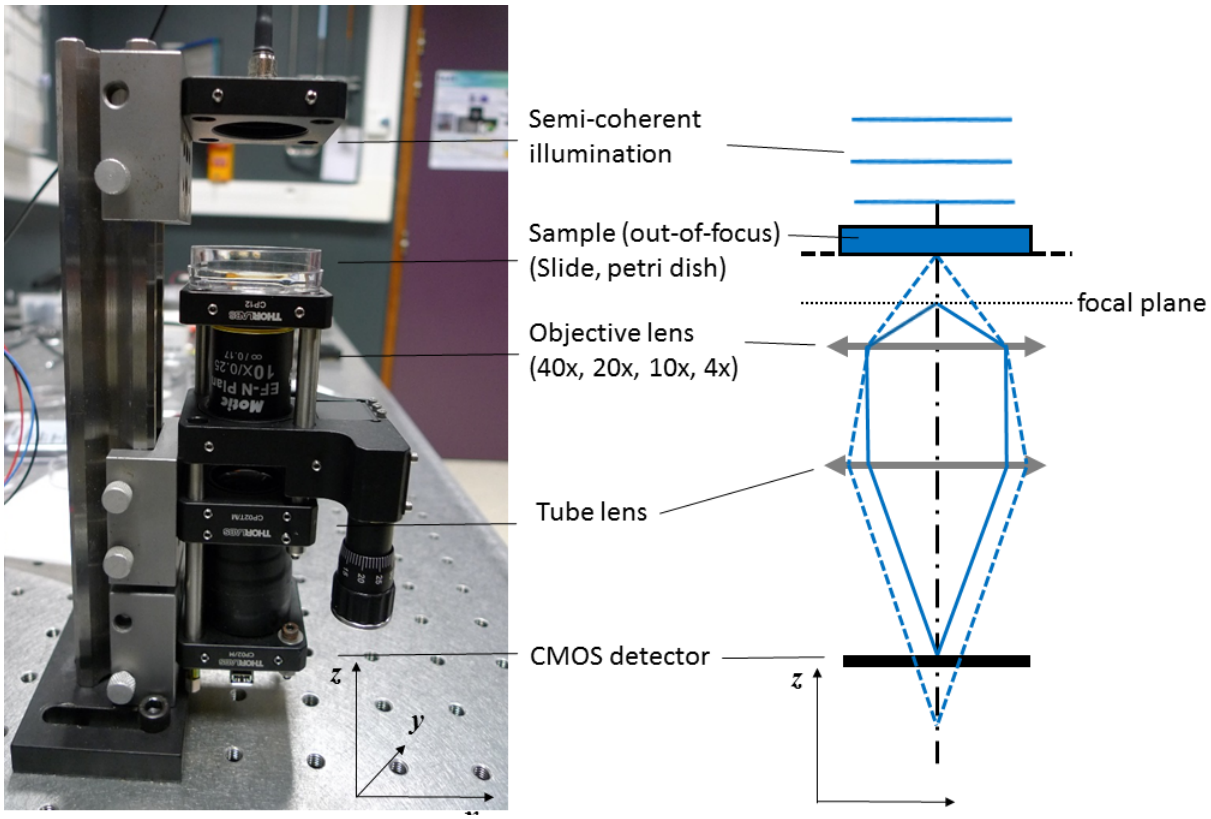


Figure 2.4: Setup for defocused imaging is a standard wide-field microscope with semi-coherent illumination. Adapted from [279].

labs, AC254-050-A, $f = 50$ $m$m) is used to create an image on a CMOS sensor (IDS UI-1492LE). Standard Thorlabs components are used for housing of the optics and the camera. Image acquisition with synchronized illumination is controlled with a Raspberry Pi (https://www.raspberrypi.org). Note, that the reconstruction of the data is performed on a different computer. The field of view of the system with 10x/0.25NA objective is $2.3 \times 1.6 = 3.7$ $m$m$^2$ and the spatial resolution is approximately 3 $\mu$m.

The reconstruction algorithm is based on an iterative optimization of Fresnel diffraction model for coherent light. The fact that the illumination is not perfectly coherent is not taken into account in the current algorithm. The reconstruction process optimizes the optical field at the object plane while maintaining a perfect agreement with measurement at the sensor plane. The reconstruction contains regularization terms based on sparsity and total variation constraints [280]. The illumination wavelength, effective pixel size (physical pixel size of the camera divided by the magnification of the system) and the out-of-focus distance are the input parameters. The out-of-focus distance can be determined from the reconstruction performed at different axial positions. A focus determination algorithm can be employed, however, we often use a manual selection. In the time-laps data the defocus is determined only once and used for the reconstruction of the whole movie. The reconstruction of a single image from our 10 Mpixel camera

takes approximately 3 minutes on our standard desktop computer (Processor Intel(R) Xenon(R) CPU E3-1240 v5 @ 3.50GHz with 32GB RAM and NVIDIA Quadro K2200 graphic card).

## 2.3.2 Staining and Pharmacological treatments

### 2.3.2.1 Fixation

The culture medium was discarded and cells were washed once in fresh PBS solution, and then fixed in paraformaldehyde (4% in DPBS) for 10 min at room temperature. After two additional PBS washings, samples were treated with permeabilization buffer (0.5% Triton® X-100 solution in PBS) for 15 minutes, followed by blocking buffer (2% Albumin Bovine Serum solution in PBS) incubation either for 1 hour at room temperature or 24 hours at 4 °C. Finally, the coverslips were mounted onto glass slides with Mowiol® 4-88 mounting medium (Polysciences, Inc.) and left to dry one night at 4 °C.

### 2.3.2.2 General immunostaining protocol

After blocking buffer treatment, cells were washed twice with PBS solution, and then incubated overnight with a primary antibody solution (1:200 YAP, 1:150 $\beta$-catenin, in blocking buffer). Samples were then retrieved, washed 3 times for 15 minutes in PBS on a rocking plate, and then incubated for 2 hours at room temperature in a secondary antibody solution (1:200 in blocking buffer). After 3 additional PBS washings (15 minutes, rocking plate) cells were, when necessary, exposed to a 1:1000 solutions of Hoechst® or Phalloidin–Atto 647N (Sigma-Aldrich) for 30 minutes, and then mounted.

### 2.3.2.3 Nuclear stainings

Nuclear stainings were performed either by exposing cells to Hoechst® 33342 (Thermo Fisher Scientific, 1 $\mu$g/ml) or NucRed™ Live 647 (Thermo Fisher Scientific, 2 drops/ml) containing medium for 45 minutes before fixation, or by incubating already blocked cells with 1:1000 solutions of Hoechst®/NucRed™ for 30 minutes prior to the mounting step.

### 2.3.2.4 Proliferation inhibition

To stop cel division, cells were treated with Mitomycin C (Sigma-Aldrich), which is known to covalently cross-link the DNA strands and impede DNA replication and, thus, mitosis. According to the manufacturer instructions, the compound was dissolved in

water continuously adjusting the pH with NaOH to a value of pH = 7. Since cell division stops $\sim$ 12 hours after treatment, we seeded cells and 12 hours before the desired density was atteined, we exposed them to Mitomycin C - containing medium (5 $\mu$g/mL). Cell were then imaged normally for the following 24-48 hours.

#### 2.3.2.5 Whole cell body staining

To measure cell height, we employed 2 fluorescent dyes: CellTracker™ Green CMFDA (Thermo Fisher Scientific) and DiI (Thermo Fisher Scientific). CellTracker is a fluorescent probe designed to freely permeate the membrane and enter the cell. Once on the inside, it is transformed to be fully retained within the cell body, characteristic that allows it to stain the full cytoplasm. The probe was used according to the manufacturer instructions: at the appropriate moment, half the culture medium was substituted by fresh and pre-warmed medium supplemented with CellTracker (20 $\mu$M). Cells were incubated for 30 minutes, washed and then either imaged or fixed for later imaging. DiI is a lipophilic molecule, which, due to its selective solubility, only stains the membrane of the cell. As per manufacturer's instructions, the dye was added to the culture medium to obtain a final concentration of 10 $\mu$g/mL. After 30 minutes, the samples were washed and then either imaged or fixed.

### 2.3.3 Quantification: single cell parameters

The parameters related to the arrangement of single cells within the model tissue were calculated using EpiTools, a free software toolkit specifically designed to extract the membrane signal from epithelial tissues and analyze their morphology [281]. The software package comprises a Matlab® script to generate cell skeletons from the raw images, and an ICY® plugin for the actual cell analysis. The software was utilized on the images displaying the E-cadherins. In many cases the skeletons were extracted by hand due to the low contrast of the signal, a task carried out with Tissue Analyzer [282], a plugin for the software ImageJ. Since cadherins mainly sit at cell-cell junctions, and a big part of the cells sitting at the edges of the tissues is only in contact with liquid, we used the images showing actin in order to help tracing the outer perimeter of the tissue. All the pictures were first rotated in order to align the major diagonal of the pattern shape with the $x$-axis of the image and then centered. This was done to ensure that the data extracted from different pictures could be compared. The skeletons (see Figure 2.5a) were generated and then used for the actual quantification. Each closed shape representing a cell in the tissue is fit with an ellipse, and the orientation of the

major axis approximates that of the cell itself. The ellipse fit is also used to estimate the elongation ratio (ER), defined as $ER = \frac{Major\ axis\ length}{Minor\ axis\ length}$. Other parameters are computed by the the software package, the data (see Figure 2.5b) is then exported and further analyzed with Matlab®.

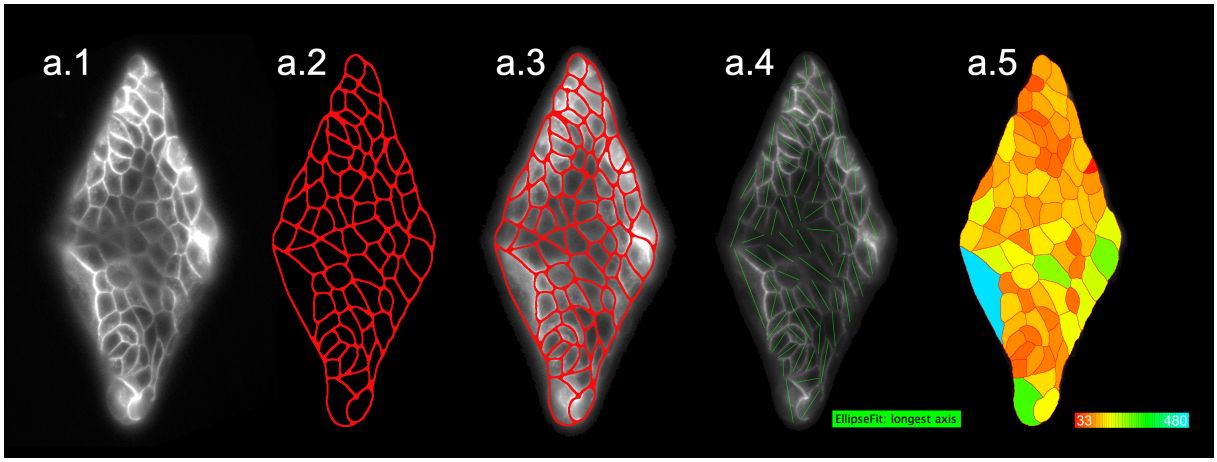


(a) Steps necessary for the extraction of single cell parameters with EpiTool. Skeletons of the cell membranes (a.2) are generated from the raw image (a.1). These skeletons are then superimposed to the original (a.3), and then used for the quantification of different parameters, such as the longest axis orientation (a.4) and the overall cell area reported in $\mu$m$^2$ (a.5).

| Centroid poition | | Polygon class | Area [pi$^2$] | Area [µm$^2$] | Major Axis Length | Minor Axis Length | Elongation Ratio | Major Axis Angle | Major Axis angle against reference point |
|---|---|---|---|---|---|---|---|---|---|
| x | y | | | | | | | | |
| 62 | 533 | 2 | 3227,5 | 151,4 | 83,3 | 49,2 | 1,7 | 176 | 3 |
| 120 | 508 | 3 | 3644,5 | 171,0 | 91,2 | 50,8 | 1,8 | 176 | 2 |
| 144 | 547 | 5 | 2625,5 | 123,2 | 114,0 | 29,3 | 3,9 | 8 | 8 |
| 182 | 503 | 3 | 2518,0 | 118,1 | 74,6 | 43,1 | 1,7 | 166 | 12 |
| 239 | 523 | 4 | 2472,5 | 116,0 | 118,1 | 26,7 | 4,4 | 9 | 10 |
| 246 | 553 | 4 | 3129,0 | 146,8 | 101,6 | 39,1 | 2,6 | 180 | 0 |

(b) Exemplary subset of data exported from EpiTools.

Figure 2.5: Representation of the main steps in the data analysis performed with EpiTools.

### 2.3.4 EdU Proliferation Essay

We used the Click-iT EdU Alexa Fluor 647 Imaging Kit according to manufacturer instructions. Cells were seeded onto micropatterns, after 48 hours, half of the culture medium was substituted with fresh EdU containing medium, to obtain a final concentration of 10 $\mu$M. Cells were generally incubated for 3 hours, after which the manufacturer fixing procedure was followed. Nuclei were counterstained with Hoechst® 33342. We settled on 3 hour incubation because longer periods would result in widespread fluorescence, with a strong correspondence of Hoechst and EdU stainings, indicating that all cells synthesized DNA. After 3 hours, we had an almost binary intensity distribution, giving us a clear way to identify cells that had already started DNA synthesis.

We then gathered images of the nuclear and EdU fluorescence intensity, which were

later aligned using images of the patterns as reference. To generate a spatial map of cell division, the intensity of all images was re-scaled in order to avoid the bias induced by variations in staining quality throughout the samples. The images were then stacked and the z-projection of the intensity provided a map of the average localization of newly synthesized DNA. All maps were confronted with those obtained by averaging the nuclear images, which were previously thresholded to avoid an effect of local Hoechst intensity. This comparison had the purpose of understanding whether local variations were due to an increase in local cell density or an effective surge in cell division probability, factors that would result in similar maps. The results obtained by averaging multiple images were then compared with distribution maps of local cell density and mitotic events generated by segmenting each nucleus and by manual detection of nuclei undergoing mitosis, respectively. The distributions were then generated using a 2-dimensional histogram function.

### 2.3.5 Measuring cell velocity: Particle Image Velocimetry (PIV)

One of the readouts we focused on is cell migration. There are two major points of view when it comes to measuring the velocity of migrating cells in a tissue. The first method involves tracking single cells over time (SPT). This is generally done by detecting the position of each and every cell within the tissue at every time point, and then associating each cell to its position in the previous/following frame. When both these steps are successful, SPT can measure cell motion extremely accurately. However, higher accuracy comes at a cost: SPT is computationally demanding and it becomes increasingly error prone with cell density. This is because cells cannot be univocally identified, so when the displacement between frames becomes comparable to the average distance between them, tracking becomes impossible. Additional complexities are cell division and apoptosis, and the fact that easy detection of cells is generally achieved with invasive nuclear staining and fluorescence microscopy.

An alternative approach is Particle Image Velocimetry [283, 284]. The idea comes from studies on the visualization of liquid flows, and it is well suited for tissues where cells move collectively in a fluid manner. Rather than trying to accurately measure the displacement focusing on single cells, PIV calculates the velocity field of a tissue by dividing it into sub-regions, or windows (see Figure 2.6). Within each window, the average displacement is calculated by comparing the intensity of the signal at different time points with cross-correlation:

$$g(\delta x, \delta y) = \langle I_i(x, y)\ I_{i+1}(x + \delta x, y + \delta y)\rangle_{x,y} \tag{2.1}$$

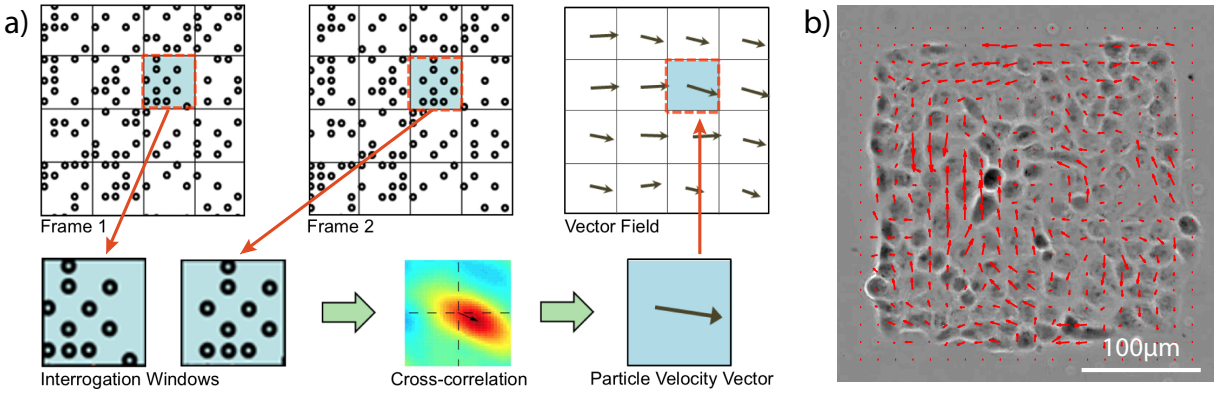


Figure 2.6: Schematic representation of interrogation windows and cross-correlation for PIV (adapted from [284, 285]) (a), and example of the velocity field calculated for MDCK cells confined on a square pattern (b). The longest vector represents a velocity of 100 $\mu m/h$

where $I_i$ is the intensity of the window at time $i$, $I_{i+1}$ the intensity in the following frame and $g(\delta x, \delta y)$ is the cross-correlation function. Naively, the idea is to superimpose the images of the window at successive time-points and shift them in $x$ and $y$ in order to find the configuration with the best overlap. This is what the correlation does: when bright or dark areas overlap, the function is positive, when dark (bright) areas overlap with bright (dark) ones, the function is negative. $g(\delta x, \delta y)$ is effectively an image describing the quality of the overlap as a function of the shift of the two images. This also means that the position of the peak in this new image represents how far the intensity of the window has moved in average between frames. If we identify this peak, knowing how far the two images are in time, we effectively calculate an average velocity within the window. This is then repeated for each window and each time point in order to generate a velocity field (see Figure 2.6b). It is important to notice that the cross-correlation always calculates an average displacement and so it provides the "best-guess" of the movement within the window. The vector calculated is in fact not associated to a single cell, but to the entire part of the tissue enclosed in the window. Also, because the analysis only considers the intensity in the sub-region, it is fundamental for PIV that each window contains enough information to follow the displacement. This is achieved both by tuning the window size and by ensuring that the images utilized have enough contrast. The windows overlap to a certain extend in order to avoid missing information from the areas at the boundaries. Because of cross-correlation, PIV is less affected by noise in the images, but it is also less sensitive to high-frequency movements happening at small scale.

We opted for this method because images obtained with Phase Contrast, such as those provided by lensless microscopy, are ideal for PIV. The modulation of thickness of the cells and the presence of many organelles create distinct patterns which make cross-

correlation more robust. This also eliminated the need for stainings and fluorescence microscopy. Another reason to use PIV is the simplicity of use. Once the window size is correctly tuned, extracting a velocity field is fast, computationally light, and requires little manual work. PIV is also less affected by cell death and division than SPT, and its suitability for the study of collective cell migration is well-recognized [128, 152, 158, 161, 164, 165, 189].

We developed our own custom-made PIV software (written by Dr. Irene Wang). To improve the accuracy of the measurement, we chose to calculate the displacement taking multiple frames into consideration. This can be done because the frame-rate of our videos (10 min) is small compared to the persistence time of cell migration ($\sim$ hours) [159, 164]. To identify and remove faulty vectors, the software has specific thresholds on both local contrast within the interrogation window and the height of the cross-correlation peak. The displacement of windows whose correlation results are discarded are calculated with an interpolation of velocities of neighbouring windows. The images were divided into windows of size 28$\times$28 $\mu$m$^2$ with 14 $\mu$m overlap. For each window, a velocity value was calculated as follows: for a given time shift (e.g. $\tau$=1 frame), the spatial correlation of each window with its corresponding time-shifted one was computed over 4 consecutive frames and averaged to improve the signal-to-noise ratio. The peak of this average correlation gives an estimate of the displacement $\delta\mathbf{r}(\tau)$. The process was repeated for different values of $\tau$ and the final velocity was deduced from a linear regression of $\delta\mathbf{r}(\tau)$. The final resolution is 20 min and 28 $\mu$m.

### 2.3.6 Kymograph

In order to visualize the behavior of cells over time and allow for a comprehensive overview of the entire time-span, we used a kymograph representation (Figure 2.7). In our iteration, a kymograph is a 2D plot of the local cell velocity as a function of time and space. To generate it, we cropped the videos in time to consider only the span we were interested in. In most of the cases, this meant only including confluent tissues, where cells filled all the available space while retaining an average absolute velocity higher than 4 $\mu$m/h. We chose this cutoff because it is the velocity of a MDCK monolayer that has reached its maximum density, and where cell motion is at its minimum [158].

As mentioned earlier, a kymograph plot is a 2D visualization of 1 parameter, in our case local velocity, over time and space. Depending on the geometrical characteristics of the tissue, especially in terms of symmetry, we chose to visualize either the absolute cell velocity, or the single components along $x$ and $y$. To this end, we averaged each component of the speed, either along the transverse direction $v_x(x;t) = \langle v_x(x,y;t)\rangle_y$, or the

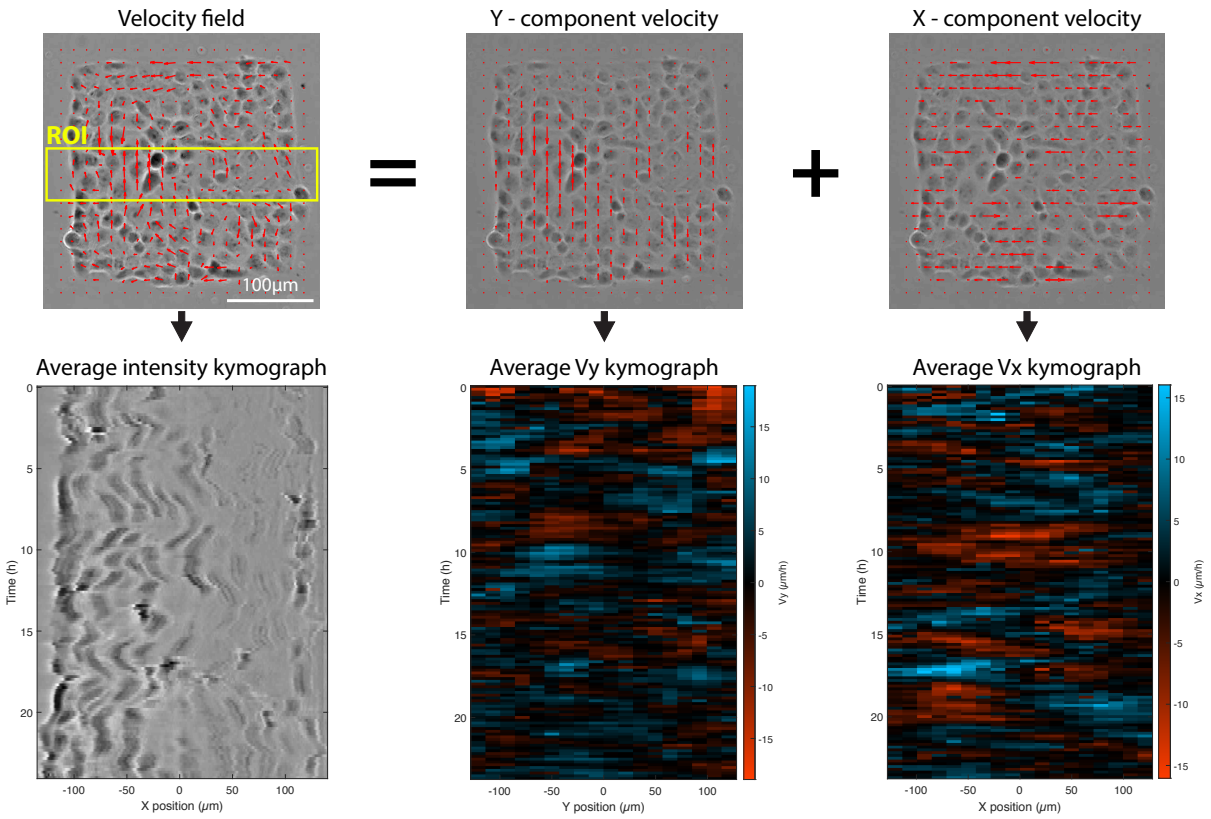


Figure 2.7: Schematic representation of the kymograph plots utilized. *Top-left*: velocity field calculated for MDCK cells on square pattern and its vertical (*top-center*) and horizontal (*top-right*) components. We visualize the behavior of $x$-velocity ($y$-velocity) by averaging it along the $y$-direction ($x$-direction) and plotting it over time (*bottom-center, bottom-right)*. To follow cell behavior, we plot the phase contrast intensity over time (*bottom-left*). Here, the signal is first averaged along $y$, only within the ROI, and then corrected for illumination flickering and dirt on the sample.

perpendicular direction $v_y(y;t) = \langle v_y(x,y;t)\rangle_x$ (see Figure 2.7 bottom). In some rare cases, especially on elongated and asymmetric model-tissues, we also tried averaging velocities along their own direction to calculate $v_y(x;t) = \langle v_y(x,y;t)\rangle_y$.

In other cases, rather then looking at the velocity within the tissue, we wanted to concentrate on the actual displacement of the cells. The difference between local cell velocity and cell displacement is not obvious. The easiest analogy if that of a compression (sound) wave propagating through a medium. Even though we have a long-range propagation, that of the velocity wave traveling through space, the single molecule is only displaced locally. PIV measures velocities from a fixed reference, so it cannot distinguish between a traveling particle or a traveling velocity wave. By following the behavior of single cells we can have a more comprehensive idea of the behavior of our system. To visualize cell motion, we plot a kymograph representing the local intensity of the phase contrast signal as a function of space and time. Since cells have specific intensity profiles, related to the local thickness, we could follow their signature over

time. To this end, we averaged the intensity of images along the transverse direction $I_x(x;t) = \langle I(x,y;t)\rangle_y$. We then removed the effect of illumination drifts and intensity variations by dividing each horizontal line-plot, related to a particular time-point, by its average. We repeated this averaging vertically, dividing the intensity profile trace of each pixel over time by its own average. This compensates for uneven background and the presence of dust that did not move in time (see Figure 2.7 bottom-left). Additionally, we can define ROIs in order to only concentrate on specific areas of the tissues.

### 2.3.7 Cellular force quantification: Traction Force Microscopy

During their lifetime, cells are in a continuous bi-directional communication with their surroundings, and a big part of this interaction travels through mechanical means. Since our experiments involve restricting cell growth by forcing specific boundary conditions, which is inherently a mechanical input, we chose to focus on the physical interaction of our tissues with the substrate as one of our readouts.

When it comes to measuring a mechanical interaction with the substrate, most techniques involve looking at the extent to which cells and their forces deform the surrounding material. Originally, this was done in the 1980's by Harris and coworkers. They cultured cells on a flexible silicone substrate, and then observed how this elastic material was wrinkled and deformed [286]. They conclude that this phenomenon is a proof of the physical interaction of cells with their surroundings. Interestingly, such technique has been revised recently, and adapted to tissues-scale force visualization [201]. Unfortunately, a quantitative analysis is made impossible by the non linearity in the elastic response of the material. This example illustrates one of the main problems in the field: measuring a deformation/strain is relatively easy and it offers a qualitative idea of how cells behave, while relating those deformations to actual forces is more challenging. This is because, just like in the case of Hooke's law ($F = k \times x$), to calculate the force ($F$) applied on a spring based on an observation of its extension ($x$), we need a very accurate knowledge of the mechanical properties of the material (i.e. the elastic constant $k$). This information is not always available when working with biological samples. Moreover, the ECM is a fibrous material, which means that not only its response to force is not linear (as the material is deformed, fibers tend to align and change its properties), but also that it is not homogeneous (cells might feel different stiffness depending on the location) [13]. A solution to render these calculations easier is the use of new synthetic bio-materials, which are isotropic and have a linear force/deformation response. Polyacrylamide is one such material, and its implementation made Traction Force Microscopy (TFM) possible.

The following paragraphs briefly explain how the technique works, and how we adjusted it to our needs. It is important to point out that, even though TFM at the multicellular level has been implemented in other labs [168, 213, 287], this technique was not present in our group. When most instances of Traction Force Microscopy rely on mathematical descriptions and software to compute the force field from the measured displacement field, we did not. This is because, in order to compensate for the presence of experimental noise, the most common TFM implementations rely on a procedure called *regularization*: several solutions (i.e. force fields) can explain the same measured deformations, and since not enough information about the real forces is known, the "most correct" solution is discerned thanks to specific criteria, such as the smoothness or the magnitude of the resulting tractions [274, 288]. In our specific case, we considered that the calculation of tractions would not add information worth justifying the added complication. For this reason, as well as all those presented above, we chose to stop at the measurement of the substrate displacement. We deemed it an easier option, particularly suitable for our initial exploratory phase. I will thus only explain how we measure such displacement. We describe our protocol in 2 steps: (I) substrate preparation and experimental procedure and (II) image analysis and displacement field extraction.

*I. Experimental procedure*

Measuring the substrate deformation is done by adding fluorescent nano-beads to the surface of the gel, just underneath the ECM protein patterns (see Figure 2.9 and Appendix A). The beads act as markers: as the cells exert forces, the polyacrylamide gel is deformed and the beads are displaced from their original locations. By tracking this movement we can extract a map of the substrate deformation [273, 274, 289]. During sample production the beads segregate at the two surfaces of the gel: that in contact with the cells and that in contact with the glass slide. This gives us the chance to measure the gel thickness, and to make sure that it is large enough (>40 $\mu$m) so that variations in thickness within the gel and between samples do not impact the deformation measured. In practice, this allows us to ignore the effect of the hard glass substrate underneath the gel.

Since the displacement of the beads is in the range of $n$m to $\mu$m, depending on gel stiffness and cell contractility, the resolution of the experimental setup has to be adapted for imaging at that scale. We used a Plan Apo VC 60x oil objective (NA 1.40) and a Nikon CFI 40X air objective (NA 0.65), and adapted the density of nano-beads to the particular objective used. Lower magnification was avoided because, in order to

facilitate subsequent image analysis, the image of the beads needs to span at least 5 pixels in width [290]. Two sets of images were gathered: one showing the substrate as deformed by cell traction, the other obtained after cell detachment with trypsin, showing the relaxed substrate. The deformation field in then extracted from the comparison between pairs of images.

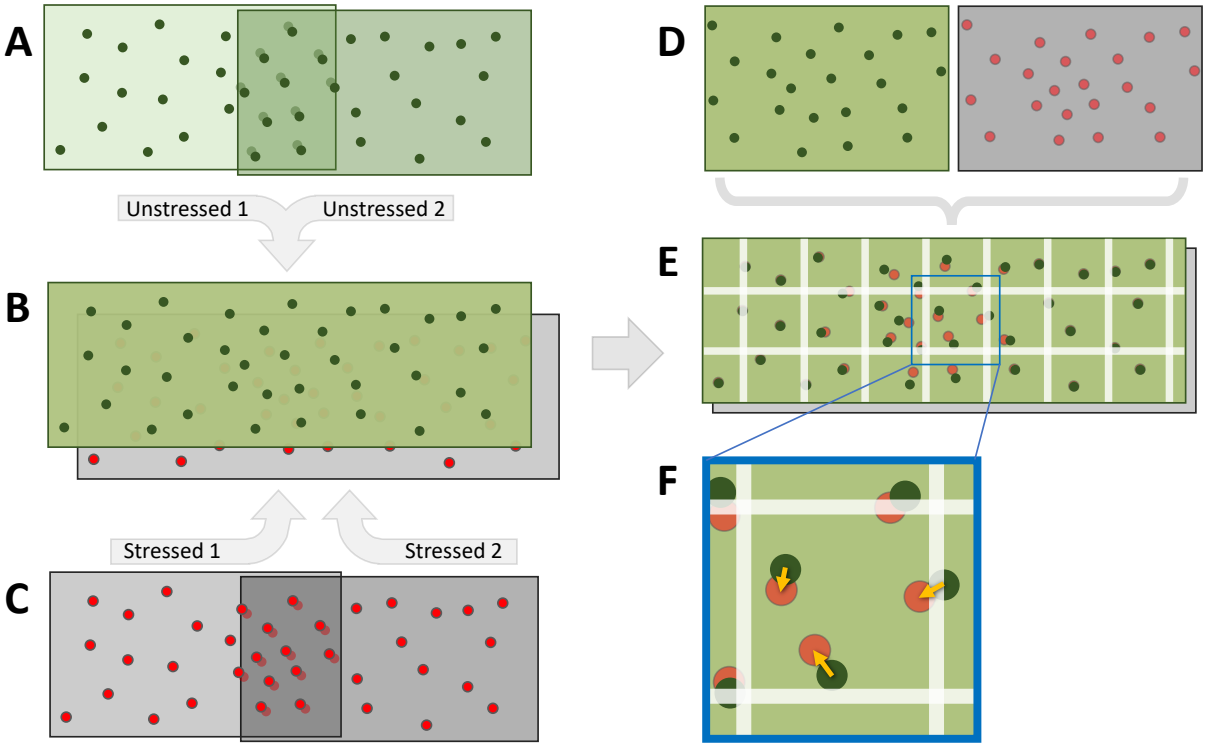


Figure 2.8: Schematic representation of the displacement field analysis. If stitching is required, the different fields of view of the unstressed sample are stitched together (**A**) to generate a global unstressed image (**B**). The field of view of the stressed sample are first aligned to the unstressed global image (**C**), and then stitched in order to obtain a stressed global image. In this case, the two global images are already aligned because they were generated using the same original field of view as a reference. If stitching is not required, the stressed and unstressed images need to be registered (**D**). The global images are then divided into interrogation windows, and PIV and PTV is then performed only within these windows (**E**). Orange arrow represent single particle displacements

*II. Displacement field calculation*

All the image analysis was performed in Matlab® using a custom-made software (written by Dr. Irene Wang, based on [291, 292]). The analysis consists on tracking the displacement of each bead between a stressed and an unstressed (reference) image (see Figure 2.8). Just like in the case of PIV (subsection 2.3.5), this task is generally approached in one of two ways: either by tracking directly the fluorescent markers (particle tracking velocimetry, PTV) or by using cross-correlation to derive local movement statistically (PIV). To improve the quality of the results, we combined both approaches

[274].

Before tracking the single particles, we needed to tackle the issue of image stitching. This because the size and geometry of the tissue chosen often meant that, to image all cells, we needed multiple fields of view. When necessary, a pair of unstressed images are first stitched using cross-correlation (Figure 2.8A). The position of the peak describes the situation of best overlap. This generates a global unstressed image (GU) (Figure 2.8B). Rather than repeating the operation with the two stressed images, we decided to use the GU as a template, and to align each single stressed image to it. The global stressed image (GS) is then generated with the parameters thus calculated (Figure 2.8C). This is the equivalent of aligning every single image to the first unstressed one, which is done to minimize errors and avoid having to go through any additional alignment step (GS-GU). The two GS and GU images were then re-sized to have the same dimension. When stitching was not necessary, we registered the images using cross-correlation to make sure that drift would not affect our subsequent analysis (Figure 2.8D). The issues we encountered during the registration and stitching processes are discussed in subsubsection 3.1.2.3.

PIV analysis was then performed on the stressed and unstressed image pair. They were divided into smaller interrogation windows (20 $\mu$m $\times$ 20 $\mu$m, 5 $\mu$m overlap) (see Figure 2.8E). The overlap between windows was set to avoid missing the movement of beads at the boundaries. The cross-correlation maximum was then calculated to measure the average displacement within the window, which was then followed by single particle tracking. This step consists in detecting all beads and correlating their position in the stressed image to their position int the unstressed counterpart (subsection 2.3.5). The difficulty stems from the fact that, when large displacements are present, beads cannot be univocally correlated. Since PIV effectively calculates large displacements, by taking this value into consideration during SPT we can correct this effect and remove ambiguity between neighboring beads. Each bead is thus associated to a displacement vector. We then generate a vector field with a 2D interpolation, yielding a deformation value for each node of an established grid (see Figure 2.9). It is now more clear how the spatial resolution of the measurement depends on the bead density, which was tuned in order to increase the particle density without compromising the tracking quality.

To better visualize the the displacement field, in many cases we divided it into its components along $x$ and $y$. We then generated plots showing only the magnitude in each direction. We included a mask in the software to exclude those areas of the images outside of the tissues and those areas near the borders of the field of view where defocus and optical aberrations made bead tracking extremely unreliable.

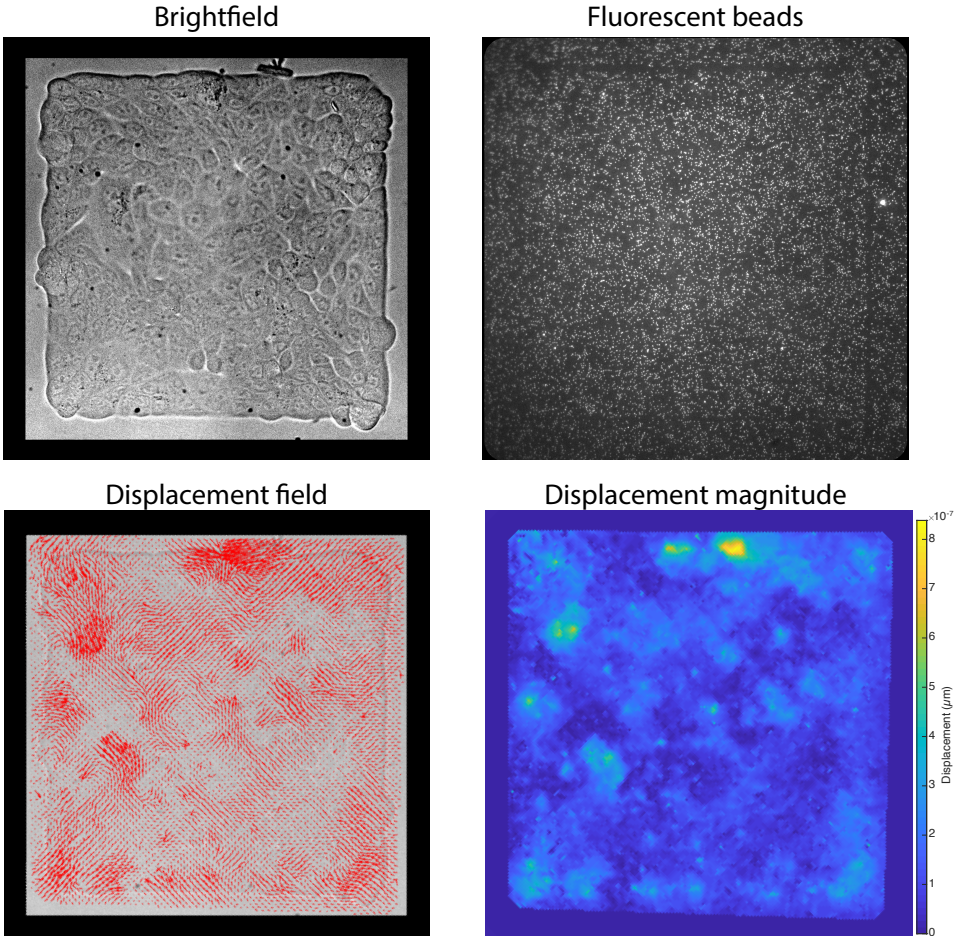


Figure 2.9: Substrate displacement calculation for MDCK cells grown on square patterned 40 kPa gel.

# 3. Results

I will first concentrate on the results obtained during our initial exploratory moment, when we tried to guide cell division only by playing with the local geometry. To this end, we developed specific new adhesive shapes, and we spent some time characterizing both, the nature of the mechanical input with TFM, and cellular response, with interesting outcomes in terms of division rates and cell morphology. We then coupled these observations with a more dynamic approach, by monitoring cell motion over time. In some cases, this new perspective allowed us to briefly recognize the presence of periodic oscillations in cell velocity.

The second part of the chapter focuses on how we adjusted our experimental aim to investigate these phenomena, with special attention to new protocols and analyses we developed or adapted to this end. Our efforts culminated in the discovery of extremely reproducible long-range oscillations in the velocity of cells, which are described in this second half.

## 3.1 Geometrical control of model-tissue heterogeneity

The presence of boundaries plays a major role in the mechanical guidance of cell behavior. Stem cells, the archetypal example, change their differentiation patterns depending on the distance from tissue edges. In planar geometry, cells confined to adhesive patterns of different shapes proliferate more actively at borders, where stress is more acute [126], while for 3 dimensional spheroids the application of external pressure confines proliferation to the surface [293]. These results are in direct contrast with the increase in proliferation measured following a wound scratch essay, where the effective removal of boundaries seemed to speed up cell division. Both cases highlight the presence of a strong "edge-effect", whereby cells positioned in the vicinity of a border behave differently, but the exact parameter or quantity controlling such effect is not clear. A direct correlation between the available space, the position of a cell within a tissue and its behavior, in terms of proliferation rate has not yet been discovered. This work is therefore aimed at understanding if the mechanical environment felt by different members of a population of cells can generate patterns of asymmetries in cellular proliferation.

To this end, we designed diamond-shaped adhesive islands (Figure 3.1a), characterized by different acute angles. The main hypothesis is that cells located at the edges are exposed to different mechanical environments, in terms of the number of first neighbors, amount of cell-cell to cell-medium contacts and, more generally, any consequence of the peculiar cellular arrangement associated with narrower spaces. By controlling the angle, and thus the perimeter, we can tune the intensity of such effect, which would manifest itself as a different proliferation rate of cell located at acute angles in comparison with those in the center. Moreover, such controlled environments would allow us to better quantify cell behavior, in terms of morphology and arrangement, and to pinpoint the actual parameter guiding cell proliferation. The diamond shape also enables us to independently change the area and the perimeter of model-tissues, thus tuning the extent of the edge and, hopefully, its effect separately from the overall area.

Throughout this work, I will refer to the specific diamond shape in question by using its acute angle as nomenclature. I will also refer to these MDCK cells colonies confined on specific geometries as "tissues". I took this choice with the awareness that such designation is generally reserved to much more complex biological structures, which are not necessarily recapitulated in our experimental setup. I opted for this nomenclature nonetheless, for the sake of simplicity.

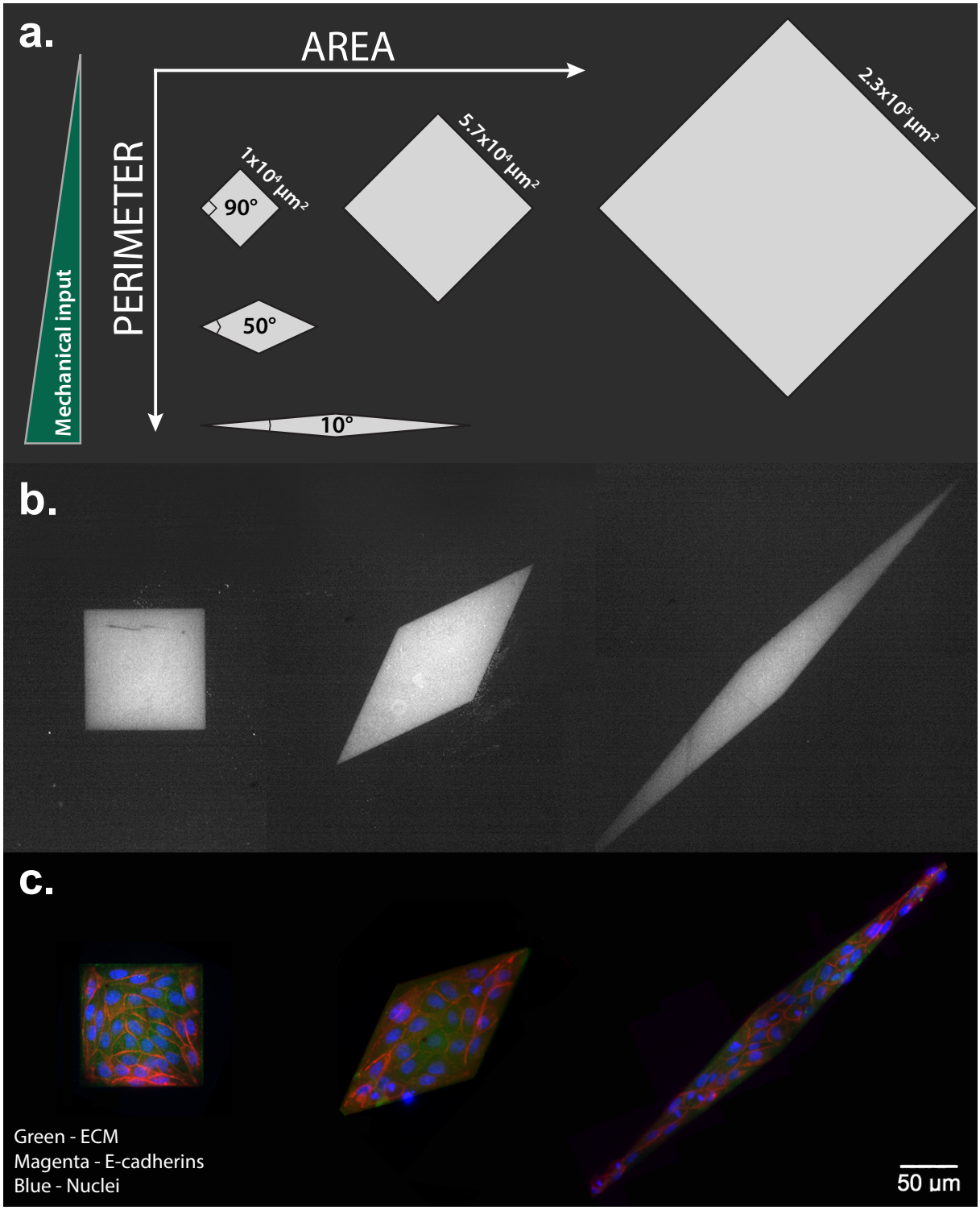


Figure 3.1: **a.**) Schematic representation of the diamond-shaped adhesive islands designed for MDCK cells. For any specific area, the mechanical input is tuned by changing the acute angle and, thus the perimeter. **b.**) The patterns are fabricated, and the fluorescent intensity of the ECM proteins deposited on the gel surface attests the quality of the procedure. **c.**) MDCK cells seeded onto diamond-shaped patterns. Nuclear (*blue*) and cadherin (*magenta*) signals are superimposed on that of the ECM on the substrate (*green*).

### 3.1.1 Sharp angles are associated with higher cell density and more frequent mitotic events

To measure the dependence of cell proliferation rate on the angle amplitude we seeded MDCK cells onto patterned PAA gels (rigidity = 40 kPa). We chose 50° diamonds because of the presence of both acute and obtuse angles, and we concentrated on two sizes (area = $1 \times 10^4$ $\mu$m$^2$ and area = $5.7 \times 10^4$ $\mu$m$^2$). After $\sim$ 24 hours of normal growth, we supplemented the culture medium with EdU for 3 hours, after which we fixed the samples at a density roughly corresponding to confluence and the onset of jamming transition ($\sim 5 \times 10^5$ cells/$\mu$m $^2$). We then gathered images of nuclear and EdU fluorescence.

The results, presented in Figure 3.2, illustrate how, for both tissue sizes, cell density follows a similar trend: the biggest amount of cells is concentrated along the borders, with clear peaks in proximity of the corners. It also appears that sharper angles have higher cell density compared to wider ones. This general trend is mirrored closely by cell division, which appears to be more frequent at the corners. The initial quantification with EdU and Hoechst staining has also been complemented with more rigorous measurements carried out by nuclear segmentation (Figure 3.2b) and manual mitotic-cell detection (Figure 3.2d). These results are free from the possible biases due to cell shape or 3D morphology, and confirm the general trends observed.

The degree of the similarity between distributions of cell density and proliferation is highlighted by the plots in Figure 3.2: where cell density is higher, so is the probability of cell division. This close resemblance makes it impossible, at least with the current set of data, to discern between the two potential explanations for higher division at the borders: locally increased mitotic probability or unchanged proliferation rate combined with elevated local cell density.

Interestingly, for larger shapes, a third local peak in both our measurables is observed in the center of the tissue, a phenomenon which could be investigated further.

These results are in partial agreement with what reported in [126]. In their paper, Nelson and colleagues show that cell density is uniform along the tissue. Therefore, local differences in division can only be attributed to increase mitotic rate. The same cannot be said about our situation, where sharper corners are associated with both, an accumulation of cells and an increase of local cell division. This makes it impossible to distinguish between faster proliferation and the mere effect of an increase of cell density. Even though both works have been carried out on kidney cells, Nelson and colleagues worked with rat cells, which might be responsible for the different results.

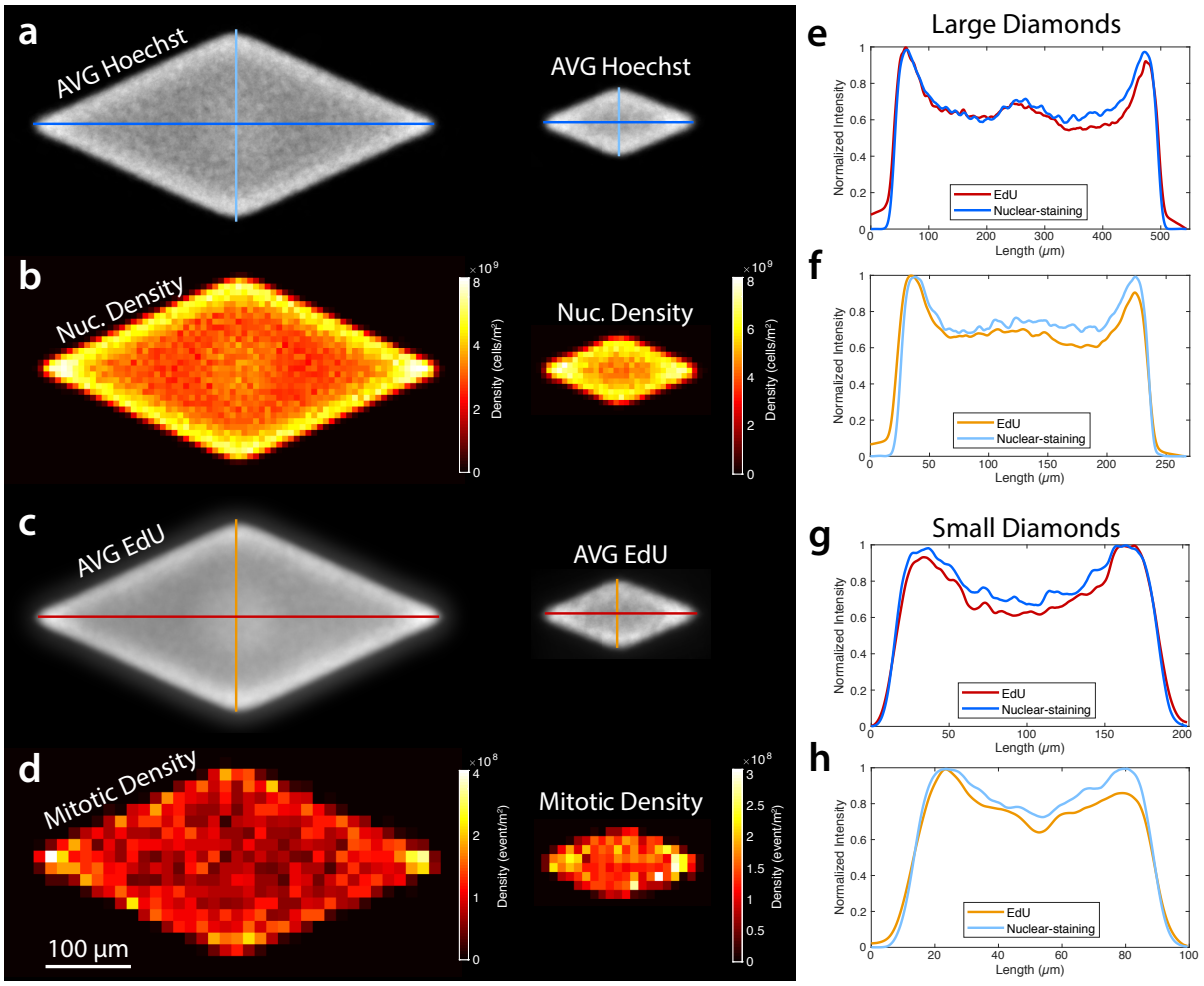


Figure 3.2: Distributions of nuclear density and mitotic events for tissues confined on 50° diamond shapes. Nuclear density has been measured by projecting thresholded nuclear images (**a**) or by single nuclear segmentation on the same images (**b**). Similarly, proliferation maps generated by projection of images of EdU-fluorescence (**c**) are juxtaposed to those obtained by manual detection of division events (**d**). On the right, we plot graphs that allow the comparison of the results obtained in **a** and **c** by directly overlaying line profiles for division and nuclear density along horizontal (**e**, **g**, dark colors) and vertical (**f**, **h**, light colors) directions (reference lines in **a** and **c**). n=570 for large tissues, n=841 for small tissues.

Regardless of specific details, the presence of an edge-effect is undoubted. Moreover, the highest magnitude of such effect in proximity of sharper angles seems to confirm our approach and the relevance of the diamond shape to induce local differences in cell behavior.

This begs the questions of what controls such a difference, i.e. what is the parameter cells use to determine whether they are next to an edge or not. Several reports attribute selective proliferation and differentiation at the borders to specific patterns of mechanical stress [126, 127]. We therefore set out to measure the interaction of our tissues with the substrate.

### 3.1.2 Substrate displacement studies

To measure how cells deform the underlying substrate, a first-approximation proxy for cell tractions (see subsection 2.3.7), we fabricated polyacrylamide gels (rigidity = 40 kPa) with diamond-shaped adhesive islands. The presence of fluorescent beads embedded next to the surface of the gel allowed us to perform TFM measurements and directly quantify the displacement of the substrate. To assess the impact of different perimeter lengths, angles and areas, we concentrated on diamonds with angles equal to 10°, 50° and 90°, and area $1 \times 10^4$ $\mu$m$^2$ and $5.7 \times 10^4$ $\mu$m$^2$. We seeded MDCK cells, waited $\sim$ 24 hours and then proceeded with static TFM measurements.

#### 3.1.2.1 Substrate displacement localizes along the edges and at sharper corners

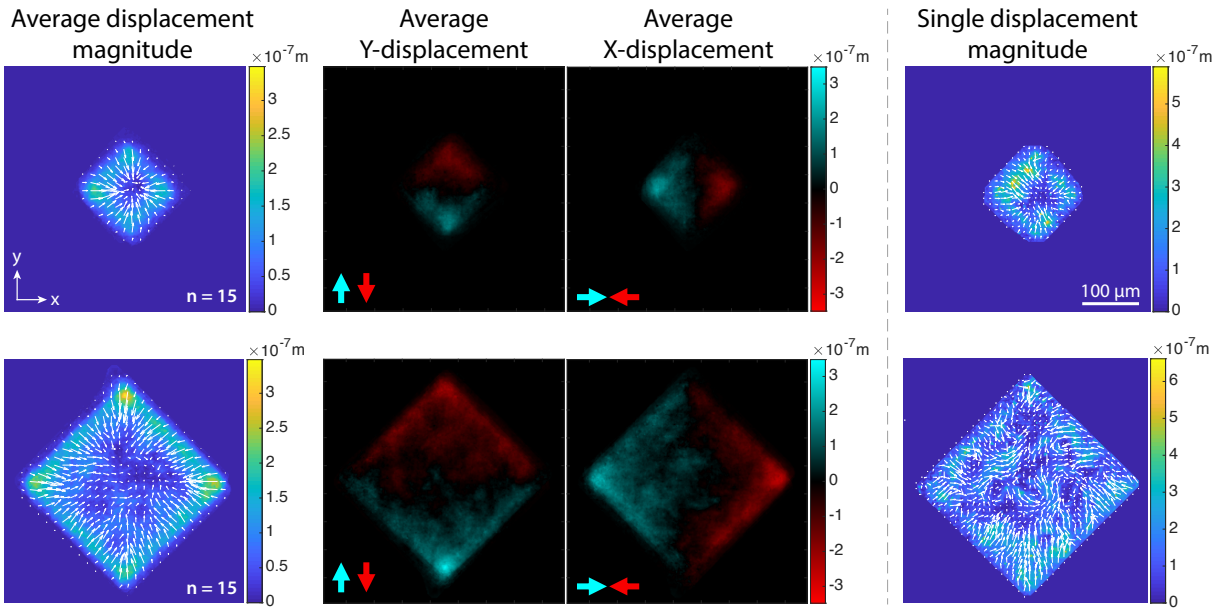


Figure 3.3: Measured substrate displacement for MDCK cells on PAA gel (rigidity = 40 kPa) confined on square islands of side 100 $\mu$m (*top*) and 240 $\mu$m (*bottom*). The general trend is displayed as the average displacement magnitude, superimposed with the displacement field direction for n=15 tissues: all cells pull inwards (*left*). The displacement is also projected along the $x$ and $y$ directions (*center*). Averaging multiple measurements can sometimes hide intrinsic variability, which is highlighted in the graphs of the displacement magnitude and direction for a single tissue (*right*).

The results for square tissues (90° diamonds) are presented in Figure 3.3, whereas a comparison of different angles is in Figure 3.4. By averaging the displacement maps of multiple tissues we can draw the first conclusions.

Generally, all cells pull the substrate inwards, towards the center of the tissue. We highlight this behavior by projecting the deformation field along the two perpendicular directions $x$ and $y$, to generate maps that detail the global nature of this phenomenon.

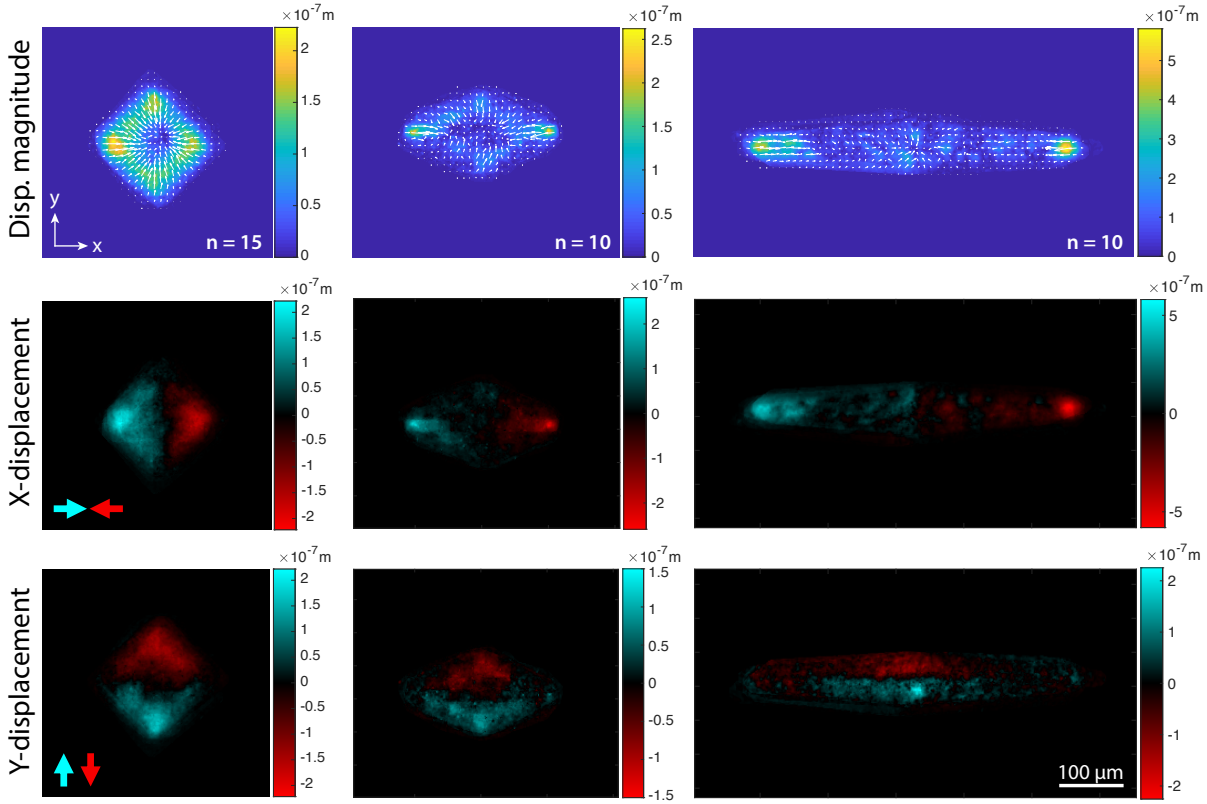


Figure 3.4: Average substrate displacements (n is reported in the figures) for diamond-shaped tissues (area $= 1 \times 10^4$ $\mu$m$^2$) characterized by different angles (from left to right: 90°, 50°, 10°). We report the average displacement magnitude with the average displacement fields (*top*), and their components along the $x$-direction (*middle*) and $y$-direction (*bottom*). Colorbars are adapted to the single image.

| | Mean absolute displacement (x$10^{-1}$ µm) | | | Max absolute displacement (x$10^{-1}$ µm) | | |
|---|---|---|---|---|---|---|
| **Angle** | **Total** | **X-comp** | **Y-comp** | **Total** | **X-comp** | **Y-comp** |
| **90°** | 1.2 ± 0.2 | 0.8 ± 0.2 | 0.8 ± 0.2 | 4.9 ± 0.6 | 4.2 ± 0.7 | 4.3 ± 0.8 |
| **50°** | 0.9 ± 0.2 | 0.6 ± 0.2 | 0.5 ± 0.2 | 6.1 ± 0.9 | 5.6 ± 1.1 | 4.8 ± 1.0 |
| **10°** | 1.2 ± 0.3 | 1.0 ± 0.3 | 0.5 ± 0.2 | 6.6 ± 1.0 | 6.5 ± 1.0 | 3.1 ± 1.2 |

Table 3.1

On average, every cell in the top half of the tissue pulls downwards, and vice versa.

The maps also highlight another characteristic of the interaction with the substrate: the majority of the deformation is concentrated along the edges. Moreover, loci of stronger deformation are clearly visible in correspondence of the corners, where the pulling forces are maximal. On the other hand, the displacement in the center of all tissues is generally buried within the experimental noise. This distribution is probably a consequence of the fact that cell-cell forces are not measurable with TFM, and we only see the components that are relayed to the substrate, losing all inter-cellular forces that are locally balanced.

Interestingly, as we move to more elongated diamonds, substrate deformation slowly

concentrates at sharper corners (i.e. smaller angles), as clearly highlighted in Figure 3.4. Overall, cells seem to orient their substrate tractions along the principal axis of the tissue.

If averaging the results for multiple tissues can help drawing general conclusions, it can also hide the variability intrinsic to biological systems and conceal important details. Single examples of the substrate deformation for small tissues are reported in Figure 3.3, to show that, while all cells on the smallest squares reproduce the average behavior, larger diamonds display strong deviations. In this latter case, vectors are significantly pointing away from the center in a manner that seems to be cooperative rather than random. Similarly to what has been reported in literature [161], we observe small swirls and a general short scale correlation in the substrate deformation. Moreover, larger tissues are marked by a higher maximum displacement magnitude.

To better quantify these general trends, we calculated the mean and maximum absolute displacement, and their components along $x$ and $y$, for each independent tissue. We then averaged all values obtained for tissues of identical shape, to obtain the data reported in Table 3.1. Even though the interval between diamonds of different angle is not always statically relevant, the data can be used to draw meaningful conclusions. In general, independently on the angle, all tissues have a similar average displacement (as seen in the first column of Table 3.1). Interestingly, what differs is the maximum displacement, which is much more pronounced for more elongated tissues (see the fourth column of Table 3.1 and Figure 3.4). The transition between squares and 10° diamonds is also associated with a general decrease of the displacement along $y$ and an increase along $x$, a trend closely mirrored by the maximum values measured.

Overall, these results prove that confining small model-tissues to diamond shapes of different aspect ratio induces an adjustment in the interaction with the substrate. Specifically, substrate displacement re-orients along the principal axis of the tissue, and concentrates at sharper corners.

These results are in agreement with what has previously been reported in literature. Small colonies, both in a confined and free state, have been shown to exert inward pointing traction stresses, predominantly at their periphery [126, 222, 294, 295]. In those same situations, stresses are further concentrated in regions characterized by high-curvature. The agreement between our results and what has been published is striking, especially considering that [295], the most elaborate study on this matter, was not published when we reached similar conclusions. Moreover, the close correspondence of the traction stresses expected from literature and the substrate displacement measured seems to reinforce our choice of only considering deformations and not cal-

culating tractions. Interestingly, these results bear similarities with those obtained in 3-dimensional complex environments, where diamond-shaped 3D tissues give rise to strong tractions at sharp angles and weak displacements at more obtuse ones [296].

Moreover, there is a strong overlap between maps of substrate deformation and those of cell density and cell proliferation presented earlier. This resemblance confirms previously published data [126], demonstrating a strong correlation between cell behavior and substrate displacement. Unfortunately, more statistics should be acquired to increase the confidence of our deductions. Even though we cannot be certain about the connection with cell division rate, cell aggregation in correspondence of increased substrate displacement is an interesting phenomenon, which, to our knowledge, has not been reported before.

#### 3.1.2.2 The edges on elongated tissues are characterized by displacement-dipoles

We have so far proved that on elongated tissues the deformations along $x$ (i.e. the longer diamond diagonal) are more important and concentrated at sharper corners, a phenomenon that interests the tissue in its entirety. Since cells are characterized by specific correlation lengths, in terms of movements, tractions and substrate displacements, we wondered whether the interaction with the substrate would lose its global nature above a certain size. For this reason, we fabricated larger tissues and measured the relative substrate displacement. An example (area = $2.3 \times 10^5$ $\mu$m$^2$) is reported in Figure 3.5. Cells located at sharp tips of the tissue retain their propensity to pull inwards, while a series of seemingly random deformation directions along $x$ follows further within the shape. This is unsurprising, as the whole adhesive island measures over 1 $m$m in length, well above any correlation length (see subsubsection 1.5.2.2). More interesting is the behavior along the perpendicular direction: the weak tendency of cells to pull towards the center along the $y$ direction is maintained for 100 $\mu$m wide shapes, but results on larger 10° tissues tell us that this tendency is generally lost on wider diamonds. This fact introduces an new correlation length, related to coherent force generation on the direction perpendicular to the major force-axis.

Another interesting feature of the maps in Figure 3.5 is the marked presence of neighboring spots of displacements of opposite signs. A comparison with the cell borders reveals that two opposite patches form a dipole, and that it generally corresponds to a single cell, pulling on the substrate in a way reminiscent of the migration of isolated cells (see subsection 1.3.4) [297]. These oscillations of substrate displacement, roughly 30 $\mu$m in length, are located next to the edges, where cells are most elongated and where their migration direction is forced along the border.

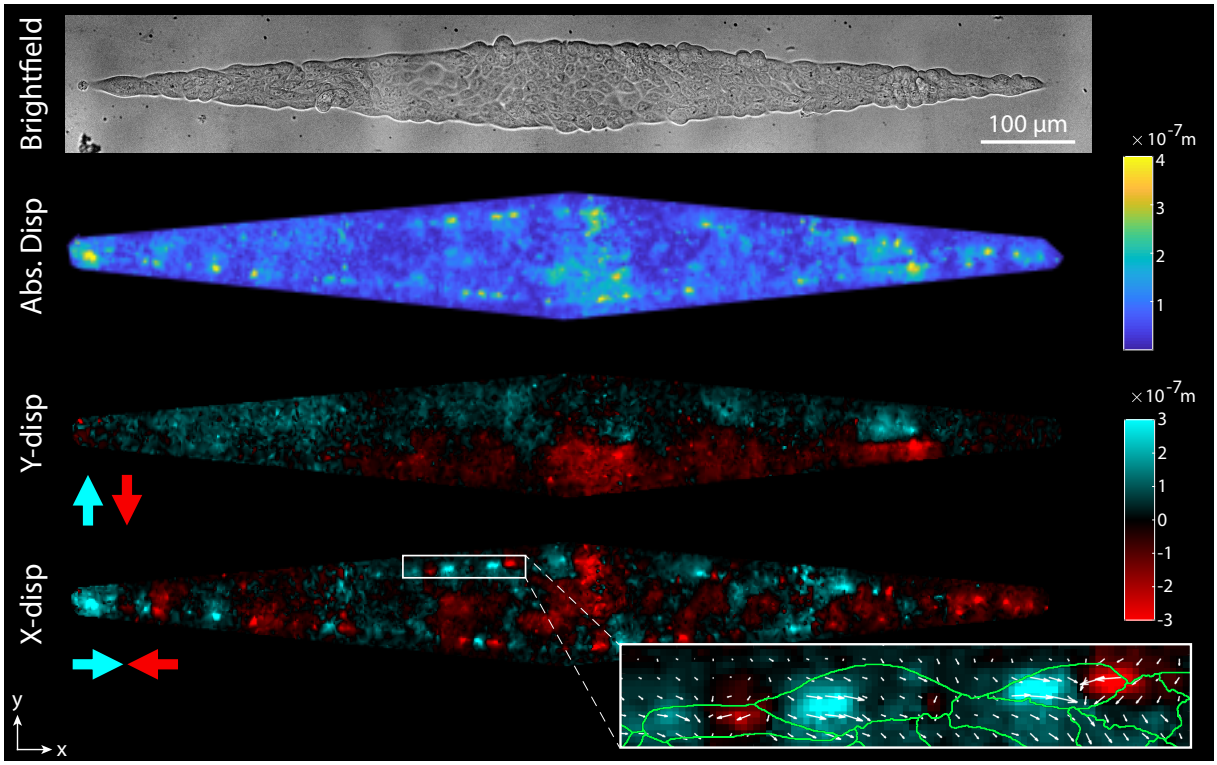


Figure 3.5: Cells confined on a 10° diamond shape of area $2.3 \times 10^5$ $\mu$m$^2$, the relative substrate deformation (*top*), and its components along the $y$-direction and $x$-direction (*bottom*). The inset shows the detail of the local $x$-displacement superimposed on the local cell borders (*green*) extracted from E-cadherin staining.

#### 3.1.2.3 Issues with deformation measurements and image stitching

While analyzing the measurements on the most elongated diamonds we realized the limitations of our implementations of TFM. Before continuing with the results, I would like to take a moment to address these issues and put them into perspective. Due to the specific geometry of 10° angles, and the requirement of a 40x objective for accurate particle tracking, a full image of the tissue requires at least 2 fields of view, that need to be stitched together. This latter step is as important for the measurement as it is challenging, and our approach revealed inadequate. The comparison of the displacement calculated for separate fields of view and that for the stitched image better delineate the problem (see Figure 3.6). Our approach is affected by 3 major issues: (i) a sizable difference in the magnitude of the measured deformations; (ii) a higher level of noise in the region where the fields of view overlap in the stitched image; (iii) a incoherence in the measured deformation for the same area (white dotted rectangle). The reasons behind these problems are mainly optical aberrations (field distortion) and defocus. Both factors are more prevalent near the edges of the field of view, and ultimately compromise the quality of the alignment and stitching of different images. These operations are carried out with the same tool: cross-correlation. In the case of a simple

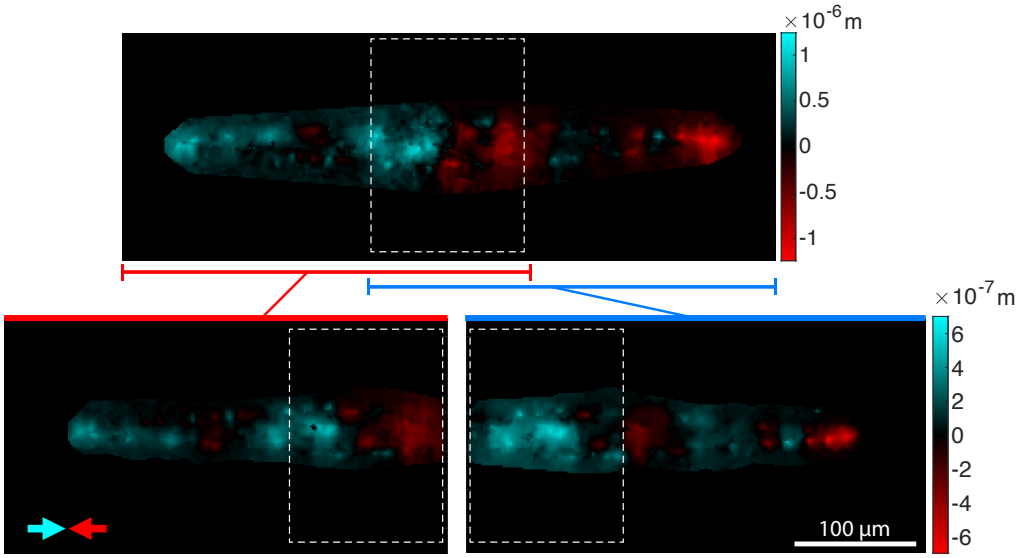


Figure 3.6: Comparison of substrate displacements for stitched (*top*) and independent (*bottom*) fields of view. The areas highlighted by the white dotted rectangle describe the same physical region.

alignment, the procedure works under the assumption that the total bead displacement averages to zero. This is true for single cells and small tissues, where the entirety of the surface covered by cells is small and fully contained in one field of view, but it is not for larger multi-cellular arrangements, where the sum of displacements in one image (not containing the whole tissue) can diverge from zero. Whereas this factor should not affect the initial stitching (between unstressed images), it undermines the quality of all subsequent alignments. Even in those cases where stitching is avoided, the initial registration of stressed and unstressed images remains biased. These issues result in a widespread deformation even in parts of the gel where no cell is present. To, at least partially, compensate, we made sure that all data presented here was free from such drift.

The root of these problems is that we calculate the stitching parameters from the stage position, which is inaccurate, and the information on the field of view, which is distorted. One possibility to improve our method is that of only considering the undistorted center of the field of view, but this would increase the number of images to treat and thus the complexity and susceptibility to mistakes. Improving our experimental apparatus with a better corrected objective would also make for more accurate stitching, which could be further refined by only considering an area devoid of cells when calculating the stitching parameters. These solutions would only partially solve the problem, because they do not take into account the registration between images taken at different time steps. Another approach, to "kill two birds with one stone", would be that implemented by Trepat and coworkers [213]. It consists on including an

additional layer of beads (diameter = 2 $\mu$m, different fluorescence spectrum) in the hydrogels, specifically attached to the bottom glass surface. While imaging the top layer, where the markers for substrate displacement are, it is possible to gather an out-of-focus image of the beads at the bottom, which is then used as template to align and stitch all other channels. Although we researched these methods to ameliorate our technique, we simply decided to concentrate on the analysis of cell motion and set TFM momentarily aside.

### 3.1.3 Three dimensional morphological transition

Increased cell density and substrate deformations at the colony edges, a characteristic of tissues in their relatively early stages of growth, are also correlated with the observations of a 2D-3D morphological transition at the periphery of the colony, typical of later stages and higher cell densities. MDCK cells, which in normal cell culture conditions (i.e. on a Petri dish) maintain a sheet-like phenotype, systematically formed a 3-dimensional peripheral rim along the borders (see Figure 3.7). We refer here to "3D" as a situation where the cell sheet develops multi-layered morphology and cells are stacked one on top of the other. Confocal microscopy confirms the presence of cells positioned higher in the $z$ direction, which are not in contact with the substrate and only share edges with cells underneath them. Interestingly, for square adhesive shapes we often found a complete 3D edge, whereas the occurrence of this phenomenon is more restricted to sharp angles as the aspect ratio of the diamond increases. The dependence of the transition to the pattern angle is briefly displayed in Figure 3.7.

This 2D-3D transition is an relevant readout because it correlates directly to the geometry of the substrate and, thus, our control parameter. Moreover, cells develop in the vertical dimension at locations where we observed enhanced substrate displacement, cell density and proliferation. These observations are extremely interesting because, even though the mechanisms underlying this phenomenon have been presented in [128], their preferential occurrence at sharper corners is not yet clear.

### 3.1.4 Collective morphology changes induced by geometrical constraints

On the smallest tissues, the direction and magnitude of substrate displacements follow the aspect ratio of the diamond itself. This means that, overall, cell rearrange to collectively pull preferentially along a specific direction, which happens to be the major axis. Since single cells on elongated patterns tend to exert stresses in the direction of

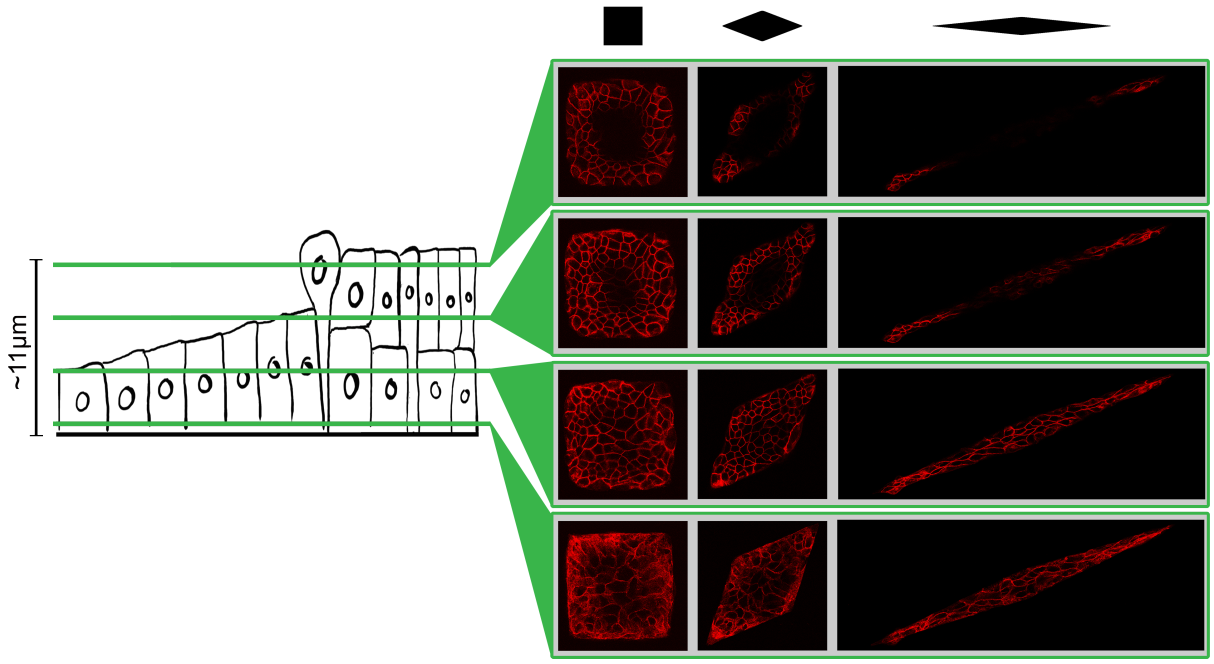


Figure 3.7: Schematic drawing of the distribution of cells along the vertical direction at the corners of small tissues (*left*) and relative images obtained with confocal microscope (*right*). The figures show E-cadherins intensity for different sections of the sample obtained at different z-positions.

their orientation (i.e. the direction along which they are elongated) [269], we wondered whether a similar phenomenon could be at play on a multi-cellular scale in our set-up. The hypothesis is that our diamond patterns force all cells to reorient along the longer diagonal. This morphological difference is then followed by a change in the force exerted, to explain the specific deformation patterns observed.

For this reason, we concentrated on the morphology of cells within monolayers confined to different geometries. For each diamond shape, we studied an average of 7 tissues at a density of $\sim 5 \times 10^5$ cells/$\mu$m $^2$. We extracted the information on the shape of each cell based on the E-cadherin staining, and we concentrated on the elongation ratio ($ER = \frac{Major\ axis\ length}{Minor\ axis\ length}$) and the orientation angle (measured as the absolute angle with the longer diagonal of the diamond shape, see Figure 3.8a). To assess the response of cells to the geometry imposed we first considered small tissues (area = $1 \times 10^4$ $\mu$m$^2$) with angles 90°, 50° and 10°, on glass patterns. In Figure 3.8a, a color map is used to display such response. On square patterns, cells retain a more round shape and a less coherent orientation. As one might expect, near the edges cells align to the direction of the constraint. As the aspect ratio of the diamond increases, cells progressively orient themselves with the longer axis of the shape and, to better accommodate the substrate geometry, take on a more elongated morphology. On 10° diamonds, cell orientation is conserved along the whole colony, a fact evidenced by the uniform color in Figure 3.8a.

The statistical analysis of cells within multiple tissues confirms these conclusions (Figure 3.8b). For what concerns the elongation ratio, we see a narrow distribution centered

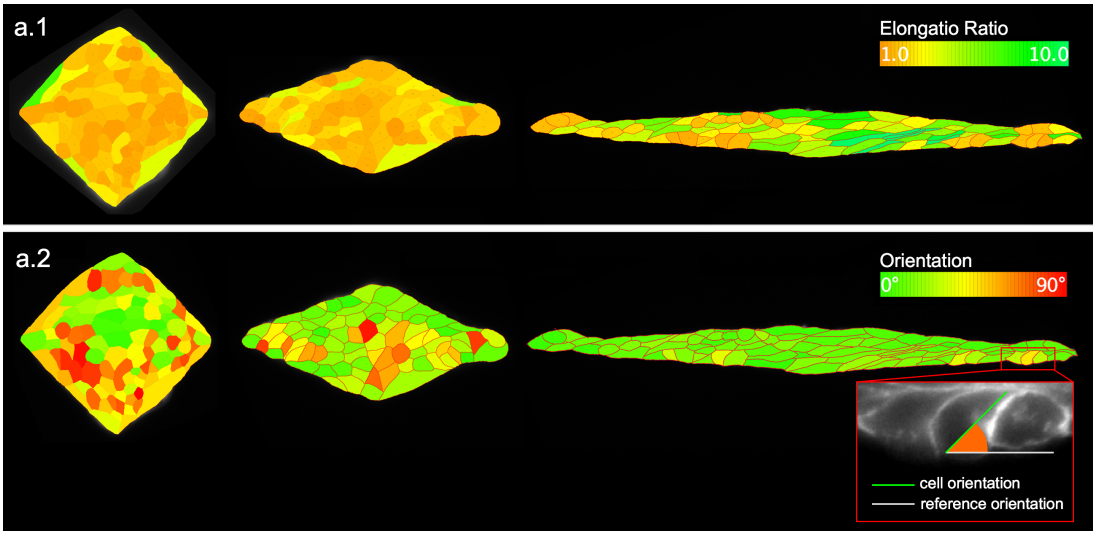


(a) Example of cell elongation ratio (a.1) and cell orientation (a.2) distribution maps of MDCK cells on glass substrates patterned with diamonds of different angles (from left to right: 90°, 50°, 10°).

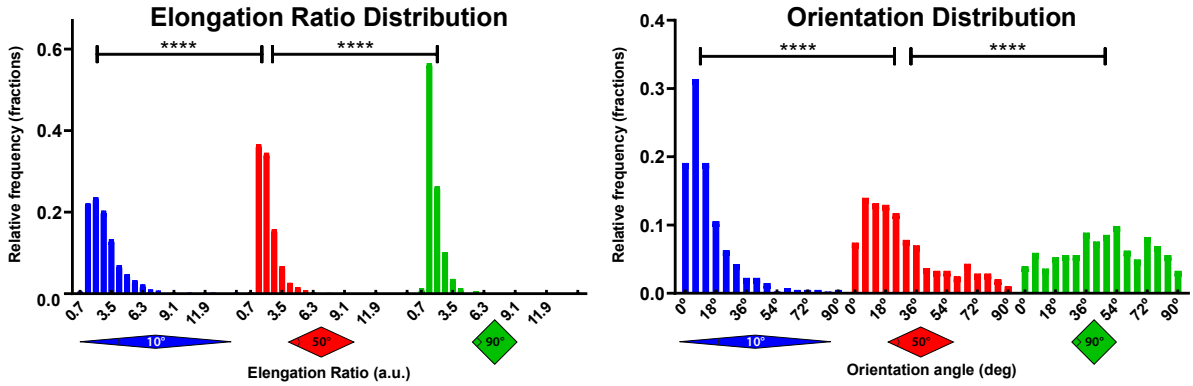


(b) Graphs reporting the distribution of elongation ratio (*left*) and cell orientation (according to scheme in (a.2), *right*) for MDCK cells on glass patterns. The legend is reported under each graph. For each geometry, the data reported is the average 7 model-tissues, approximately 400 cells. Black lines reported above the graphs between data series are used to represent the results of the statistical significance of differences (unpaired t-test) analysis.

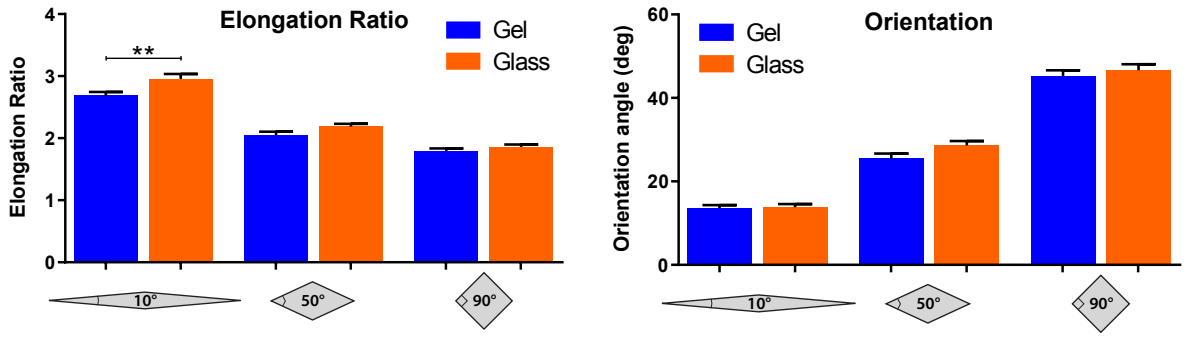


(c) Comparison of the distribution of ER (*left*) and cell orientation (*right*) for MDCK cells on glass and soft polyacrylamide gels (40 kPa). For each geometry, the data reported is the average value for all cells within 7 tissues. Error bars are the standard error of the mean. The difference between pairs (unpaired t-test) is only significant when reported above the bars.

Figure 3.8: Cell morphology study results.

on small values for square shapes. As we move to smaller angles, there is a progressive increase in the width of the distribution, as the average shifts towards higher values. Cell orientation follows a somewhat opposite trend, it is evenly distributed in the case of 90° shapes, but strongly concentrates around $\sim$ 15° as we move to more elongated diamonds. This value differs significantly from 0, not because cells effectively orient at 15°, but because we considered the absolute angle. This pushed a distribution, which would otherwise be centered around 0, to all positive values. To assess whether the rigidity of the substrates could affect these distributions, we then repeated the analysis on PAA gels of rigidity equal to 40 kPa. As reported in Figure 3.8c, within this rigidity range, the morphology of cells is unaltered.

It appears that very elongated diamond patterns induce global cell re-orientation and increased ER. The cells in the center of the tissue, even though not in contact with any edge, somehow change their behavior to accommodate for the presence of boundaries. There is, therefore, a communication between cells, relaying morphological information from the edge further within the tissue. To investigate how far this transmission could travel, we fabricated PAA gels (rigidity = 40 kPa) patterned with larger diamonds, always characterized by an acute angle of 10°. We then measured, for each cell, the orientation angle against the edge of the tissue. Considering the intrinsic symmetry of the diamond shape, we pulled together the data from the four symmetric triangular quadrants, in order to effectively consider a single triangle (see Figure 3.9). To obtain a map of cell orientation against the distance from the edge, we divided the space into thin 5 $\mu$m stripes parallel to the boundary, and binned the data relative to all cells whose centroid fell within a well defined stripe. This allowed us to obtain different sub-populations of cells, depending on their distance from the edge. For each bin, we then calculated the weighted average angle against the edge. We decided to use the elongation ratio as a weight because the measurement of the orientation (i.e. the direction of the longer cellular axis) is more affected by noise on rounder cells, distinguished by lower ER.

The results are presented in Figure 3.9. In all cases, cells within the first 10 $\mu$m from the boundary show strong alignment (the angle is smaller than 15°), which then tends to weaken further from the edge in a fashion dependent on the size of the adhesive island. For the smallest tissues (short diagonal = 42 $\mu$m), there is a slight increase in the average angle towards the center, but overall all cells orient within $\sim$ 20° from the direction of the edge. On medium (short diagonal = 100 $\mu$m) and large (short diagonal = 200 $\mu$m) diamonds, the average angle increases more sharply, and seems to saturate at 45° for a distances between 60 $\mu$m and 100 $\mu$m. This particular value is significant

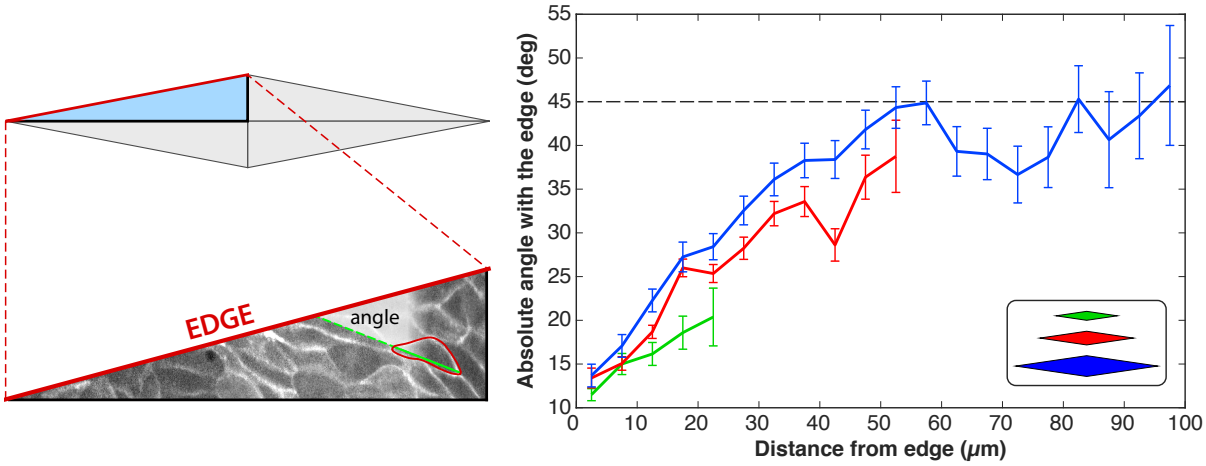


Figure 3.9: The symmetry of the shapes chosen allowed us to collapse the data and only consider a single triangular quadrant (*top-left*). The absolute angle of the major axis of the cell (green) with respect to the direction of edge (red) is measured (*bottom-left*). All cells are then binned depending on the distance from the edge, and the average angle is then plotted (*right*). Since the angle can vary between 0° and 90°, random orientation is associated with an angle of 45°, marked by the dotted horizontal line. Error bars are the standard error on the mean. For both the smallest tissues n = 10, for the largest n = 4.

because, since the angle measured can vary between 0 and 90, 45° represents random orientation, a behavior typical of unconfined tissues where cells are not affected by boundaries. This also explains the deviation between diamonds of different sizes. On very large tissues, cells coordinate their morphology to a distance of $\sim$ 60 $\mu$m, because further than this cells are oriented randomly. On small tissues, on the other hand, all cells fall within this distance from both boundaries, and this creates a more global effect. As the diamonds increase in size, the edges become further apart and cells in the center are less affected by their presence until, on the largest patterns, these cells lose all information on the boundaries and their orientation becomes random. This value also correlates well with the loss of a global substrate displacement along $y$ for shapes wider than 100 $\mu$m (see subsubsection 3.1.2.2).

Taken together these results indicate the presence of a strong correlation between cell orientation and substrate displacement: when cells are globally oriented in the $x$ direction, so are the deformations caused by traction forces. These observations are also supported by literature. Isolated cells on round patterns display an even distribution of inward pointing forces. When placed onto more elongated patterns of same surface, stronger tractions are concentrated on areas of small curvature, in a manner that maintains the mechanical work constant [269]. If we assume that cells within tissues behave in a similar way (i.e. the preferred direction of the stresses exerted by a cell follows the orientation of the cell itself), then our results are coherent. Elongated diamonds cause global cell re-orientation, which in turn makes for a global change in the mechanical

interaction with the substrate, with an increase of $x$ displacement and a decrease in the perpendicular direction. In fact, in our experiments, multicellular ensembles coordinate their behavior so that the substrate displacement matches closely what we might expect from a single cell of similar shape, a conclusion also present in [295]. Moreover, our measurement of a "morphology correlation length" of approximately 60 $\mu$m is coherent with the substrate deformation along the $y$ direction. On small 10° diamonds, all cells are aligned with the edges, and this makes for the neat bi-color distribution in Figure 3.5 and Figure 3.4. This is because, although cells pull preferentially along $x$, a small component of deformation along $y$ is measured. For shapes narrower than 100 $\mu$m, all cells are oriented, and so the deformation distribution is maintained. For wider shapes, cells lose information about the edge, orient randomly and so the direction of pulling forces lose global coherence.

### 3.1.5 Dynamic observations of cell migration

The characterization of the mechanical interaction with the substrate and the static behavior of cells raised numerous questions, which could only be answered with extended studies. Cells are inherently motile and their continuous locomotion, a possible source of noise and disturbance, has to be reconciled with the presence of what seemed like stable distributions of substrate displacements, cell density and cell divisions. Moreover, the presence of dipoles in the deformation under single cells (see Figure 3.5) seemed to suggest a strongly motile phenotype along the edges. For these reasons, we continuously observed tissues for long periods of time ($\sim$ 72 hours).

Preliminary videos of small 10°, 50° and 90° diamond shapes were gathered with a lensless microscope (subsubsection 2.3.1.2). At relatively high cellular densities, the resolution is not sufficient to distinguish single cells, but general conclusions can be drawn by projecting all frames to calculate average intensity, standard deviation and maximum value for each pixel (Figure 3.10b). The average intensity is higher along the edges, an effect enhanced at the corners. This signal is distributed evenly for square patterns, but tends to be more concentrated towards sharper angles as the diamond is distorted, in a fashion reminiscent of how cells displace the substrate (see Figure 3.4). Assuming the refractive index to be constant in the body of the cell, the signal intensity is proportional to the local "quantity of matter" and, thus, local cell thickness. This means that sharper angles are characterized by cells that develop more in the $z$ direction. This intensity distribution correlates with the locations where cell density was shown to be higher, and, even though the images concentrate on a time period antecedent to the appearance of 3-dimensional rim, with those positions where cell morphology

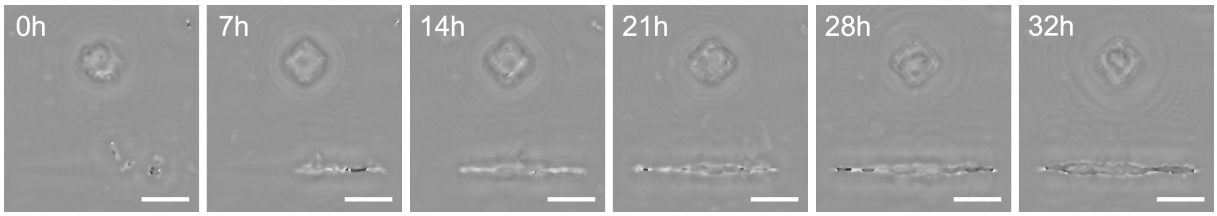


(a) Examples of cell on patterns at different times after seeding (top-left corner). The images, taken with a Cytonote® lensless microscope, show the reconstruction of the phase shift caused by the sample. Black dots represent stronger phase shift, caused by the higher thickness of the cell at its center. (Scale bars, 200$\mu$m).

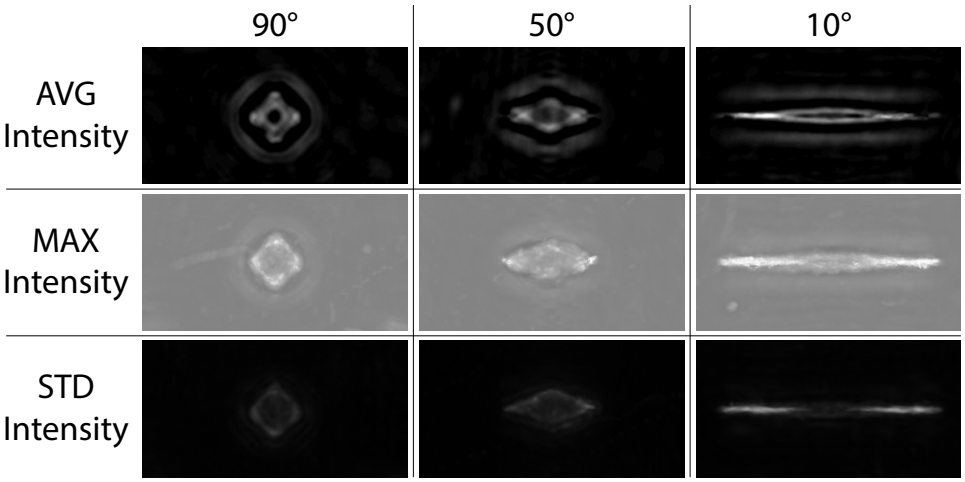


(b) Results of the projection off all frames gathered during a 32 h observation for different shapes. The color of each pixel is proportional to the average intensity (*top row*), maximal intensity (*central row*) and intensity standard deviation (*bottom row*) of all the frames obtained.

Figure 3.10: Lensless microscope observation results.

becomes multi-layered. What is somehow more interesting is the picture reporting the standard deviation of the signal for each pixel, a quantity once again higher at the sharper corners. At those particular locations, the thickness of the cell sheet oscillates in time more than in the center of the figure. Since we know for a fact that mitotic events are associated with fluctuations of cells thickness (cells need to first round-up, and then spread again), this seems to hint again towards higher proliferative activity.

Given the inadequacy of this microscope for a more detailed analysis, we repeated the experiments utilizing a different microscope equipped with a 10x objective. The improved resolution allowed us to get a better idea of cell motion and track their migration with PIV (see Figure 3.11).

Even though the movement of cells seemed chaotic, a set of characteristic behaviors could be distinguished. On 90° diamonds (see Figure 3.11a), tissues rotate consistently around their axis in a coordinated manner. Even though on these smaller diamonds all cells participated in the global rotation, on larger tissues we observed the appearance of multiple independent swirls, as previously reported for round adhesive islands [165].

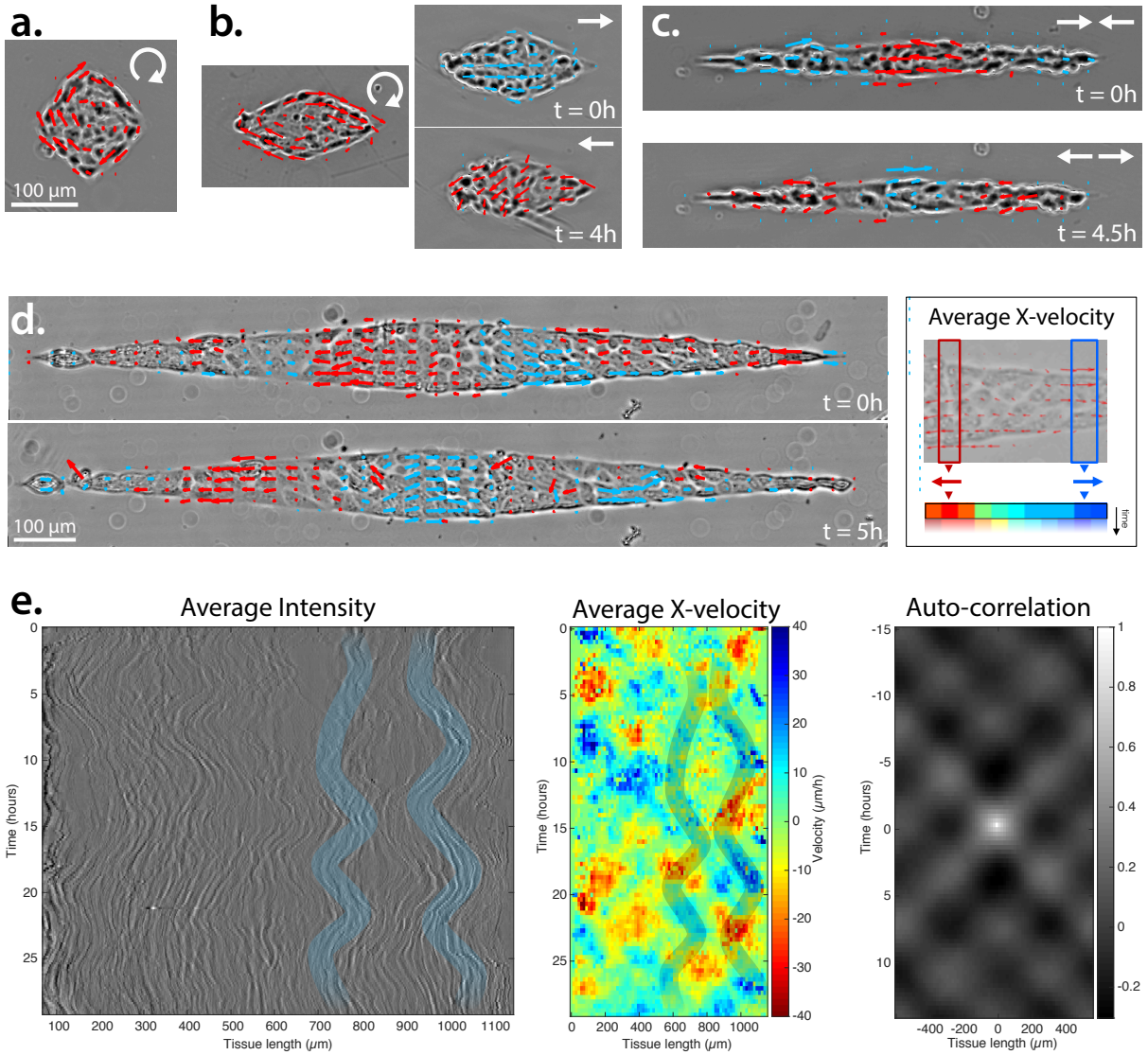


Figure 3.11: Dynamic observation of cell movement on diamond-shaped tissues. Small tissue (*top*) display a different phenotype depending on the angle: sustained rotation for 90° (**a.**), left-right oscillations for 10° (**c.**) and a combination of both for 50° (**b.**). On larger 10° diamonds, the oscillations become more evident (**d.**) and sustained, as highlighted with a more dynamical analysis extended in time (**e.**). The movement of cells is appreciated by plotting the average phase-contrast intensity (**e.** *left*), where a clear "hourglass" pattern can be seen (blue-shaded areas). These movements translate directly into patches of velocity of opposing sign the kymograph of the $x$-velocity (**e.** *center* - dark-shaded areas), calculated according to (**d.** *right*). The standing-wave characteristics of these oscillations are confirmed by the clear patterns present in its auto-correlation of the kymograph (**e.** *right*).

Global rotations are also present on 50° diamonds (Figure 3.11b), albeit in a less consistent manner, and are accompanied by moments of global leftward and rightwards motion. On the most elongated 10° diamonds, rotations disappear altogether and, since cell motion is strongly confined to the $x$ direction, oscillations become more evident (Figure 3.11c). Interestingly, whereas on 50° shapes the oscillations were of a global nature (i.e. all cells move either towards the left or the right in a coordinated manner),

on these elongated diamonds the behavior is reminiscent of a standing wave with at least one node in the center.

In many physical contexts, the establishment of such standing waves is correlated with constructive interference, which is in turn controlled by the dimensions of the accessible space. In keeping with this comparison, we considered larger 10° tissues to investigate how a modulation of the length along the $x$ direction would affect this oscillatory behavior (Figure 3.11d). In this situation, we observed what seemed like a long-range standing wave in the local cell velocity. Moreover, the number of nodes increased, thus maintaining the wavelength approximately constant. Figure 3.11e represents the behavior of tissues in time. On the left we directly observe the displacement of cells, which first move towards and then away from each other in a periodic manner. We can then plot a kymograph of the local velocity, where this behavior appears as patches of positive (*blue*) and negative (*red*) velocities. Interestingly, this alternation occurs in both time and space, suggesting once more the establishment of long-range coherent standing waves in cell velocity. The periodicity can be visualized, and later measured, by calculating the auto-correlations of the kymograph. In this case, we observe an extremely regular pattern, which reproduces perfectly what we would expect from a standing wave (see subsubsection 3.2.5.1).

Altogether, these results are in agreement with the presence of an "edge effect", which selectively affects cells sitting at the borders of the tissues. Our observations of different aspects of cell behavior, mainly correlated to proliferation and morphology, corroborate this effect, and seem to be coherent with the establishment of a long-range mechanical landscape.

Even though these results constitute a solid base to structure future research on, we chose to concentrate on what was, in our opinion, the best path to bet our limited time on: the observations of sustained oscillations of cell velocity.

## 3.2 Wave-like collective cell migration modes

Considering our previous results, we chose to develop a new experimental protocol to reproduce and characterize periodic oscillations in cell velocity. Even though similar waves had previously been observed, our choice is justified by the potential novelty of our findings.

We worked on confined environments to obtain a phenotype reminiscent of a standing wave. In that, our observations represented something different from traveling velocity waves in expanding monolayers (see subsection 1.8.1). On other hand, since cells were often shown to migrate in opposite directions, our results are not well described as breathing oscillations neither (see subsection 1.8.2).

Moreover, if the presence of these different oscillations is generally accepted, their origins are still unknown. Setting momentarily aside the biological components that make oscillations possible, we feel like the question of what controls their characteristics, in terms of wavelength and period, is extremely relevant. Does the environment dictate the way cells oscillate? Or is their behavior a consequence of some innate feature?

In light of this reflection, our observations of different migratory modes controlled by the environmental geometry (Figure 3.11) were especially intriguing. They suggested that the specific shape chosen does, indeed, affect the way cells oscillate, but our experimental setup was not suited to confidently answer this question. We therefore decided to refine our approach, and to concentrate on understanding whether collective wave excitation in epithelial cell monolayers are intrinsically encoded in the activity of the cell, or if they are affected by external constraints.

### 3.2.1 The new experimental approach

Diamond shapes, especially those characterized by more acute angles, allowed us to recognize the presence of wave-like oscillations in cell velocity (Figure 3.11). The inspection of our preliminary data revealed three noteworthy observations: (i) the size of the confinement along $y$ seems to control the appearance of swirls or vortices in cell motion, so that, below a certain size ($\sim$ 100 $\mu$m in our case), no vorticity is allowed; (ii) the confinement along $x$ controls the number of nodes in cell velocity and the overall shape of the waves obtained; (iii) based on a closer inspection of 50° diamonds, the two phenomena (oscillations and vortices) seem mutually exclusive. Building upon these observations, we adjusted our experimental aim to specifically target velocity waves.

We abandoned diamonds shapes and simplified our design to create rectangular tissues, or strips. On the one hand, we lost the additional control parameter offered by the presence of angles of different sizes, on the other, width and length of rectangular shapes can be scaled independently. By fixing our width to 40 $\mu$m, we avoid the additional difficulty of dealing with vortices and 2-dimensional motion in general, and we are left with a single control parameter, the length ($L_X$), to change the behavior of our system.

Moreover, in line with our bottom-up approach, thin rectangles should create global cell alignment in the $x$ direction, a hypothesis supported by our preliminary data on cell orientation (see Figure 3.9) and by literature (subsection 1.7.2) [256, 257]. This fact, accompanied by a restriction of cell motion in the same direction, should allow us to average all measurables along $y$, creating a situation we refer to as *quasi one-dimensional*. Even though this averaging was already performed for diamonds, the peculiarity of that shape meant that each position along $x$ corresponded to a different confinement, i.e. a different tissue width, a situation that is avoided for thin lines.

The width of the strip, although kept constant throughout our experiments, remains a valuable control parameter for future investigations.

### 3.2.2 Preliminary observations

To verify whether we could reproduce oscillatory behavior on thin lines, we repeated our experiments on newly fabricated patterned gels (rigidity = 40 kPa). We created lines whose length ($L_X$) varied between 100 and 2000 $\mu$m, and seeded MDCK cells with an initial concentration of $\sim 2.5 \pm 0.5 \times 10^4$ cells/cm$^2$. The samples were washed with fresh medium 1.5 hours after seeding, then placed in the incubator (37 °C and 5% $CO_2$) for the remainder of the experiment. Cells were imaged for $\sim$ 72 hours gathering one frame every 10 minutes, beginning some time before confluence. Since the initial number of cells on each adhesive island was impossible to control accurately, the observation was continued until $\sim$ 48 hours after confluence for all tissues in the field of view. PIV then allowed us to follow the movement of cells (final resolution = 20 min and 28 $\mu$m). An example of a field of view containing strips of different lengths and the relative cell velocity is reported in Figure 3.12.

The first brief visual inspection of cell motion, done to verify whether we could reproduce those wave-like patterns observed on diamonds and if we could shed more light on the existence of different migration modes, quickly reveled the almost ubiquitous presence of self-sustained oscillations. The results are reported in Figure 3.13. Cells over the whole range of lengths were observed to move in an wave-like alternating

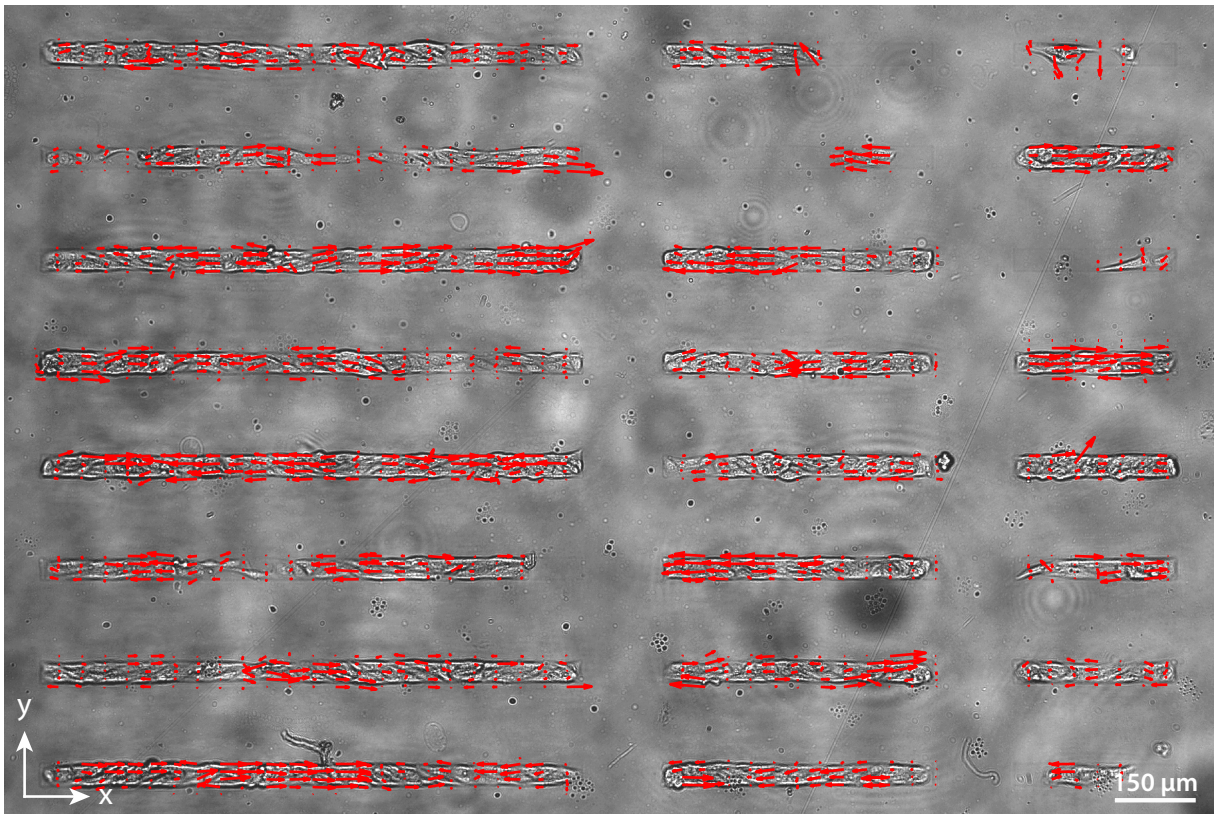


Figure 3.12: Example of the movement of MDCK cells confined to strips of different lengths (from left to right: 1000 $\mu$m, 500 $\mu$m, 300 $\mu$m). Local velocities measured with Particle Image Velocimetry (*red arrows*) are superimposed on a phase contrast image obtained with lensless microscopy.

fashion, and all instances can roughly be divided into two major categories: (i) **global oscillations**, where all cells move alternatively leftwards and rightwards in phase, and (ii) **multi-nodal oscillations**, characterized by multiple iterations of these global movements, in phase opposition and separated by locations at which cells do not move. Because of their resemblance to standing waves, we refer to these locations as nodes. Short lines are characterized by global oscillations, whereas for $L_X > 500$ $\mu$m nodes are present in the majority of cases. It also appears that on long lines cells located at the nodes are being alternately compressed and dilated.

The examples reported in Figure 3.13 are extremely efficient at explaining our observations, but they do not necessarily represent the whole range of behaviors observed during our experiments. The instances reported have approximately the same wavelength, whereas a brief examination of multiple tissues reveals the presence of strong intrinsic variability, as often the case with biological samples. Also, these modulations in cell velocity are often superimposed on long-range deformations, which can be thought of as monotonic stretchings of large parts of a tissue (in the order of $m$m). These issues, together with the difficulty of clearly identifying and discriminating different oscillation modes, convinced us of the need for better tools. We briefly realized that being able to

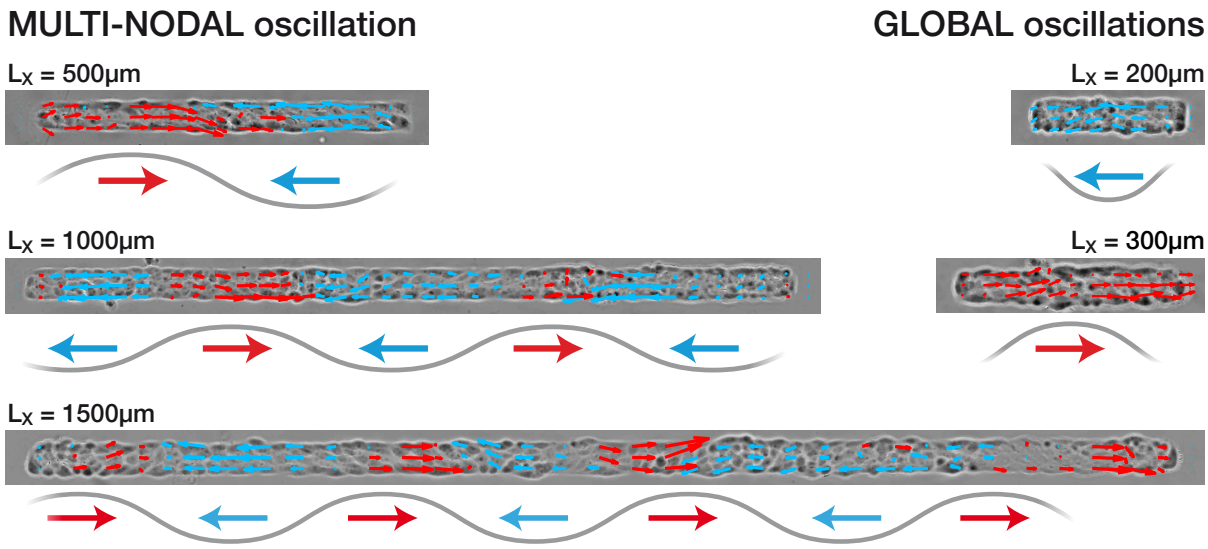


Figure 3.13: Preliminary observation of oscillations in tissues of different length. Arrows represent local cell velocities measured with PIV, velocities pointing in the positive (negative) $x$-axis direction are shown in red (blue). Two main migration modes are observed: global (*right*) and multi-nodal oscillations (*left*). A scheme summarizing the general trend of the velocity is reported underneath each image. The gray wave-like dashed line illustrates and reinforces the similarity between cell movement and a standing wave in cell velocity.

reproduce such phenomena would only be useful if complemented with a strong protocol to measure their properties, in terms of wavelength and period. The techniques we implemented to this end are presented in the following sections.

### 3.2.3 Velocity oscillations are typical of a specific time-window

MDCKs were seeded onto the patterned substrates and imaged for $\sim$ 72 hours. Averaging the velocity magnitude over the entire line revealed a trend common to all tissues (see Figure 3.14). Before confluence, the average velocity increases, it then reaches a maximum around the moment where all available space is occupied, and finally displays a slow decrease which stops with jamming. A quick observation immediately revealed that velocity oscillations were typical of an intermediate period of time (red-shaded area in Figure 3.14).

Even though cells were actively migrating before confluence, their motions seemed erratic and disordered. To exclude this initial period and to ensure that the tissue would be in contact with the entirety of the confinements imposed, we restricted our observations to consider only confluent tissues. Since cell motion is strongly inhibited after jamming, and so are oscillations, we also excluded all time-points where the average absolute velocity was lower than 4 $\mu$m/h (see subsubsection 1.5.2.2). Given the short doubling-time of MDCK cells ($\sim$ 20 hours), the window considered encompassed

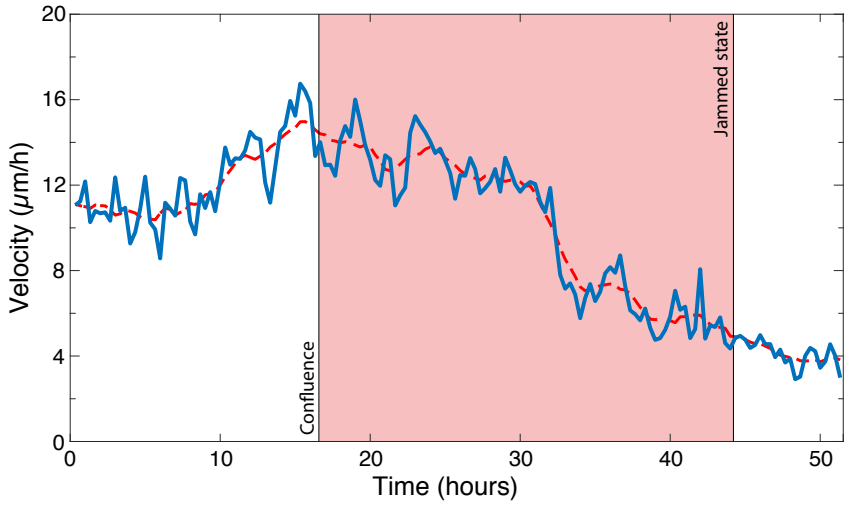


Figure 3.14: Plot of the temporal evolution of the average velocity magnitude for an exemplary tissue of length 1500 $\mu$m (*blue-line*), and the trend obtained with sliding average (size = 10 points, *red-dotted line*). The area shaded in red represents the time-window where oscillations are most visible, and, thus, the interval considered for further analysis.

roughly 24-32 hours. For the remainder of this work, all quantification is done only on data that falls within this time-window, which was calculated for each line individually.

### 3.2.4 Velocity is limited to the x-direction

Cell movement appeared to be predominantly confined within the $x$ direction, which was one of the objectives we had in mind while designing the lines. To estimate the magnitude of this confinement we calculated the ratio of the average absolute velocity along the two directions ($V_{ratio} = \langle|v_x|\rangle/\langle|v_y|\rangle$). In order to compare strips and diamond shapes, we also calculate $V_{ratio}$ for small diamond tissues. The results are in Table 3.2.

A value of $V_{ratio} = 1$ represents an unconfined situations where cells move equally in all direction, whereas the prevalence of movement along $x$ pushes $V_{ratio}$ to higher values. As expected, cell on square shapes have a $V_{ratio} = 1$, indicating that migration does not happen over any preferential direction. The disappearance of swirling motion on more elongated tissues is then associated with an increase in $V_{ratio}$, which reaches $V_{ratio} = 3.9$ for 10° diamonds. The same value is obtained for 500 $\mu$m long lines, whose length and width approximately match that of elongated diamonds. This indicates that thin strips replicate the general velocity confinement previously associated with oscillations. Moreover, these results confirm that cell movement in the vertical direction can be neglected to focus mainly on $x$, the only variable in our quasi one-dimensional system.

By making these lines longer, we notice a steady increase in $V_{ratio}$. This can be

| | Diamond | | | Line | |
|---|---|---|---|---|---|
| | 90° | 50° | 10° | 500x40µm | 2000x40µm |
| $V_{ratio}$ | 1.0 ± 0.1 | 1.8 ± 0.1 | 3.9 ± 0.2 | 3.9 ± 0.4 | 5.2 ± 0.6 |

Table 3.2: Table reporting the average absolute velocity along $x$ divided by the average absolute velocity along $y$ for tissues of different shapes. The error is calculated as the standard deviation. All diamonds had area $= 1 \times 10^4$ $\mu$m$^2$.

| $L_x$ (µm) | $\langle \lvert v \rvert \rangle$ (µm/h) | STD | SEM |
|---|---|---|---|
| 100 | 5.2 | 7.0 | 0.04 |
| 150 | 6.2 | 7.6 | 0.03 |
| 200 | 7.4 | 8.3 | 0.02 |
| 300 | 8.6 | 8.9 | 0.01 |
| 500 | 9.0 | 8.9 | 0.01 |
| 1000 | 10.2 | 9.5 | 0.02 |
| 1500 | 9.7 | 9.1 | 0.01 |
| 2000 | 10.8 | 9.7 | 0.01 |

Table 3.3: Table reporting the average absolute velocity for tissues of different length. For each value of $L_X$, we report the standard deviation (*STD*) and standard error on the mean (*SEM*).

explained by considering the effect of the vertical edges: their presence slows cells down and acts as a defect, disrupting coherent orientation and creating a more noisy velocity field. Since their presence has higher relative impact on shorter tissues, we can explain the measured increase of $V_{ratio}$ with the length of the strip.

To quantify this effect, we calculated the average absolute velocity for lines of different lengths ($\langle |v| \rangle$). We considered all PIV measurements and all frames falling within the time window mentioned earlier. The results are presented in Table 3.3. Shorter lines are associated to a lower average velocity, which seems so corroborate our previous deduction. The high STD value indicates the great variability within PIV windows, but the difference in average velocity remains relevant because of the high number of measurements, which makes for a small SEM.

### 3.2.5 Methods for the quantification of oscillating behavior

To follow cell motion over time and obtain a visual representation of the oscillations, we average the $x$-velocity over $y$ ($v_x(x;t) = \langle v_x(x,y;t) \rangle_y$) to yield the kymographs reported in Figure 3.16, Figure 3.17, Figure 3.18 and Figure 3.19. This choice was further supported by the predominance of cell motion in the $x$ direction. We also repeated the operation averaging $y$-velocity over $x$ and averaging $y$-velocity over $y$, but none of these attempts yielded any measurable periodicity.

To better visualize the presence of cyclical velocity inversions we computed the auto-correlation (AC) function of the kymograph $g(\delta x, \delta t) = \langle v_{\parallel}(x,t)\ v_{\parallel}(x+\delta x, t+\delta t)\rangle_{x,t}$.

Before diving into the specifics of the protocols implemented, I want to reserve some time to describe this tool, which revealed itself to be of the utmost versatility throughout my thesis.

#### 3.2.5.1 Brief interpretation of the auto-correlation image

The auto-correlation, already introduced in the context of PIV and image stitching (see chapter 2), was chosen because it is an effective instrument to highlight periodicity while averaging over large signals, in this case the entire kymograph. This section is meant to give a practical working knowledge of how the auto-correlation was used in my work, enough to understand my interpretation of the omnipresent images in the remainder of this chapter, and it is not to be mistaken with a complete treatment of its mathematical background, which can be found elsewhere [298].

A simple interpretation of the auto-correlation image is as follows. The intensity of every pixel represents the degree of similarity between two images superimposed in a specific manner. In our case, both pictures are identical and correspond to the $x$-velocity kymograph. The procedure consists on multiplying the image with itself, and then repeating this operation adding a misalignment, or shift ($\tau$), between the two pictures. Since the multiplication of matrices (i.e. pictures) results is another matrix, every step of this operation introduces a third image, which is then collapsed to a single value, or score, by summing all of its pixels. This means that for each value of the shift $\tau(x,t)$, which is a function of space and time, we obtain a score corresponding to the degree of similarity between the image and itself shifted by that exact $\tau(x,t)$. By plotting this "similarity score" as a function of the shift we obtain the auto-correlation image in Figure 3.15 and Figure 3.16b. right.

If the two images are identical or have a high degree of similarity, the multiplication results in a high score. On the other hand, if the images are different, or simply misaligned, there is a higher chance that areas of positive values will overlap with areas of negative values, and their multiplication will thus yield negative results, lowering the overall score. Briefly, the lower the similarity, the lower the score and vice versa.

With this in mind, we can now understand the images in Figure 3.15 and Figure 3.16. The peak corresponding to $\tau(x,t) = 0$, which is conventionally placed in the center of the image rather than in the corner, is the integral of all pixels of the image obtained by multiplying the kymograph by itself. In this case, superimposition is perfect and this means that there is no other value of $\tau(x,t)$ that can cause the two

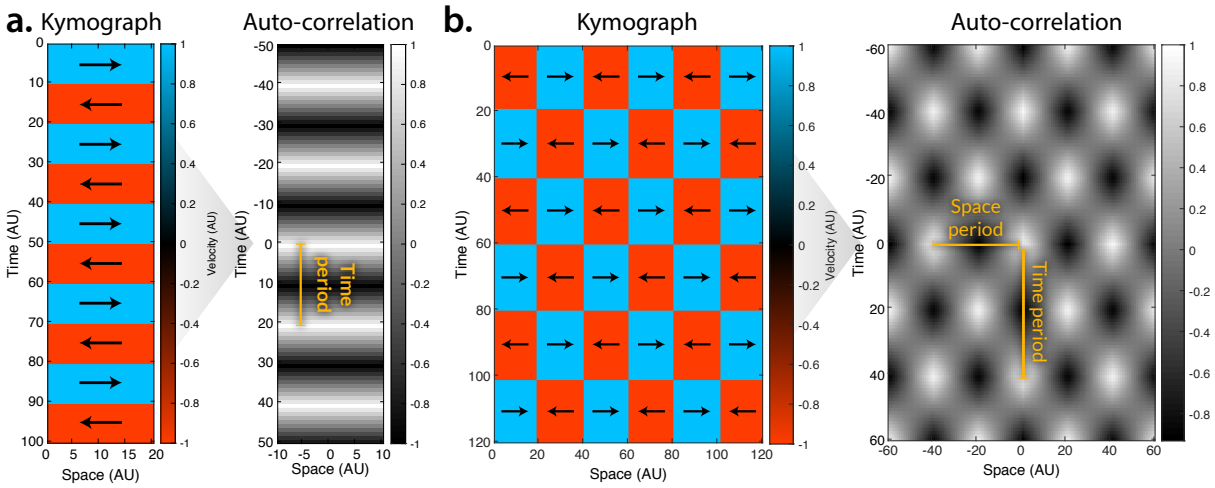


Figure 3.15: Simplified models of kymographs and their auto-correlation. In the examples reported, the migration of cells is modeled as square standing waves, with 5 nodes (**b.**) or without (**a.**). The auto-correlation images clearly display a pattern, whose periodicity, mirroring that of the square standing waves, can be easily measured.

images to have higher similarity. The intensity of the central peak is maximal, and it is therefore set to 1. For what concerns any pixel at a certain distance $\tau(x, t)$ from the center, its intensity is proportional to the degree of similarity of the kymograph with itself after that much time and after that much space. Being the kymograph a representation of cell velocity, the presence of a peak in the auto-correlation at a certain time-shift tells us that, after that much time, cell are moving similarly to how they were moving originally. Contrarily, a negative peak means that after that much time, cells are moving in the opposite direction. The same holds true for the $x$-direction, or space.

A periodicity in the auto-correlation image directly mirrors a periodicity in the way cells move, and this is the reason why we chose it as a tool to put numbers on our oscillations.

Figure 3.15 shows two examples of over-simplified kymographs and their relative auto-correlations. The movement of cells is here modeled, I use the word in its broadest meaning possible, as a square standing wave. Cells are either moving rightwards or leftwards with unitary velocity, and their behavior is inverted periodically. Two things are noteworthy: (i) the auto-correlation images oscillate between values of 1 (the image is symmetric, so it overlaps perfectly with itself) and -1 (all positive areas overlap with negative ones); (ii) the distance between peaks in the AC matches exactly that between areas with same sign in the kymograph, i.e. the periodicity of a kymograph and its AC is identical. This fact is utilized later on to calculate the time period and wavelength for real, more noisy, experiments. The peculiar kymographs generated in Figure 3.15 are somehow archetypal of those encountered during our experiments, and should, as

such, be used as a reference throughout the remainder of the chapter.

#### 3.2.5.2 Noise-removal with Gaussian filters

Moving on to real examples, the presence of wave-like motion was immediately evident by the observation of brightfield images and the relative velocity field (Figure 3.16a). Unfortunately, such oscillations did not manifest themselves as distinctly in the relative kymographs (see Figure 3.16b), where the presence of periodic movement is all but clear. On the other hand, regularly spaced bands and motives appear in the auto-correlation, which, thanks to its averaging of the entire experiment, manages to highlight periodicity in noisy environments. A brief comparison of the images reported in Figure 3.15 and Figure 3.16 reveals the strong difference in the background intensity of the AC. The difficulty of a direct wave-identification in kymographs and the possibility of increasing the quality of the auto-correlation and the successive quantification convinced us of the need for improvement.

We realized that two major factors were affecting the kymographs: (i) the presence of long-range tissue deformations, or stretchings, highlighted in the white dashed box in Figure 3.16; and (ii) local noise in the PIV quantification. Following the path taken in [195], we decided to filter the kymographs utilizing a Gaussian blur.

Basically, this consists in convoluting an image with a 2D-Gaussian function, an operation whose net result is to blur the picture, which appears out-of-focus. An equivalent way to imagine it is by considering a sliding average whose kernel has a Gaussian shape: each pixel becomes the weighted average of the intensities of all pixels within a neighboring area, an the weight is defined by the Gaussian function itself. By changing the characteristics of this function, in both space and time, we choose the size of the area over which the average is performed, and this results in a different amount of blur. This operation is done because the net effect is that of a filter: by blurring an image we lose detail. With a small amount of defocus we only lose very tiny detail, contrarily, with a large defocus we lose all but extremely large objects. In general, the size of the objects becoming indistinguishable increases with the amount of defocus. In our case, the defocus is externally-imposed, so we can directly control it by changing the size of the Gaussian kernel. This means that by carefully selecting and applying different blurs, we effectively choose which details to retain and which to lose.

In general, when we apply a Gaussian blur, whose kernel is defined by a certain $\sigma_x$ and $\sigma_t$, we lose all detail whose size is smaller than the $\sigma$ chosen. From the shape of the Gaussian kernel

$$G(x) = \frac{1}{\sqrt{2\pi}\sigma_x} \cdot e^{-\frac{x^2}{2\sigma_x^2}} \tag{3.1}$$

we can calculate the precise transfer function of the filter, which describes the intensity transmitted at each frequency:

$$G(f) = e^{-\frac{f^2}{2\sigma_f^2}} \tag{3.2}$$

with $\sigma_x\sigma_f = \frac{1}{2\pi}$ and $f = \frac{1}{x}$. I report here the 1-dimensional case for simplicity, the equations in 2-dimensions are the product of the two Gaussians, one per each direction chosen.

A Gaussian blur is traditionally a low-pass filter, meaning that it tends to attenuate all signals with frequencies higher than a certain cutoff. This is ideal to remove local noise, which is characterized by an extremely high spatial and temporal frequency. To achieve this, we treated the images with a low-pass Gaussian filter ($\sigma_x$=20 $\mu$m, $\sigma_t$=30 min, kernel size = 3×$\sigma$), obtaining the image in Figure 3.16c center. To remove large deformations, which are associated with an extremely low frequency and are thus removed with a high-pass filter, we work in the opposite direction. We first applied a low-pass Gaussian filter ($\sigma_x$=120 $\mu$m, $\sigma_t$=130 min, kernel size = 3×$\sigma$) to generate an image only retaining the deformations we want to exclude (Figure 3.16c left), and we then subtract this image from the one obtained by removing high-frequency noise. By applying these two filters in succession we effectively remove the contribution of large deformations and local noise, obtaining a kymograph only reporting those frequencies we associate with oscillations in cell motion (Figure 3.16d left). The transfer functions of the filters applied are reported in (Figure 3.16c right). By calculating the auto-correlation function of the filtered kymograph we obtain an image which reproduces much of the original periodicity, without the presence of strong backgrounds related to the contribution of noise.

The use of filters, although so far presented in a positive light, is in fact a “double edged sword”. If, on the one hand they are a great tool to extract features from noisy environments, on the other they can be responsible for the generation of artifacts. In the specific configuration we implemented, this latter situation has to be taken into considerations. When applying two Gaussian filters, the overall transfer function has a clear peak in the center. If we treat white noise, which contains every frequency in equal amounts, with such filters, the output will reflect the shape of the filter, presenting a clear signal at exactly the position of the peak in the transfer function. In this situation, we artificially create the signal we are seeking in data which would otherwise only contain noise.

In order to avoid this artifact, we always juxtaposed all observations of the filtered data with both the original, untouched data and that obtained by only removing long-

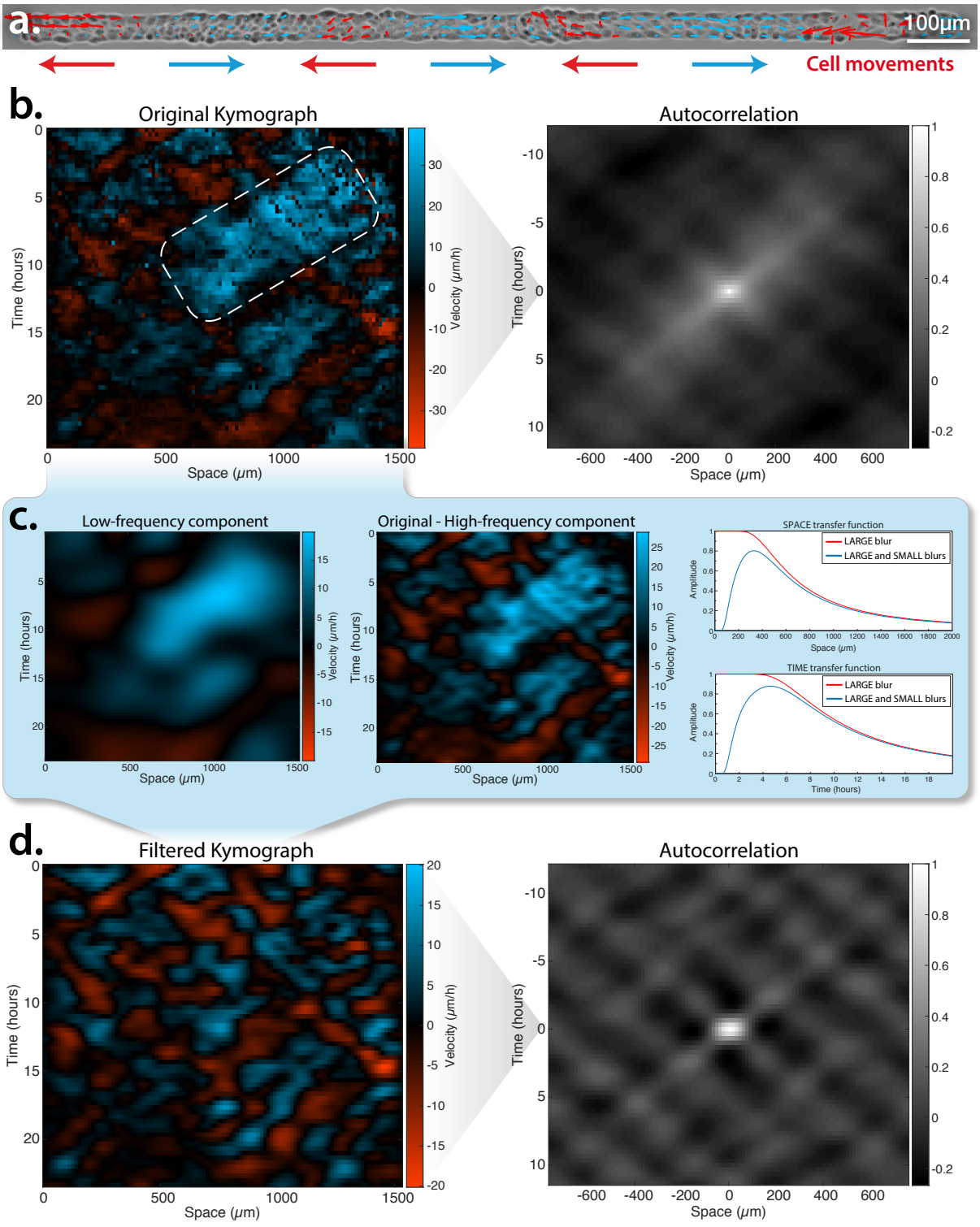


Figure 3.16: Example of the filters applied to kymographs. Oscillations identifiable by observing brightfield images and local cell velocity (**a.** - blue arrows = positive $x$-velocity, red arrows = negative $x$-velocity) are not always evident in the kymograph (**b.** - left), often due to the presence of tissue deformations (*white dashed rectangle)* and noise. Even though the presence of periodicity is evident by calculating the auto-correlation (**b.** - right), quantification is hindered. The effect of tissue stretchings (i.e. low-frequency motion) is estimated by applying a large Gaussian blur to the kymograph (**c.** - left), whereas a small Gaussian blur is applied in order to remove high-frequency local noise (**c.** - center). A final filtered kymograph is the calculated by subtracting the low-frequency components from the de-noised image (**d.** - left). The auto-correlation of the filtered kymograph shows all the periodicity of the original, with a smaller noise component. The transfer functions relative to the application of both filters or only the large one are reported in (**c.** - right).

range tissue deformations. The plots of all three data-sets are present in Figure 3.17 and Figure 3.18, in a way that matches exactly the graphs we utilized for the quantification. This allowed us to discern between peaks characteristics of cell behavior, and those that could be affected by the artifacts mentioned above. Throughout the analysis presented below, we used the unfiltered plots to determine whether a periodicity was effectively present, and the filters to help us guide the eye and better pinpoint the peaks associated to the oscillations.

In light of these observations, the size of the filters is of the utmost importance because, even though precautionary measures were put into place, it can drastically bias the quantification. To minimize this effect, we first ran one cycle of analysis without filters on all our data relative to lines longer than 500 $\mu$m. This yielded very noisy measurements of the space and time periods, which were then utilized as targets to center the transfer functions on.

#### 3.2.5.3 Periodicity calculation with auto-correlation

A schematic representation of the procedure followed to calculate the periodicity is reported in Figure 3.17. After filtering the kymograph, the presence of oscillations in both time and space is more evident, as highlighted in Figure 3.17-top. The quantification of the typical period, corresponding to the average time necessary for cells to change direction twice, i.e. a full wavelength, is done thanks to the auto-correlation. By plotting a vertical line-profile crossing the central peak of the AC image (Figure 3.17f), we effectively observe how cell velocity evolves in time. The presence of a negative peak at a specific time shift $(\tau(t))$ indicates that, on average, the local velocity has changed sign. Accordingly, the presence of positive peak at $\tau(t)$ tells us that cell velocity is back to its original direction. The time period was measured by manually detecting all peaks in the auto-correlation plots. The same is true for what concerns the space period (i.e. the wavelength), which was calculated by measuring the time-shift associated with a peak in the horizontal plot-profile (Figure 3.17e).

The specific method employed to calculate the AC, two successive fast Fourier transforms, introduces an additional effect that has not yet been tackled. As mentioned above, the calculation of the auto-correlation implies shifting two images with respect to each other. While doing so, the area where they overlap, and where we can effectively multiply the two, decreases. In the specific situation of this work, this is not a problem because the methods utilized include the equivalent of periodic boundaries conditions. In layman's terms, this is equivalent to calculating the auto-correlation of an infinite image created by stitching the kymograph together in a sort of tile-work. This

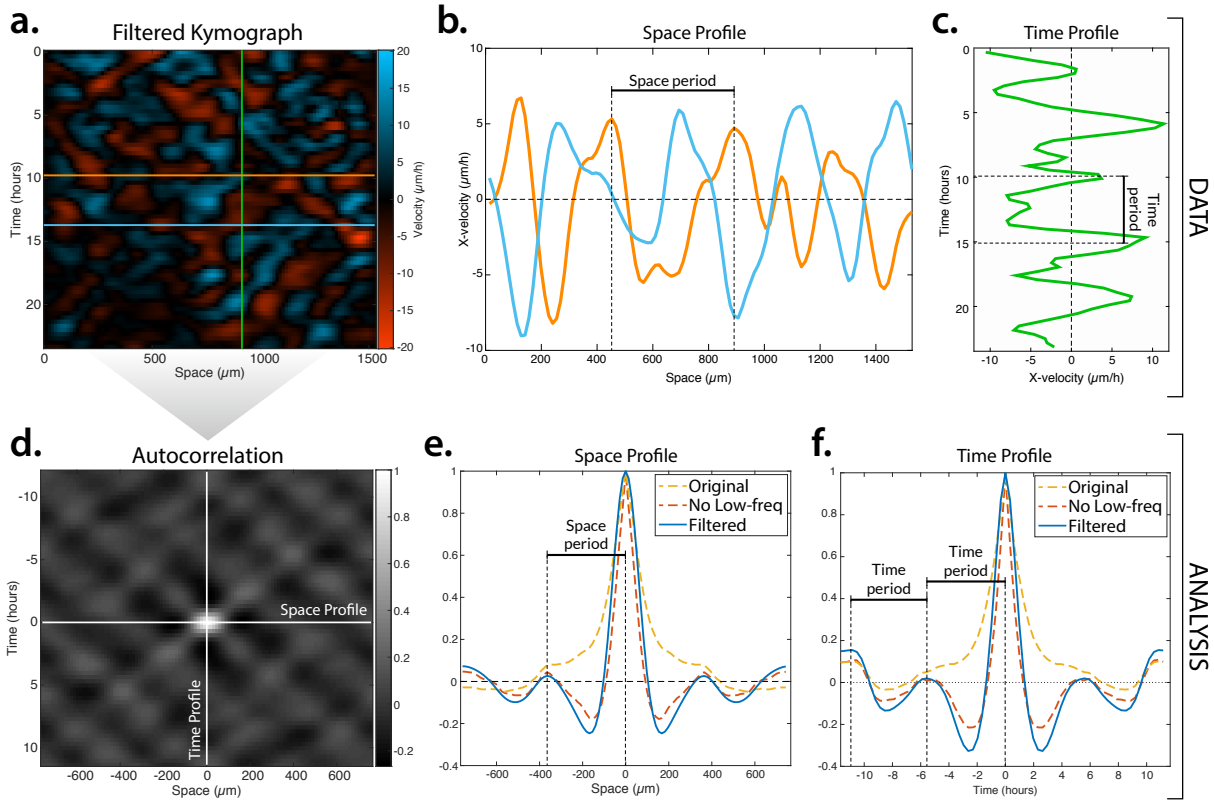


Figure 3.17: Schematic representation of data analysis on full kymographs. Examples of the filtered kymograph (**a.**) for a 1500 $\mu$m long tissue displaying clear oscillations in space (**b.**) and time (**c.**). Two plots of the velocity profile $\sim$ 4 hours apart are presented in (**b.**), showing a clear phase opposition: all cells have inverted their velocity direction. The same periodic inversion is true for the velocity in time at a specific location (**c.**). The typical local time and space periods can be visualized on these plots, but a more thorough calculation of these variables relative to the whole kymograph is carried out from the auto-correlation (**d.**). The vertical (**e.**) and horizontal (**f.**) plots represent the periodicity of the entire kymograph in time and space, respectively. By identifying the peaks we can estimate the typical periods.

also means that, because of symmetry considerations, shifting by half length towards the right or towards the left becomes equivalent, and, finally, that we can only measure the correlation in space for $1/2 \times L_x$ and in time for $1/2$ of the total experiment duration. This effect strongly limits our ability to see higher order peaks, which would be visible for longer lines or for experiments where oscillations lasted for more extended periods of time. Nevertheless, higher order peaks were observed in space, especially for 1500 $\mu$m and 2000 $\mu$m long lines, and often in time, as reported in Figure 3.18. In those cases, the position of each peak was divided by a number defining its order, so that the second peak would be divided by 2, the third by 3 and so on. All the values obtained were then averaged to generate a single value of the period.

For these same symmetry factors, on 500 $\mu$m long lines, the first peak, situated at a shift of $\sim$ 400 $\mu$m, was not visible. For this value of $L_X$, the wavelength was calculated by measuring the position of the first negative peak, and then multiplying it by 2 to

estimate the hypothetical position of the first positive peak.

#### 3.2.5.4 Horizontal and vertical sub-kymographs

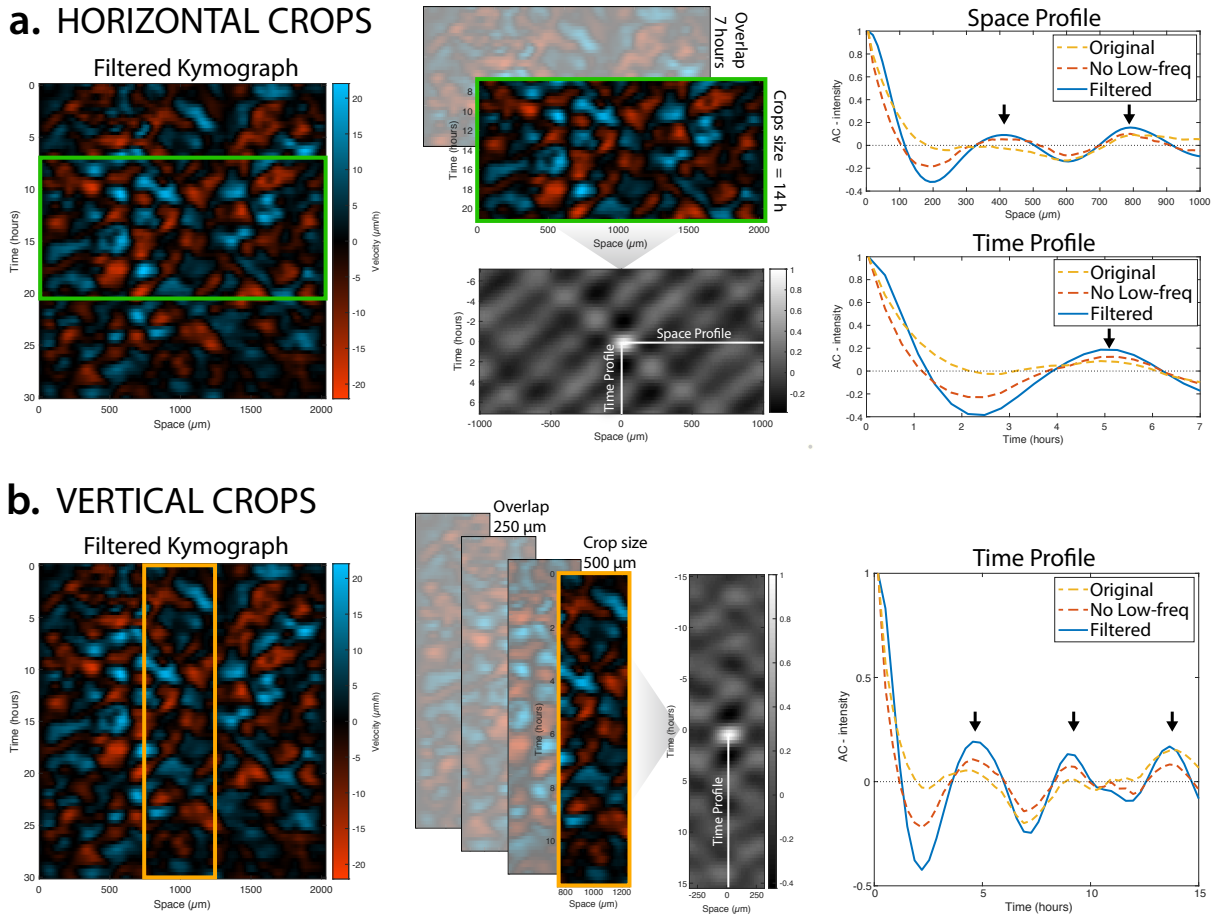


Figure 3.18: Schematic representation of data analysis performed by sub-dividing kymographs. To improve the quantification of space and time periods, we divide the filtered kymograph into overlapping horizontal (**a.**) and vertical (**b.**) sub-kymographs. These represent the behavior the tissue within specific time or space windows. The size of each sub-kymograph is chosen to identify 1 period ($\sim 3 \times$ period). For each sub-kymograph, we calculate the auto-correlation and then identify all peaks (*black arrows*), in time for vertical crops (**b.**-right), and in both space and time for horizontal crops (**a.**-right).

The experiments are associated with a slow increase of cell density, which in turn affects the average migration velocity and the velocity-correlation length (see subsection 1.5.2). We therefore wondered whether these phenomena could result in a slow change, increase or decrease, of the typical period in time, which could potentially render our data analysis ineffective. A strategy to avoid this effect consist on measuring the period more locally in time, by sampling the kymographs and dividing them into sub-kymographs, only concerned with shorter amounts of time. This strategy, summarized in Figure 3.18, allowed us to measure the space period for different time points. Based on preliminary results obtained by considering experiments as a whole, we de-

cided to crop the kymographs into sub-units of 14 hours, with an overlap of 7 hours (Figure 3.18a). This size is more than double the expected time period, which allows the visualization of the first peak in time, and since these horizontal crops span the whole $x$-axis, we could also measure the space period. We also applied the same procedure in the vertical direction, by sub-dividing the kymographs into vertical stripes 500 $\mu$m wide with an overlap of 250 $\mu$m (Figure 3.18b). In this case, we only measured the time period.

For each crop, we calculated the auto-correlation, and then measured the periodicity by manually detecting the peaks in the plot profiles. Just like explained above, all peaks were divided by their order-number and averaged to obtain one value per sub-kymograph. All the values corresponding to different crops were then averaged to yield one final estimation of the time and space period for that specific tissue. Even though we measured all of these quantities, we eventually considered the time period estimation obtained from vertical sub-kymographs, and space period estimation obtained from horizontal sub-kymographs. This because the values of time period calculated from horizontal and vertical crops did not differ substantially, so those from vertical crops were deemed better because of the possibility to visualize peaks of higher order, which could make the estimation more accurate.

**PERSONAL NOTE**

*I like to think that I am aware of the risks of over-analyzing one's data. Every step, every filter, every mathematical function tends to introduce a bias, which is, in my opinion, too often not duly assessed or considered. With the proper combination of data analysis, data selection and a pinch of (purposeful or not) neglect, we can draw any result from any data set, regardless of the presence of a signal or not. With this in the back of my mind, I quickly grew aware of the need to employ many such strategies in order to reach meaningful conclusions. The almost ubiquitous presence of the unfiltered data throughout our analysis was one of the precautionary measured I put in place, while I tried to double-check every step of the way. Ultimately, what convinced us of the quality of the data was the almost constant presence of periodicity in the auto-correlation of untouched data. We then used more "insidious" analysis in order to put numbers on a phenomenon we could, first of all, see with our eyes.*

*The reader will be the judge of our approach.*

### 3.2.6 Transition between wave-like modes

After the application of the Gaussian filters and the calculation of the AC function, approximately 95% of experiments could be clearly separated into the two categories previously mentioned: global or multi-nodal oscillations. To quantify the appearance of either phenotype as a function of $L_X$, we systematically calculated the filtered AC image for each experiment and assigned it to one of the categories. Those instances where no clear pattern could be recognized were counted separately, and represent the missing fraction for those values of $L_X$ where the sum of occurrence of both phenotypes differs from 100%. The results, together with some examples of kymographs and their relative AC, are reported in Figure 3.19.

The relative incidence of the two behaviors depends strongly on $L_X$, with a clear transition between modes for $L_X^c \simeq 400$ $\mu$m. Global oscillations are overwhelmingly prevalent for $L_X < L_X^c$, tissues whose length is comparable with $L_X^c$ can display both phenotypes in variable ratio, and above $L_X^c$ multi-nodal oscillations dominate statically.

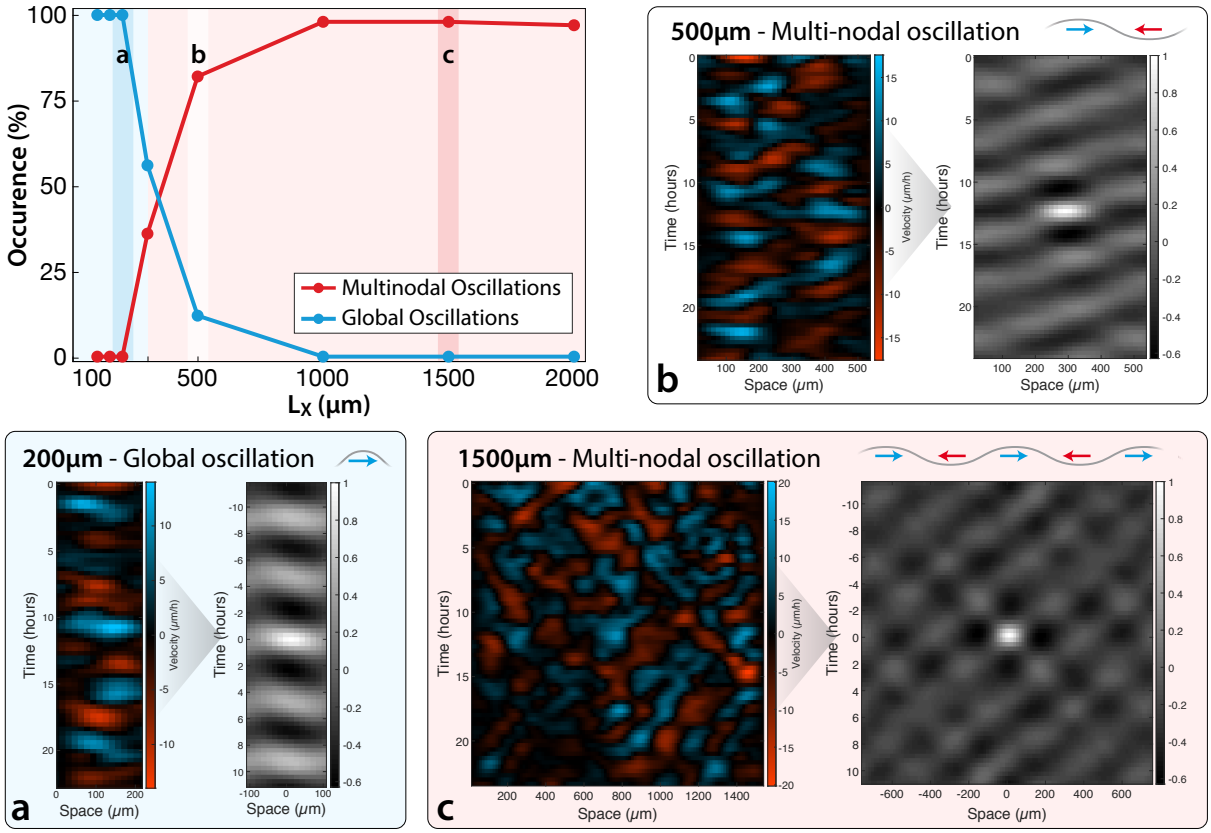


Figure 3.19: Transition between global and multi-nodal migration modes. The relative occurrence of each phenotype as a function of tissue length is reported in the top-left corner. For each point, we considered on average 39 tissues, obtained from three independent experiments. The square boxes report examples of global (**a**) and multi-nodal (**b**, **c**) oscillations. Tissues of $L_X = 500$ $\mu$m display a mix of both phenotypes, but the example reported is that of a clear standing wave with a node in the center (**b**).

### 3.2.7 Time period and wavelength do not adapt to the confinement

These results seem to suggest that, when possible, tissues establish multi-nodal oscillatory modes with predetermined features. When confined to spaces smaller than those characteristic of a full wavelength, the behavior changes.

To verify whether the typical periodicity is predetermined, or if it adapts to the confinement, we measured the time and space-periods for tissues of different $L_X$. For each experiment, we calculated the auto-correlation of the sub-kymographs to extract the periodicity in the two dimensions. We then averaged all values to obtain the results in Figure 3.20. In those cases displaying global oscillations, the space period is imposed by the confinement. Since a measurement is impossible, it is not reported.

The graph in Figure 3.20 confirms the presence of two regimes with a transition around $L_X^c \simeq 400$ $\mu$m. For relatively short tissues, where global oscillations are the prevalent phenotype, the time-period scales linearly with the tissue size, while the wavelength, imposed by the confinement, is not calculated here. On the contrary, when multi-nodal waves dominate ($L_X > 500$ $\mu$m), both time-period and wavelength are approximately independent of $L_X$. To estimate such periodicity, we averaged all data obtained for tissue lengths only displaying multi-nodal oscillations ($L_X = 1000$, 1500, 2000 $\mu$m) to obtain values of wavelength and period equal to $\lambda = 380 \pm 40$ $\mu$m and $T = 4.7 \pm 0.8$ hours, respectively (errors represent the standard deviation, $n = 130$).

Using the typical time and space-period, we also calculate an effective velocity $u = L_X/T \simeq 78 \pm 13$ $\mu$m/h, which is approximately independent of the tissue length. Even for short lines, in the global oscillation regime, $u$ is preserved because the time-period scales linearly with the pattern length. Moreover, we notice that $u$ is approximately 10 time larger than the velocity of single cells (Table 3.3).

Taken together, these results confirm the existence of self-sustained oscillations in epithelial monolayers. Thin lines of different length, combined with a robust protocol to highlight specific components, allowed us to emphasize the presence of a transition between wave-like migration modes. Such transition between global and multi-nodal oscillations happens for tissue sizes around $\sim 400$ $\mu$m, a length that matches the typical wavelength measured. Moreover, since the time and space periods do not adapt to the confinement, we can conclude that these oscillations are intrinsically encoded in the cells.

All these result have been recently published [279] (see section A.3), together with the theoretical model that helped us guide our choices. Such model was developed by

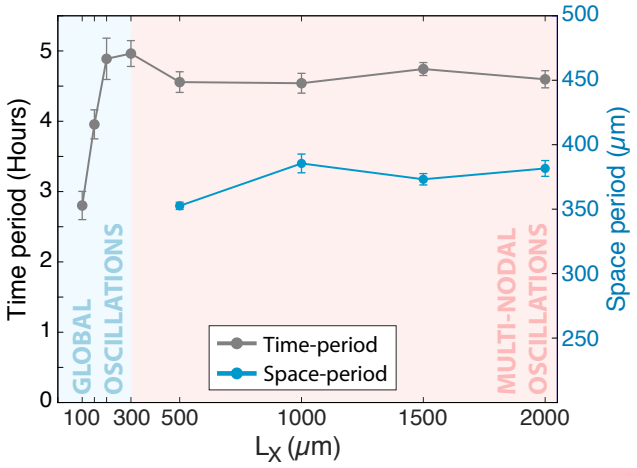


| $L_X$ (μm) | Space (μm) | STD | SEM | Time (hours) | STD | SEM |
|---|---|---|---|---|---|---|
| 100 | / | / | / | 2.8 | 0.6 | 0.2 |
| 150 | / | / | / | 4.0 | 0.8 | 0.2 |
| 200 | / | / | / | 4.9 | 1.2 | 0.3 |
| 300 | / | / | / | 5.0 | 1.6 | 0.2 |
| 500 | 353 | 25 | 3 | 4.6 | 1.0 | 0.1 |
| 1000 | 385 | 47 | 7 | 4.5 | 0.9 | 0.1 |
| 1500 | 373 | 34 | 4 | 4.7 | 0.7 | 0.1 |
| 2000 | 382 | 35 | 6 | 4.6 | 0.7 | 0.1 |

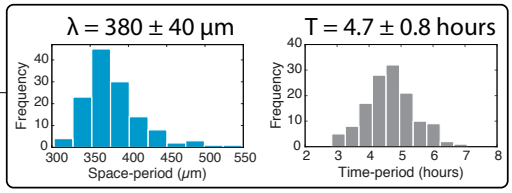


Figure 3.20: Dependence of space and time period on tissue length. Quantification of the typical periodicity for tissues of different length seeded on PAA gels (rigidity = 40 kPa). The typical space-period (*blue*) and time-period (*gray*) as a function of tissue length are plotted on the *left*. Error-bars represent the standard error on the mean. The same data is reported in more detail in the table (*right*), together with the standard deviation (*STD*) and the standard error on the mean (*SEM*). We considered on average 39 tissues per each value of $L_X$, obtained from three independent experiments. The space ($\lambda$) and time ($T$) periods typical of multi-nodal oscillations are calculated as the average of the measurements of all tissues for which $L_X$ >500 $\mu$m. The values and relative histograms are reported in the inset (*bottom-right*).

Magali Le Goff and Kirsten Martens [1], and it constitutes an integral part of the work we have summarized in the article. As such, I briefly introduce it here, limiting myself to its basics and the general conclusions it led to.

## 3.2.8 Oscillations are reproduced by a Self-propelled Vertex model

Without diving into a detailed review of existing physical models, which can be found elsewhere [178, 179, 299, 300], a number of recent works have demonstrated the adequacy of Self-propelled Vertex models (SPV) to describe collective cell motility [180, 189, 264]. For this reason, we adapted a SVP model in order take into account the presence of boundaries, a fundamental component of our experiments. This implementation helped us in understanding the basic ingredients for oscillations and ultimately predicted the presence of the phase transition we have confirmed experimentally.

### 3.2.8.1 Implementation of the Vertex model

A complete description of the model and our implementation can be found in [279, 301]. Briefly, the confluent cell monolayer is modeled as a two-dimensional network of

[1] Kirsten Martens, Université Grenoble Alpes, Laboratoire Interdisciplinaire de Physique, CNRS, F-38000 Grenoble, France

Voronoi polygons, where each cell is described by the position of its centroid ($\mathbf{r}_i$) and the portion of space which is closer to its own centroid than to all others. The energy of each configuration is described by:

$$E = \sum_{i=1}^{N_{cells}} \frac{K}{2} \left(A_i - A^0\right)^2 + \sum_{i=1}^{N_{cells}} \frac{\Gamma}{2} \left(P_i - P^0\right)^2 \tag{3.3}$$

where $N_{cells}$ is the total number of cells, $A_i$ and $P_i$ are the area and perimeter of the i-th cell, $K$ and $\Gamma$ are the area and perimeter stiffness respectively, $A^0$ is the target area and $P^0$ the target perimeter, identical for all cells.

In the absence of other forces like self-propulsion, the mechanical behavior of the tissue is governed by a model parameter, the shape factor ($p^0 = P^0/\sqrt{A^0}$), that encodes single-cell properties such as cell-cell adhesion and cortical tension [185]. It was shown that for small values of the shape factor ($p^0 < 3.81$) the tissue behaves as a solid, i.e. it has a finite yield stress, while for large values of $p^0$ (> 3.81), cell shape deformations require no energy and frequent neighbor exchanges lead to a fluid-like behavior. In our case, these parameters were chosen to describe a monolayer in a solid-like regime ($p^0 =$ 2.5).

The dynamic response of the system is calculated by solving the equation of motion, describing the evolution of the position of each centroid over time. In our implementation, as is previous studies [180, 264, 301], we consider overdamped dynamics, i.e. a force balance between frictional forces with the substrate and the forces acting on each centroid:

$$\gamma \frac{\partial \mathbf{r}_i}{\partial t} = \mathbf{F}_i + f_a \mathbf{n}_i + \nu_i(t) \tag{3.4}$$

where $\gamma$ is the friction coefficient describing the interaction between the cell and its substrate. The force acting on each cell has 3 components: (i) a mechanical force between cells, calculated as the negative gradient of the energy functional ($\mathbf{F}_i = -\nabla_{\mathbf{r}_i} E$); (ii) a self propulsive active force, at constant velocity ($v_0$), acting along the direction of cell polarity ($\mathbf{n}_i$); (iii) a uncorrelated stochastic force ($\boldsymbol{\nu}_i(t)$), which introduces noise.

Finally, as discussed elsewhere (see subsection 1.8.3), any model explaining the presence of waves in an overdamped system requires an additional component to play the role of the "effective inertia". In our case, we introduce a feedback mechanism reorienting the polarization of each cell with the direction of its motion. If we describe cell polarity based on the angle ($\theta_i$) with the $x$-axis [i.e., $\mathbf{n}_i = (\cos(\theta_i), \sin(\theta_i))$], the

dynamics of $\mathbf{n}_i$ follow the equation:

$$\frac{\partial \theta_i}{\partial t} = \frac{1}{\tau_{al}} \sin(\theta_i - \phi_i) + \nu_i^r(t) \tag{3.5}$$

where $\phi_i$ is the angle between the velocity of cell $i$ and the x-axis and $\nu_i^r(t)$ an orientational Gaussian noise. The key ingredient is $\tau_{al}$, which represents the typical time required by the cell to reorient its polarization with its velocity.

This model describes the dynamics of an active elastic material, with a delayed alignment mechanism between the directions of self-propulsion and velocity. This alignment is a key ingredient to observe oscillations, which are reproduced when the timescale of the feedback ($\tau_{al}$) is smaller than that of rotational diffusion.

So far, the model is extremely similar to that used by Giavazzi et al. to describe flocks in non-confined confluent tissues [264]. One major difference is that, whereas other implementations of the SPV generally assume periodic boundary conditions, in our case we need to include the confinement typical of the experimental geometry. This is done considering two types of "special" particles, which do not represent actual cells: (i) *wall* particles are introduced to model a confined tissue; (ii) immobile repulsive particles form a rectangular barrier of size $L_X$ and $L_Y$ to reproduce the confinement imposed in the experiments (repulsive interaction with the cell centroids, no interactions with boundary particles).

#### 3.2.8.2 The SPV model predicts a transition between oscillatory modes

An example of the SPV configuration is reported in Figure 3.21. Throughout the simulations, $L_Y$ was kept constant at $\sim 3$ cells, in order to mimic the real situation, while other parameters where changed to explore the dynamics of the system in different conditions.

For $\tau_{al} = 0.3$, SPV simulations display steady state oscillations, similar to those observed during our experiments. On long confining tissues (i.e. high aspect ratio), the simulations reproduce multi-nodal oscillations (see Figure 3.21b), and a decrease of $L_X$ is associated to a reduction of the number of nodes. Ultimately, below a critical length, only half a wavelength fits in the tissue, and the model correctly reproduces a regime characterized by global oscillations. Moreover, in this latter situation, the oscillation period increases approximately linearly with the system size.

The periodicity of multi-nodal oscillations, calculated thanks to the auto-correlation of the kymograph, can be estimated as 22 model length units in space and 8 model time units in time. Using cells velocity ($v_0$) to approximately match model and experi-

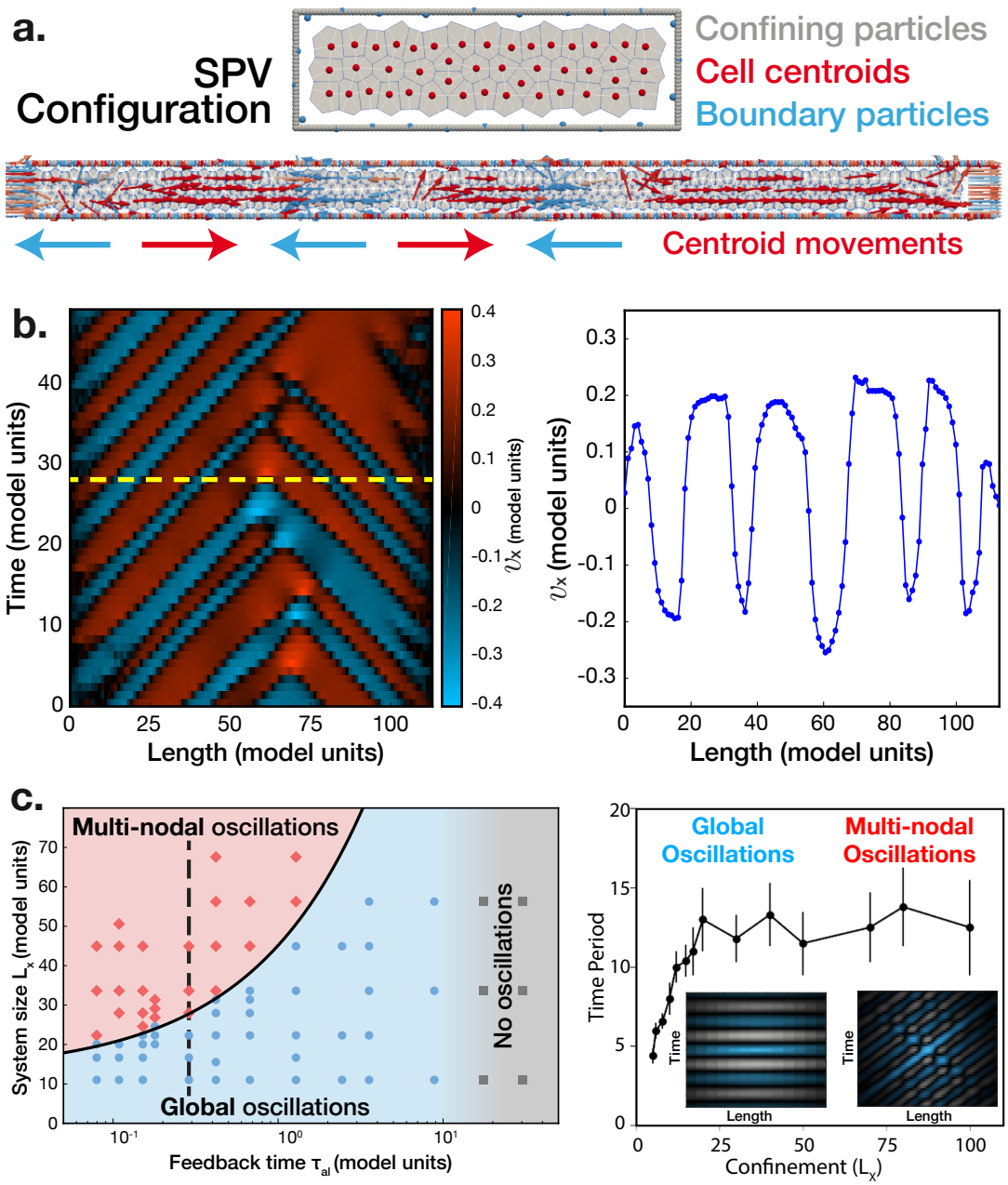


Figure 3.21: Self-propelled Voronoi Model for collective oscillations in confluent tissues. **a.**) Example of the configuration of the Self-propelled Voronoi model reproducing a confined tissue (*top*) and the velocity field of the centroids (*bottom*). **b.**) Kymograph of the average velocity along $x$ (*left*) and its profile along the dashed line (*right*). **c.**) Phase diagram (*left*) of the different oscillation modes predicted by the SPV model in the $\tau_{al} - L_X$ plane (*left*), and the time period for different values of $L_X$ (*right*) along the black dashed line. Depending on the system size ($L_X(\tau_{al})$), two phenotypes are observed: for large systems where $L_X > L_X^c(\tau_{al})$ the auto-correlation of the kymograph is reminiscent of that of multi-nodal oscillations (*left inset*), whereas for small systems ($L_X < L_X^c(\tau_{al})$) the behavior is that typical of global oscillations (*right inset*). The dots in the diagram represent simulation data points indicating whether the system exhibits global (*blue disks*), multi-nodal (*red diamond*), or no oscillations (*grey squares*) for large values of the feedback timescale ($\tau_{al} > \tau_{al}^c \approx 17$ model time units). The solid line delimiting the global and multi-nodal oscillation phases is a power law fit of the transition data points ($L_X^c(\tau_{al}) = a\tau_{al}^b + c$ with $a \simeq 32$, $b \simeq 0.62$, $c \simeq 13$).

mental units, we can predict a periodicity around $\lambda \simeq 300$ $\mu$m and for the period $T \simeq$ 2 hours. This demonstrates that, although some additional tuning of the parameters is needed, the model is able to reproduce the oscillatory behavior and the transition between modes, together with an approximate estimation of the periodicity.

It is important to note that, although the simulations reproduce the velocity profiles (Figure 3.21b *right*) and auto-correlation (Figure 3.21c *bottom*), the full dynamics of the model (Figure 3.21b *left*) do not correspond to standing wave oscillations.

In the global oscillation regime, the period increases approximately linearly with $\tau_{al}$. This confirms, once more, its role as effective inertia, and highlights the importance of a delayed feedback for the presence of oscillations altogether. The transition between different modes, studied in the $\tau_{al} - L_X$ plane, is reported in Figure 3.21c. For extremely high values of $\tau_{al}$, the feedback is so slow that rational noise dominates and no oscillations are observed. On the other hand, when oscillations can be observed, $L_X^c$ is a function of the specific $\tau_{al}$ chosen.

In conclusion, we demonstrate the existence of epithelial tissue oscillations and calculate their typical period and wavelength. Moreover, since these quantities are not adapted to external confinements, we conclude that they are intrinsically encoded in the cells.

# 4. Preliminary results

After we gathered definitive evidence of the existence of periodic oscillations in cell motion and we characterized such movements as having a specific wavelength and period, we had to choose how to direct our future investigations. Two roads lay ahead. On the one hand, we could try to obtain a more thorough characterization and understanding of the key components of these oscillations, a task aided by the presence of the model to guide our experiments. A different prospect, perhaps more risky in terms of short-term outcomes, was to concentrate on finding a biological counterpart to these oscillations, i.e. a cellular function that appeared to be selectively activated at the nodes or the anti-nodes of the wave.

Of the two roads, I chose to concentrate more on the second, and try to look for a proof that our waves play a part in the biochemistry of cellular development. Since I did not completely abandon trying to better characterize oscillatory motion, and our preliminary experiments probe a wide range of subjects, I divide them into two categories: those related to understanding which components are fundamental for the waves, and those related to a biological counterpart.

I chose to present all these results here, rather than in the previous chapter, in order to stress their preliminary nature. Also, I include all experiments where the readout was negative, or where we could not reach a definitive answer, both for lack of statistics and more technical problems. This was guided by the belief (and hope) that negative results can steer future work as well as positive ones.

## 4.1 Preliminary characterization of oscillatory motion

### 4.1.1 The role of proliferation

In the SPV simulations we carried out, cell proliferation was implemented in order to reach the correct cell density in a manner compatible with the vertex energy functional, and was then tuned off. This suggests that cell division is not a fundamental component for oscillatory motion. To verify whether this hypothesis is correct, we treated our

tissues with Mitomycin C, a compound known to inhibit proliferation in cell cultures, to then measure if the absence of cell division affected the presence or the typical periods of the oscillations.

Upon a first visual inspection, waves are present and cell behavior does not seem to be affected. We therefore quantified the typical periodicity, by considering 15 tissues ($L_X$ = 500 and 1000 $\mu$m), as $\lambda = 350 \pm 40$ $\mu$m and $T = 4.5 \pm 0.7$ hours, respectively (errors represent the standard deviation).

Although these results need additional statistics, they suggest that cell division does not play a role in the presence of oscillations. This conclusion agrees with what is reported in literature, indicating that collective cell motility in general is unperturbed by inhibition of proliferation [128, 189, 197]. More specifically, wave-like phenomena have also been studied in the absence of cell division [128, 195, 259], condition that does not affect the presence of oscillations. In these papers, proliferation is regarded as a source of noise, whose removal helps making cell motion clearer. In the present case, even though oscillations were unaffected by the absence of cell division, we do not notice an improvement in the quality of the kymographs. This might due to the toxicity of Mitomycin C. After $\sim$ 15 hours of treatment cell death was widespread, even though cell division was not completely inhibited. Future experiments could be carried out using different compounds, e.g. Thymidine [302], to avoid the possible negative effects such toxicity might have on cell motion.

### 4.1.2 The role surface adhesion

Most model implementations, including our own, incorporate a term for the friction with the substrate or, almost equivalently, for surface adhesion. This made us wonder whether we could change the characteristics of our oscillations by modifying cell-substrate adhesion.

To this end, we fabricated patterned PAA gels (rigidity = 40 kPa) with different concentrations of fibronectin. Since we could not directly control the amount of protein deposited on the surface, we decided to act on the concentration of the protein solution we utilized during the patterning procedure (see subsection 2.2.1). The default concentration is 20 $\mu$g/mL, and we produced gels with 2 $\mu$g/mL and 100 $\mu$g/mL. This solution is first in contact with a coverslip, on which fibronectin adsorbs, to be later transferred onto the gel during the successive polymerization. The high number of steps makes for a procedure which cannot be accurately controlled. To verify whether a different concentration of fibronectin in solution would effectively change the final amount of protein present on the surface of the gel, we prepared 2 samples for each concentration

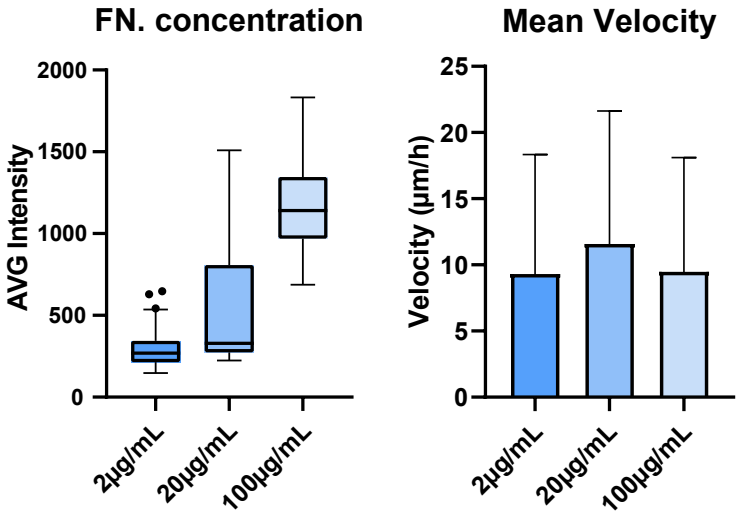


| | Space (µm) | SDT | SEM |
|---|---|---|---|
| 2µm/mL | 510 | 112 | 40 |
| 20µm/mL | 383 | 34 | 7 |
| 100µm/mL | 386 | 75 | 24 |

| | Time (hours) | STD | SEM |
|---|---|---|---|
| 2µm/mL | 4.5 | 0.2 | 0.1 |
| 20µm/mL | 4.7 | 0.7 | 0.1 |
| 100µm/mL | 4.7 | 0.5 | 0.1 |

Figure 4.1: Study of the response of velocity oscillations to changes in surface adhesions. **Left**: To quantify the average amount of fibronectin (FN) deposited on the surface of 40 kPa PAA gels, we measure the average FN-staining intensity for different concentrations (2, 10 and 20 $\mu$g/mL) during the patterning procedure. Whiskers and outliers are calculated according to the Tukey method. The difference between distributions is significant (**** - unpaired t-test). **Center**: The difference in surface protein concentration corresponds to a slight change in the velocity distributions. The height of the column represents the mean velocity, the bars the standard deviation. Even though the distributions are highly overlapping, the difference between them is significant (**** - unpaired t-test). **Right**: The difference in surface protein affects the periodicity of oscillations, reported here with the standard deviation (*STD*) and the standard error of the mean (*SEM*) for n=10 tissues. The difference is not significant (unpaired t-test).

amount, which we stained for fibronectin. We then gathered $\sim$ 10 images of each gel with an optical microscope. We chose the parameters so that no saturation would occur even on the brightest samples, and kept all imaging parameters unaltered throughout the procedure. For each image, we measured the average intensity in a ROI selecting only the area associated with adhesive surface. The results (see Figure 4.1) demonstrate that the gels thus created have a different protein amount on the surface, even though the distribution of intensity are extremely broad and overlapping.

We then fabricated new gels, seeded MDCK cells onto them and imaged them for multiple days. In keeping with published literature [303], we measured the average cell velocity to verify whether surface protein concentration could affect the migratory properties of our tissues. For each sample, we measure local velocity with PIV within the time windows mentioned earlier (see subsection 3.2.3). We then averaged the values obtained from each sub-window to calculate the mean velocity in Figure 4.1. The overall distribution of velocity for 20 $\mu$g/mL is shifted towards higher values, which amount to a more elevated average velocity. Even though the distributions overlap, the difference is statistically significant.

To verify if such a change in motile behavior would affect the characteristics of the oscillations, we measured the periodicity of 10 tissues grown on substrates with different protein content. The values obtained, reported in Figure 4.1, do not differ significantly.

If, on the one hand, these preliminary results prove that we can control the surface-fibronecting content, and that this effectively changes the average migration velocity, on the other, the distribution of both quantities (fibronectin concentration and cell velocity) is extremely broad and overlapping. This fact evidences the poor control and high level of noise in the system. For this reasons, in order to obtain a statistical difference in the periodicity of the oscillations, a large number of experiments is necessary. With the small pool of data we gathered, we can only conclude that the velocity is indeed affected, but more definitive interpretations are hard to draw. If there is a small difference between samples due to surface adhesiveness, it is buried within the experimental noise. Interestingly, there seems to be an optimal fibronectin concentration ($\sim$ 20 $\mu$g/mL) when it comes to maximizing cell velocity, a value which corresponds to what had been previously reported [303].

In the future, if a more thorough characterization of this aspect of the waves will be necessary, more statistics should be acquired. Moreover, a better control of the protein deposition on the surface can be achieved using the PRIMO technology (AlveoleLab), which is now present in our lab.

This work has been carried out in collaboration with Monika Tadrous, a visiting student from CSU (California State University Fullerton).

### 4.1.3 The role of gel rigidity

Just like surface friction, the rigidity of the substrate can potentially play an important role in determining the characteristic of migratory behavior, at both the single cell and the tissue level. Accordingly, we wondered what effect a change in gel rigidity would have on oscillatory motion.

To answer this question, we fabricated patterned glass substrates, whose rigidity is seemingly infinite, and polyacrylamide gels with elastic modulus equal to 5 kPa. We then repeated our experiments, concentrating on lines for which $L_X \geq 500$ $\mu$m. Since oscillations in cell velocity were clearly observable, we measured the typical periodicity for $\sim$ 10 tissues for each rigidity value (see Figure 4.2). For what concerns $\lambda$, the trends are extremely similar, the plots overlap and are well within each others uncertainty. For the time period, on the other hand, the values are further apart and the difference is, in some cases, statistically significant, although no clear trend can be recognized.

| | Time period (hours) | | | | | | | | | | | | Space period (hours) | | | | | | | | | | | |
|---|---|---|---|---|---|---|---|---|---|---|---|---|---|---|---|---|---|---|---|---|---|---|---|---|
| | $L_X$ = 500µm | | | $L_X$ = 1000µm | | | $L_X$ = 1500µm | | | $L_X$ = 2000µm | | | $L_X$ = 500µm | | | $L_X$ = 1000µm | | | $L_X$ = 1500µm | | | $L_X$ = 2000µm | | |
| | T | STD | SEM | T | STD | SEM | T | STD | SEM | T | STD | SEM | λ | STD | SEM | λ | STD | SEM | λ | STD | SEM | λ | STD | SEM |
| 5 kPa | 5.1 | 1.1 | 0.4 | 4.8 | 0.8 | 0.2 | 5.0 | 0.5 | 0.2 | / | / | / | 348 | 30 | 10 | 372 | 30 | 8 | 383 | 49 | 15 | / | / | / |
| 40 kPa | 4.6 | 1.0 | 0.1 | 4.5 | 0.9 | 0.1 | 4.7 | 0.7 | 0.1 | 4.6 | 0.7 | 0.1 | 353 | 25 | 3 | 385 | 47 | 7 | 373 | 34 | 4 | 382 | 35 | 6 |
| Glass | 4.5 | 0.5 | 0.2 | 4.8 | 0.9 | 0.3 | 4.2 | 0.8 | 0.2 | 4.1 | 0.6 | 0.2 | 369 | 37 | 15 | 380 | 54 | 19 | 382 | 27 | 8 | 377 | 41 | 15 |

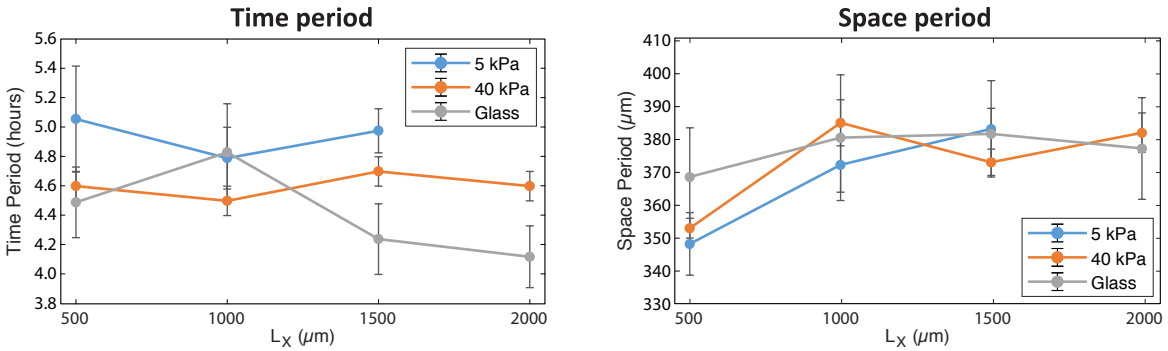


Figure 4.2: Preliminary studies of velocity oscillations and substrate rigidity. The typical periodicity of the oscillations for MDCKs seeded on substrates of different rigidity is measured (*top*), and is reported together with the standard deviations (*STD*) and the standard error on the mean (*SEM*). The trends are also displayed as plots, where the errorbars correspond to the SEM (*bottom*).

The intrinsic variability and noise in our measurements dominates over the (possible) difference induced by the substrate rigidity. To overcome this issue, more data should be acquired in the future, although the effect of rigidity does not appear to be substantial.

### 4.1.4 Contractility inhibition with Blebbistatin

Another fundamental component of all models is cell contractility, which is directly responsible for migration and the reaction to mechanical inputs in general. Contractility has also been identified as a key ingredient for the propagation of mechanical waves [174, 194], the existence of breathing oscillations [128, 172] and, more generally, the presence of swirls and different migration modes in tissues [257].

Therefore, we set out to verify whether cell contractility was also important for the oscillations present in our system. To that end, we seeded cells on 40 kPa PAA gels and, once the tissues reached a density previously associated with the presence of velocity oscillations ($\sim 5 \times 10^5$ cells/$cm^2$), we treated the samples with blebbistatin (20 $\mu$M), an inhibitor of myosin II-mediated contractility, and then imaged over time.

Surprisingly, immediately after the exposure to blebbistatin, cell motion abruptly slowed down, stopped being confined along the $x$ direction, and cells left the adhesive island to invade the cell repellent space between patterns (see Figure 4.3). Interestingly, it seems that the locations where cells leave the strips sooner correspond to those

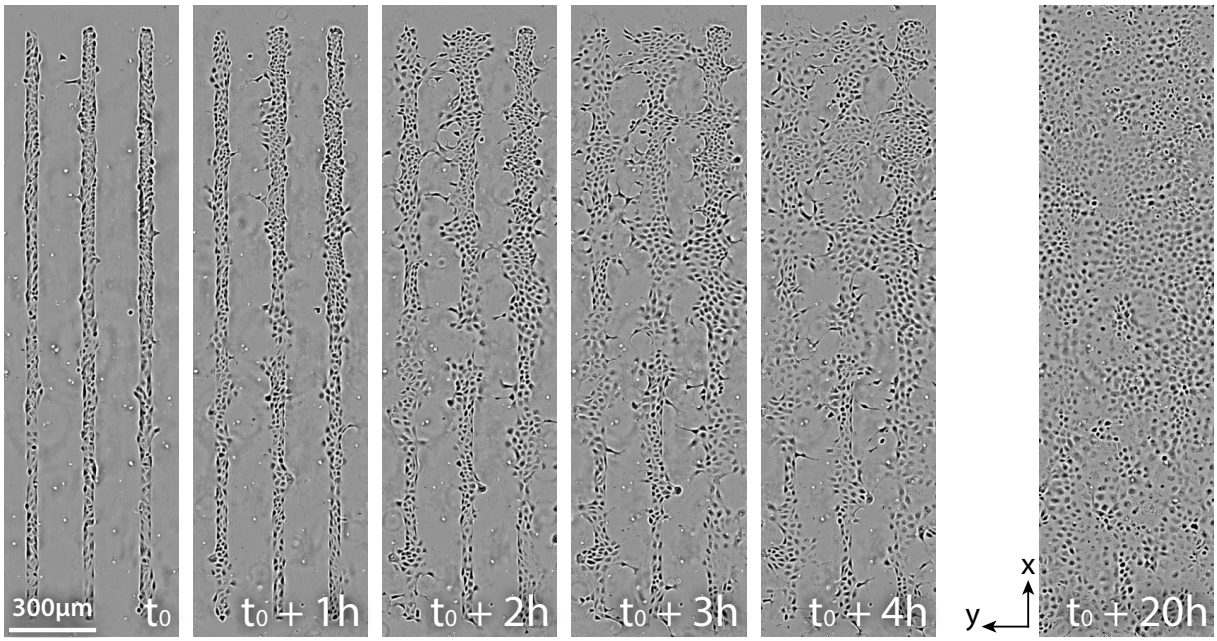


Figure 4.3: Results of the inhibition of contractility during oscillatory motion. Phase contrast images of MDCK cells on thin strips ($L_X$ = 2000 $\mu$m) before treatment with 20 $\mu$M blebbistatin ($t_0$), after 1 ($t_0$+1), 2 ($t_0$+2), 3 ($t_0$+3), 4 ($t_0$+4) and 20 ($t_0$+20) hours.

positions where cells were accumulating (i.e. approximately one anti-node every two) prior to the exposure to blebbistatin. This phenomenon, which, to our knowledge, has never been reported before, made the observation of oscillations impossible.

One explanation for this effect is the low quality of the confinement imposed by gels. To rule this out, we repeated the experiment on glass substrates patterned with PNIPAM polymer, which is known to have better cell-repellent properties and impose a stronger confinement. On this new substrate, we observe the same behavior, with cells leaving the micro-patterned area within $\sim$ 5 hours of treatment.

To try to decrease the level of cell contractility without losing tissue integrity, we decreased the concentration of blebbistatin to 3 $\mu$M. It is reasonable to assume that, for concentration of 20 $\mu$m, blebbistatin has already reached almost 100% of its ability to inhibit myosin ATPase activity, whereas 3 $\mu$M should decrease such activity to approximately half its original value [304]. We repeated the experiments on both PAA gels and glass. Interestingly, even at lower concentrations, cells seeded on gels leave the adhesive strips, while tissues on glass remained intact, cell motion continued and velocity oscillations were visible for $\sim$ 24 hours after blebbistatin treatment. Whether this difference is related to the rigidity or the confinement quality is not clear. We then measured the typical periodicity in these conditions (glass substrate, $L_X$=2000 $\mu$m, 3 $\mu$M blebbistatin) to obtain the data reported in Table 4.1. When compared to the values relative to the absence of blebbistatin, we notice that, whereas the space period is unaffected, the time period is strongly increased. This is also accompanied by a reduc-

| | $\langle\|v\|\rangle$ (μm/h) | STD | SEM | $T$ (hours) | STD | SEM | λ (μm) | STD | SEM |
|---|---|---|---|---|---|---|---|---|---|
| **40kPa** | 10.80 | 9.69 | 0.01 | 4.7 | 0.7 | 0.1 | 382 | 35 | 6 |
| **Glass** | 10.49 | 9.21 | 0.02 | 4.1 | 0.6 | 0.2 | 377 | 41 | 15 |
| **Glass + 3$\mu$M Blebb** | 9.40 | 8.19 | 0.02 | 6.0 | 0.7 | 0.3 | 384 | 64 | 22 |

Table 4.1: The average velocity ($\langle|v|\rangle$), time ($T$) and space ($\lambda$) periods are reported for cells on glass patterns with and without 3 $\mu$M blebbistatin treatment, and on 40 kPa PAA gels for comparison.

tion of the average velocity from 10.5 $\mu$m/h to 9.4 $\mu$m/h. This drop in cell motion is unsurprising, cell migration is unequivocally dependent on contractility, and might be the cause of the increase time period.

The peculiar behavior of cells observed upon treatment with high doses of blebbistatin is, to our knowledge, a novelty. On similar conditions, previous studies report a general loss of all characteristics of collective migration: swirling and contraction-relaxation motion disappear [257] and wave-like phenomena are lost [128, 172, 174, 194]. Conversely, in our case, when contractility is inhibited, cells abandon the confinement. Interestingly, cells leave the patterns sooner in areas where the density is higher, which in turn seem to correspond to locations where the velocity field was converging (i.e. approximately the anti-nodes). If, on the one hand, this observation seems to suggest the presence of a "pre-existing stress", on the other, the outward migration appears to have an active component: cells increase their size massively and cover distances larger than 100 $\mu$m. This phenomenon could be caused by protrusive actin-polymerization, a process that does not require myosin II activity. We can also conclude that contractility (i.e. tension) is fundamental for cells to remain on the patter.

To gather meaningful data, associated with tissues that respect the confinement, we decreased the dosage of blebbistatin. This strategy is only successful on glass substrates and yields an increase in the time period and a decrease in the average cell velocity. Interestingly, only one work, published extremely recently, reports a behavior which corroborates our results [266]. Peyret and colleagues describe a strong decrease in cell velocity and wavelength coupled with a delayed periodicity upon addition of 50 $\mu$M blebbistatin. Even though there are strong experimental differences (drug dosage, PDMS substrates, different cell type), the general trends are comparable.

Even though the data points, in terms of blebbistatin concentrations and tissues observed, are not sufficient for a complete statistical analysis, these results seem to confirm the importance of contractility for mechanical waves.

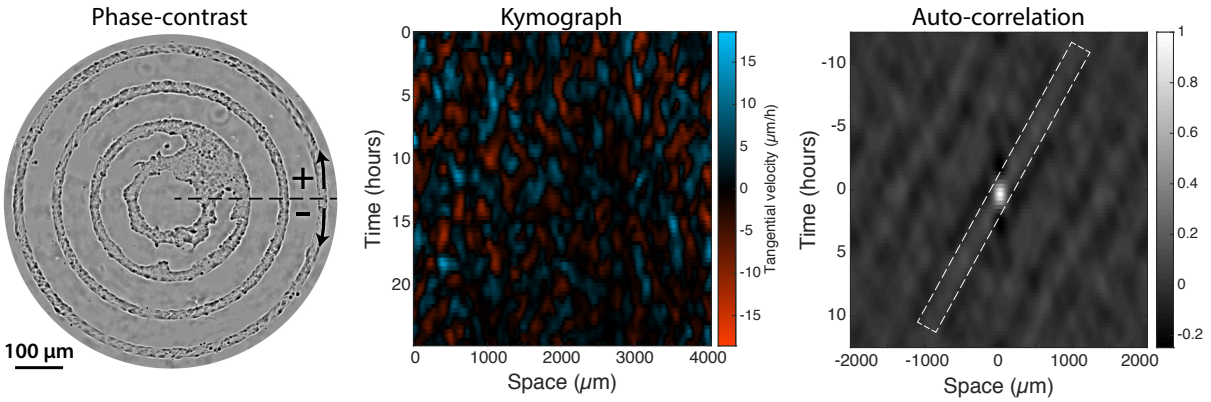


Figure 4.4: Results obtained with periodic boundary conditions. Cells are seeded onto ring-like tissues (*left*) of length 1000, 2000, 3000 and 4000 $\mu$m, to simulate periodic boundary conditions. The presence of velocity oscillations is studied by plotting the average tangential velocity over time (*center*) and by calculating its auto-correlation (*right*), which displays diagonal bands (*white-dashed rectangle*). The space is measured according to the convention reported on the left, where the black line represents $x$=0. The examples reported are relative to a ring of radius = 4000 $\mu$m.

### 4.1.5 Oscillations with periodic boundary conditions: ring-like tissues

Another relevant question is whether epithelial waves are propagative (i.e. traveling waves) or stationary. Experiments on confined tissues prove their existence, but the presence of boundaries at both ends does not allow us to distinguish the two scenarios, a result that could be achieved by making our strips indefinitely long. This is impossible due to limitations of the imaging system we utilized. To overcome such issue, we designed circular tissues, or rings, whose width was equal to 40 $\mu$m, and length varied between 1000 and 4000 $\mu$m. Ignoring the effect of curvature, which is considerably smaller than in cases where collective migration responds to its presence (see subsection 1.7.1), this geometry simulates the effect of periodic boundary conditions: there is no break in the tissue along the tangential direction.

An example of such tissues, seeded on 40 kPA PAA gels, is reported in Figure 4.4. In this specific case, the quality of the confinement was not perfect, but the outer rings are not affected by this issue. The presence of oscillatory motion is evident upon a first visual inspection. To better visualize this phenomenon, we average the tangential component of the speed along the radial direction $v_{\parallel}(x;t) = \langle v_{\parallel}(x,r;t)\rangle_r$, where $x$ is the position along the ring measured according to the convention reported in Figure 4.4. A kymograph of $v_{\parallel}(x;t)$ over time, filtered according to the protocol in subsubsection 3.2.5.2, shows the presence of red and blue spots, a proof that the ring shape can reproduce similar oscillations to those measured for long strip. The auto-correlation

(Figure 4.4 right) also shows the presence of periodicity, although superimposed to long diagonal bars (*white-dashed rectangle*). These represent the propagation of traveling velocity waves, similar to those our SPV model predicted, moving with a velocity of $\sim 100$ $\mu$m/h. Since this number is in the range of the effective velocity measured for tissue on closed lines, we can speculate that the absence of boundary conditions generates traveling waves, which, in a ring-like structure, rotate at a specific speed. Interestingly, the presence of multiple bars suggests that this rotation happens at a global scale, which requires the coordination of cell motion over large distances ($\sim 4\ m$m). These preliminary result seem to suggest that periodic oscillations are indeed propagative.

These conclusions arise from one single experiment. Even though they are, in our opinion, extremely interesting, they are preliminary and have to be considered as such.

### 4.1.6 Cells as single oscillators

In literature, the presence of mechanical waves has generally been modeled in one of two ways. The first is continuum models, where a tissue is described at a coarse-grained level. The physical variables describing cell behavior are necessarily averaged over volume elements encompassing multiple cells, and this makes it extremely difficult to link single cell properties, those we can alter pharmacologically, to parameters in the model. The second option are vertex or particle models, which consider cells as single entities, but the large number of constitutive (unknown) variables tends to hinder a qualitative link to the real system.

To somehow bridge these two domains, our collaborator Pierre Recho[1] proposed the development of a simple continuum model. Each cell is described as an active gel, and multiple cells are then linked by visco-elastic springs into long chains, which reproduce a simplified quasi one-dimensional geometry [305, 306]. Moreover, since the polarity of a single cell in the tissue is controlled by the balance between its molecular motor self-organization and external forces applied by its neighbors, the presence of oscillations does not require any additional component to introduce an artificial relaxation time. This would allow the activity of each cell to have a direct counterpart in the mathematical description, and the parameters could be derived experimentally.

In this context, a characterization of the behavior of single cells becomes a necessary basis to build upon. We therefore wondered how single MDCK cells would behave when confined on lines, and whether they would display periodic motion. This could support a mathematical description of mechanical waves as single oscillators connected

[1]Pierre Recho, Université Grenoble Alpes, Laboratoire Interdisciplinaire de Physique, CNRS, F-38000 Grenoble, France

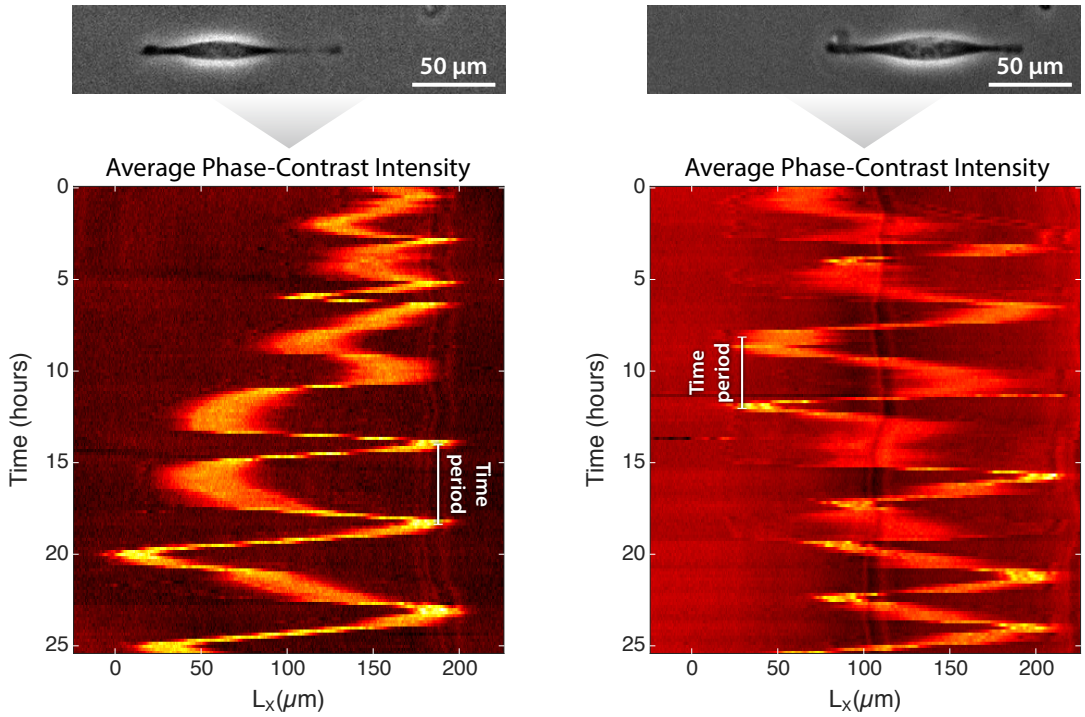


Figure 4.5: Single MDCK cells seeded on PAA gels (rigidity = 40 kPa) display oscillatory behavior in roughly 50% of the cases. The phase contrast images of two examples (*top*) illustrate the elongated phenotype, while the dynamics of the movement can be visualized by plotting the average phase-contrast intensity over time (*bottom*). In these kymographs, we can clearly appreciate the presence of periodic oscillations of right and leftward motion.

by springs, and prove the efficacy of our method to provide the initial characterization needed to develop a model.

To this end, we fabricated 40 kPa polyacrylamide gels patterned with thin lines (5×200 $\mu$m), on which we seeded MDCK cells at low density ($\sim$ 0.2 $\times 10^4$ cells/cm$^2$). We washed $\sim$ 2 hours after seeding in order to remove all non-spread cells, and then imaged until all line-patterns were populated by at least 2 cells, a condition we were not interested in. The experiment was repeated twice.

Cells moving in a back and forth oscillatory manner are visible in $\sim$ 50% of the cases. Two examples, where such oscillations are roughly periodic, are reported in Figure 4.5. A quick quantification, based on a visual inspection of the kymographs and a peak-to-peak distance measurement (see white bars in Figure 4.5), yield a value for the time period of $T = 3.9 \pm 0.9$ hours (n=10, the error represents the standard deviation).

Interestingly, this value is comparable with what obtained for our tissues on strips, which seems to corroborate the idea of a mechanical wave as synchronization of single oscillators. Moreover, this preliminary conclusion is in agreement the results obtained on micropatterns constituting two squares separated by a thin adhesive bridge, albeit on a widely different cancerous cell type [307]. In those conditions, Bruckner and colleagues measured stochastic movement of cells between the two squares with a peri-

odicity of $\sim$ 4 hours. Oscillations seem to be also present on lines with 2 cells, although they assume a more erratic behavior.

These interesting conclusions are extremely promising for the development of the hybrid model, but they suffer from a general lack of statistics. In the future, if deemed necessary, experiments should also be carried out on longer lines. The time period measured might, in fact, be a consequence of the particular confinement imposed. If we assume that cells "bounce" every time they meet a boundary (i.e. the end of the line), and that the nucleus is $\sim$ 30 $\mu$m wide, then an oscillation in the order of 4 hours could be caused by cell moving at a speed of $\frac{(200-30)\mu m}{4h} \simeq 40\mu$m/hour. This speed is more elevated that that typical of MDCKs, but not far enough to completely disregard this possibility.

## 4.2 The biological counterpart

This second part of the chapter gathers all the work we carried out while looking for a biological counterpart. This concept represents a specific biological function that is selectively activated (or inhibited) by the waves. If found, this could ultimately distinguish velocity oscillations from mere observations, and demonstrate their active role in morphogenesis, intended here in its broadest of meanings. This idea stems from two basic considerations: (i) an intrinsic quantity ($\lambda \simeq 400$) seems to control both the spacing between nodes and their presence altogether (no nodes are present in a regime of global oscillations); (ii) cells located at the anti-nodes appear to be alternatively stretched and compressed. This selective mechanical stimulus could somehow distinguish those cells, cause them to undergo a different fate and ultimately lead to phenotypic patterning and supra-cellular organization. Moreover, such stimulus only happens above a certain size, and its localization appears to be spatially controlled. In our opinion, all these factors point towards the role of oscillations as regulators in morphogenesis. At this stage, this is nothing more than a, possibly far-fetched, hypothesis, but one we deemed worth investigating.

Velocity oscillations can affect cell behavior over a wide range of timescales: cellular organization in the order of hours and genomic effects on longer time scales. For this reason, we employed different combinations of imaging techniques and fluorescent probes, which I will describe throughout the chapter.

### 4.2.1 Velocity oscillations correlate with local monolayer thickness

Our previous observations suggest that where the velocity field converges, the tissue is more crowded, cells are more compressed and under tension (see subsection 4.1.4). For this reason, we wondered whether such positions would also be associated with a thicker cell sheet, which would develop further in the $z$ direction (see Figure 4.6). Moreover, fluctuations in cell volume within a tissue have already been observed, and their periodicity measured as 4 hours, a value that rises to 6 hours when exposed to blebbistatin [308]. The striking resemblance between these values and the period we measured further supported the idea that velocity oscillations might modulate the height of the tissue.

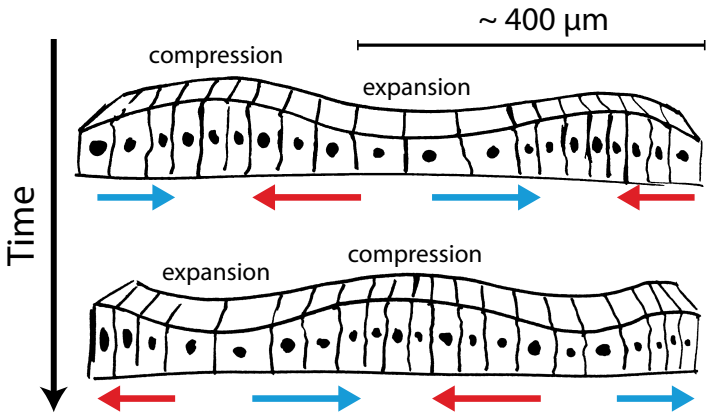


Figure 4.6: Schematic representation of the hypothesis behind the investigations of cells height: where cells converge, the tissue is more crowded and extended in the vertical direction.

#### 4.2.1.1 Results obtained on fixed samples are not conclusive

We therefore set out to measure the local thickness of the cell layer. Initially, we combined confocal imaging with three fluorescent stainings: CellTracker, DiI and the GFP-cadherin system already present in the MDCK cells utilized. We seeded cells on 40 kPa PAA gels patterned with 1500 $\mu$m long lines, and, at the appropriate density, fixed, stained and imaged the samples. From the stack of images, a mono-dimensional profile of the local cell height was obtained by dividing the tissue into smaller 10 $\mu$m wide sections along the $x$ direction (see Figure 4.7). For each section, a profile of the signal intensity over $z$ was obtained by averaging the intensity for each slice. We then set an arbitrary threshold and calculated the local thickness as the distance (in $z$) between the intercepts. Since this quantification method is somewhat crude, the quality of each profile measured was verified by visual inspection against the original images.

An example of the height profile, together with a schematic representation of the data analysis, is reported in Figure 4.7. The data obtained from the three different fluorescent molecules did not differ significantly, so we averaged the three curves. Upon a first visual inspection, the presence of periodicity is only evident in $\sim$ 50% of the cases. To quantify the typical space period, we calculated the auto-correlation function, and manually identified the peaks. The average periodicity is $\lambda = 201 \pm 70$ $\mu$m (the error represents the standard deviation). This value is extremely far from the periodicity typical of the velocity oscillations ($\sim$370 $\mu$m), and might represent something completely different. Figure 4.7 reports the full distribution of values measured, which is wide and does not show a clear focus around the average value.

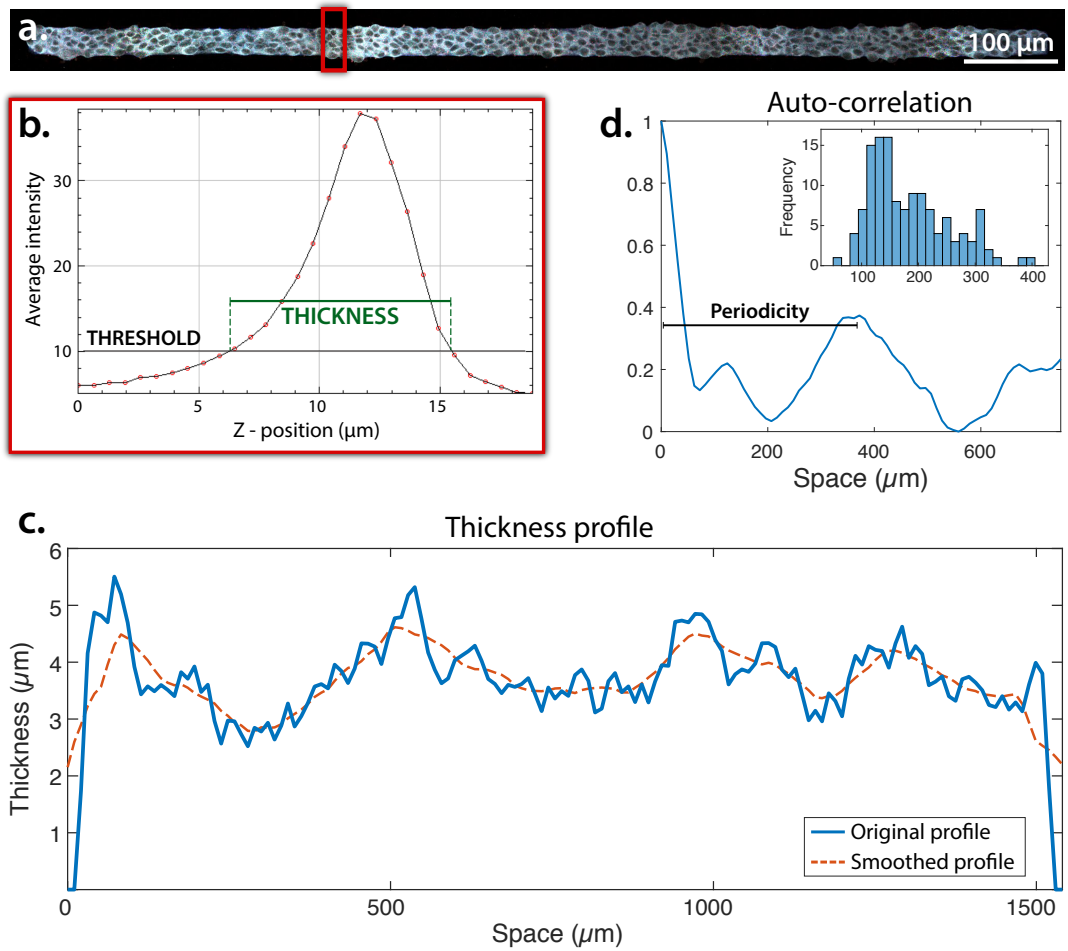


Figure 4.7: Quantification of the height of fixed tissues. **a.**) To quantify the height of cells, tissues were stained with CellTracker (*blue*), DiI (*red*) and the GFP-cadherin (*green*), and then imaged with a confocal microscope. **b.**) The sample is divided into 10 $\mu$m wide segments (*red-square*), and the local height is measured by plotting the average intensity for each slice and setting a threshold. **c.**) This is repeated for each segment, to yield the a full profile. **d.**) The periodicity is then calculated by plotting the auto-correlation function and manually identifying the peaks. The distribution of values is reported in the inset (n=64).

#### 4.2.1.2 Live imaging confirms the presence of shorter periodicity.

One of the suspicions we had about working with blocked samples was whether the fixing process could affect the 3-dimensional conformation of cells. To avoid such issue, we repeated the experiments in live conditions. Rather than working with possibly harmful molecules, we decided to mimic a fluorescence-exclusion cell-volume measurement [309], without a microfluidic chamber. When cells seeded on gels (40 kPa) reached a density usually associated with velocity oscillations, we added sulforhodamine in solution (1:500). This fluorescent molecule cannot enter the cell, so 3-dimensional imaging with a confocal microscope yields what effectively is a negative of the cell body. We then proceeded with the measurements of the height profile.

The analysis procedure, reported in Figure 4.8, is similar to that presented above,

with the addition of a background removal steps. Briefly, tissues are binned into thin 10 $\mu$m wide strips. An example of the average intensity profile over $z$ is reported in blue in Figure 4.8b. As we can see, the somewhat Gaussian profile we are interested in superimposed to a monotonic intensity decrease in fluorescence, attributed to the fact that we are imaging further within the sample. To compensate for this fact, we sub-divide each thin strip into two areas, a central one relative to the tissue, and two lateral ones only containing culture medium (see the orthogonal view in Figure 4.8). We then use the lateral ones to estimate the background (red line), which is subtracted from the original to obtain the profile reported in yellow. A steady decrease of intensity over $z$ remains, which is also visualized as the "shadow cone" on the right of the dark area in the orthogonal view. To compensate, we subtract a linear profile (black-dashed line), and we finally obtain the corrected intensity profile in $z$ (green). We then impose and arbitrary threshold and define, like above, local thickness as the distance (in $z$) between the intercepts. Once more, the quality of the profiles calculated is checked by visual inspection, and by comparing the results with those obtained from the analysis of the GFP-cadherin live imaging.

An example of a line profile is reported in Figure 4.8. In the majority of cases, the height of live tissues estimated is considerably larger than that of fixed samples, and fluctuations appear to be more pronounced. The presence of periodicity is confirmed by plotting the 3-dimensional auto-correlation, which considers all tissues (n=32) in one calculation. The plot in Figure 4.8d suggests the presence of periodicity at $\sim$ 200 $\mu$m. A more thorough analysis, by manual detection of the peaks in AC of single tissue, confirms this observation. The distribution of peaks, reported in the inset in Figure 4.8d, is centered around 200 $\mu$m as well. The average value, calculated by excluding all peaks $>$ 300 $\mu$m as outliers, is $\lambda = 190 \pm 40$ $\mu$m (the error represents the standard deviation).

From these preliminary experiments, it appears the tissue height has a periodicity of $\sim$ 200 $\mu$m. This value is not correlated with any phenomena we have observed nor data are aware of. It is possible that such periodicity is an artifact due to the lack of refinement of the techniques used. On the other hand, the average height measured corresponds to those reported in literature [266, 308], and a visual inspection confirms the general trends measured. One discrepancy with the work of Zehnder and colleagues [308] lies in the magnitude of the height variations. They attribute strong fluctuations in volume predominately to cell area, with height changes in the order of $\sim$ 300 $n$m. This means that the periodicity we measure might represent something completely different, and that, if velocity oscillations do have an effect on cell height, it has to be investigated with a much more sensitive and sophisticated protocol.

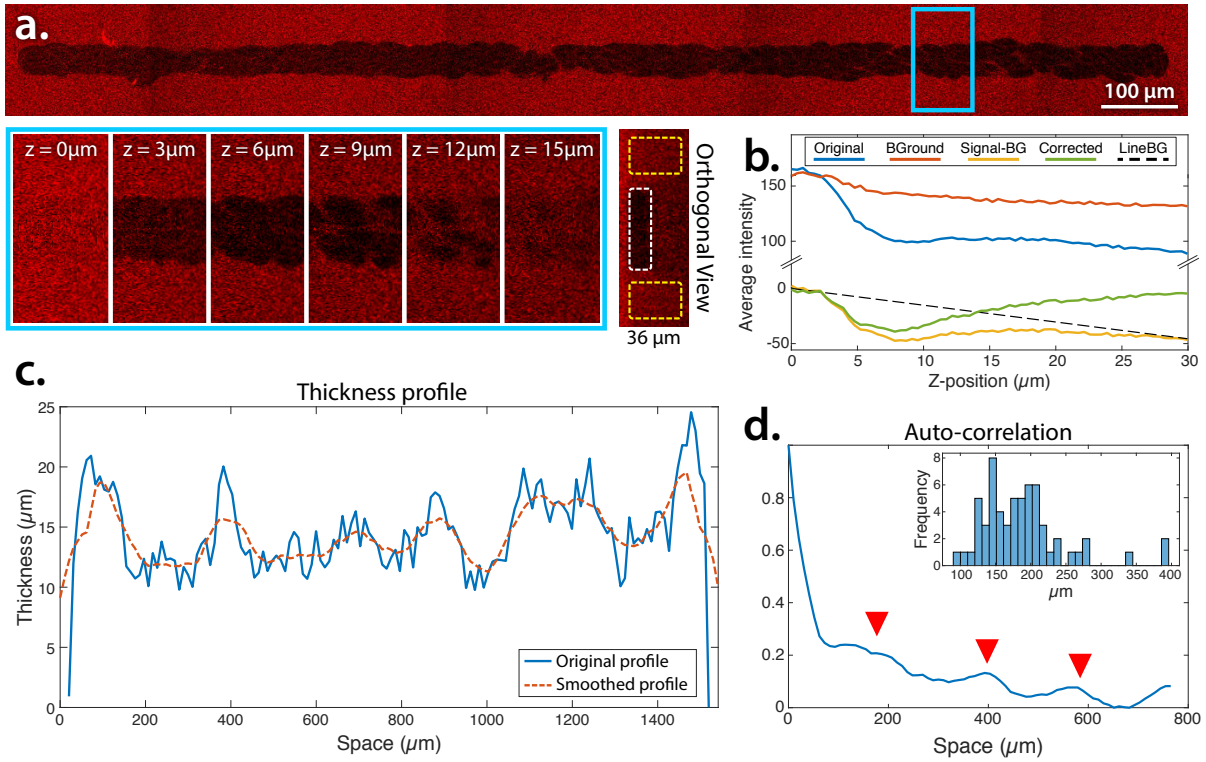


Figure 4.8: Quantification of the height of live tissues. **a.**) Sulforodhamine cannot enter cells, so when images are gathered with a confocal microscope, dark areas correspond to the tissue, bright areas to the outside medium. Images of the fluorescence at different $z$ positions are reported together with a orthogonal view of the tissue (cells are highlighted with a *white dotted line*). **b.**) In order to measure the thickness, we divide the tissue into small 10 $\mu$m wide segments, and treat them independently. For each one we remove the background (*BGground*) caused by the fact that images are taken further within the sample. We then subtract a second, linear background (*LineBG*), and finally impose an arbitrary threshold (like in Figure 4.7) to the corrected line (*green*). The final profile is plotted in (**c.**). **d.**) The periodicity is calculated thanks to the auto-correlation. What is reported here is the 3 dimensional auto-correlation, which takes all samples (n=32) into consideration, and it shows a clear periodicity at $\sim$ 200 $\mu$m (*red arrowheads*). A more accurate quantification is done considering single tissues and calculating the periodicity for each one (*inset*).

Interestingly, the periodicity in tissue height measures approximately half of that of the velocity oscillations. Whether there is a causal link between the two phenomena, and if they are correlated at all is not clear yet, and it could be a matter of future investigations.

### 4.2.2 Local cell density measurements

According to our hypothesis (see Figure 4.6), the anti-nodes should be characterized by an increase in cell density. Specifically, in keeping with a standing-wave analogy, the negative peaks of the periodic cell-velocity curve would be associated with a diverging field, meaning that local density is minimal. On the contrary, positive peaks relate to

converging velocity and local density increase. So at every point in time, we might expect cells accumulation in correspondence of those positive anti-nodes, i.e. one anti-node every two, at a spacing of $\sim 400$ $\mu$m. Moreover, the volume fluctuations, occurring with the same periodicity of our velocity oscillations, are often attributed to projected area changes [308], which should manifest themselves as density changes. To measure local density, we stained tissues (40 kPa PAA gel, $L_X = 1500$ $\mu$m) with Hoechst in order to visualize all nuclei.

As a first attempt, we identified all nuclei, divided the tissue in sub-sections and counted the number of nuclei for each bin. Unfortunately, the accuracy of this strategy decreases with the size of the bin: in order to detect a possible periodicity we need small sections, while to have accurate measurements we need large ones. For these reasons such direct approach was abandoned.

To detect a periodicity in nuclear distribution without measuring an actual cell density we changed strategy. We thresholded the nuclear images to remove the effect of stitching and fluctuations in Hoechst staining, and then applied a spatial Gaussian filter equivalent to those introduced in subsubsection 3.2.5.2 ($\sigma_{small} = 30$ $\mu$m). To extract a periodicity, we calculated the auto-correlation of the images and manually detected the peaks which, once more, shows a somewhat bi-modal distribution. For this reason, we identified all peaks whose adjusted positions (already divided by the number identifying their order) was higher than 350 $\mu$m, and divided them by a factor of 2. We then proceeded as explained earlier (see subsubsection 3.2.5.3) to calculate the average period as $\lambda = 230 \pm 45$ $\mu$m (n=64, the error represents the standard deviation).

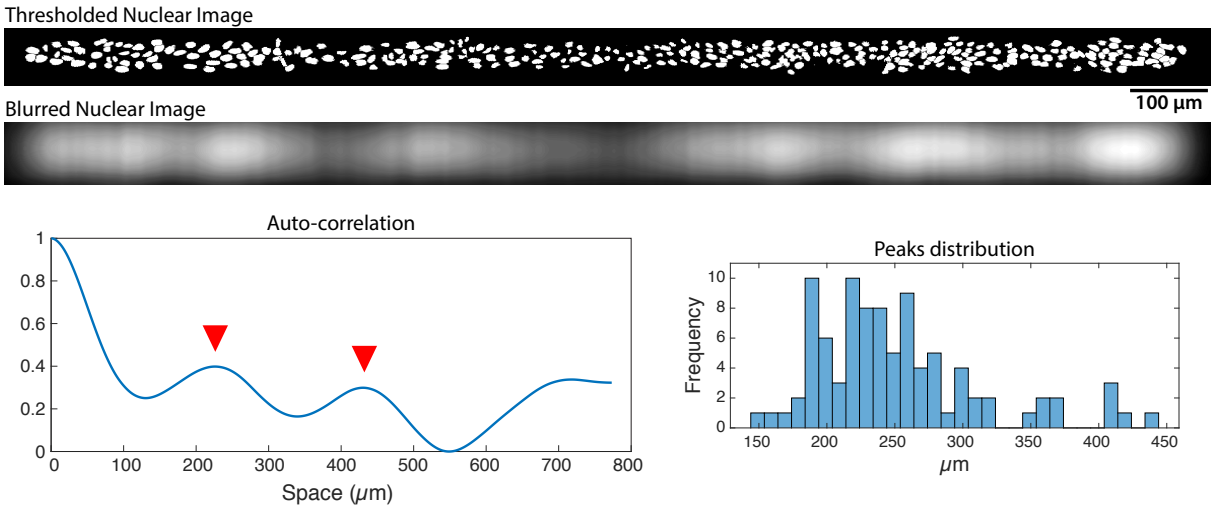


Figure 4.9: Results of the study of periodicity in nuclear density. An image of Hoechst stained tissues is first thresholded (*top*), and then blurred with a Gaussian filter (*middle*). The periodicity (*red arrowheads)* is calculated from the peaks in the auto-correlation of each image (*bottom-left*). The distribution of peaks is also reported (*bottom-right*) for n=64 tissues.

The data analysis and quantification performed are extremely "rough", a fact that, together with the high noise present in the data, undermines the quality of the conclusions we can draw from these experiments. Nonetheless, these results seem to corroborate the presence of a periodicity around $\sim 200$ $\mu$m.

### 4.2.3 YAP translocates to the nucleus in areas of low cell density

In our research of a biological counterpart for mechanical oscillations, the obvious "culprit" are all proteins responsible for mechanotransductive pathways (see subsection 1.3.3 and subsection 1.4.2). We decided to target Yes-associated protein (YAP), a molecule known to shuttle to the nucleus in response to mechanical inputs, where it interacts with transcription factors to control many cellular functions [62, 70]. Specifically, YAP accumulates within the nucleus when cells are stretched or increase their volume [310], an event we often observe during the experiments.

To verify whether we could measure a distribution of YAP activity correlated to the presence of waves, we seeded cells on new samples (40 kPa PAA gel, $L_X = 2000$ $\mu$m), waited until oscillations were visible, and then fixed and stained specifically for YAP. All experiments were carried out in collaboration with Christophe Guilluy[2] and Valentin Buffière-Ribot[2].

A first observation of the images reveals a general trend: YAP accumulates in the cytoplasm of crowded cells, whereas it appears to translocate to the nucleus in areas of low density (see Figure 4.10a). To quantify such trend, we developed the analysis protocol reported in Figure 4.10. A nuclear mask, representing all nuclei in white, is generated from the image of Hoechst. We use this mask as a reference in order to extract the data relative to the number of nuclei, their position, and the intensity in all channels. Moreover, we combine the nuclear mask and the image of YAP to generate two sub-images: one only reporting nuclear YAP and one with the cytoplasmic counterpart. The activity of YAP is generally quantified with the ratio of nuclear to cytoplasmic fluorescence ($N/C$) of the single cell, a high ratio representing elevated activity. We could not segment cells borders, so rather than calculating the ratio on the single cell body, we divide the tissue in 70 $\mu$m wide vertical strips, and perform the analysis on each of these bins. For each one, we calculate the average nuclear and cytoplasmic fluorescence with the images previously generated, and their ratio. We also measure the average nuclear area and the number of cells (based on their centroids), which allows us to calculate the average cell area as $A_{mean} = \frac{A_{bin}}{N_{cell}}$. The data relative to

[2]Team Guilluy, Institute for Advanced Biosciences, Centre de recherche UGA - INSERM U1209 - CNRS UMR 5309, Grenoble, France.

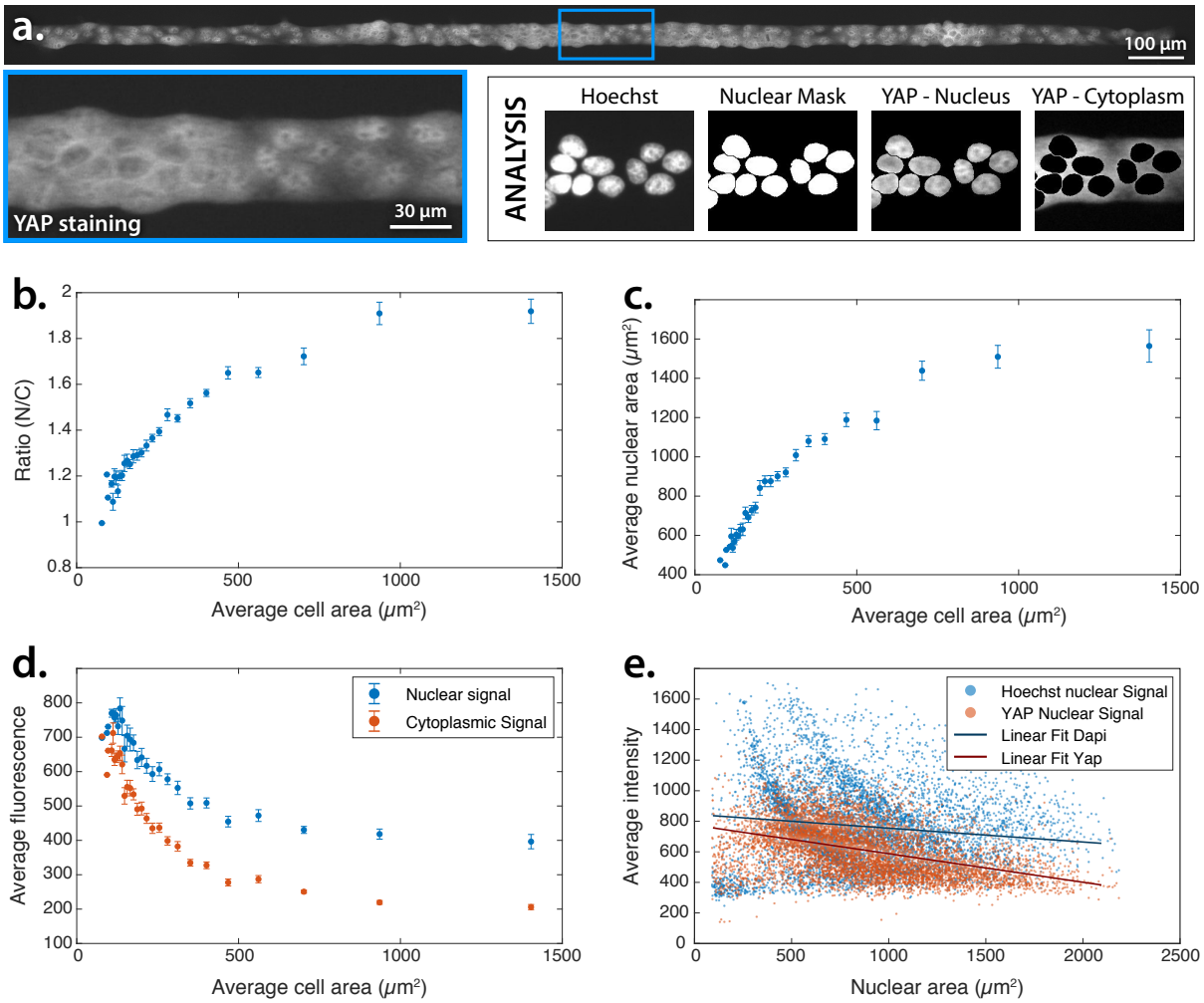


Figure 4.10: Results of studies of YAP localization. **a.**) Images of the fluorescence of YAP display high nuclear localization for low-density areas. To quantify this effect, we use the image of Hoechst staining to define nuclear and cytoplasmic areas. **b.**) The ratio between nuclear and cytoplasmic fluorescence ($N/C$) is plotted as a function of local cell area. **d.**) To assess the effects of the different deformation of cytoplasm and nucleus, it is useful to plot their relative YAP signals as a function of cell area (1/density). **c.**) The plot of cell area against nuclear area is displayed for the same reasons. **e.**) The actual deformation of the nucleus is estimated thanks to the Hoeachst staining, which is juxtaposed to the YAP nuclear fluorescence for comparison. The data for each cell (n $\sim$ 7000) is plotted, the lines represent linear fits to guide the eye. All data is obtained from n=23 tissues. Errorbars represent the standard error on mean.

all vertical strips containing the same number of cells (i.e. same $A_{mean}$) is then pulled, and their average values are calculated to generate the plots in Figure 4.10b,c,d.

Our initial observation is confirmed by the graph in Figure 4.10b, which describes a strong increase in $N/C$ as cells become larger. This result is extremely interesting, because it seems to suggest that the alternation of contraction and relaxation typical of velocity oscillations might directly affect the localization of YAP, a protein involved in mechanotransduction. A periodicity in space could not be measured because the lack of cadherin images meant that we had to bin the data into strips. Their width cannot be

reduced indefinitely since thinner bins make for higher noise level. Future sets of data might easily solve this issue.

#### 4.2.3.1 Issues with the quantification of YAP distribution

Several considerations risk invalidating this result. All images are gathered with an epifluorescence microscope in 2 dimensional geometry, which measures the projected intensity over $z$. As cells become more packed, it is reasonable to think that they get thicker in the z-direction (we measured fluctuations of $\sim 10$ $\mu$m), which could change the projected fluorescence. This is not necessarily a problem if nucleus and cytoplasm deform in to a similar extent in response to cell packing. One of the doubts we retained is related to this last statement. This is well described thanks to the extreme example of a cell whose nucleus that does not deform. In this case, as cells become more packed, the cytoplasm develops more in the vertical direction, while no change is recorded for the nucleus. The measurement of the average fluorescence in the cytoplasm would then increase, because we are imaging through more of it, causing a subsequent decrease in the $N/C$ ratio without actual YAP translocation. This is obviously an exaggerated example, and the nucleus changes morphology as well as the cytoplasm, but it illustrates a possible effect which might bias the data measured, an effect we wanted to try to take into consideration.

From the pool of data we already had, we tried to distinguish the effects of nuclear compaction and YAP translocation. To this end, we estimate nuclear compaction by measuring the average Hoechst intensity for each nucleus. This is then compared with the average YAP intensity, which is affected by both nuclear deformation and YAP translocation. We plot these variables for each cell (n $\sim$ 7000) as a function of the nuclear area (Figure 4.10e). In the picture, it appears that the distributions follow slightly different trends. In our mind, the difference could be attributed to the morphological change of the nucleus. With the data we currently have, the noise level is so elevated that a better quantification is impossible, but future experiments might solve this issue.

A different approach, to estimate the cytoplasmic compressibility, is to plot the average nuclear area against the average cell area (Figure 4.10c). For a nucleus and cytoplasm that deform proportionally, we would expect a linear dependence. In the graph, this is true only for small cells, whereas a strong deviation is evident for higher average area values. Interestingly, this graph follows a similar trend to that of Figure 4.10b, a fact that seems to further undermine the solidity of this data. Staining of cadherins and the resulting cell-border segmentation could help with this quantification in the future.

The strong presence of noise, insufficient amount of data and time restrictions made

this work incomplete. It still lacks better quantification methods tailored for each bias, and concrete strategies to take them into account, which I did not develop. Even though these problems affect our results, they are corroborated by similar conclusions reported in literature [266], confirming that cell compaction leads to an decrease in the nuclear localization of YAP. This results suggest that YAP, and the Hippo pathway in general, could represent a biological counterpart to the wave-like phenomena we measured, ultimately providing a role for velocity oscillations in regulating cell behavior through mechanotransduction.

Unfortunately, we could not measure a periodicity of YAP activity to match that of the waves. On the other hand, more dense cells display increased YAP translocation, and cell density seems to have a $\sim$ 200 $\mu$m periodicity. A correlation between these phenomena could be the subject of future investigations. Moreover, the employment of live YAP reporters could enable the simultaneous observation of velocity oscillations and YAP activation levels and directly assess the presence of a correlation.

**PERSONAL NOTE**

*Even though this work is incomplete, I wanted here to shed some light on the doubts I had during this analysis and the reasons why we did not trust this data enough to consider it conclusive. I also included some of the possible strategies we devised to estimate and take eventual biases into account, in the hope that these approaches might, in the future, be carried on to yield better measurements of YAP activity.*

### 4.2.4 $\beta$-catenin translocates to the nucleus in compacted cells

Another mechanosensistive protein is $\beta$-catenin, which normally resides at adherens junctions. Mechanical stimuli have been shown to lead to the accumulation of $\beta$-cat in the cytoplams and its eventual translocation to the nucleus, where is acts as a transcriptional co-activator for the Wnt pathway (see subsection 1.4.2).

We therefore repeated the experiments performed for YAP, always in collaboration with Christophe Guilluy and Valentin Buffière-Ribot, staining for $\beta$-catenin. The analysis procedure followed is also similar, and it led to the results presented in Figure 4.11. As cells become smaller, the nuclear intensity of $\beta$-cat increases progressively. We also plot Hoechst vs $\beta$-cat intensity for all cells (Figure 4.11b), the idea being that, if the measured change in $\beta$-cat nuclear intensity were only due to changes in nuclear conformation, we would see a linear distribution of points. All deviations from such distribution can be attributed to cells whose $\beta$-cat translocation is not correlated to the nuclear

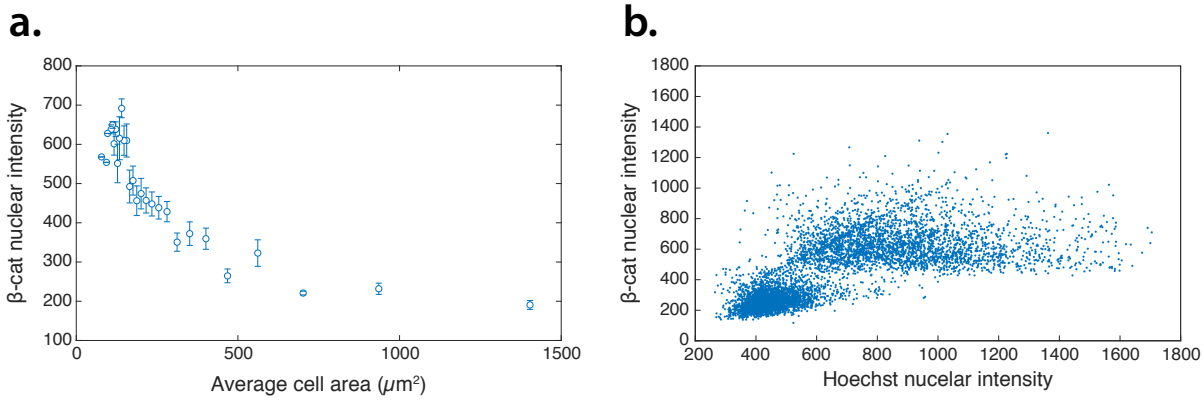


Figure 4.11: Results of studies of $\beta$-catenin localization. The experiments and data analysis, performed as explained earlier, result in the plot of average $\beta$-cat nuclear intensity against the average cell area (1/density) (**a.**). The data is obtained from n=23 tissues. Errorbars represent the standard error on mean. To distinguish nuclear accumulation from the mere conformational changes, we plot the average nuclear Hoechst fluorescence against the average $\beta$-cat nuclear fluorescence (**b**.). The data for each cell (n$\sim$6000) is plotted.

compaction. The graph also shows a strong accumulation of point around an almost perfect line. Those are probably mistakes in the detection of nuclei.

We conclude that area of tissues where cells are more compacted display a higher level of nuclear $\beta$-catenin translocation. This, just like the results obtained for YAP, is interesting in itself. On the other hand, we cannot yet directly correlate such effect with the presence of velocity waves.

### 4.2.5 Calcium signaling

The level of cytoplasmic calcium, normally confined to intracellular stores and released upon specific signaling, regulates multiple cellular functions [311], among which the control of cytoskeletal activity, actomyosin contraction and ultimately cell shape changes. Interestingly, coordinated cell behavior in cultured epithelia has been previously associated to spikes in the cytoplasmic levels of calcium. Such spikes have been shown both in single cells and at a multi-cellular level, where they spread between neighboring cells [312–314]. For these reasons, we wondered whether calcium signaling could be relevant to the presence of waves, and if we could measure oscillations at similar time-scales.

Moreover, a preliminary experiment, carried out by our collaborator Monika Dolega[3] supports such investigations. During a wound healing essay, after the removal of the PDMS block confining the cells, a calcium wave precedes the actual invasion of the

[3]Team Guilluy, Institute for Advanced Biosciences, Centre de recherche UGA - INSERM U1209 - CNRS UMR 5309, Grenoble, France.

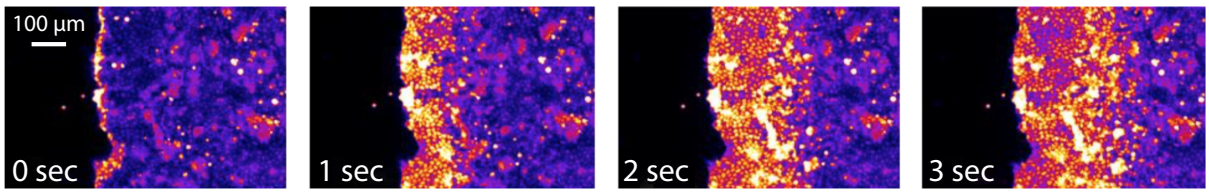


(a) Preliminary results obtained by Monika Dolega using MDCK cells. An epithelium is confined thanks to a PDMS block. When the block is removed, a wave of intracellular calcium, originating at the leading edge, propagates backwards through the tissue. Intracellular calcium is imaged with Fluo-4. Black = no cells, Yellow = high $Ca^{2+}$, Purple = low $Ca^{2+}$.

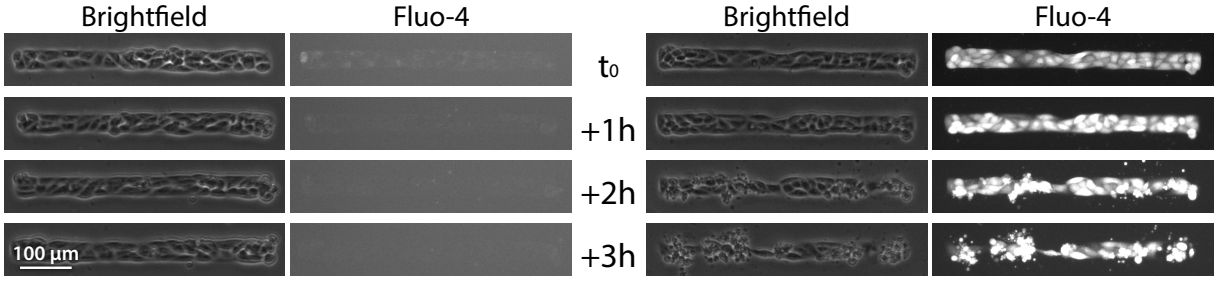


(b) Results of $Ca^{2+}$ imaging on lines. Brightfield and Fluo-4 fluorescence images are reported for two experimental conditions: the manufacturer suggested protocol (**left**), which leads to fast fluorescence decrease, and the most extreme situation where Fluo-4 is not removed (**right**). This latter case has high fluorescence, but cell death compromises the experiments.

Figure 4.12: Results of $Ca^{2+}$ imaging on lines.

available space. This wave travel backwards through the tissue, at speeds in the order of $\sim$ 100 $\mu$m/s (Figure 4.12a). Even though the typical timescale of this phenomenon is considerably shorter than that of mechanical waves, we decided to try and replicate these experiments for longer times.

To that end, we fabricated 40 kPA PAA gels, seeded MDCK cells and, at densities associated with the presence of waves, treated the tissues with Fluo-4 (Thermo Fisher Scientific) according to the manufacturer's instructions (30 minutes incubation, followed by 2x washing). Once internalized, Fluo-4 cannot leave the cell, and upon binding with $Ca^{2+}$, its fluorescence intensity increases >100 fold. The results obtained are reported in Figure 4.12b-*left*. In these conditions, the average fluorescence is extremely low and no spike is measured. Moreover, the fluorescence decreases steadily until, after $\sim$ 1 hour, no signal is present. We therefore tried leaving Fluo-4 in solution (Figure 4.12b-*right*), which increased the intensity of the stain, but within $\sim$ 3 hours widespread cell death compromised the experiments. When Fluo-4 was diluted before imaging (1:2, 1:10, 1:50), we faced one, or both of the situations explained above. To quantify the possible effect of bleaching, we imaged our cells with a fast frame rate (2 sec) and more than 2000 frames were acquired before we could measure a considerable loss of fluorescence.

The major problem with Fluo-4 is the constant decrease in fluorescence intensity with time, which compromises the long-term imaging (> 5 hours) necessary for a comparison with velocity waves. In conclusion, we feel like the idea of imaging calcium is valid and supported by preliminary data, but the probe chosen is not ideal for the task at hand.

### 4.2.6 Studies of wave-like velocity patterns in primary mouse keratinocytes

Our research of a biological counterpart is driven by the belief that a precise and organized mechanical pattern, i.e. our velocity waves, could serve as a guide, or a blueprint, during the morphogenesis of an organism. Among the many biological systems that self-assemble with a specific periodicity, one is of special interest for this work: the spontaneous formation of hair follicles (HF). The reason for this fascination (see section 1.1) is that, whereas the formation of follicles was generally attributed to the so-called "Turing patterns", there is recent evidence of the role of mechanical signals in the positioning of the HFs [25–27].

The morphogenesis of the skin is an extremely complex process, which is reviewed in detail in [315, 316]. For what concerns this work, a brief and simplified explanation of how hair follicles form will suffice. The (mouse) skin begins as a single layer of ectodermal cells in the embryo. Around day E9.5, the ectoderm specializes to become the epidermal basal layer, which will later stratify and give rise to all structures typical of a fully formed epidermis. Immediately underneath it, a layer of mesenchyme (dermis) forms, and their mutual interaction is key for the formation of appendages such as hair follicles and sweat glands. The first sign of the presence of HFs, which are epidermal appendages, is the formation of a hair placode around day E14.5. This is an accumulation of cells, initially dermal fibroblasts and then epidermal cells, which begin to aggregate following the release of bio-chemicals by the epidermis. The presence of a Turing pattern (short-range stimulation attributed to FGF20, long-range inhibition to BMP [25, 27]) ensures the correct placement of these hair placodes. Two facts are noteworthy: (i) the mechanical stress induced by the accumulation of cells in the dermis is an active component of the process; (ii) cell that will later belong to hair follicle are separated from the interfollicular epidermis linages at this specific stage. All HF cells, in fact, derive from progenitors expressing a specific protein called Sox9, which is also important for stem cells specification later on [316, 317]. The hair placode will then elongate into the underlying dermis to form the hair peg, which engulfs a small group

of dermal cells. The hair will form in the center of this peg, and grow outwards.

The similarities between cell aggregation under the placode and the spontaneous accumulation we observe at the anti-nodes were striking. This made us wonder if the experimental setup we developed to induce and quantify velocity oscillations could somehow be used to control placode formation. To that end, we partnered with Sara A. Wickström[4] and Yekaterina (Kate) Miroshnikova[4], experts in stem cell culture, differentiation and interaction with their niche. The aim of the collaboration was to verify whether the oscillations observed on MDCK epithelial cells could be reproduced on primary keratinocytes (extracted from the mouse skin), and, secondly, if such oscillations could give rise to patterns of differentiation markers.

**PERSONAL NOTE**

*Before diving into the specifics of which experiments and how they were performed, it is important to point out that all the work is the result of a 2 weeks collaboration. I spent that time in Helsinki, where I worked with Kate to make sure I could bring back with me the largest amount of data possible. The great hospitality I received made our work extremely efficient, so efficient in fact, that I could not analyze all the data we gathered. At the same time, oddly, 2 weeks was not long enough to solve all the technical issues and explore the entirety of the parameter space. What I will present here are the protocols followed for the experiment we had time to perform, and the general conclusion we can draw to help guide future analysis and investigations.*

To test the response of keratinocytes to 2-dimensional confinement, we produced gel (rigidity = 10 and 20 kPa) and glass substrates micropatterned with lines of different length (between 500 and 2000 $\mu$m) and width (20, 40, 60 $\mu$m). All samples were functionalized with 20 $\mu$g/mL fibronectin and 20 $\mu$g/mL Matrigel. Freshly isolated adult (telogen) and embryonic (E14.5) primary keratinocytes were then plated directly onto the samples, previously sterilized by immersion in 70% EtOH, and allowed to attach for $\sim$ 24 hours in low-calcium (100 $\mu$M) 3C medium [318], sufficient to support cell-cell adhesion without inducing differentiation. Once confluence was reached, tissues were exposed to fresh medium (either starvation medium supplemented with 200 $\mu$M calcium, or low-calcium 3C medium) and then imaged for $\sim$ 24-48 hours.

Initially, we worked on adult primary cells, which were starved immediately before imaging. The idea was that, since a combination of starvation, high calcium content and confinement/high-density induce epidermal fate differentiation, we could detect a

[4]Helsinki Institute of Life Science, Biomedicum Helsinki, University of Helsinki, Helsinki, Finland.

pattern of differentiation in the tissues corresponding to the eventual wave-like motion. Some of the cells lines contained a GFP-Sox9 construct, that allowed us to quantify the expression level of this protein. Since the spreading process was considerably faster on glass substrates, we concentrated on those samples. Immediately after starvation, cells changed their morphology (see Figure 4.13a), diminished their size and slowly decreased their motility. Nonetheless, in $\sim$ 5% of the cases, velocity oscillations were visible, and example is reported in Figure 4.13a. Within $\sim$ 15 hours, the average velocity dropped to $\sim$ 4 $\mu$m/h (Figure 4.13a.d), a situation associated to cells that barely move and, thus, the absence of waves. Moreover, our observations of Sox9 expression yielded no measurable periodicity.

We quickly realized that the cell type chosen was not ideal for our experiments. Adult cells come from a situation where HF morphogenesis has already taken place and they are fully specialized. We therefore repeated our experiments on embryonic (E16.5) primary keratinocytes. These cells are chronologically closer to the moment when hair placodes and HF linages are specified, and are further from the terminal differentiation (keratinization) that most cells will undertake. Unfortunately, we had no way to image Sox9 expression. We repeated the experiments by starving the cell right before imaging. In this situation, no oscillations were visible and cells barely moved (the average cell velocity, calculated by averaging all vectors for n=30 tissues, is $v_{mean}$ = 2,7085 $\pm$ 3,6827 $\mu$m/h).

Therefore, we decided to image the tissues without starvation, in freshly added 3C medium. This strategy lead to the presence of more widespread oscillations ($\sim$ 30% of the cases), one example of which is reported in Figure 4.13b. Even though we measured a steady decrease in the average velocity (Figure 4.13b.d), it was not as steep as for adult cells, and this allowed us to gather longer observations. Without starvation, the phenotypic change is not observed, although we notice a higher level of extruded cells (Figure 4.13b.a). Interestingly, thinner (20 $\mu$m) lines seem to improve the quality of our measurement.

The presence of more widespread velocity oscillations in embryonic cells is extremely interesting, in that it is a base to structure future investigations on. A better quantification protocol, specifically optimized for this cell type, could allow us to measure a periodicity. With the same tissue, we could then induce epidermal fate differentiation by adding calcium in solution, and verify whether such phenotypic change happens in correspondence of the nodes. Our experiments prove that starvation is better avoided to preserve cell motion. Moreover, mice transfected with a GFP-Sox9 reporter could be bred to have embryonic cells where this specific differentiation marker, relevant at this

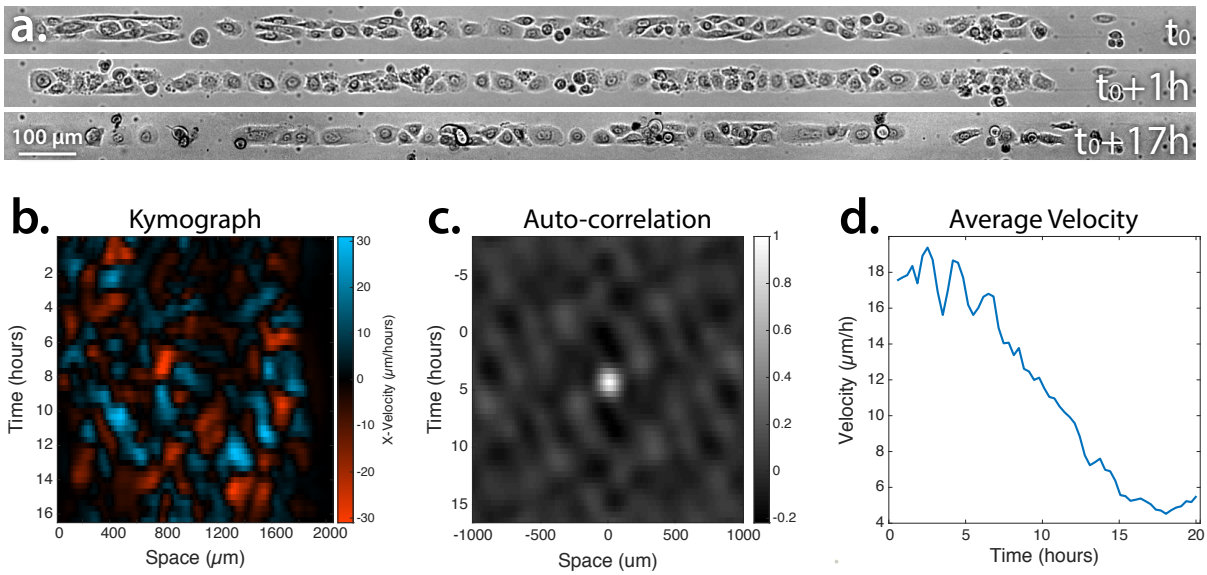


(a) Adult mice primary keratinocytes seeded onto thin strips (2000×40 $\mu$m) are imaged right after starvation medium is added. Almost immediately, cells change morphology (**a.**), a process accompanied by a steady decrease in velocity (**d.**, mean velocity of n=11 tissues). Nonetheless, in $\sim$ 5% of tissues, oscillations are visible, as reported in the kymograph of the velocity along $x$ (**b.**) and the relative auto-correlation image (**c.**).

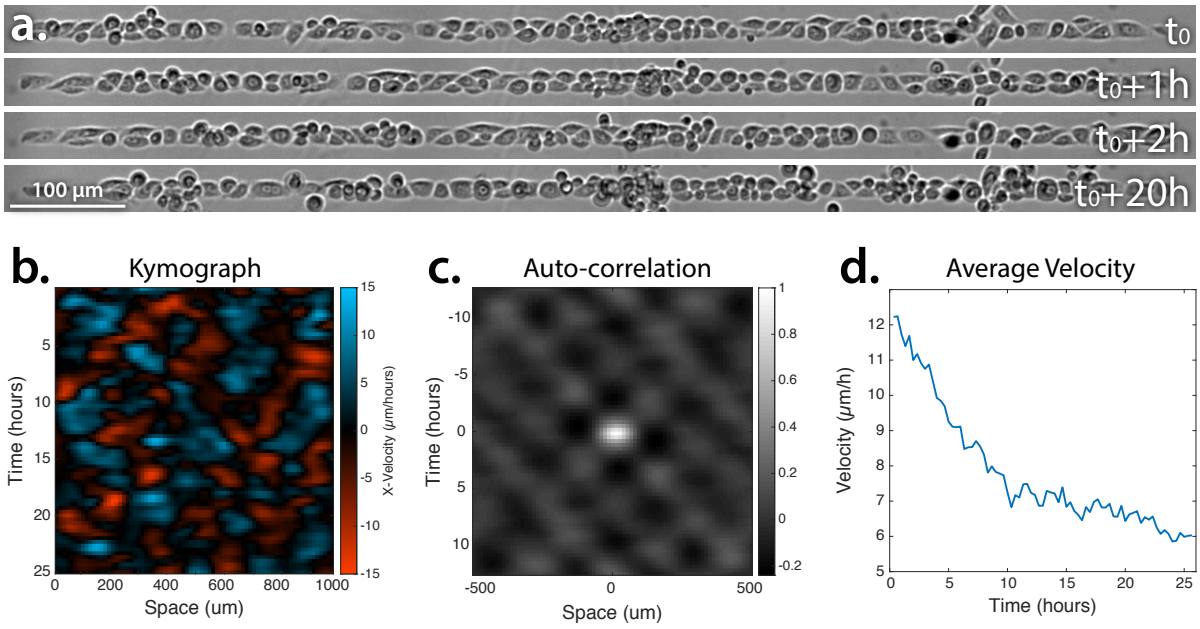


(b) Embryonic (E14.5) primary keratinocytes confined on thin strips (1000×20 $\mu$m) are imaged directly in 3C medium (**a.**). Even though a steady decrease of the average velocity is present (**c.**, mean velocity of n=19 tissues), periodic oscillations in cell velocity are more abundant and better defined. An example of such oscillations is reported in the kymograph of the velocity along $x$ (**b.**) and the relative auto-correlation image (**c.**).

Figure 4.13: Results of the studies on primary mouse keratinocytes.

specific age, can be visualized.

In conclusion, we can say that embryonic (E14.5) primary keratinocytes seeded on glass and PAA gel substrates patterned with thin strips display oscillations. We cannot yet give a definitive number for the periodicity, nor confirm the correlation with the expression of differentiation markers, but these experiments could be reserved for the future.

# 5. Conclusions and Future Perspectives

## 5.1 Diamond shapes tune the mechanical landscape

To explore the role of the local environment on proliferative heterogeneity we designed diamond-shaped adhesive areas, both on glass and soft gels. This geometry was chosen to control the anisotropicity of the mechanical landscape induced: depending on the size of the angle created, cells are subjected to different inputs in terms of spreading morphology, interactions with the neighbors, substrate deformation and stress propagation.

The viability of this approach is confirmed by our preliminary measurements of local cell density and proliferation, showing that both these quantities increase in proximity of the edges, with stronger values at sharper corners. TFM experiments on similar conditions also demonstrate that the substrate displacement follows a similar trend: all tissues pull inwards, but sharper angles are associated with deformations of higher magnitude. Interestingly, we also show that tissues pull more strongly along the direction of elongation of the diamond. These results confirm that our input parameter, the diamond angle, effectively tunes the mechanical landscape created, thus confirming the correlation between substrate tractions and cells division reported previously [126]. Our experiments then focused on finding how such landscape might come about, and in which other ways it affects the behavior of cells. We show that changes in tissue shape correlate with cell morphology: an elongation of the tissue along $x$ leads to a global cell alignment and deformation in the same direction. The two phenomena seem correlated, but a causal dependence has not been confirmed. Strong deformations at acute angles are also shown to correlate with a thicker cellular sheet and the appearance of multi-layered morphology.

In comparing cell division and mechanical stress, the work of Nelson and colleagues is the point of reference [126]. Our preliminary data corroborates their results, with the strong difference that, whereas they show a homogeneous cell density and increased proliferation uniquely at the edges, we find that both quantities raise together near the

borders. On the one hand, this hinders our ability to distinguish the contribution of the two phenomena, while on the other, it constitutes a novelty. Setting cell division aside, the link between mechanical stress and cell density has not, to our knowledge, been shown before. Moreover, cells do not simply accumulate at the edges of the tissue, a fact fascinating *per se*, but 50° diamonds consistently display selective gathering at the center of the shape, an oddity worth further investigation.

Mechanical stress is also indirectly correlated to cell morphology. Specifically, our results confirm the connection between cell elongation, a proxy for cell polarity, and substrate deformation. When seeded on 10° diamonds, cells globally align with the long diagonal of the tissue, and this in turn gives rise to a re-orientation of the substrate displacement in the same direction. Increasing the size of the tissue allowed us to slowly release the confinement, and quantify the alignment correlation distance as $\sim 60$ $\mu$m. Interestingly, for patterns wider than 100 $\mu$m, i.e. twice the alignment correlation distance, we measure both random cell orientation and a loss of the typical bi-polar displacement pattern.

This joint loss of cooperative behavior has also been observed by Schaumann and colleagues, who notice strong cell forces situated in the center of colonies, albeit in situations where the average cell velocity is extremely elevated ($> 100\mu$m/h) [295]. These values are at least one order of magnitude higher than what we record. Despite this fact, for cell types characterized by lower cell motility, the overall displacement distribution we measure is strikingly similar to that reported in the paper, which concludes that elongated colonies reorient their distribution in a matter reminiscent of single cells [295]. This paper, which contains many of the conclusions our results were pointing towards, was published in 2018, after we obtain our data.

A different interpretation for the loss of large-scale coherent displacement has to do with Kenotaxis (see subsection 1.6.6). When faced with areas that cannot be invaded, cells always exert forces in a manner that would cause them to invade said space, i.e. towards the center of the colony, or away from the obstacle. This guidance cue originates at the periphery of the colony, and is communicated through the tissue for distances estimated in the order of $\sim$ 150 $\mu$m (see substrate deformation correlation length in [161]). When the colony is large enough (roughly twice this correlation length), cells in the center lose information about the edges and displace the substrate in an unkenotactic manner. Even though the values do not agree perfectly, the general order of magnitude is the same, proving that this might be a useful paradigm to explain the loss of coordinated substrate displacement in the center of large tissues.

Another interesting question is whether cell tractions correlate with cell movement.

On 10° diamonds, where cells are more elongated and coherently oriented, cell motion happens predominantly along the $x$ direction. This observation is mirrored by a stronger magnitude in cell forces along the same axis, which means that, at least on such long diamonds, cell motility, morphology and substrate displacements are strongly correlated and focused along the same direction. Whether this is also true for more isotropic and larger tissues was not studied here, and it is still a matter of debate (see subsubsection 1.5.2.3).

Altogether, these results are in agreement with the strong presence of an "edge effect", influencing the behavior of cells at the periphery of the colony. This impacts not only the way cells deform the substrate, but also their division, morphology, orientation and their predisposition to proliferate in 3D. The mechanical environment established in response to the imposed geometry, i.e. our control parameter, seems to be an underlying feature, correlating all other observations. From our point of view, as biophysicist interested in mechanotransduction, these phenomena and their possible dependence on active cell forces are as natural an idea as they are interesting to investigate. If, on the one hand, all the results presented so far are to be regarded as preliminary, on the other, they paint a coherent picture with many cues that could serve as solid bases to develop a study upon.

## 5.2 A new wave-like phenomenon

Our measurements of cell migration on diamond-shapes highlighted the presence of periodic velocity oscillations comparable with those mechanical waves already reported in literature. To shed light on the origin of these phenomena, we confined tissues on thin *quasi one-dimensional* strips. Observations of cell velocity on strips of different length highlighted the widespread presence of oscillatory motion, and a transition between global (the entire layer moves back and forth alternatively) and multi-nodal (reminiscent of a standing wave) oscillations for a tissue length of $L \approx 400$ $\mu$m, also predicted by SPV simulations. We characterize the periodicity of this motion as $\lambda = 380 \pm 40$ $\mu$m and $T = 4.7 \pm 0.8$ hours, and, since these values do not adapt to the external confinement, we conclude that velocity oscillations are intrinsically encoded in the cells.

To our knowledge, these velocity waves are a novelty. Compared to what had previously been published, we measured multi-nodal oscillations in confined environments, features that set these supra-cellular waves (hereafter called SupraWaves) aside from both breathing oscillations (characterized by phase coherence) and traveling waves. Nonetheless, all these mechanical phenomena share many similarities, which we will

concentrate on after spending some time on the work of Peyret and colleagues on the presence of sustained oscillations of cell velocity in confined epithelial sheets [266]. We had previously set their paper aside because of its contemporaneity and high similarity to our own.

### 5.2.1 Simultaneous reports of oscillations in confined environments

PERSONAL NOTE

*Before describing and putting these results in perspective, I would like to shed some light on the striking contemporaneity between the paper from the group of B. Ladoux and ours. Around September 2018, B. Ladoux shared a draft of his paper with Magali Le Goff, a close collaborator of ours. This is how we came to know that his group had worked on the very same phenomena we concentrated on: they had thoroughly studied the presence of velocity waves, the correlation with YAP activation, and reproduced them with a model. Even though the similarities were striking, both in terms of the actual investigations carried out and their interpretation, one strong difference lied in the point of view on the phenomenon: whereas Ladoux's work focused more on the biological perspective, we worked to achieve a physical characterization.*
*If, on the one hand, this knowledge discouraged us, on the other, it sedated our hesitation and convinced us of the quality of our work, which had effectively been reproduced independently and anonymously in another lab.*
*We, therefore, reached out to Ladoux to confront our data and begun an extremely constructive dialogue (which we have him to thank for). Together, we decided to write 2 complementary articles, one concerned with the physics of these oscillations [279] and one more focused on biology [266], and to up-load them on bioRxiv simultaneously.*

In their paper, Peyret and colleagues confine human keratinocytes (HaCaT) tissues to square patterns (side 200-1000 $\mu$m), where they notice the presence of global rotations, somehow comparable to the swirling motion reported previously. When separated into its $x$ and $y$ components, the velocity field displays oscillations in both directions, with a $\pi/2$-phase shift, whose typical period (in time) and amplitude (in $\mu$m) increases linearly with the confinement size (2-10 hours, 20-100 $\mu$m). The authors then confine cells on long rectangles (width 200-500 $\mu$m, length 2000-3000 $\mu$m), where the rotatory nature of velocity and cell polarity is confirmed. In this case, they report the presence of (what we would call) global oscillations along the short direction, and multi-nodal

oscillations along the long one, describing a phenomena reminiscent of standing waves. Interestingly, the phase coherence length (which is half of the wavelength $\lambda$) along both directions matches the tissue width, leading to the conclusion that "the period and amplitude of the oscillations are [...] only dependent on the smallest confinement size" [266]. By calculating the divergence of the velocity field, the authors demonstrate that these oscillations are accompanied by fluctuations in density and, thus, phases of compression and extensions, although a direct measurement of cell density is lacking. Further studies also revealed that areas of low cell density are characterized by high YAP nuclear localization and thicker cellular layers. On a side note, related to the velocity-traction alignment debate (see subsubsection 1.5.2.3), the authors state that, only on a local scale, the velocity of each cell aligns with the traction forces with a delay of $\sim$ 30 minutes.

The most obvious conclusion from the comparison of the two papers is that, whereas with our work we demonstrated that the periodicity of SupraWaves does not depend on the length of the tissue, its dependence upon its width is something we have ignored so far, and we will have to assess in the future.

Although the oscillations described by Peyret and colleagues have deep similarities with those we observe, mainly the fact of being in confined environments and happening over time and distances of similar magnitude, there are strong differences. The main distinction is the transition between migration modes we observe thanks to our quasi one-dimensional geometry, a transition that is not present in [266]. Peyret and colleagues also report that the period and amplitude of oscillations scale linearly with tissue size. We have already quantified the behavior of the period (see subsection 3.2.7), but for the sake of comparison, we estimate the amplitude of the displacement of cells from the period (Figure 3.20) and average velocity (Table 3.3) as $A = \frac{1}{2} \cdot \frac{V_{mean}}{T}$ (see Figure 5.1d). The graphs confirm the difference: the periodicity of SupraWaves is only affected by the characteristics of the confinement within the regime of global oscillations, where the period and wavelength increase linearly with tissue length, a trend that characterizes the whole range of experiments reported in [266]. This discrepancy might be attributed to the different velocity-correlation length of MDCKs ($\sim$ 150 $\mu$m) and HaCaT ($\sim$ 600 $\mu$m). Whereas our tissues are designed to span a wide range of lengths, both considerably smaller and larger than the correlation length, the squares remain in the former regime, a fact that could hide the presence of a transition. From these considerations, it seems that the experiments in [266] remain in the "2D version" of the global oscillation regime, controlled by the smaller of two confining lengths.

Peyret and colleagues report that, in the 2D case, the periodicity along $x$ is equal

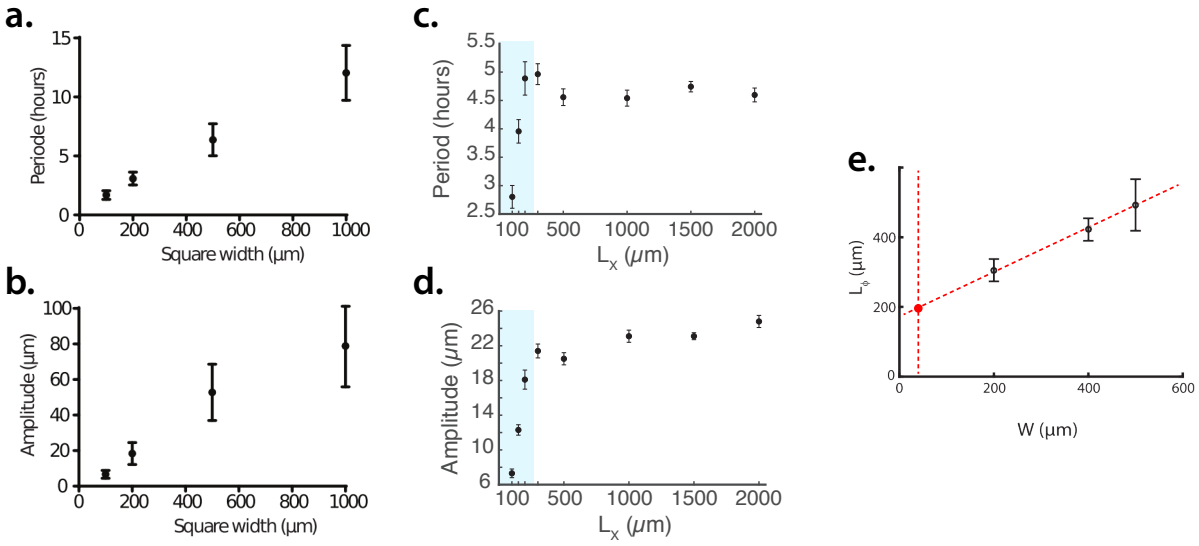


Figure 5.1: Comparison between the results obtained in [266] (*a,b,e*) and during our experiments (*c,d*, blue shaded areas highlight the global oscillation regime). The period in time (*a,c*) and amplitude (*b,d*) for the two cases are compared. The phase coherence length (*e*) as calculated in [266] is also reported, together with an estimation of the working conditions for our strips (red dot).

to the confinement in $y$. This is quantified as the phase coherence length (defined as the distance over which $v_x$ reverses direction, i.e. half of our $\lambda$), and the authors find a linear behavior (see Figure 5.1e). If we extrapolate based on the graph reported in the paper, for widths of 40 $\mu$m (those of our strips), we obtain a phase coherence length equal to exactly half our period, a match that is somehow surprising given the profound difference between the cell types. The intercept of this linear behavior suggests that the confinement along $y$ only affects the behavior in the perpendicular direction above a certain threshold.

Interestingly, an effect is observed in the magnitude of the velocity oscillations (in $\mu$m/h), a quantity we did not measure. Around $\sim$ 600 $\mu$m, a distance equal to the correlation length, Peyret and colleagues report a change between a linear increase of magnitude with the confinement size, and a regime of constant magnitude. The transition is attributed to the decrease in migration speed due to the proximity of the walls, an effect that we observe as well (see Table 3.3), mainly for global oscillations. In the future, it might be interesting to measure the amplitude of the oscillations (in velocity) in our case, and verify whether we observe a comparable behavior.

A difference between the papers lies in the behavior of cell polarity, a quantity describing the direction of cell migration: in 2D it rotates in time, a situation which does not seem to be the case for our thin strips. To verify this, we plotted kymographs of $v_y(y;t) = \langle v_y(x,y;t)\rangle_x$, which only displayed periodicity in $< 5\%$ of the cases, and with high variability between 1 and 8 hours. On the other hand, a similar quantification in

the case of large 10° diamonds (see Figure 3.11) revealed the more frequent presence of periodicity around $\sim$ 4 hours, indicating the results obtained in [266] might be reproduced with our setup. It is possible that our quasi one-dimensional situation forces inversions of polarity along $x$ rather than a rotation, although a direct measure of this quantity is all but trivial.

Finally, like in our case, the authors measure YAP translocation. Setting our doubts aside, we feel like both works suffer from a lack of a direct causality between the presence of waves and the activity of YAP and/or local cell density. There is no direct evidence of a periodicity in neither of these two quantities, a fact that, in our minds, undermines the credibility of these results.

### 5.2.2 Wider comparison with literature

The transition we observe between global and multi-nodal oscillations around $\sim$ 400 $\mu$m happens for values approximately equal to double the velocity correlation length ($\sim$ 150 $\mu$m). The factor of 2 makes sense because the correlation length describes how far the motion of cells is coordinated. As a gross simplification, to have cells moving in opposite directions you need, at least, two groups of coordinated cells, which, in a quasi one-dimensional geometry, requires twice the correlation length. Interestingly, the presence of a change in cell behavior at this length coincides with the transition between global coordinated rotation and the presence of multiple swirls for discs of diameter $\sim$ 300 $\mu$m [165].

SupraWaves share similarities with the breathing motion of cells on round patterns. We measure a linear increase in period with tissue length in a situation of global oscillations, which is mirrored by a similar behavior in [128]. A breathing oscillation has a node in the center, and cells are also immobile at at the external edge of the tissue. If we only consider the radial direction, we can reduce the system to one dimension, where the radius plays the role of $L_X$. With this in mind, breathing oscillations are global oscillations, with an additional circular symmetry. Interestingly, we measure global oscillations for $L_X < 400$ $\mu$m, and all works reporting breathing oscillation were carried out on discs whose radius was smaller than 350 $\mu$m [128, 163, 172]. Whether different migration modes, characteristic of larger discs, exist is still not clear.

The linear dependence of the period on the confinement size is attributed to the constant speed of propagation of the oscillations. In our case, we measure this as the effective velocity, a value approximately equal to 80 $\mu$m/h. When comparing this number with those present in literature, we notice that it is quite recurrent. Even if not clearly specified, we can estimate an almost identical value from [266]. For what con-

cerns traveling velocity waves at tissue boundaries, their speed is slightly higher ($\sim$ 120 $\mu$m/h [194]) but still in the same order of magnitude. This is interesting for our initial interpretation of oscillations as standing waves, which are the superimposition of 2 identical waves traveling in opposite direction. If what reported in [194] applies for thin strips, and we assume that wave-fronts are "launched" at the short edges inwards in a periodic manner, than what we measure and what Rodriguez-Franco et al. observe might represent the same phenomenon. Another occurrence, which shares many similarities with fluctuating migratory phenomena, is the propagation of ERK waves at this very same speeds [198]. Stress and strain waves in expanding monolayer, on the other hand, are somewhat different, reporting value ether too low [174] or too high [195]. Nonetheless, a more comprehensive study of the forces exerted by the cells on the substrate could allows for a better comparison with these works.

## 5.3 Future perspectives

As often the case in science, the future perspectives we can think of are endless and extremely varied. I will first highlight what we feel are the most stimulating ones, to then quickly run through a series of possible future investigations.

#### Transition to 2-dimensional oscillations

We worked on a quasi one-dimensional geometry in order to find the simplest system possible where we could reproduce velocity oscillations, which had already been observed on planar geometry. Our original idea was to follow a bottom-up approach, and slowly steer our work towards more complicated geometries, an approach which was somehow confirmed by the work of Peyret and colleagues [266]. Three future ideas are related to the second dimension, i.e. the width, that we have so far ignored. The first is to assess whether changes in the width of our tissues affect the periodicity of oscillations and the critical length associated to the transition. Secondly, we would like to bridge the gap between $\sim$ 1D and 2D by progressively making our strips wider. In a way, this process would be aided by the other published data, which could tell us what to look for. The third perspective is related to the considerations mentioned above, which seem to point towards the fact that the experiments carried out in [266] remain in a sort of equivalent global oscillation regime in 2 dimensions. The oscillations along the short direction, in fact, are global, and no nodes are reported. This begs the question of whether there is a 2D-phase transition between migration modes over $y$, and for what distance that could happen. Based on a comparison with our cell type, we could hazard

a guess: if the transition for MDCKs happens at double the correlation length, then in HaCaT this could happen around $\sim 1000$ $\mu$m. It could be interesting to investigate this by extending the width of the strips further, to find a situations of multi-nodal oscillations in both $x$ and $y$ directions, and understand if the two influence each other and how.

Moreover, our studies on 50° diamonds highlighted the presence of a nuclear accumulation in the center of the shape. This could be the consequence of a 2-dimensional standing wave, the presence of which can be verified with the experiments proposed above.

**Assessing the periodicity of cell conformation**

Our preliminary studies of the 3D conformation of tissues reveal the presence of strong fluctuations in local cell thickness, with a periodicity of $\sim 200$ $\mu$m. This number, for which we do not have an explanation yet, is further corroborated by the studies on local cell density, which measure a similar period. Given the preliminary nature of these results, it would be, first of all, interesting to confirm their solidity with more consolidated techniques, such as fluorescence exclusion microscopy [309], and simply increase the statistics on the local cell density.

The second perspective is related to the interpretation of this number. We measure oscillations at $\sim 400$ $\mu$m, and a possible periodicity of cell density for $\sim 200$ $\mu$m. The obvious question is related to the nature of the factor of 2. Initially, we expected cells to be thicker where the velocity field was converging, where they are compressed, an idea driven by the (erroneous [308]) assumption that cells maintain a constant volume. A different hypothesis could be that either motile or non-motile cells develop more in the vertical direction. The presence of two cell sub-populations (motile and non) could explain a periodicity at $\sim 200$ $\mu$m, and could be further verified with other experiments of cytoskeletal morphology and cellular signaling. To test this hypothesis, we would perform live imaging with a confocal microscope over longer periods of time ($\sim 10$ hours). The low frame-rate necessary to identify oscillations could allow for long observations of cell thickness, to be accompanied with PIV measurements of cell velocity to identify nodes and anti-nodes.

**The effect of SupraWaves on stem cells**

The possible role of oscillations in cell physiology, particularly in stem cell differentiation, was tested on primary embryonic keratinocytes which, before artificial induction of epidermal fate differentiation, display oscillatory behavior. Due to the limited time on

our hands, these results remained in a preliminary state, but the presence of oscillations in a different cell type is very promising *per se*. Even from a theoretical point of view, periodic compression and expansion alone are not sufficient to generate patterning. The necessary components (i.e. morphogenes) must be put in place to create the basis for differentiation. This is why the natural progression for this project is to try to induce epidermal fate and verify whether SupraWaves result in preferential differentiation at specific loci. The presence of an ongoing collaboration makes this experiments feasible.

The other paths we can envision for the continuation of this work, scattered throughout the manuscript, can be summarized and divided into three main categories.

### 5.3.1 Finding the minimal ingredients for coordinated oscillations

Firstly, we would like to identify the minimal physical and biological ingredients leading to the emergence of SupraWaves. This could be achieved thanks to the development of a specifically tailored hybrid continuum model (introduced in subsection 4.1.6), and the design of experiments to bridge the single and the multi-cellular regimes. To this end, we have already performed some preliminary experiments to prove that single cells oscillate. We could repeat these tests with an increasing number of cells, in order to understand how collective oscillations emerge as a function of crowding and confinement size.

These investigations could be complemented with a more thorough study of the forces exerted on the substrate, at both the single cell level and for entire tissues. The simplified quasi one-dimensional geometry could help with the extraction of meaningful data, and the calculation of forces and stresses might shed light on the mechanical components of SupraWaves and, ultimately, allow for a comparison with other reports of waves in literature.

### 5.3.2 Testing the resilience of waves to external perturbations

To fully understand SupraWaves, another possibility is that of testing how resilient they are to external perturbations, being them mechanical or bio-chemical.

We have already ventured this path by blocking cell division with Mitomycin C, experiments we do not fully trust due to the presence of widespread cell death. Since it has been suggested that the lack of cell division leads to patterns characterized by lower noise [194, 195], these experiments could be repeated with a different drug, such as

thymidine.

Other drugs or knockdowns, specifically inhibiting cellular components, could be used to assess the importance of those very same components for the presence of oscillations. We have tested blebbistatin, but other possibilities are numerous, the most interesting being cadherin junction disruption by calcium chelation (EGTA) and cytoskeletal disruption with Cytochalasin D and Nocodazole.

A more dynamic approach involves the use of optogenetic probes to locally perturb cell contractility. As a matter of fact, a specific MDCK photo-activatable-ArhGEF11 cell line (PA-ArhGEF11-CRY2-CIBN system, light exposure leads to Rho-dependent signaling and contractility increase) is present in the lab and has already been tested on lines to verify the presence of oscillations in velocity. Moreover, a second RhoA-targeting optigenetic cell line is currently at the lab, albeit with no previous characterization. We can envision four types of experiments to test SupraWave resilience to inconsistent contraction patterns: (i) real-time illumination with a pattern that matches the native periodicity of SupraWaves, in phase or out of phase, to affect oscillation amplitude; (ii) illumination with a different periodicity, to see if and to what extent the system can accommodate for a different wavelength; (iii) saturating the tissue with widespread illumination, which is likely to make the cells "deaf" to mechanical stimuli; (iv) imposing a traveling contraction wave at different speeds, to verify the response of the system to different velocities and the eventual presence of an intrinsic maximum (mimicking the experiments performed in [198]). These last experiments can be done on ring-like tissues, where traveling excitations have already been observed.

### 5.3.3 Determining the biological impact

The presence of an intrinsic metric controlling both, the transition between migration modes and the location of the nodes, could be biologically relevant. If cells positioned at the nodes feel specific mechanical stimuli (e.g. periodic stretching and compression), they might undergo different fates, laying the foundations for the supra-cellular patterning characteristic of morphogenesis. Equivalently, could this intrinsic metric be used to measure distances and, ultimately lead to positional sensing? Following these hypotheses, we have and will carry out some experiments looking for a biological function that could be activated (or inhibited) in correspondence of the oscillations.

Such studies will need to probe the biological impact of SupraWaves on two distinct regimes. On the shorter timescale (minutes to hours), we expect changes in the cytoskeletal architecture, whereas at longer timescales we aim at identifying transcription factors and, possibly, a readout of their impact on cell physiology.

### Cytoskeletal organization

The morphology of the cell in response to the oscillations can be assessed by combining confocal-imaging and adequate staining molecules (SiR actin, SiR tubulin, Myosin II-GFP). Mimicking our experiments on diamond patterns, it would be interesting to repeat the quantification of cell shape thanks to the cadherin staining, and accompany this information with knowledge about the size and distribution of focal adhesions. Since we believe that oscillations could cause periodic inversions of cell polarity, it would be interesting to measure such quantity, a feature that could be achieved with these very same techniques by observing the relative positions of the nucleus, cytoskeleton and centrosomes [319].

### Signaling molecules

Two proteins (YAP and $\beta$ catenin), known for being part of mechanotransduction pathways, are also shown to translocate to the cytosplasm where cells are more packed, but whether this periodicity matches that measured for tissue height and nuclear density could not be verified. Moreover, these studies are affected by several issues. A more thorough quantification of the area and YAP activation for single cells could lead to more trustworthy data.

One possible approach to find direct correlations might be that of identifying each tissue/strip with a code during the gel patterning protocol. This could allows us to observe oscillations, stain for specific proteins, and then univocally associate each tissue with its oscillating motion and the specific distribution of the chosen protein.

The effect of other signaling molecules could be assessed, primarily that of ERK, whose wave-like activation has been shown to be concomitant with mechanical waves, and calcium, for which our preliminary experiments have excluded the use of Fluo-4.

### Cell cycle progression

The effect of SupraWaves on cell division could be assessed by repeating the experiments we performed with EdU. Another interesting readout of the SupraWaves could be cell cycle progression. A thymidine block can synchronize all cells in the G1/S boundary [302]. When such block is released, all cells resume the normal cell cycle, whose progression can be followed with MDCK cells stably expressing the Fucci construct.

**Selective extrusion**

Elevated rates of cell extrusion have been measured in correspondence of high density [163], enhanced monolayers stress and singularites in cell orientation [255]. All these phenomena are typical of nodes, anti-nodes, or possibly the space in between, so future investigations could concentrate on cell extrusion as a possible readout.

## 5.4 Concluding remarks

Patterning in Nature, and specifically in biology, is as fascinating as fundamental for our understanding of life and our own workings. We begun this work with this in mind, aware that our contribution would be extremely specialized and, if relevant at all for this field, limited. Nonetheless, we proved the existence of patterns in cell velocity and we took the first steps towards assessing their possible contribution for morphogenesis. Our initial idea emerged from observations of the existence of mechanical actors in the patterning of hair follicles, and we somehow concluded by circling back and performing experiments to verify the presence and relative importance of SupraWaves in primary skin cells.

All our hypotheses and experiments are driven by the same basic thought: oscillations have the purpose of separating cells into sub-populations and, ultimately, creating heterogeneity. This idea inevitably leads to investigations to determine if cells perceive their distant environment through the propagation of mechanical waves, and to what extent they respond to those waves. We need to acknowledge the fact that this might be a fundamentally flawed idea, and that mechanical waves might have the exact opposite purpose. Marel and colleagues advance this idea throughout their studies of collective cell migration in channels, where they interpret cell migration as the sum of 2 components: a constant drift and diffusion-mediated transport, which might effectively serve the purpose of "evening out cell-density gradients at large scales" [192]. The outcome of our investigations, so far headed in the opposite direction, will necessarily reveal the veracity of our hypothesis.

Setting all this aside, we are convinced of the importance of testing our idea. The possibility that intrinsic velocity oscillations might be the foundations of patterning is potentially revolutionary for the field of developmental biology. One could argue that the probability of success is low, but no matter how improbable, we feel like the potential novelty and drastic paradigm shift is worth the effort.

## *Personal note*

*The writing of this manuscript has been somehow painful: looking back through what I have done forced me to acknowledge the mistakes I silently accepted and the (hopefully marginal) laziness I passively welcomed. In the writing, I believe I managed to solve many of these issues, and where I could not, I tried to make the remaining flaws as transparent as possible. According to a recent survey by Nature [**?** ], the roots of the reproducibility crisis that is spreading through science is to be found on selective reporting, something I have tried to avoid as much as possible. Mistakes are ok, fraud is not.*

*Looking back, I would change my approach in 2 ways: I would take the initiative more often, and I would listen to Giovanni when he repeated: "a work not finished is a work not done". As a matter of fact, this manuscript contains almost 2 chapters of preliminary data and only 1 of confirmed results. If one were to put the priority on publishing as much as possible, this would not be a very efficient approach. Luckily, and this is something I have my supervisors to thank for, I learnt that science is not about the number of papers. Even if my work discovered numerous paths without actually reaching the end for all of them, something I still recognize as a flaw, it served to lay the foundations for the future of our group, and I am immensely proud of this.*

*"Hindsight is a gift"*[1]*, and I like thinking that the retrospective offered by this manuscript taught me a fair bit about how to tackle future endeavors.*

*Part of being a scientist is dealing with the so called "impostor syndrome", and I am sure my supervisors will agree with my self-diagnosed condition. I feel and hope that, even though one could argue with the choices we took and the specific methods we employed, a debate which is as characteristic as fundamental to science, ultimately the phenomenon and its interpretations are authentic. The reader will be judge of that.*

[1] Gadsby, Hannah - *Nanette*, Comedy show on Netflix, 2018.

Appendix A

# Protocols

## A.1 POLYACRYLAMIDE gel patterning - Glass method

### Glass coverslip activation.

- Use a nitrogen air gun to make sure the 32x0,17mm round are dust free before the plasma activation.
- Put the coverslips in the plasma cleaner. Lay the coverslips flat in the plasma chamber.
- Turn on the pump and wait until the pressure is around 0.2-0.3 mbar. Open the AIR inlet and regulate it until the pressure stabilizes at around 0.4 mbar.
- Turn the Plasma on at maximum power for 40 seconds (0.6 in timer of plasma machine).
- Close the gas inlet, stop pumping, and ventilate the reactor (a filter should be placed on the air inlet to avoid dust intake into the reactor).

### pLL–PEG glass coverslip coating

- Put a drop of pLL–PEG solution (25 mL/cm2 - 70$\mu L$) on parafilm.
- Take each coverslip with tweezers and flip it on the droplet in order to have the plasma-activated side of the coverslip facing the pLL–PEG solution and let incubate in the dark for 30 min.
- At the end of the incubation, lift the coverslips carefully without scratching the coating.
- Dip the coverslips into washing PBS solutions (you will use this one for all washing steps)
- Rest the coverslips vertically against a support, and leave them drying on a kimwipe facing out.

## Mask treatment

- Wash the mask with hot water (NO SOAP). Use your gloves gently rubbing on the surface.
- Rinse the mask with plenty of deionized water and dry the mask with nitrogen air gun.
- Rest the mask on a kimwipe and pour isopropanol on it. Use another kimwipe to rub the surface of the mask and make sure it is clean.
- Rinse the mask with isopropanol and make sure all the liquid is removed with a Nitrogen air gun.

## Deep UV insolation and protein coating

- Heat up the UV lamp (max 5 min, I try to avoid the machine from getting too warm). This is very important.
- Rest the mask on a horizontal surface, chrome facing up. Use a kimwipe to press on the coverslip (like PNIPAM protocol) to remove excess water and maximize vicinity between coverslip and mask
- Put the entire setup in the warmed up UV lamp (5 min). Flip the mask to have the coated side away from the UV source. Expose to UV for 4 min. (5 min usual time, now I do less and if it gets warmer in the room you might want to decrease this time)
- Prepare protein coating solution: we use a solution of 20 $\mu g/mL$ of fibronectin diluted in sodium bicarbonate 100 mM. (2 $\mu L$ fibronectin + 98 $\mu L$ $Na_2CO_3$) (I don't use fibrinogen anymore to avoid wastes, but otherwise the formula is 2 $\mu L$ fibronectin + 2 $\mu L$ fibrinogen + 96 $\mu L$ $Na_2CO_3$) (Dissolve 420mg of sodium bicarbonate in 50 ml of Milli-Q water using a 50ml falcon tube)
- After 5 min UV-light exposition. Pour deionized $H_2O$ to help detaching the coverslips from the mask.
- Rest them on a kimwipe to dry.
- Put a drop of ECM solution on parafilm (70 $\mu L$ for 32 mm coverslips) and put the pLL–PEG–UV-insolated side of the coverslip on the droplet. Protect from light and let it incubate for 30 min.

## Preparation of acrylamide solution and protein transfer

- Again, as acrylamide is carcinogenic, handle it with care under chemical hood and using proper user protection. (POLYacrilamide is not hazardous)
- Take 165 $\mu L$ of acrylamide + bisacrylamide solution (CHOOSE RIGIDITY NOW) and put it in a 500 $\mu L$ vial, and put it in the degassing chamber upstairs. We only work with multiples of this quantity, which is good for 3 coverslips.
- Gently lift the coverslips after 30min incubation, dip them in the PBS washing solution and then rest them on a kimwipe to dry.
- Collect the acrylamide solution from the vacuum bell and keep the container closed. (Remember to close the valve before removing the pipe, let slowly air inside with the valve)
- Vortex the fluorescent beads (use far red beads) solution.
- Add 1.5 $\mu L$ of fluorescent beads (FluoSpheres™ Carboxylate-Modified Microspheres, 0.2 $\mu m$, dark red (660/680)) solution (1:10 in $H_2O$) to the acrylamide solution if you need beads for TFM. (This is for 40x wide field imaging, normal quantity for 60x is 0.2 $\mu L$ of undiluted solution)
- Vortex again. Sonicate for 3 min to destroy any bead aggregates that could have formed during the storage.
- Prepare the TEMED and APS and silanized coverslips under the hood.
- Move the patterned coverslips under the hood and prepare parafilm (you can reuse same one but pay attention to dust that might cause a tilt in your coverslips).
- Put 10 $\mu L$ H2O and rest the non-functionalized side of the patterned coverslips on it.
- You will add TEMED and APS solution to the acrylamide with the following proportions: 1 $\mu L$ of TEMED and 1 $\mu L$ of APS 10% for 165 mL of acrylamide solution. You should proceed as fast as possible in the next steps.
- First, add TEMED to the acrylamide solution, briefly but vigorously mix. (black vial)
- Second, add APS solution to the acrylamide solution, briefly but vigorously mix. (transparent vial)
- Vortex again.
- Put a drop of 47 $\mu L$ of the acrylamide polymerization mix on coverlips (stack on parafilm thanks to the water).
- Slowly place the salinized coverslip on top while taking extreme care to avoid bubbles (place silanized side on polyacrilamide).

- Let polymerization proceed for 30 min under a lid. You can turn the hood off.
- Pour PBS on the samples coverlips to help the detachment and wait for 5 min so gels are softer.
- Detach the two coverslips using a scalpel.
- Store in PBS.

## Mask cleaning

- Wash the mask with hot water AND soap. Use your gloves gently rubbing on the surface.
- Rinse the mask with plenty of deionized water and dry the mask with nitrogen air gun.
- Rest the mask on a kimwipe and pour isopropanol on it. Use another kimwipe to rub the surface of the mask and make sure it is clean.
- Rinse the mask with isopropanol and make sure all the liquid is removed with a Nitrogen air gun.
- Put the mask (chromium side facing the air) in the plasma cleaner (oxygen cleaner).
- Start pumping out the air in the reactor and wait for the pressure to stabilize at 0.3 mbar.
- Open the O2 inlet and let plenty of oxygen flow for a 8 min.
- Pump out the air in the reactor and wait for the pressure to stabilize at 0.3 mbar.
- Run the plasma at 100% power for the max time of allowed by the machine (17min).
- Close the gas inlet, stop pumping, and ventilate the reactor.
- Store the mask in a dust free environment.

## Coverslip salinization

- This glass treatment is necessary to ensure a good attachment between the PAA gel and the underlying coverslip.
- As silane solutions are very toxic, this process should be performed under a chemical hood with appropriate user protection, at least the silane solution should not leave the hood outside of a hermetically closed container.
- Mix in a 15 ml falcon: 5ml of 100% alcohol, 161ul of 10% acetic acid and 18,5ul bind silane.
- Put 100-200ul of silane solution on each coverslip and distribute it evenly. I generally leave an external ring of width  1mm free of silane solution. This makes it

easier to detach the gels later on.

- After 3-4 min wipe each coverslip with a kimwipe. (Do not let the coverslip dry before wiping it).
- Leave for 10 min to make sure the coverslips are dry and store them at room temperature in a petri dish. Seal the petri dish with parafilm to avoid air dust and the coverslips to inadvertently turn.
- This treatment is quite stable over few weeks so you can do many coverslips at the same time to avoid always repeating this fastidious time-consuming process.

### Electroscrub treatment [in case of problems with gel quality]

- Place your mask on a glass container.
- Carry the next steps out in the chemical hood.
- Pour electroscrub solution in the container, make sure the mask is fully covered.
- For 3-5 min move the container and gently rub the surface of the mask.
- Remove the mask from the solution and pour abundant warm water onto it.
- Proceed with the normal mask washing without soap.

## A.2 PNIPAM glass patterning

### Surface functionalization with ATRP initiator

- Wash the glass coverslips with Milli-Q water, acetone and ethanol in this order. Dry them with nitrogen gas flow.
- Put the coverslips in the in the plasma cleaner. You can put them in a previously washed (acetone-ethanol-$N_2$ dry) glass dish or rest them directly on the glass tray inside the plasma cleaner.
- Turn on the pump and wait until the pressure is around 0.2-0.3 mbar. Open the $H_2O$ vapor inlet and regulate it until the pressure stabilizes at 0.4 mbar.
- Turn the Plasma on at maximum power for 6 min.
- Clean (acetone-ethanol-$N_2$ dry) 2 100ml beakers. Add a magnetic stirrer to one.
- Pour 100 ml of toluene in each beaker.
- Add 1250 $\mu L$ of APTES [(3-Aminopropyl)triethoxysilane] and 2500$\mu L$ of Triethylamine to the small beaker.
- After 6 min, close all plasma camber inlets and start ventilating the chamber. Remove the samples, stack them into a sample holder and dip it in the prepared toluene solution. Wait for 15 min.

- Put the beaker filled with washing toluene in the sonication bath and dip the surface activated coverslips in for 10-30 seconds.
- Wash the coverslips with ethanol, Milli-Q water and ethanol in this order, then dry them with nitrogen gas flow.
- Dispose of the solutions.

- Clean (acetone-ethanol-$N_2$ dry) the two beakers. Again add a magnetic stirrer to one of the two.
- Pour 100 ml of dichloromethane in both beakers.
- Add 5 ml of Triethylamine and 1000 $\mu L$ of $\alpha$-Bromoisobutyryl bromide to a beaker while stirring.
- Dip the coverslip in the solution for approximately 1 min, and then immerse them into the washing solution.
- Wash the coverslips with ethanol, Milli-Q water and ethanol in this order, then dry them with nitrogen gas flow. [At this point the surface should be hydrophobic]
- Dispose of the dichloromethane solutions.

## Deep UV patterning of the initiator layer

- Put 2 $\mu L$ of hexadecane on the metal side of the mask.
- Place the initiator-functionalized coverslip on the mask, with the functionalized side in contact with the hexadecane drop. Press manually on the coverslip in order to expel the excess of hexadecane and ensure a good coverslip/mask contact.
- Put the quartz mask with its quartz side facing away from the lamp (the coverslip on the lower side holds in place by capillarity). [use a kimwipe to ensure that the mask and the coverslip do not touch a hard substrate directly]
- Illuminate for 1.5-2 min
- After illumination, drop copious amount of ethanol on the mask to help peeling of the coverslip. You can help yourself with the tip of the wash bottle.
- Once you retrieved the coverslip, wash with acetone and ethanol in this order, then dry them with nitrogen gas flow. [You can usually already see the pattern.]
- Put the coverslip in another, previously cleaned, glass dish, with the functionalized side facing up.
- You can just wash the mask with ethanol and then drying it with gentle nitrogen air flow.

## PNIPAM brush growth

- The polymerization solution is prepared as follows (for 100 ml):
  - weight 5000 mg of NIPAM monomer and add them to 100 ml $H_2O$ in a beaker;
  - sonicate for 30sec.
  - add 17-20 mg of Copper(II) bromide while stirring [weight in metal dish and add it to previous solution]
  - add 300 $\mu L$ of PMDETA (Pentamethyldiethylenetriamine).
  - add 150 $\pm$ 10 mg of ascorbic acid while stirring.
  - sonicate 10 sec.
- Dip the sample holder with all coverslips in the solution for 30 min. Use another, bigger, glass dish as a lid.
- Wash with Milli-Q water and ethanol in this order, then dry them with nitrogen gas flow.

## A.3 Petrolli, Vanni, et al. "Confinement-Induced Transition between Wavelike Collective Cell Migration Modes." Physical review letters 122.16 (2019)

# Confinement-Induced Transition between Wavelike Collective Cell Migration Modes

Vanni Petrolli,[1] Magali Le Goff,[1] Monika Tadrous,[1,*] Kirsten Martens,[1] Cédric Allier,[2] Ondrej Mandula,[2] Lionel Hervé,[2] Silke Henkes,[3] Rastko Sknepnek,[4,5] Thomas Boudou,[1] Giovanni Cappello,[1,†] and Martial Balland[1,‡]

[1]*Université Grenoble Alpes, Laboratoire Interdisciplinaire de Physique, CNRS, F-38000 Grenoble, France*

[2]*CEA, LETI, MINATEC, 17 rue des Martyrs, 38054 Grenoble cedex 9, France*

[3]*Department of Mathematics, University of Bristol, Bristol BS81TW, United Kingdom*

[4]*School of Science and Engineering, University of Dundee, Dundee DD1 4HN, United Kingdom*

[5]*School of Life Sciences, University of Dundee, Dundee DD1 5EH, United Kingdom*

(Received 17 December 2018; published 24 April 2019)

The structural and functional organization of biological tissues relies on the intricate interplay between chemical and mechanical signaling. Whereas the role of constant and transient mechanical perturbations is generally accepted, several studies recently highlighted the existence of long-range mechanical excitations (i.e., waves) at the supracellular level. Here, we confine epithelial cell monolayers to quasi-one-dimensional geometries, to force the establishment of tissue-level waves of well-defined wavelength and period. Numerical simulations based on a self-propelled Voronoi model reproduce the observed waves and exhibit a phase transition between a global and a multinodal wave, controlled by the confinement size. We confirm experimentally the existence of such a phase transition, and show that wavelength and period are independent of the confinement length. Together, these results demonstrate the intrinsic origin of tissue oscillations, which could provide cells with a mechanism to accurately measure distances at the supracellular level.

DOI: 10.1103/PhysRevLett.122.168101

Supracellular organization plays a key role in establishing and maintaining structure, function, and homeostasis in tissues. In the early stages of embryonic development, where features need to arise spontaneously from a homogeneous state, this organization closely follows morphogenic chemical patterns. In the most general case, however, chemical reactions, osmotic pressures and mechanical forces all cooperate to determine tissue-level organization. This is confirmed by an increasing number of recent studies indicating that cell proliferation, differentiation, and motility are strongly impacted by the mechanical properties of the microenvironment [1–5]. Several recent works reported that wavelike patterns of the local cell velocity spontaneously appear in colonies of epithelial cells. Those velocity waves have also been observed in spreading epithelial sheets [6–9], regardless of cell proliferation [10], and are correlated to oscillations of the forces exerted by the cells on the substrate [11]. Such long wavelength patterns also appear in confined geometries where cell migration is limited to local cell rearrangements [12–16]. These waves are characterized by a wavelength $\lambda$ and a period $T$, and show a surprisingly large spatial and temporal coherence. They can be modeled either at the particle level [15] or using continuum approaches [10,16], based on a coupling between cell motility and intercellular forces.

In this Letter, we explore whether the period and wavelength of collective wave excitation in epithelial cell monolayers are intrinsically encoded in the activity of the cell, or if they are affected by external constraints such as a specific set of boundary conditions. To achieve this, we analyzed the collective motion of epithelial cells confined to a quasi-one-dimensional channel. The experiments were accompanied by a series of numerical simulations, based on a self-propelled Voronoi model (SPV) [17–19], adapted to take into account the confining geometry. Our results show that tuning the length of the confining channel drives a phase transition between a state of global oscillations and a multinodal wave state. This transition is a consequence of the interplay between local cell active dynamics and global confinement. The effect is robust and does not require detailed knowledge of molecular processes but relies on a simple polarity-velocity alignment mechanism studied in the physics of dense active matter systems.

To confine cells to a quasi one-dimensional pattern, we prepared adherent stripes on soft polyacrylamide gels ($E \simeq 40$ kPa), as described previously [20] [outlined in Fig. 1(a)]. Stripes of different length ($L_X = 100$ to 2000 $\mu$m), but of the same width ($L_Y = 40$ $\mu$m), were patterned on the same substrate. Epithelial Madin-Darby Canine Kidney (MDCK) cells were then seeded on the patterned substrates with initial concentration of $2.5 \pm 0.5 \times 10^4$ cells/cm$^2$. The samples were washed with fresh medium 1 h after seeding, then placed in the incubator (37 °C and 5% $CO_2$) until the end of the experiments. Cells were imaged *in situ* using an in-line holographic (defocus) microscope (see and Fig. SI-1 and Supplemental Material [21],

 

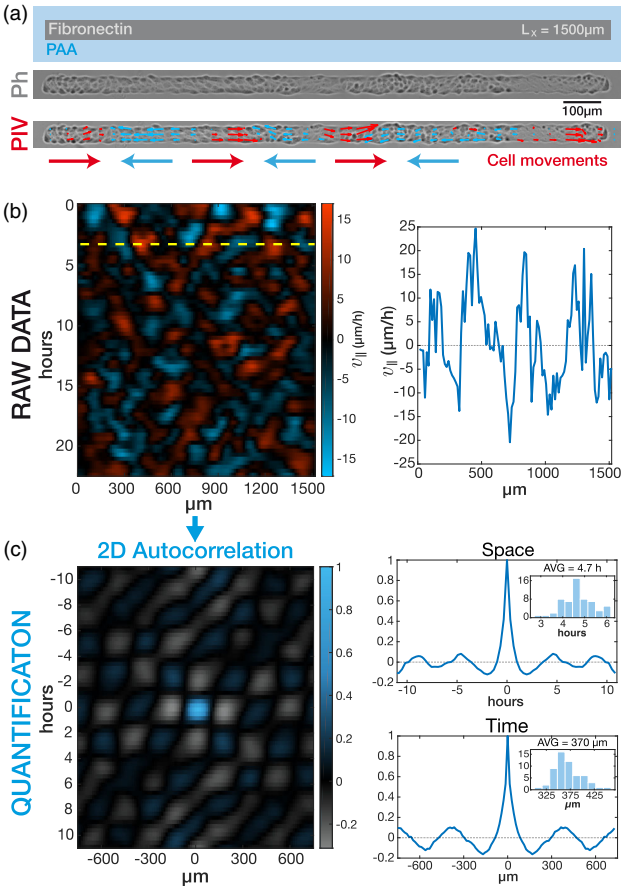


FIG. 1. (a) Top: MDCK cells are seeded onto a polyacrylamide (PA) gel patterned with fibronectin stripes (width: $L_Y = 40$ $\mu$m, length: $L_X = 1500$ $\mu$m). Middle: phase-contrast image of a confluent tissue. Bottom: velocity field measured by PIV. Velocities pointing in the positive (negative) $x$-axis direction are shown in red (blue), in agreement with the arrows reported under the image. (b) Left: kymograph representing the average horizontal velocity $v_\parallel(x;t)$ in time. Right: an example of velocity profile along the dashed line. We removed low frequency drifts using a Gaussian high-pass filter. (c) To quantify the periodicity of oscillations, we calculate the spatiotemporal autocorrelation of the kymograph (left) and measure peak spacing along the spatial (top-right) and temporal (bottom-right) coordinates (insets: distribution of peak periodicity for $n = 59$ independent stripes). Images in panels (b), (left) and (c), (left) were smoothed for visualization purposes with a low-pass Gaussian filter ($\sigma_x = 15$ $\mu$m, $\sigma_t = 30$ min).

which includes Refs. [22,23]) [24] for ≃48 h after confluence, gathering one image every 10 min [e.g., Fig. 1(a), middle]. Cell velocities were computed with a custom-made particle image velocimetry (PIV) algorithm with a final resolution of 20 min and 14 $\mu$m. To generate the kymograph, we cropped the videos in time to consider only confluent tissues, in an interval where the average absolute velocity was higher than 4 $\mu m/h$ [25]. We then averaged the horizontal component of the speed along the transverse direction $v_\parallel(x;t) = \langle v_x(x,y;t)\rangle_y$. We removed low frequency drifts using a Gaussian high-pass filter cropping 50% of the signal at 700 $\mu$m and 10 h. The kymograph in Fig. 1(b), left represents the spatiotemporal evolution of the velocity field over 22 h and over the whole stripe. A typical instantaneous velocity profile [Fig. 1(c), right] displays periodic oscillations in space. To quantify the period and the wavelength of these oscillations, we computed the autocorrelation function of the kymograph $g(\delta x,\delta t) = \langle v_\parallel(x,t)v_\parallel(x+\delta x,t+\delta t)\rangle_{x,t}$, displayed in Fig. 1(c), left. We observe an oscillating pattern in the autocorrelation function, both along the spatial and the temporal directions [Fig. 1(c), right]. This pattern indicates the establishment of an extended multinodal standing wave, with wavelength and period equal to $\lambda = 370 \pm 30$ $\mu$m and $T = 4.7 \pm 0.7$ h, respectively (errors represent the standard deviation, $n = 59$) [see histograms in Fig. 1(c), right].

To obtain a detailed understanding of oscillations in tissues, we consider a computational framework based on a recently introduced self-propelled Voronoi model [17–19]. The model used in this study is similar to that used in Ref. [19] to describe flocking transitions in confluent tissues, but rather than using periodic boundary conditions, we imposed confinement through a repulsive rectangular wall of size ($L_X$, $L_Y$) to reproduce the experiments' geometry. Full details of the model and its implementation can be found in Ref. [18] (also see Supplemental Material [21] for the parameters used). Briefly, the confluent cell monolayer is modeled as a two-dimensional network of Voronoi polygons covering the plane [Voronoi tessellation of all cell center positions, see Fig. 2(a)]. Each configuration of cells is described by the positions of cell centroids with energy given by the commonly used Vertex model [26], which depends on the area and perimeter of each cell. The parameters of the Vertex model include area and perimeter stiffness constants ($K$ and $\Gamma$) and target area and perimeter ($A^0$ and $P^0$). These parameters were chosen to describe a monolayer in a solidlike regime (with a shape factor $p^0 = P^0/\sqrt{A^0} = 2.5$) [17,27], to avoid shear flows induced by the boundaries. As in Refs. [17–19], we consider an overdamped dynamics, i.e., a force balance between frictional force with the substrate, self-propulsion at a constant velocity $v_0$ along the direction of cell polarity $\mathbf{n}_i$, and mechanical forces between the cells determined as a negative gradient with respect to cell position of the SPV model energy functional. The value of $v_0$ can be set to match the experimental observations, but does not affect the general oscillatory behavior. The dynamics of the cell polarity $\mathbf{n}_i$, described by the angle $\theta_i$ with the $x$ axis of the laboratory reference frame [i.e., $\mathbf{n}_i = (\cos(\theta_i), \sin(\theta_i))$] are

$$\frac{\partial\theta_i}{\partial t} = \frac{1}{\tau_{al}}\sin(\theta_i - \phi_i) + \nu_i^r(t), \tag{1}$$

with $\phi_i$ being the angle between the velocity of cell $i$ and the $x$ axis, and $\nu_i^r(t)$ being an orientational Gaussian noise. The angular dynamics is thus controlled by the interplay of

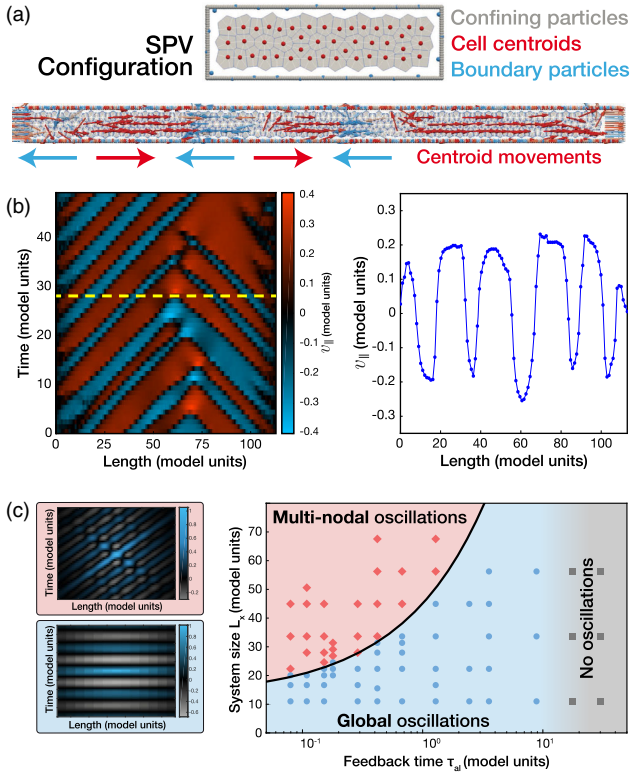


FIG. 2. Self-propelled Voronoi model for collective oscillations in confluent tissues.(a) Top: Example of tissue configuration obtained from the integration of the SPV model. Voronoi tessellation of the plane and centroid positions. Bottom: Velocity field of the centroids of the tesselation. Velocities pointing to the positive direction on the $x$ axis are represented in red and to the negative direction in blue. (b) Left: Kymograph representing the average horizontal velocity $[v_{\parallel}(x;t)]$ over time and right: its profile along the dotted line. (c) Phase diagram of oscillation patterns in the SPV model in the $(\tau_{al} - L_X)$ plane. Two types of oscillations are observed depending upon the system size $L_X(\tau_{al})$: Top left: For large systems where $L_X > L_X^c(\tau_{al})$ the autocorrelation of the kymograph shows multinodal oscillations whereas for small systems (bottom, left) where $L_X < L_X^c(\tau_{al})$ the autocorrelation exhibits global oscillations. Right: Simulation data points indicating whether the system exhibits global (blue disks), multinodal (red diamond), or no oscillations (gray squares symbols) for large values of the feedback timescale ($\tau_{al} > \tau_{al}^c \approx 17$ model time units). The solid line delimiting the global and multinodal oscillation phases is a power-law fit of the transition data points $[L_X^c(\tau_{al}) = a\tau_{al}^b + c$ with $a \simeq 32$, $b \simeq 0.62$, $c \simeq 13]$.

rotational diffusion (kept constant in this study) and the polarity-velocity alignment with rate $\tau_{al}^{-1}$, with $\tau_{al}$ being the time required by the cell to reorient its polarization in the direction of its velocity. This feedback mechanism leads to oscillations in confinement, where $\tau_{al}$ plays the role of an effective inertia, and the oscillations are along the lowest-energy elastic modes of the material [28]. This feedback mechanism is also at the origin of flocks in nonconfined tissues [19]. Simulations of confined tissue layers show steady state oscillations akin to those observed in experiments [Fig. 2(a), bottom]. In the following, we study the dependence of these oscillations on the confining length $L_X$ and show that a feedback mechanism for alignment (through $\tau_{al}$) is key to observe such mechanical waves in the SPV model. First we consider the case of long confining channels, where multinodal oscillations were observed experimentally [Fig. 1]. The simulation results displayed in Fig. 2(b) are obtained for a system with the same transverse confining length $L_Y$ (about 3 cells in the $y$ direction) and aspect ratio as in the experiments in Fig. 1 (and a value $\tau_{al} = 0.3$). We observe a pattern in the $x$ component of the velocity $v_{\parallel}$, and using the same analysis tools as in Fig. 1, we extract the wavelength $\lambda_{\mathrm{SPV}} \approx 22$ model length units and the period $T_{\mathrm{SPV}} \approx 8$ model time units. Note that by approximately matching the timescale of the model to the experiments (through the cells velocity $v_0$), one would get from these simulation data $\lambda \approx 300$ $\mu$m and for the period $T \approx 2$ h. This indicates that this model is able to reproduce the features observed in the experiments, although some fine-tuning of parameters $(\tau_{al}, v_0)$ is required for a quantitative match. Note that although the instantaneous velocity profiles [Fig. 2(b), right] and autocorrelation [Fig. 2(c), top left] plots appear to be similar to the experiments, the full spatiotemporal dynamics of the model [Fig. 2(b), left] do not correspond to standing wave oscillations. If the system size $L_X$ is decreased (keeping the value of $\tau_{al}$ constant), the number of nodes also decreases down to a point where the system size can only accommodate a single spatial period of oscillation, reaching a regime of global oscillation, where the direction of motion of all cells is coordinated [Fig. 2(c), top left]. This transition, illustrated in Fig SI-3 [21], is shown in the $\tau_{al} - L_X$ plane in Fig. 2(c), right. The feedback timescale also plays an important role as no oscillations are observed if $\tau_{al}$ is too large (i.e., the noise dominates over the coupling), and the critical length $L_X^c$ at which one observes multinodal oscillations increases with $\tau_{al}$. In the small system regime, the oscillation period increases linearly with the system size, as previously reported [15,16], and with $\tau_{al}$ (until oscillations eventually vanish for large values of $\tau_{al}$), consistent with the role of the feedback mechanism as an effective inertia [28]. Therefore, the SPV model describes a transition controlled by the stripe length $L_X^c(\tau_{al})$ between global oscillations where all cells coordinate their motion to a regime where groups of cells coordinate their motion direction locally.

To verify this prediction, we varied the length $L_X$ of the stripe between 100 and 2000 $\mu$m (examples between 200 and 1000 $\mu$m in Fig. 3), in order to tune the system across the critical length $L_X^c$. In approximately 95% of experiments, in agreement with model predictions, we observed two types of behaviors: (i) A global movement of all cells alternating between rightward and leftward motion [as seen

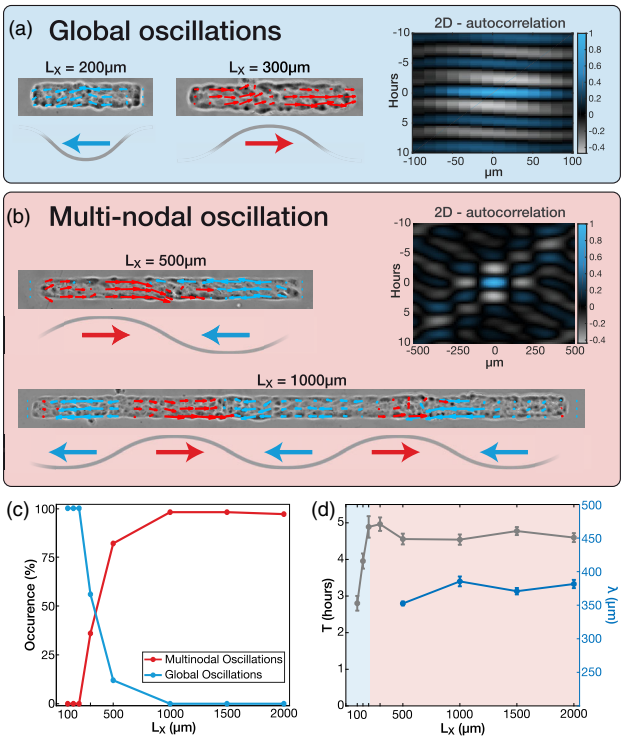


FIG. 3. Dependence of oscillatory behavior on the stripe length. (a) The velocity field superimposed on phase contrast images for short stripes of length 200 and 300 $\mu$m displays global oscillations, generating a characteristic two-dimensional autocorrelation (right). Longer lines (500 and 1000 $\mu$m) display multinodal oscillations (b), which give rise to a different pattern in the autocorrelation image (right). Velocities pointing in the positive $x$-axis direction are represented in blue, those pointing in the negative $x$-axis direction are represented in red, in agreement with the arrows reported in the schemes under each image. For each length, we display the frequency of each phenotype (c) and the characteristic time and space periodicity (d) calculated. Bars represent the standard error of the mean.

from the autocorrelation function of the kymograph in Fig. 3(a)] and (ii) the establishment of a multinodal standing wave with antinodal cells moving back and forth and cells at the nodes being alternately compressed and dilated [Fig. 3(b)]. The incidence of the two behaviors strongly depends on $L_X$, with a transition for $L_X \simeq \lambda$. In the experiments with $L_X < 200$ $\mu$m, the global oscillation statistically dominated. In this case, the period scales linearly with the tissue size [Fig. 3(d), blue area], while the wavelength is imposed by the confinement. In large structures ($L_X > 500$ $\mu$m), we only found multinodal waves, with the period and wavelength independent of $L_X$ [Fig. 3d, red area]. Figure 3(c) quantifies the transition, with on average 39 tissues per point, obtained from three independent experiments. Our experiments confirmed the existence of a self-sustained oscillatory mode in epithelial layers. Using the typical period and wavelength, we can define an effective velocity $u_\phi = L_X/T \simeq 78 \pm 13$ $\mu$m$/h$, which is independent of the pattern size. Even for small patterns ($L_X < 500$ $\mu$m), this velocity is preserved as the period scales linearly with the pattern length. We also note that $u_\phi$ is approximately tenfold larger than the average speed of individual cells within the epithelial layer (between 4 and 12 $\mu$m$/h$, depending on cell density [25,29]). Eventually, the spatial coherence of supracellular waves exceeds the largest pattern observable with our microscope.

Simulations using the SPV model show the emergence of sustained collective oscillations in confined monolayers. We identified two crucial conditions to produce these oscillations: (i) The existence of a delayed feedback between cell velocity and self-propulsion direction to introduce a new timescale in the dynamics and (ii) a very limited number of cellular rearrangement, at the limit of the solidlike regime. These ingredients allow the system to be described by linear elasticity, and for oscillations along the lowest energy elastic modes to dominate the dynamics [28]. One could thus envision tuning the oscillations by controlling cell-cell interactions through RAB5 or cadherin-mediated junctions, without affecting cells' individual mobility [19,30]. Contrary to experiments, where multinodal standing waves are observed, the SPV model describes propagating oscillations. Several reasons may explain this difference. First, a standing wave is only established when the wavelength exactly matches the boundary conditions. Thus, models require fine-tuning of the pattern length, while the intrinsic variability between cells could make the real epithelium more adaptable to small variations of the confinement size. Second, a different choice of the coupling mechanism could also introduce a new timescale in the model and better describe standing waves in confined tissue. Two-dimensional SPV models are usually adapted to describe spatially extended monolayers, while the stringent confinement used experimentally makes the system quasi-one-dimensional and induces strong constraints on the shape of cells near the boundary. Such boundary effects are difficult to capture in the SPV model due to the constraint of maintaining a Delaunay triangulation (dual of the Voronoi tesselation) [18], but do not seem to be essential to account for the oscillatory dynamics observed experimentally. One could thus consider building a one-dimensional continuum model based on an elastic description of the monolayer [28] in order to predict the transition between the different oscillatory regimes observed experimentally.

In conclusion, we demonstrate that the typical period and wavelength of epithelial tissue oscillations are intrinsically encoded in the cells, and are not adapted to external confinements. For this system, our SPV model predicts a transition between global oscillation and multinodal waves, the existence of which is confirmed experimentally for a pattern length $L_X^c \simeq 400$ $\mu$m. From a biological perspective this transition could be significant. If in small systems all the cells behave similarly—the entire layer alternately moves back and forth—in large systems cells located either at the nodes or at the antinodes experience different

mechanical stimuli and may undergo different fates, which can ultimately lead to supracellular patterning. The existence of an intrinsic wavelength $\lambda$ also provides an intrinsic metric, likely encoded in the cell. It is interesting to note that $\lambda$ roughly corresponds to the typical size of a Drosophila embryo (both length and circumference approach 400–500 $\mu$m, while cell size is $\simeq$15 $\mu$m), the most studied model system for morphogenesis. Based on this consideration, two important biological questions arise. Is this intrinsic metric used by the organism to measure distance inside a developing embryo? Does a collective long range excitation allow cells to probe their distant environment, in a timescale much shorter that allowed by their own motility?

The authors would like to acknowledge I. Wang for the development of Particle Image Velocimetry and P. Moreau for his technical support. We also thank K. Hennig, T. Andersen, E. Vitiello, and C. Guilluy for valuable and supportive discussions. G. C. has been supported by the Institut National de la Santé et de la Recherche Médicale (Grant "Physique et Cancer" PC201407). T. B. and M. B. acknowledge financial support from the CNRS "Mission pour l'Interdisciplinarité" and the Center of Excellence of Multifunctional Architectured Materials "CEMAM" (n AN-10-LABX-44-01). M. B. acknowledges financial support from the ANR MechanoSwitch project, Grant No. ANR-17-CE30-0032-01 of the French Agence Nationale de la Recherche. R. S. and S. H. the UK BBSRC, Grants No. BB/N009789/1 and No. BB/N009150/1-2. M. T. acknowledges iREU NSF Grant No. 1560390 and LSAMP NSF Grant No. 1302873.

*Present address: Mechanical Engineering Department, California State University, Fullerton, CA 92831, USA.
†Giovanni.Cappello@univ-grenoble-alpes.fr
‡Martial.Balland@univ-grenoble-alpes.fr

[1] A. J. Engler, S. Sen, H. L. Sweeney, and D. E. Discher, Cell **126**, 677 (2006).
[2] B. Trappmann, J. E. Gautrot, J. T. Connelly, D. G. T. Strange, Y. Li, M. L. Oyen, M. A. Cohen Stuart, H. Boehm, B. Li, V. Vogel, J. P. Spatz, F. M. Watt, and W. T. Huck, Nat. Mater. **11**, 642 (2012).
[3] G. Helmlinger, P. A. Netti, H. C. Lichtenbeld, R. J. Melder, and R. K. Jain, Nat. Biotechnol. **15**, 778 (1997).
[4] M.-E. Fernandez-Sanchez, F. Serman, P. Ahmadi, and E. Farge, Methods Cell Biol. **98**, 295 (2010).
[5] C.-M. Lo, H.-B. Wang, M. Dembo, and Y.-l. Wang, Biophys. J. **79**, 144 (2000).
[6] B. Ladoux and R.-M. Mège, Nat. Rev. Mol. Cell Biol. **18**, 743 (2017).
[7] V. Hakim and P. Silberzan, Rep. Prog. Phys. **80**, 076601 (2017).
[8] X. Serra-Picamal, V. Conte, R. Vincent, E. Anon, D. T. Tambe, E. Bazellieres, J. P. Butler, J. J. Fredberg, and X. Trepat, Nat. Phys. **8**, 628 (2012).
[9] P. Rodríguez-Franco, A. Brugués, A. Marín-Llauradó, V. Conte, G. Solanas, E. Batlle, J. J. Fredberg, P. Roca-Cusachs, R. Sunyer, and X. Trepat, Nat. Mater. **16**, 1029 (2017).
[10] S. Tlili, E. Gauquelin, B. Li, O. Cardoso, B. Ladoux, H. Delanoë-Ayari, and F. Graner, R. Soc. Open Sci. **5**, 172421 (2018).
[11] X. Trepat, M. R. Wasserman, T. E. Angelini, E. Millet, D. A. Weitz, J. P. Butler, and J. J. Fredberg, Nat. Phys. **5**, 426 (2009).
[12] T. E. Angelini, E. Hannezo, X. Trepat, J. J. Fredberg, and D. A. Weitz, Phys. Rev. Lett. **104**, 168104 (2010).
[13] K. Doxzen, S. R. K. Vedula, M. C. Leong, H. Hirata, N. S. Gov, A. J. Kabla, B. Ladoux, and C. T. Lim, Integr. Biol. **5**, 1026 (2013).
[14] G. Duclos, M. Deforet, H. G. Yevick, O. Cochet-Escartin, F. Ascione, S. Moitrier, T. Sarkar, V. Yashunsky, I. Bonnet, A. Buguin *et al.*, in *Cell Migration* (Springer, New York, 2018), pp. 387–399.
[15] M. Deforet, V. Hakim, H. Yevick, G. Duclos, and P. Silberzan, Nat. Commun. **5**, 3747 (2014).
[16] J. Notbohm, S. Banerjee, K. J. Utuje, B. Gweon, H. Jang, Y. Park, J. Shin, J. P. Butler, J. J. Fredberg, and M. C. Marchetti, Biophys. J. **110**, 2729 (2016).
[17] D. Bi, X. Yang, M. C. Marchetti, and M. L. Manning, Phys. Rev. X **6**, 021011 (2016).
[18] D. L. Barton, S. Henkes, C. J. Weijer, and R. Sknepnek, PLoS Comput. Biol. **13**, e1005569 (2017).
[19] F. Giavazzi, M. Paoluzzi, M. Macchi, D. Bi, G. Scita, M. L. Manning, R. Cerbino, and M. C. Marchetti, Soft Matter **14**, 3471 (2018).
[20] T. Vignaud, H. Ennomani, and M. Théry, Methods Cell Biol. **120**, 93 (2014).
[21] See Supplemental Material at http://link.aps.org/supplemental/10.1103/PhysRevLett.122.168101 for experimental setup, image analysis and numerical simulations.
[22] J. W. Goodman, *Introduction to Fourier Optics* (Robertsand Company Publishers, 2005).
[23] L. Herve, O. Cioni, P. Blandin, F. Navarro, M. Men-neteau, T. Bordy, S. Morales, and C. Allier, Biomed. Opt. Express **9**, 5828 (2018).
[24] S. V. Kesavan, F. P. Navarro, M. Menneteau, F. Mittler, B. David-Watine, N. Dubrulle, S. L. Shorte, B. Chalmond, J.-M. Dinten, and C. P. Allier, J. Biomed. Opt. **19**, 036004 (2014).
[25] L. Petitjean, M. Reffay, E. Grasland-Mongrain, M. Poujade, B. Ladoux, A. Buguin, and P. Silberzan, Biophys. J. **98**, 1790 (2010).
[26] R. Farhadifar, J. C. Röper, B. Aigouy, S. Eaton, and F. Jülicher, Curr. Biol. **17**, 2095 (2007).
[27] D. Bi, J. H. Lopez, J. Schwarz, and M. L. Manning, Soft Matter **10**, 1885 (2014).
[28] S. Henkes, Y. Fily, and M. C. Marchetti, Phys. Rev. E **84**, 040301 (2011).
[29] A. Puliafito, L. Hufnagel, P. Neveu, S. Streichan, A. Sigal, D. K. Fygenson, and B. I. Shraiman, Proc. Natl. Acad. Sci. U.S.A. **109**, 739 (2012).
[30] C. Malinverno, S. Corallino, F. Giavazzi, M. Bergert, Q. Li, M. Leoni, A. Disanza, E. Frittoli, A. Oldani, E. Martini *et al.*, Nat. Mater. **16**, 587 (2017).

# Supplementary material for: "Confinement-Induced Transition between Wavelike Collective Cell Migration Modes"

Vanni Petrolli,[1] Magali Le Goff,[1] Monika Tadrous,[1,*] Kirsten Martens,[1] Cédric Allier,[2] Ondrej Mandula,[2] Lionel Hervé,[2] Silke Henkes,[3] Rastko Sknepnek,[4,5] Thomas Boudou,[6] Giovanni Cappello,[6,†] and Martial Balland[6,‡]

[1] *Université Grenoble Alpes, Laboratoire Interdisciplinaire de Physique, CNRS, F-38000 Grenoble, France*
[2] *CEA, LETI, MINATEC, 17 rue des Martyrs, 38054 Grenoble cedex 9, France*
[3] *Department of Mathematics, University of Bristol, Bristol BS81TW, United Kingdom*
[4] *School of Science and Engineering, University of Dundee, Dundee DD1 4HN, United Kingdom*
[5] *School of Life Sciences, University of Dundee, Dundee DD1 5EH, United Kingdom*
[6] *Université Grenoble Alpes, Laboratoire Interdisciplinaire de Physique, CNRS, F-38000 Grenoble, France*

(Dated: July 31, 2019)

## PHASE FROM DEFOCUS MICROSCOPY

**Experimental Setup** We used low-cost components to build an in inverted configuration. The setup and a schematic drawing is shown Fig. 1. Blue LED (CREE, max 450 nm, FWHM 18 nm) source coupled with 400 $\mu$m multimode fibre (Thorlabs) with a narrow band filter (Thorlabs FB450-10, max 450 nm, FWHM 10 nm) is used for illumination in transmission geometry. Semi-coherent light passes through the sample and is collected by 10x/0.25 NA Objective (Motic CCIS EF-N Plan, Achromat). A short tube lens (Thorlabs, AC254-050-A, $f = 50$ mm) is used to create an image on a CMOS sensor (IDS UI-1492LE). Standard Thorlabs components are used for housing of the optics and the camera. Image acquisition with synchronized illumination is controlled with Raspberry Pi (https://www.raspberrypi.org). Note, that the reconstruction of the data is performed on a different computer. The field of view of our system with 10x/0.25NA objective is $2.3 \times 1.6 = 3.7$ mm$^2$ and the spatial resolution is approximately $3\mu m$. With the current camera and Raspberry Pi we can perform time-laps movies with time resolution of several seconds.

**Data Acquisition** Data are acquired approximately 50 $\mu$m out-of-focus by physically moving either the sample or the objective. The out-of-focus distance does not require high precision as the correct defocus value is determined post-acquisition. Note that there is no mechanical movement of the sample or the objective during the time-laps acquisition. The defocus is performed before the start of the measurement and left for the rest of the experiment. The potential slight drift in the axial direction can be compensated in the reconstruction process post-acquisition, however, a rigid construction of our microscope reduces the axial drift and vibrations to negligible levels.

**Data Reconstruction** Our reconstruction algorithm is based on an iterative optimization of Fresnel diffraction model for coherent light [1]. The fact that the illumination is not perfectly coherent is not taken into account in the current algorithm. The reconstruction process optimizes the optical field at the object plane while maintaining a perfect agreement with measurement at the sensor plane. The reconstruction contains regularization terms based on sparsity and total variation constraints [2]. The illumination wavelength, effective pixel size (physical pixel size of the camera divided by the magnification of the system) and the out-of-focus distance are the input parameters. The out-of-focus distance can be determined from the reconstruction performed at different axial positions. A focus determination algorithm can be employed, however, we often use a manual selection. In the time-laps data the defocus is determined only once and used for the reconstruction of the whole movie. The reconstruction of a single image from our 10 Mpixel camera takes approximately 3 minutes on our standard desktop computer (Processor Intel(R) Xenon(R) CPU E3-1240 v5 @ 3.50GHz with 32GB RAM and NVIDIA Quadro K2200 graphic card).

## IMAGE ANALYSIS

**Particle image velocimetry (PIV):** The images were divided into windows of size $28\times28$ $\mu$m$^2$ with 14 $\mu$m overlap. For each window, a velocity value was calculated as follows: for a given time shift (e.g. $\tau$=1 frame), the spatial correlation of each window with its corresponding time-shifted one was computed over 4 consecutive frames and averaged to improve the signal-to-noise ratio. The peak of this average correlation gives an estimate of the displacement $\delta\mathbf{r}(\tau)$. The process was repeated for different values of $\tau$ and the final velocity was deduced from a linear regression of $\delta\mathbf{r}(\tau)$. The final time resolution is 20 min.

## MODEL AND NUMERICAL DETAILS

**Details of the SPV model**: Each cell is characterized by its position $\mathbf{r}_i$ and shape as determined by the Voronoi tessellation of all cell centre positions and an energy is

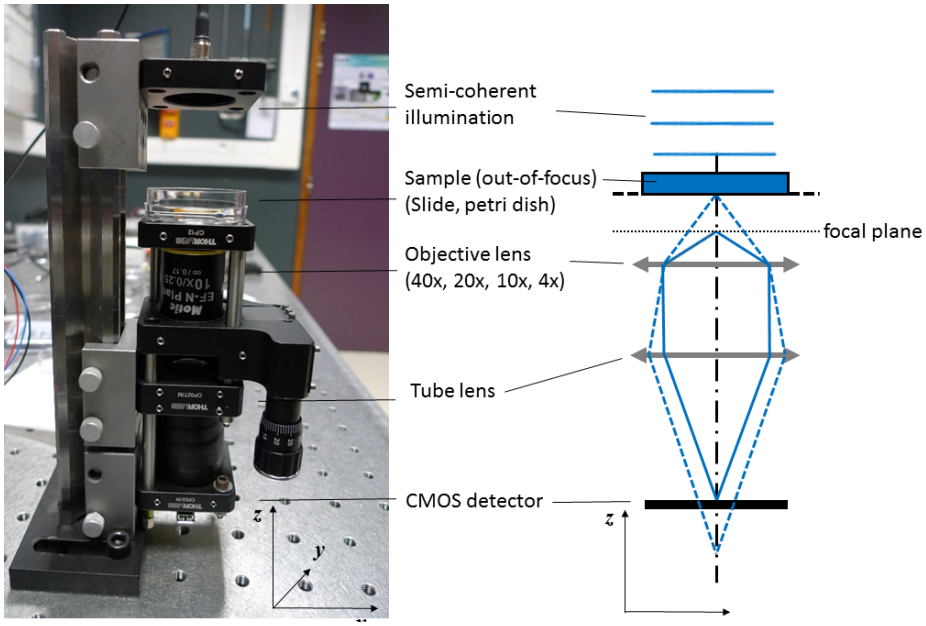


FIG. 1. Setup for defocused imaging is a standard wide-field microscope with semi-coherent illumination.

associated to each configuration of the mesh:

$$E = \sum_{i=1}^{N_{cells}} \frac{K}{2}\left(A_i - A^0\right)^2 + \sum_{i=1}^{N_{cells}} \frac{\Gamma}{2}\left(P_i - P^0\right)^2 \qquad (1)$$

$N_{cells}$ is the total number of cells, $A_i$ and $P_i$ are the area and perimeter of the i-th cell, $K$ and $\Gamma$ are the area and perimeter stiffness respectively, identical for all cells. In the overdamped limit, the equation of motion is:

$$\gamma \frac{\partial \mathbf{r}_i}{\partial t} = f_a \mathbf{n}_i + \mathbf{F}_i + \nu_i(t) \qquad (2)$$

with $\mathbf{F}_i = -\nabla_{\mathbf{r}_i} E$, the force arising from the tissue energy and from a soft-core repulsion introduced to stabilize the simulations (described as a quadratic potential of stiffness $k_{cc}$ with an interaction radius of half the typical distance between cell centres $a_c$) [3]. $\boldsymbol{\nu}_i(t)$ is an uncorrelated stochastic force and $f_a \mathbf{n}_i$ models the self-propulsive force. The dynamics of the cell polarity $\mathbf{n_i}$, described by an angle $\theta_i$, is described in the main text. Cell division can also be included in this model but does not affect the oscillations, as reported in previous works [4, 5].

**Confinement in SPV:** The SAMoS implementation of the SPV [3] (https://github.com/sknepneklab/SAMoS) enables for open flexible boundaries which is convenient to model systems with a small number of cells as it is the case in the confined tissues experiments. In SAMoS, the boundaries are imposed through a special type of particles (called "boundary" particles, and denoted $b$ in the parameters list) that form a "boundary line" that delineates between the tissue and its surrounding (described through a boundary line tension $\lambda_b$ and a bending stiffness $\kappa_b$). The confinement is introduced through a rectangular assembly of immobile particles ("wall" of dimensions ($L_X$ , $L_Y$), denoted $w$ in the parameters) that interact through a repulsive potential with the cells, characterized by a stifness $k_{cw}$ and a characteristic length $a_w$. Note that the boundary particles do not represent cells and hence do not interact with the confining layer of immobile particles (interaction potential $k_{bw} = 0$ between the boundary and the wall).

**Simulation methods and parameters:** We integrate the above model using Brownian dynamics [3]. We first prepare the monolayer configurations and oscillations are then studied in steady state with a fixed number of cells. The layer is initialized with a cell number that is fixed by the system size $N_{init} = (L_X - 2)(L_Y - 1)$, and cells are able to divide during a time $T_{growth}$ at a rate $d = d_0(1 - z/\rho_{max})$ (with $z$ the number of neighbours and $\rho_{max}$ a parameter describing the maximum number of neighbours), to achieve a given cell number density. Division is then turned off and the study focuses on times $t > T_{growth}$. The total duration of simulation $T_{run}$ depends on the time period of oscillations $T$ but is usually $T_{run} > 10T$. The parameters of the vertex model ($A^0$, $P^0$, $K$ and $\Gamma$) are chosen such that the monolayer is in a solid-like state ($p^0 = P^0/\sqrt{A^0} = 2.5$) and cells are mostly hexagonal. Note that keeping very low values of $p^0$ is important in order to avoid to have only square cells due to the rectangular confinement constraints, and to prevent

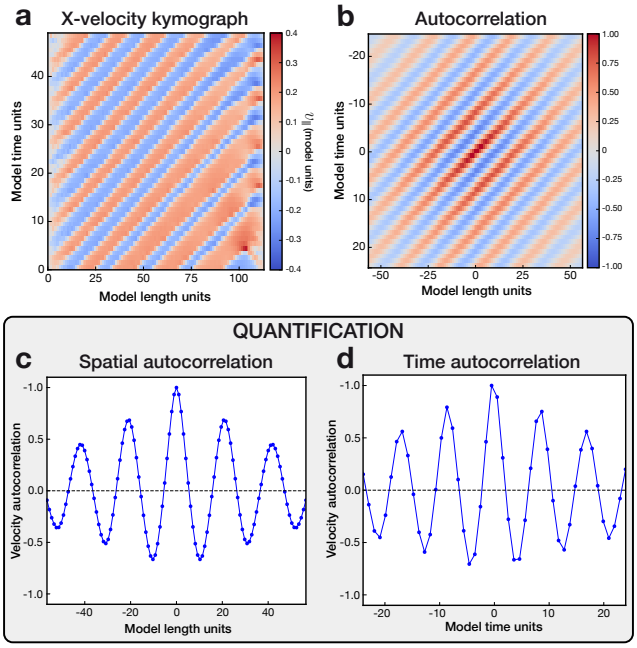


FIG. 2. Illustration of simulation data analysis. **(a)** Kymograph of the x-component of the velocity averaged along the y-direction. **(b)** Autocorrelation of the kymograph. **(c)** Spatial autocorrelation used to extract the wavelength of oscillations. **(d)** Time autocorrelation used to extract the time period of oscillations.

shear flow induced by the boundaries, that prevents the formation of oscillations. In the simulations, the average value of the shape factor $p = \langle P/\sqrt{A} \rangle \simeq 3.85$. The value of self-propulsion velocity is set to $v_0 = 0.2$, but note that changing the value of $v_0$ doesn't affect the features of the oscillations much (it only dictates the amplitude of velocity oscillations). The rotational diffusion coefficient $D_r$ is set to a constant value. The values of all the parameters are listed below.

**Simulation data analysis:** Similarly as for processing experimental data, once in the steady state regime, we average the horizontal component of the centroids velocity along the transverse direction and generate the kymographs of $x$-velocity by displaying this average value as a function of time and space along the horizontal direction $x$. The period and wavelength of oscillations are then extracted from the autocorrelation of the kymograph of x-component of velocity, as shown in Fig. 2.

Fig. 3 shows a typical example of system near the transition between global and multi-nodal oscillations. We define multi-nodal oscillations when, at any time, there are groups of cells moving in opposite directions along the x-axis. From both the kymograph of Fig. 3(a) and its autocorrelation (b), it is clear that this system is at the limit of this regime of multi-nodal oscillation.

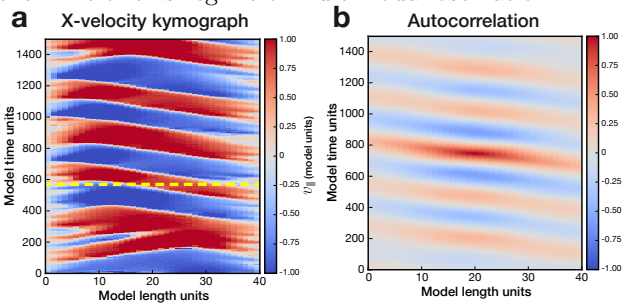


FIG. 3. Illustration of simulation data near the transition between global and multi-nodal oscillations, for $L_X^c(\tau_{al}) = 40$ model length units and $\tau_{al} = 0.5$ model time units. **(a)** Kymograph of the x-component of the velocity exhibiting 2 nodes of velocity at any time, thus corresponding to the onset of the multi-nodal oscillatory mode (as evidenced along the dashed line as an example) **(b)** Autocorrelation of the kymograph.

TABLE I. SPV model, boundary and potential parameters. Raw simulation parameters

| Parameter | Meaning | Value |
|---|---|---|
| $K$ | Area stiffness | 1.0 |
| $\Gamma$ | Perimeter stiffness | 1.0 |
| $A^0$ | Target area | 1.0 |
| $P^0$ | Target perimeter | 2.5 |
| $k_{cc}$ | Repulsive potential strength | 5.0 |
| $a_{cc}$ | Repulsive potential length | 1.0 |
| $k_{cw}$ | Confinement strength (cells) | 5.0 |
| $k_{bw}$ | Confinement strength (boundary) | 0.0 |
| $a_w$ | Confinement potential length | 1.0 |
| $\kappa$ | Boundary bending | 0.1 |
| $\lambda$ | Line tension | 0.1 |

* Mechanical Engineering Department, California State University,Fullerton, California United State
† Giovanni.Cappello@univ-grenoble-alpes.fr
‡ Martial.Balland@univ-grenoble-alpes.fr

[1] J. W. Goodman, *Introduction to Fourier optics* (Roberts and Company Publishers, 2005).
[2] L. Herve, O. Cioni, P. Blandin, F. Navarro, M. Menneteau, T. Bordy, S. Morales, and C. Allier, Biomed. Opt. Express **9**, 5828 (2018).
[3] D. L. Barton, S. Henkes, C. J. Weijer, and R. Sknepnek, PLoS computational biology **13**, e1005569 (2017).
[4] M. Deforet, V. Hakim, H. Yevick, G. Duclos, and P. Silberzan, Nature communications **5**, 3747 (2014).
[5] S. Tlili, E. Gauquelin, B. Li, O. Cardoso, B. Ladoux, H. Delanoë-Ayari, and F. Graner, Royal Society open science **5**, 172421 (2018).

TABLE II. Dynamics parameters

| Parameter | Meaning | Value |
|---|---|---|
| $v_0$ | Self propulsion velocity | 0.2 |
| $\gamma$ | Friction | 1.0 |
| $\gamma_r$ | Orientational friction | 1.0 |
| $\mu$ | Mobility | 1.0 |
| $\mu_r$ | Rotational mobility | 1.0 |
| $\nu_r$ | Rotational noise (rate) | 0.1 |

TABLE III. Preparation (tissue growth) parameters

| Parameter | Meaning | Value |
|---|---|---|
| $d_0$ | Division rate | 0.5 |
| $\rho_{max}$ | Maximum number of neighbours | 10.0 |
| $T_{growth}$ | Growth time | 4000 |

## A.4 Brunel, Benjamin, et al. "Structure and dynamics of multicellular assemblies measured by coherent light scattering." New Journal of Physics 19.7 (2017)

New Journal of Physics
The open access journal at the forefront of physics

Deutsche Physikalische Gesellschaft DPG
IOP Institute of Physics

Published in partnership with: Deutsche Physikalische Gesellschaft and the Institute of Physics

OPEN ACCESS

RECEIVED
7 March 2017

REVISED
13 June 2017

ACCEPTED FOR PUBLICATION
22 June 2017

PUBLISHED
27 July 2017



PAPER

# Structure and dynamics of multicellular assemblies measured by coherent light scattering

**Benjamin Brunel**[1], **Carles Blanch**[2], **Aurélien Gourrier**[1], **Vanni Petrolli**[1], **Antoine Delon**[1], **Jean-François Joanny**[2,3], **Rémi Carminati**[4], **Romain Pierrat**[4,5] **and Giovanni Cappello**[1,5]

[1] Université Grenoble Alpes, Laboratoire Interdisciplinaire de Physique, CNRS, F-38000 Grenoble, France
[2] Institut Curie, CNRS, Université P. et M. Curie, UMR 168, F-75231 Paris, France
[3] ESPCI Paris, PSL Research University, 10 rue Vauquelin, F-75005 Paris, France
[4] ESPCI Paris, PSL Research University, CNRS, Institut Langevin, 1 rue Jussieu, F-75005 Paris, France
[5] Authors to whom any correspondence should be addressed. Theory: Romain Pierrat and experiments: Giovanni Cappello .

**E-mail:** romain.pierrat@espci.fr **and** giovanni.cappello@univ-grenoble-alpes.fr

**Keywords:** dynamic light scattering, multicellular structures, coherent optics

## Abstract

Determining the structure and the internal dynamics of tissues is essential to understand their functional organization. Microscopy allows for monitoring positions and trajectories of every single cell. Those data are useful to extract statistical observables, such as intercellular distance, tissue symmetry and anisotropy, and cell motility. However, this procedure requires a large and supervised computational effort. In addition, due to the large cross-section of cells, the light scattering limits the use of microscopy to relatively thin samples. As an alternative approach, we propose to take advantage of light scattering and to analyze the dynamical diffraction pattern produced by a living tissue illuminated with coherent light. In this article, we illustrate with a few examples that supra-cellular structures produce an exploitable diffraction signal. From the diffraction signal, we deduce the mean distance between cells, the anisotropy of the supra-cellular organization and, from its fluctuations, the mean speed of moving cells. This easy to implement technique considerably reduces analysis time, allowing real time monitoring.

## 1. Introduction

In this article, we describe a non-imaging approach to investigate the structure and dynamics of living multicellular structures. The proposed method is based on the analysis of the dynamic speckle pattern produced by a set of cells illuminated with coherent light.

Determining the structure and the internal dynamics of tissues is essential to understand their functional organization. In fact many of their features, such as symmetry and topology, cannot be inferred from those of the composing cells [1]. Conversely, long range self-organization also emerges from cell division, migration and death [2]. Video microscopy allows to monitor such complex cascade of events in great details and the analysis of the acquired time sequence of images provides accurate measures of position, shape and trajectory of each cell inside the tissue, from birth to death [3]. Nevertheless, in most instances, the net result of such analytical procedures is to reduce those large data to only a few statistical observables, such as the mean cell-to-cell distance, the local/global symmetry or anisotropy of the tissue and the crawling speed of the cells or their diffusion coefficient. Here, we propose to directly measure these observables by analyzing the dynamical speckle pattern produced by a living tissue illuminated with a collimated laser beam. The drawback of this self-averaging method is to lose the cell-to-cell heterogeneity, which might be crucial in certain circumstances.

Light, x-ray and neuton scattering are long-time known and widely used tools to investigate microscopic to nanoscopic structures [4–6]. In biology, light scattering has been used to measure single cell size or nucleus size *in vitro* [7, 8] and more recently *in vivo* [9]. Light scattering is not limited to stucture identification and many light scattering-based methods have emerged in biology [10]. One of them is speckle analysis or dynamic light

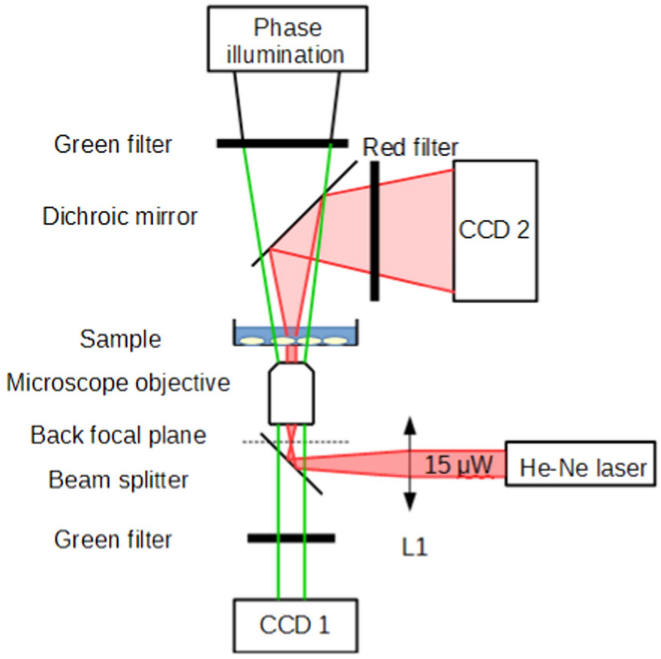


**Figure 1.** Experimental setup.

scattering (DLS), which was already well-established in soft matter [11–13]. In the multiple scattering regime, it has been used for functional imaging such as the measure of brain activity [14–16]. While DLS has also been applied to characterize internal cells dynamics [17–19] or cellular suspensions [20], its use for the investigation of multicellular structures remains very limited [21]. This is mainly due to the fact that the analysis can be performed by directly visualizing the cells with classical microscopy, while the interpretation of the speckle pattern in reciprocal space is, in principle, a non- trivial task that requires solving an inverse problem through modeling and computational efforts. Nevertheless, we have several reasons to believe that this approach is extremely promising to investigate tissue dynamics:

(i) The large scattering produced by cells, which severely limits the use of microscopy in case of thick samples, intrinsically carries structural information that can be analyzed by DLS and, thus, becomes an advantage.

(ii) Because of the intrinsic scattering contrast in cells, this approach does not require preliminary staining. With no constraints imposed by the fluorescent dyes, the illumination wavelength can be tuned to maximize the penetration depth (near infrared) in 3D samples, whose thickness is limited by light scattering. This also makes the technique suitable to investigate primary living tissues.

(iii) Speckle analysis inherently averages the statistical observable over the whole cell population, which size is determined by the illumination area (1 $\mu$m–1 mm).

(iv) As multicellular structures scatter strongly even with low illumination ($<$100 nW/cell), DLS allows fast and long acquisitions with reduced photo-damage. On the other hand, one could also increase the illumination power to image samples that strongly absorb light.

In this article, we propose several examples illustrating how to extract the structural and dynamic features af a multicellular ensemble, from time resolved speckle patterns.

## 2. Methods

### 2.1. Experimental setup

The setup bears some similarities to earlier one designed by *Suissa et al* [17]. In order to combine phase contrast imaging and speckle analysis, the experimental setup was based on an inverted Zeiss Axiover 100 microscope (figure 1). The microscope was equipped with a phase-contrast condenser, a 10$\times$ objective (Zeiss EC Plan-Neofluar, N.A. 0.3) and a charge-coupled device camera (CCD1; Allied Vision Guppy). To generate a speckle pattern, the sample was illuminated using an attenuated (2.0 ND; Thor Labs) He–Ne laser (Uniphase 1101,

1.5 mW, 633 nm) focused on the back focal plane of the objective using an achromatic lens (L1: $f = +100$). In this way, we illuminated the sample with a Gaussian beam, with a divergence of $\sim$0.01 rad and a width on the sample of about 80 $\mu$m (FWHM). The speckle pattern was collected on a second charge-coupled device camera (CCD2; Allied Vision Pike F 046B) positioned as close as possible above the sample (sample to detector distance : 77.7 mm). At this position, the CCD2 camera collected the scattered light for angles up to 7°, corresponding to $q < 1.2\ \mu\text{m}^{-1}$, with an angular resolution of 0.007° (0.001 $\mu\text{m}^{-1}$) per pixel. Angles inferior to 0.3° ($q < 0.05\ \mu\text{m}^{-1}$) were also inaccessible because of the laser divergence. Angular calibration was perfomed using an diffraction grating. To combine phase-contrast imaging and speckle analysis, we used two different wavelengths. We added a monochromatic filter (550 nm) above the condenser and separated the two optical paths with a beam splitter and a dichroic mirror (700–900 nm pellicle beam splitter; ThorLabs).

### 2.2. Cell culture

CT26 (mice colon carcinoma) cells were used and cultured at 37 °C and 5% $CO_2$ in a DMEM (gibco Life technologies) medium supplemented with 10% of fetal bovine serum and 1% Penicillin-Streptomycin (Sigma). Cells were detached from flask using trypsin, resuspended in medium and seeded in a 35 mm VWR round petri dish.

### 2.3. Adherent stripes

In order to artificially arrange cells in lines, we used adherent micropatterned substrates fabricated as described in [22]. Adherent stripes were prepared on 32 mm round glass coverslips, which surface had previously been cleaned and activated with an air plasma cleaner (exposure: 5 min at 0.2 mbar). To create non-adherent surfaces, the coverslips were coated with a 0.1 mg $\text{ml}^{-1}$ pLL-PEG solution in 10 mM HEPES buffer at pH 7.4 (incubation time 30 min). Then, to create the patterns (local degradation of the pLL-PEG coating) the coverslips were exposed to UV light (190 nm) through a photolithography mask (chromium on quartz) with the appropriate pattern geometry for 5 min at 6 mW $\text{cm}^{-2}$. The patterned coverslips were eventually incubated for 30 min in a ECM protein solution (20 $\mu$g $\text{ml}^{-1}$ fibronectin, 20 $\mu$g $\text{ml}^{-1}$ fluorescently labeled fibrinogen in 100 mM sodium bicarbonate). Proteins only adsorb on the pLL-PEG free regions thus promoting selective cell adhesion. The patterned coverslips were shortly stored in PBS buffer at 4 °C.

### 2.4. DLS and tracking

In order to measure the intensity-intensity autocorrelation function, frames were acquired every 20 s over a period of at least 90 min. For isotropic samples (2D), only the absolute value of the scattering vector is relevant, thus correlation functions were averaged over pixels located in a ring corresponding to a given $q$ value. The characteristic size of speckles on the CCD was about 650 pixels, so that $q$-rings contained between 230 (inner ring) and 890 (outer ring) speckles. For 1D sample, correlation functions were averaged over $20 \times 20$ pixels squares, containing approximately 3 speckles of 120 pixels area. Then for a given $q$ value in a direction, results located in a rectangle centered on the direction axis (60 pixels along the direction, 40 pixels perpendicularly) were averaged. We limited our analysis to $q > 0.1\ \mu\text{m}^{-1}$ because the laser beam saturates the CCD. If readers are interested in ultralow angles, we recommend them to reffer to [23]. To assess results obtained by DLS, we manually tracked cell motion, by clicking on their nuclei on each frame of the movie to get the trajectory [$x(t)$, $y(t)$]. Then, the instantaneous speed is computed for each cell from its trajectory and averaged over the whole set of trajectories.

### 2.5. Simulations

In addition to experiments, numerical simulations of the multicellular system were performed. We used a simple run and tumble-like model to capture the motion of individual cells in 2D environments. We ignored the internal structure of cells, modeling them as point-like objects, and avoided physical interactions between them using a dilute approximation. Hence our individual particles were allowed to lie in two states: either motile or quiescent. In the first state, the speed $v$ followed a narrow Gaussian distribution with mean value $\bar{v}$ and variance $\sigma_v^2 \ll \bar{v}^2$. The direction of motion was also defined as a random variable following a uniform distribution. The transitions between states were represented by two independent rates, namely $k_{\text{on}}$ (switching rate between the non-motile to the motile state) and $k_{\text{off}}$ (switching rate from motile to non-motile state). As a result the typical trajectories of those particles were a stochastic alternation of runs and pauses with a short time-scale ballistic motion and a long-time scale diffusive behavior. Unless stated otherwise, the set of parameters was: $k_{\text{on}} = 0.3\ \text{h}^{-1}$, $k_{\text{off}} = 0.2\ \text{h}^{-1}$, $\bar{v} = 10\ \mu\text{m h}^{-1}$ and $\sigma_v = 5\ \mu\text{m h}^{-1}$. The typical observation time was in the order of one hour, so that the dynamics was expected to be confined in the short time-scale regime.

### 2.6. Speckle computation

From cells dynamics simulations, the time-dependent speckle correlation was computed and compared with experimental data. Since the evolution time of the cellular structures is slow compared to the Thouless time (i.e. the light diffusion time through the system), each speckle was computed from the configuration of cells obtained at fixed time $t$. The autocorrelation of those speckles were then computed to calculate the time-dependent intensity correlation function. Since the cells dynamics involves large time scales compared to $2\pi/\omega$, with $\omega$ the frequency of the incident laser beam, there was a full decoupling between $t$ (the time evolution of the structure) and $\omega$.

To compute a speckle pattern, we first had to solve Maxwell's equations for an ensemble of cells. For that purpose, we chose to approximate each cell by a point scatterer in the electric-dipole limit. Strictly speaking, this approximation is valid under two conditions: the typical size of a cell is small compared to (1) the wavelength $\lambda$ and (2) the average distance between two different cells. Since the samples used in the experiments did not meet these requirements, the computation of speckle patterns could not be used for precise quantifications. Nevertheless, this procedure is well-suited to retrieve general trends such as the decorrelation time as a function of the scattering vector. The optical response of a point dipole scatterer was described by its polarizability $\alpha(\omega)$, which links the dipole moment $\mathbf{p}(\omega, t)$ created inside the scatterer to the exciting electric field $\mathbf{E}^{(\mathrm{exc})}(\omega, t)$ through the relation:

$$\mathbf{p}(\omega, t) = \epsilon_0 \alpha(\omega) \mathbf{E}^{(\mathrm{exc})}(\omega, t), \tag{1}$$

where $\epsilon_0$ is the vacuum permittivity. The polarizability was computed using the scattering cross-section given by

$$\sigma_{\mathrm{s}}(\omega) = \frac{k_0^4}{6\pi} |\alpha(\omega)|^2, \tag{2}$$

where $k_0 = 2\pi/\lambda$ is the incident wavevector and $\lambda$ the wavelength. $\alpha(\omega)$ is a complex number and a second equation is needed for its full determination. Due to energy conservation during the scattering process, the scattering cross-section must equal the extinction cross section (assuming a non-absorbing medium). This leads to

$$\sigma_{\mathrm{e}}(\omega) = k_0 \,\mathrm{Im}\, \alpha(\omega) = \sigma_{\mathrm{s}}(\omega). \tag{3}$$

Using equations (2) and (3) we obtained the polarizability:

$$\alpha(\omega) = \frac{-6\pi}{k_0^3} \left[ \sqrt{\frac{6\pi}{k_0^2 \sigma_s(\omega)} - 1} + \mathrm{i} \right]^{-1}. \tag{4}$$

In principle, $\sigma_{\mathrm{s}}$ and $\sigma_{\mathrm{e}}$ can be determined from the geometry of the cell and its refractive index. Since this last quantity was not easily accessible experimentally, we chose to consider the scattering mean-free path instead, defined as

$$\ell_{\mathrm{s}}(\omega) = \frac{1}{\rho \sigma_{\mathrm{s}}(\omega)}, \tag{5}$$

where $\rho$ is the density of scatterers. In the following, we consider a system composed of cells on a 2D surface, which is expected to fall into a single-scattering regime. For that reason, we chose to consider a large scattering mean-free path, i.e. $k_0 \ell_{\mathrm{s}} = 1 \times 10^8$. We also assumed a density $\rho = (N/L^2)^{(3/2)}$ (2D density extrapolated in 3D), where $N \sim 100$ is the number of cells and $L = 868$ $\mu$m the size of the system. Once the polarizability known, the coupled dipoles method was used to solve Maxwell's equations. It consisted in solving a linear set of coupled equations involving the exciting field $\mathbf{E}_j^{(\mathrm{exc})}(\omega, t)$ on scatterer $j$ lying at position $\mathbf{r}_j$. As reported in [24]:

$$\mathbf{E}_j^{(\mathrm{exc})}(\omega, t) = \mathbf{E}_{\mathrm{in}}(\mathbf{r}_j, \omega) + k_0^2 \alpha(\omega) \sum_{l=1, l\neq j}^{N} \mathbf{G}_0(\mathbf{r}_j(t) - \mathbf{r}_l(t), \omega) \mathbf{E}_l^{(\mathrm{exc})}(\omega, t), \tag{6}$$

where $\mathbf{G}_0$ is the Green tensor in vacuum linking the electric field at any position in vacuum to a source dipole through the relation

$$\mathbf{E}(\mathbf{r}, \omega) = \mu_0 \omega^2 \mathbf{G}_0(\mathbf{r} - \mathbf{r}_0, \omega) \mathbf{p}_0(\omega), \tag{7}$$

where

$$\mathbf{G}_0(\mathbf{r} - \mathbf{r}_0, \omega) = \left[ \mathbf{I} - \frac{\boldsymbol{\nabla}_{\mathrm{r}} \otimes \boldsymbol{\nabla}_{\mathrm{r}}}{k_0^2} \right] \frac{\exp[ik_0 |\mathbf{r} - \mathbf{r}_0|]}{4\pi |\mathbf{r} - \mathbf{r}_0|}, \tag{8}$$

$\otimes$ denoting the tensor product operator. To be consistent with experimental conditions, the incident field $\mathbf{E}_{\mathrm{in}}(\mathbf{r}, \omega)$ was chosen to be a gaussian beam of waist $w = 69$ $\mu$m and wavevector $\mathbf{k}_{\mathrm{in}}$. Once the exciting field on each scatterer was known, the field at any position inside or outside the system was computed using a relation similar to (6):

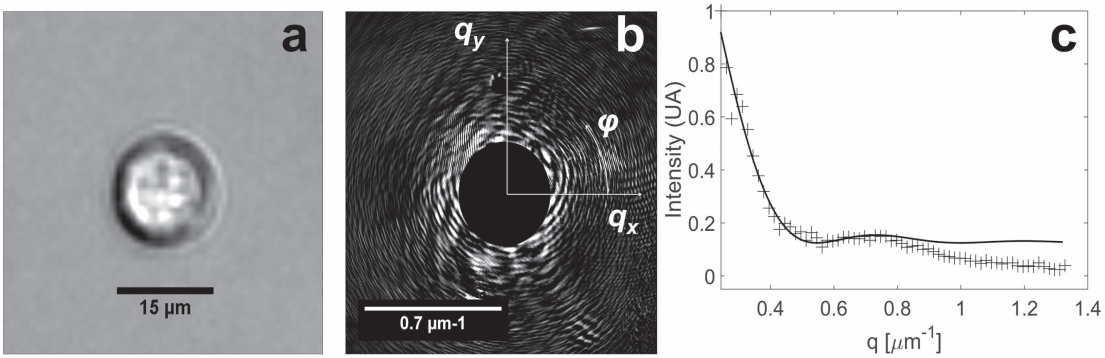


**Figure 2.** Single cell analysis. Bright field image of a rounding cell (a), and the corresponding speckle pattern (b). (c) Speckle intensity integrated over the azimuthal angle $\chi$ (crosses) is used to determine the cell diameter from the speckle pattern: $d = 14.0 \pm 0.6\ \mu$m.

$$\mathbf{E}(\mathbf{r}, \omega, t) = \mathbf{E}_{\text{in}}(\mathbf{r}, \omega) + k_0^2 \alpha(\omega) \sum_{l=1}^{N} \mathbf{G}_0(\mathbf{r}(t) - \mathbf{r}_l(t), \omega) \mathbf{E}_l^{(\text{exc})}(\omega, t). \tag{9}$$

Considering an observation point $\mathbf{r}$ in the far field (i.e. such that $r \gg \lambda$), the scattered field $\mathbf{E}_{\text{sca}} = \mathbf{E} - \mathbf{E}_{\text{in}}$ was simplified into

$$\mathbf{E}_{\text{sca}}(\mathbf{r}, \omega, t) = \frac{A}{k_0 r} \exp[ik_0 r] \mathbf{E}_{\text{sca}}(\mathbf{q}, \omega, t), \tag{10}$$

where $A$ is a numerical constant, $\mathbf{q} = \mathbf{k}_{\text{out}} - \mathbf{k}_{\text{in}}$ is the scattering wavevector and $\mathbf{k}_{\text{out}} = k_0 \mathbf{r}/r$ the observation wavevector. Defining the scattered intensity by

$$I_{\text{sca}}(\mathbf{q}, \omega, t) = |\mathbf{E}_{\text{sca}}(\mathbf{q}, \omega, t)|^2 \tag{11}$$

we finally obtain the time-dependent intensity autocorrelation function

$$C(\mathbf{q}, \tau, \omega) = \frac{\langle I_{\text{sca}}(\mathbf{q}, \omega, t) I_{\text{sca}}(\mathbf{q}, \omega, t + \tau) \rangle}{\langle I_{\text{sca}}(\mathbf{q}, \omega, t) \rangle \langle I_{\text{sca}}(\mathbf{q}, \omega, t + \tau) \rangle} - 1, \tag{12}$$

where the brackets $\langle \ldots \rangle$ denote the statistical average over all configurations of the cellular structure. This average was typically performed using 10 000 configurations generated using a run and tumble-like model. Assuming a statistical steady-state regime, $C$ only depends on $\tau$ and not on $t$. It is important to note that, $I_{\text{sca}} = I$ and $\mathbf{E}_{\text{sca}} = \mathbf{E}$, with the exception of the forward direction. Thus in the following, $I$ and $\mathbf{E}$ are used to denote the scattered intensity and field respectively. For the sake of simplicity, the $\omega$-dependence is also dropped.

## 3. Results

### 3.1. Speckle intensity

*3.1.1. Isolated cell*

We first observed the speckle pattern produced by a single rounding cell, which bright field image is shown in figure 2(a). The cell is illuminated with a vertical laser beam of wavevector $\mathbf{k}_{\text{in}}$, which modulus is $2\pi/\lambda$. The light scattered by the cell is collected in the forward direction by the CCD2 camera (figure 2(b)). Each pixel of the CCD2 camera corresponds to a different scattering angle and, thus, to a different wavevector $\mathbf{k}_{\text{out}}$. In this setup, the incident beam is superimposed on the low-angle scattering region of the speckle pattern. Due to saturation effects, this part was suppressed by applying a virtual beamstop at the center of the detector (black disk in the center of figure 2(b)). Background light is substracted and vignetting effects are corrected [25]. We record the speckle pattern $I(\mathbf{q})$, $\mathbf{q} = \mathbf{k}_{\text{out}} - \mathbf{k}_{\text{in}}$ being the scattering wavevector.

As the rounding cell has spherical symmetry, we integrate the speckle pattern $I(\mathbf{q})$ over the azimuthal angle

$$I(q) = \int_0^{2\pi} I(q, \chi) \mathrm{d}\chi, \tag{13}$$

where $q$ is the magnitude of the vector $\mathbf{q}$ and $\chi$ the azimuthal angle. The radial intensity profile $I(q)$ is plotted in figure 2(c) (crosses) and compared to the intensity profile expected for a scattering disk of diameter $d$:

$$\tilde{I}(q) \propto \left| J_1\left(\frac{qd}{2}\right) \Big/ \left(\frac{qd}{2}\right) \right|^2, \tag{14}$$

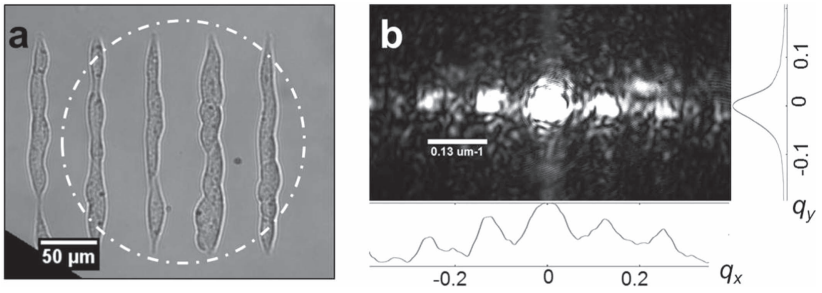


**Figure 3.** 1D structure. (a) Bright field image of cells deposited on adherent stripes of 200 $\mu$m and (b) its corresponding measured speckle pattern. The dashed circle shows the approximate laser beam width. The interference fringes are separated by $\Delta q = 0.13\ \mu\text{m}^{-1}$ along $q_x$ corresponding to a distance of $\sim$50 $\mu$m between cell stripes. No interference pattern was observed along the $q_y$ direction, as the laser spot is of the same order of magnitude of the stripes length.

where $J_1$ is the Bessel function of order one. The best fit between the measured intensity $I(q)$ and the expected one $\tilde{I}(q)$ is obtained for a cell diameter $d = 14.0 \pm 0.6\ \mu$m. This value is in good agreement with the cell diameter measured in figure 2(a), which is also $15 \pm 1\ \mu$m.

At wavevectors larger than $1\ \mu\text{m}^{-1}$, which correspond to distances smaller than 6.28 $\mu$m in direct space, the speckle pattern carries information, mostly related to the intracellular structure. As we aim at characterizing multicellular structures, collecting speckle patterns at $q < 1.2\ \mu\text{m}^{-1}$ (set up limitation) is enough.

*3.1.2. Cell on 1D lines*

To create a simple and controlled multicellular structure, we deposited around 30 cells on adherent stripes prepared as stated in section 2. The stripes were 200 $\mu$m long, 10 $\mu$m wide and 50 $\mu$m apart from each other. The width was adjusted to accommodate at most one cell in the transversal direction and to produce a 1D cell lines. Figure 3(a) shows a bright field image of the aligned cells, and figure 3(b) the corresponding speckle pattern. The speckle pattern exhibits clear interference fringes along the $q_x$ direction, separated by $\Delta q = 0.130 \pm 0.005\ \mu\text{m}^{-1}$. This length corresponds to a distance of $48 \pm 2\ \mu$m in direct space, which matches the spacing between adherent stripes, within the experimental error. Interestingly, there are no interference fringes along the $q_y$ direction. This is due to the fact that the laser spot has a width of $\sim$200 $\mu$m (see dashed circle in figure 3(a)) and therefore only illuminates a single row of stripes.

*3.1.3. Sparse cells on a 2D surface*

When cells are homogeneously deposited on a surface (figure 4(a)), the speckle pattern looks significantly different as compared to those in previous examples. The anisotropy induced by the stripes vanishes and, compared to that of a single cell, the speckle is characterized by an increased granularity. On the one hand, the typical grain size scales with the inverse of the laser beam width [26]. In this case, we chose to remove lenses to illuminate the sample with the full widht of the laser (FWHM about 260 $\mu$m) and thus probing a larger cell population. On the other hand, this granularity depends on the optical details of the illuminated area, but the overall decay is linked to the statistical properties of the multicellular structure. As we limit the acquisition to small wavevectors, filtering out the intracellular details, the cells appear as uniform scattering objects in first approximation. In the single scattering regime, the speckle intensity is related to the autocorrelation function of the surface cell density $P(\mathbf{r})$ through the equation

$$\langle P(\mathbf{r}')P(\mathbf{r}+\mathbf{r}')\rangle_{\mathbf{r}'} \propto \int I(\mathbf{q})\exp[-i\mathbf{q}\cdot\mathbf{r}]\,d\mathbf{q}. \tag{15}$$

In figure 4(c) we report the azimuthally averaged speckle $I(q)$ together with the corresponding density–density autocorrelation function $P(\mathbf{r})$ (figure 4(d)). The incident beam ($q < 0.1\ \mu\text{m}^{-1}$) is cut to not impair the autocorrelation function. When cells are sparse there is no spatial correlation between scatterers, but as the cell layer becomes confluent a typical cell-to-cell distance appears. Near the confluence point, the autocorrelation function exhibits a maximum corresponding to the mean distance between first neighbors. In the example shown in figure 4, this maximum happens at $r = 25 \pm 5\ \mu$m which is in good agreement with the correlation distances $r = 22.6\ \mu$m measured from the bright field image (continuous line).

### 3.2. Speckle fluctuation and cell motility

The cell movements inside the sample modifies the speckle pattern during the time sequence of acquisition. Thus, the details of the speckle dynamics depend on the trajectory of each cell. While the loss of phase information does not allow recovering single trajectories, the speckle intensity fluctuations are statistically

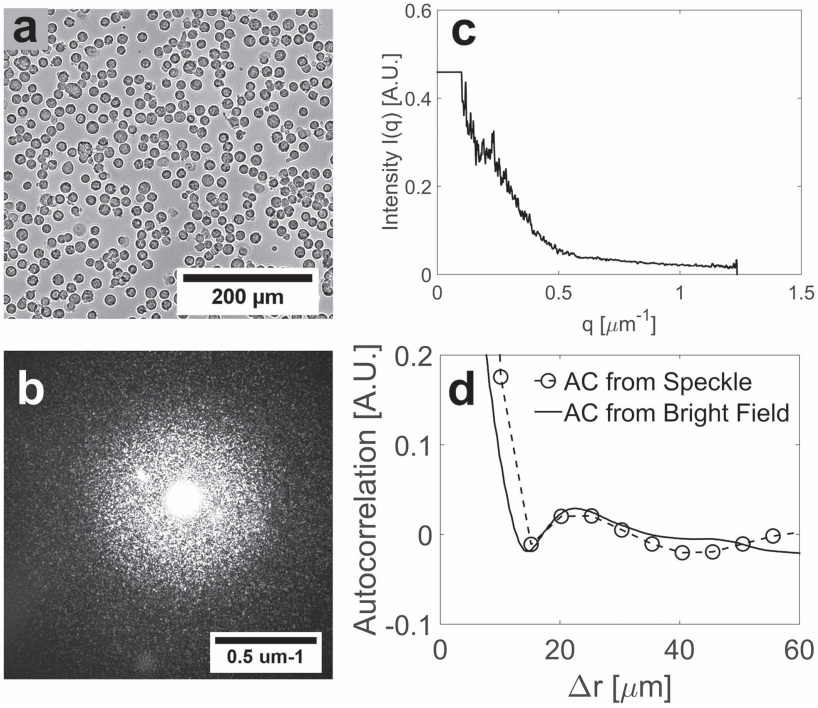


**Figure 4.** Cell monolayer. Here cells have been deposited 10 min before imaging, thus they are not spread and adherent to the surface yet. (a) Bright field image. (b) Speckle pattern. (c) Structure factor and (d) associated cell–cell autocorrelation function. In (d) we represent the cell-to-cell distance correlation function directly computed from the bright field image (full line) and, by inverse Fourier transform, from the speckle pattern (empty circle and dashed line). Both exhibit a maximum around 23 $\mu$m, corresponding to the mean distance between neighboring cells.

related to the kinetic properties of the multicellular ensembles. In this section, we derive an analytical expression to describe the time-dependent intensity correlation function under the assumptions that (1) the Siegert relation is valid and that (2) the system operates in the single-scattering regime. We also assume that the scalar approximation is valid and that the incident laser beam can be approximated by a plane-wave (valid in case of large waist).

For a fully developed speckle pattern, the electric field is statistically gaussian (which corresponds to a Rayleigh statistics for the intensity distribution) and the intensity–intensity correlation function factorizes into the square of the field–field correlation function $g_1(q, \tau)$, a result known as the Siegert relation. We have numerically checked that for all sets of parameters considered in this study (velocities, directions and times), the intensity statistics is exponential (Rayleigh distribution), only very slight deviations being observable. This proves the validity of the Siegert relation here. We end up with [27]

$$C(\mathbf{q}, \tau) = \frac{\langle I(\mathbf{q}, t) I(\mathbf{q}, t+\tau)\rangle}{\langle I(\mathbf{q}, t)\rangle \langle I(\mathbf{q}, t+\tau)\rangle} - 1$$
$$= \beta \left| \frac{\langle E(\mathbf{q}, t) E^*(\mathbf{q}, t+\tau)\rangle}{\langle E(\mathbf{q}, t)^2\rangle} \right|^2 = \beta |g_1(\mathbf{q}, \tau)|^2, \quad (16)$$

where $\beta$ is the coherence factor of the experiment, which can be approximated to 1 as pixels are way smaller than speckles. In the single-scattering regime, the scattered electric field from an ensemble of $N$ cells located at positions $\mathbf{r}_j(t)$ is a superposition of spherical waves with a resulting amplitude:

$$E(\mathbf{q}, t) \propto \sum_{j=1}^{N} e^{-i\mathbf{q}\cdot\mathbf{r}_j(t)}. \quad (17)$$

This can be easily obtained from (6), (9) and (10) removing the terms relative to multiple scattering. Thus, combining (16) and (17), we obtain

$$C(\mathbf{q}, \tau) = \left| \frac{S(\mathbf{q}, \tau)}{S(\mathbf{q}, 0)} \right|^2, \quad (18)$$

where

$$S(\mathbf{q}, \tau) \propto \left\langle \sum_{j,k} \mathrm{e}^{-\mathrm{i}\mathbf{q}\cdot[\mathbf{r}_j(t+\tau)-\mathbf{r}_k(t)]} \right\rangle. \tag{19}$$

It is worthwhile noting that the last term is proportional to the dynamical structure factor of the system. The displacement of $j$th cell over the elapsed time $\tau$ is defined as follows $\Delta\mathbf{r}_j(t+\tau) = \mathbf{r}_j(t+\tau) - \mathbf{r}_j(t)$. Thus assuming that all cells are identical and that the initial position $\mathbf{r}_j(t)$ of cells and their displacements $\Delta\mathbf{r}_j(t+\tau)$ are uncorrelated quantities, (19) turns into

$$S(\mathbf{q}, \tau) = S(\mathbf{q}, 0)\langle \mathrm{e}^{-\mathrm{i}\mathbf{q}\cdot\Delta\mathbf{r}(t+\tau)}\rangle \tag{20}$$

and (21) can be simplified to

$$C(\mathbf{q}, \tau) = |\langle \mathrm{e}^{-\mathrm{i}\mathbf{q}\cdot\Delta\mathbf{r}(t+\tau)}\rangle|^2. \tag{21}$$

The details of the dynamical behavior of cells is reflected in the intensity autocorrelation function. For instance particles moving in a persistent manner with an average speed $\bar{v}$ have net displacement $\Delta\mathbf{r}(\tau) = \mathbf{v}\tau$. Thereby the characteristic correlation time $\tau_{1/2}$, chosen to be the width at half maximum of the correlation function, scales as $\tau_{1/2} \propto 1/\bar{v}q$ (see figure 5(b), (d)). In the case of immobile particles, the displacements $\Delta\mathbf{r}(\tau)$ are null rendering to a correlation time scale $\tau_{1/2}$ independent of the wavenumber $q$ (see figure 5(d)). Alternatively, in the case of an ensemble of Brownian particles with a diffusion coefficient $D$, the mean squared displacement is $\langle\Delta r^2(\tau)\rangle = 2D\tau$. Thus the characteristic correlation time $\tau_{1/2}$ scales as $\tau_{1/2} \propto 1/Dq^2$. Hence, in three cases a power law relationship relates the correlation time to the scattering wavevector $\tau_{1/2} \propto q^{-n}$ with $n$ equals to 0, 1 or 2 accordingly. These three scenarios may coexist in the same multicellular ensemble at different time or length scales. In the following we propose two examples to illustrate this approach.

*3.2.1. Cells deposited on the surface*

We monitor the speckle pattern of a layer of cells uniformly spread on a surface (see figure 4(a)). Four petri dishes were seeded at different concentrations (2 ml with $150 \times 10^3$, $300 \times 10^3$, $600 \times 10^3$ and $10^6$ cells respectively) and incubated for 24 h. After incubation, we measure the confluence degree as the percentage of the surface covered by cells.

As we are only interested in the decorrelation time, we normalize $C(\mathbf{q}, \tau)$ to 1 at the origin. The less confluent samples are reported in the inset of figure 5(a) for four different values of the scattering wavevector $q$. The set of measured correlation functions collapse into a single master curve after scaling the time $\tau$ by the factor $q^{-1}$ (see figure 5(a)), which means that the characteristic correlation time scales as $\tau_{1/2} \propto 1/q$, thus cells moves in a persistent manner. This may come as a surprise as we do not see this ballistic motion when watching cells moving, but rather a run and tumble motion. The reason is that intensity decorrelates within times (from 100 to 300 s) shorter than the average running time (1000 s). In this short time regime, displacements are dominated by ballistic runs. The power law is also apparent in figure 5(b), where the $q$-dependance of $\tau_{1/2}$ are reported for the different degrees of confluence. For values of $q$ within the range $0.1\ \mu\mathrm{m}^{-1} < q < 1.1\ \mu\mathrm{m}^{-1}$, we find a power law with an exponent close to $-1$, for any degree of confluency (lines). This means that cells move ballistically over these timescales, regardless of the local cell density.

By fitting the curve $\tau_{1/2} = \alpha/q$, we estimate the mean velocity of cells as $\bar{v} = 1/\alpha$, as explained in the previous section. Compared to the average cell speed obtained from single cell tracking, relative values are acurate (<5%). However absolute values are systematically underestimated by 18% (figure 5(c)) because the exact pre-factor is unknown. Figure 5(b) shows that $\bar{v}$ depends on the cell density so that the denser the layer, the smaller the average cell's speed. This effect may either indicate that the internal friction of the cell layer increases with density, or that collisions between cells occur more often, slowing them down.

In order to obtain the exact pre-factor, we build from equation (21) using the ballistic regime property $\Delta\mathbf{r}(\tau) = \mathbf{v}\tau$. Notice that those displacements are independent of the initial time $t$ and only depend on the elapsed time $\tau$. In the absence of external cues, all directions are equally probable and thus the initial orientation of cells turns into a uniformly distributed random variable. For empirical reasons, the cell speed $v$ will be also treated as an independent random variable obeying an exponential distribution $f(v) = \frac{4}{\bar{v}^2}\mathrm{e}^{-2v/\bar{v}}$ with a mean speed $\bar{v}$. Under these assumptions, the average over all the possible configurations in (21) can be replaced by the average over these internal variables

$$\langle \mathrm{e}^{-\mathrm{i}\mathbf{q}\cdot\Delta\mathbf{r}(\tau)}\rangle = \frac{1}{2\pi}\int_0^{2\pi}\int_0^{\infty} \mathrm{e}^{-\mathrm{i}qv\tau\cos\zeta} f(v)v\,\mathrm{d}v\,\mathrm{d}\zeta, \tag{22}$$

$\zeta$ being the angle between the direction of motion and $\mathbf{q}$ the scattered wavevector. The intensity autocorrelation function of our ensemble of particles can be computed analytically and it reads

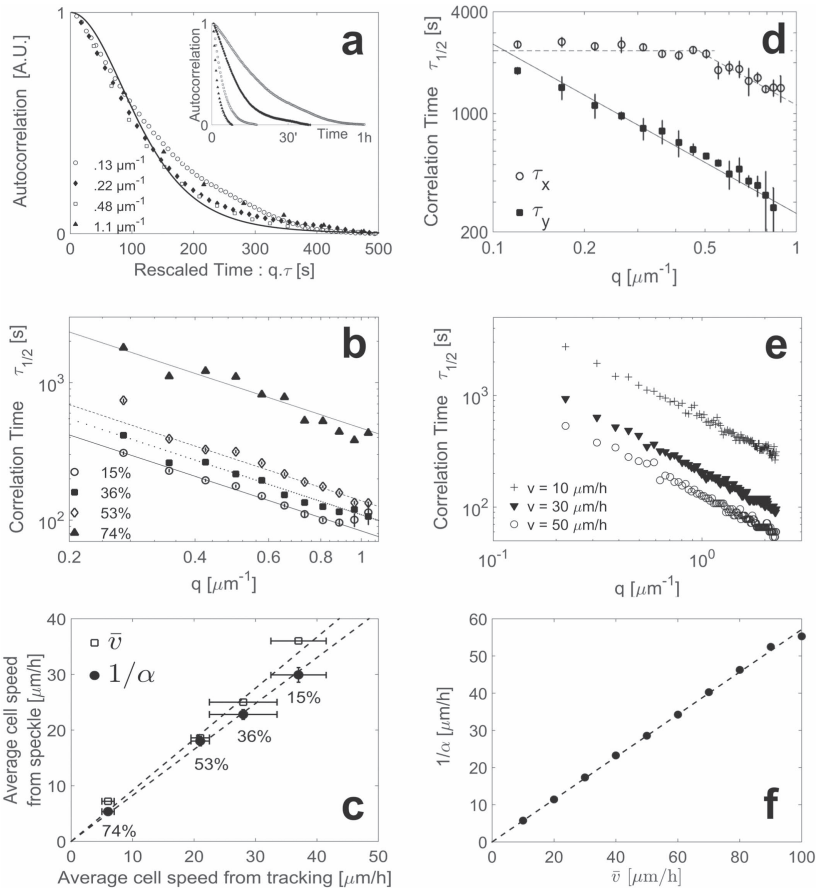


**Figure 5.** Speckle time-correlation function and mean cell velocity. (a) Intensity–intensity autocorrelation functions for different values of $q$, in the case of 2D cellular layer (15% confluency). Renormalizing time ($q.\tau$) from curves in the inset shows the $1/q$ scaling scaling of the correlation timescale. Results are fitted (plain line) with equation (23) ($\bar{v} = 36.0 \pm 0.3$ $\mu$m h$^{-1}$). (b) $\tau_{1/2}$ versus $q$, for 2D cellular layers with increasing confluences (percentage of the surface covered by the cells). The decorrelation time increases with the cell density in the layer. The associated mean speeds are reported in panel (c) (black circles), compared to mean speed measured by tracking mehod. Fitting intensity correlation functions with equation (23) gives better absolue values (white squares). (d) Dynamics of cells patterned on 1D lines (see figure 3). Correlation times computed for increasing $q$, both along the directions perpendicular (empty circles) and parallel (filled squares) to the cell lines. The decorrelation time relative to the motion along the lines is fitted to the function $[q\bar{v}]^{-1}$, which leads to an average cell speed of ($10 \pm 0.5$) $\mu$m h$^{-1}$. The decorrelation time relative to the motion across the lines does not depend of $q$, meaning that the cells almost do not move perpendicularly to the lines. (e) Decorrelation time curves $\tau_{1/2}(q)$ for an ensemble of dipolar scatterers with a run-and-tumble motion. At a constant wavevector, $\tau_{1/2}$ is computed for ensembles of particles moving at different mean velocities $\bar{v}$. The decorrelation time curves are fitted with the function $\tau_{1/2} = \alpha/q$. (f) $\alpha^{-1}$ versus $\bar{v}$ for our ideal system of self-propelled dipolar scatterers. The linear relationship between both suggest that $\alpha \propto v^{-1}$.

$$C(\mathbf{q}, \tau) = |\langle e^{-i\mathbf{q}\cdot\Delta\mathbf{r}(\tau)}\rangle|^2 = \left[1 + \left(\frac{q\bar{v}\tau}{2}\right)^2\right]^{-3}, \tag{23}$$

which is univocally related to a single characteristic time scale of the system $\tau_{1/2} \simeq 1/q\bar{v}$, as expected for ballistic motion. Fitting intensity correlation functions in figure 5(a) using (23), we find $\bar{v} = 36.0 \pm 0.3$ $\mu$m h$^{-1}$. The master curve is in excellent agreement with the analytical expression, meaning that the behavior of our ensemble of cells is compatible with a system of dipole scatterers moving at constant speed with the speed distribution $f(v)$. Using equation (23), the pre-factor is almost corrected (underestimated by 8%) (figure 5(c)). Notice that if a relative measurement or an approximate absolute value is enough, fitting directly $\tau_{1/2}(q)$ has the advantage of beeing free of any modeling efforts or peculiar hypotheses on the ballistic movement.

Those observations are in agreement with the behavior of an ideal system of point dipole scatterers with a run-and-tumble-like dynamics. Accordingly, we computed the time-dependent autocorrelation functions $C(\mathbf{q}, \tau)$ and its width at half maximum $\tau_{1/2}$ with a coupled-dipoles method. They are reported as a function of the wavevector $q$ in figure 5(e). For all analyzed cases, the behavior of $\tau_{1/2}$ follows this of $1/q$ for more than one decade, meaning that our particles move in a ballistic manner over shorter timescales than the tumbling time. Thus, $\tau_{1/2} = \alpha/q$ where $\alpha$ is thought to be inversely proportional to the mean particle's speed $\bar{v}$. In order to validate the generality of this relationship, we computed the coefficient $\alpha$ of the curves $\tau_{1/2}(q)$ for different values of $\bar{v}$. The results displayed in figure 5(f) show the linear dependence between $1/\alpha$ and $\bar{v}$ for velocities between 10 and 100 $\mu$m h$^{-1}$. The slope deviates from 1 as it is a quantity dependent on this specific model.

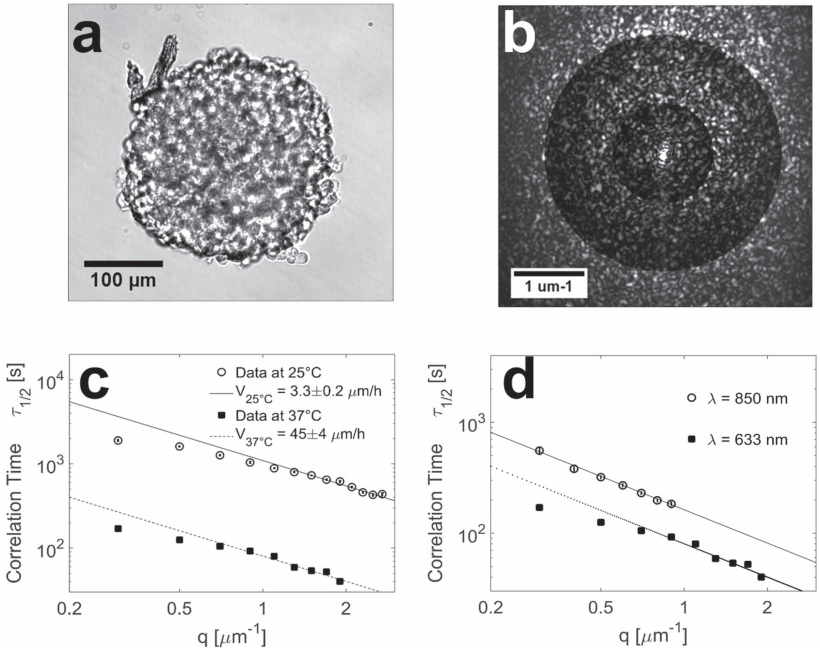


**Figure 6.** Speckle fluctuation analysis on 3D multicellular aggregates. (a) Bright-field image of a spherical aggregate of radius $R \simeq 100\ \mu$m. (b) Speckle pattern generated by the aggregate. To avoid saturation, shorter exposure times are used at small $q$. (c) Cell dynamics in 3D aggregates. Correlation times are computed both at physiological (37 °C) and at low (25 °C) temperature. At 25 °C (empty circles) the mean speed is $\bar{v}_{25°} = 3.3 \pm 0.2\ \mu$m h$^{-1}$. At 37 °C (filled squares) we measure $\bar{v}_{37°} = 45 \pm 4\ \mu$m h$^{-1}$. (d) Comparison between experiments performed in multiple-scattering regime (illumniation wavelength $\lambda = 633$ nm) and in the single-scattering regime ($\lambda = 850$ nm).

*3.2.2. Cells on stripes*

Another interesting example is provided by the experiment illustrated in figure 3. The cells are deposited on adherent lines, which induce a strong anisotropic structural arrangement. The anisotropy found in the speckle pattern (figure 3(b)), is also visible in the dynamic structure factor or, experimentally, in the intensity-intensity autocorrelation function. Plotting $C(\mathbf{q}, \tau)$ as a function of $\mathbf{q}$, we observe two different behaviors along the directions parallel ($q_\parallel$) or perpendicular ($q_\perp$) to the stripes. Along $q_\parallel$ (vertical direction in figure 3), the decorrelation time decreases proportionally to $q_\parallel^{-1}$ (filled squares in figure 5(d)), meaning that cells move directionally along the lines. The theoretical best agreement between the experimental data and the power law $\tau_{1/2} = [q\bar{v}]^{-1}$ is obtained for a mean speed $\bar{v} = (10 \pm 0.5)\ \mu$m h$^{-1}$. On the contrary, along the direction perpendicular to the stripes the correlation time is independent of the scattering wavevector $q_\perp$ (see figure 5(d), empty circles). This indicates that the cells do not move along this direction (horizontal in figure 3) due to the confinement imposed by the adherent stripes. Nevertheless, there is a noticeable decrease of the correlation time at $q_\perp$ larger than 0.55 $\mu$m$^{-1}$. In the real space this corresponds to 11.5 $\mu$, which is very close to the stripes width (10 $\mu$m). This is compatible with a residual motility of the cells along the perpendicular direction, provided that they do not exit the adherent stripes.

*3.2.3. 3D aggregates*

Analysis of speckle fluctuation is specially relevant in three-dimensional multicellular structures, where video microscopy cannot easily measure cell speed. As a proof of concept, we apply the method to multicellular spheroids (figure 6(a)), equation (21) beeing also valid in three dimensions. The speckle pattern produced by the spheroid is shown in figure 6(b). The scattered intensity drops considerably at large $q$. To preserve the signal-to-noise ratio at large $q$ and to avoid saturation at low $q$, the exposure time changes with the scattering angle, (see rings of different intensities in figure 6(b)). In order to modulate cell activity and speed, the experiment is performed at two different temperatures: the physiological 37 °C and 25 °C, where cell activity almost vanishes. Figure 6(c) displays the decorrelation time $\tau_{1/2}(q)$, both for experiments done at 25 °C (empty circles, error bars inside the circles) and at 37 °C (black squares). In both cases, the experimental data scales reasonably well with the inverse of the scattering vector. From figure 6(c) we deduce that the mean speed $\bar{v}$ increases considerably with the temperature. In particular, at 25 °C the best fit between the theoretical curve and the data is obtained for a speed $\bar{v}_{25°} = 3.3 \pm 0.2\ \mu$m h$^{-1}$ (continuous line), while at 37 °C we measure $\bar{v}_{37°} = 45 \pm 4\ \mu$m h$^{-1}$ (dashed line). Due to the presence of multiple-scattering events, this speed is overestimated. As described by Pine *et al* [28], the decorrelation time varies inversely to the number of scattering events. With a wavelength

$\lambda = 633$ nm, the mean free-path of photons $\ell_p \simeq 60\mu$m is four times smaller than the spheroid diameter. Thus, the measurement is semi-quantitative and allows one to compare velocities in the same sample, but under different conditions (e.g. temperature, mechanical stress, confinement, drugs, ...). Multiple scattering also impacts the $q$-dependency of $\tau_{1/2}$ at low $q$, where a deviation from the theoretical curve appears ($q < 0.5\ \mu\text{m}^{-1}$ in figure 6(c)). For an absolute measurement of the cell speed and to avoid the deviation at low $q$, the illumination wavelength $\lambda$ must be tuned to satisfy the single-scattering condition, i.e. a mean free-path of photons comparable to the spheroid size ($\ell_p \geqslant D$). In CT26 spheroids with a diameter of $\sim$250 $\mu$m, this condition is satisfied for $\lambda = 850$ nm, at which $\ell_p \simeq 220\ \mu$m. As show in figure 6(d), at this wavelength the deviation at low $q$ vanishes and we measure a mean cell velocity of $\sim 20\mu$m h$^{-1}$, comparable to that of single adherent cells.

## 4. Conclusion

The examples presented here show that cellular structures produce a clear and exploitable diffraction signal. This approach represents a valuable alternative to optical microscopy to measure the structure and the dynamics at the supracellular scale. Speckle analysis does not require image analysis and segmentation and it is self-averaging. This makes it a fast technique suitable to compare large sets of samples prepared under different conditions (drugs, temperature, genetic mutations or mechanical perturbations). It is also promising for investigating the dynamics of 3D multicellular samples, where microscopy is limited in therm of sample thickness, staining and light dose. In the most basic version, the experimental setup is also compact (a laser diode and a CMOS detector) and fits in a standard incubator.

## Acknowledgments

We thank François Ingremeau, Arnaud Millet, Monika Dolega, Jacques Derouard and Erik Geissler for helpful discussions. The research was supported by LABEX WIFI (Laboratory of Excellence within the French Program 'Investments for the Future') under references ANR-10-LABX-24 and ANR-10-IDEX-0001-02 PSL*, by the Agence Nationale pour la Recherche (Grant ANR-13-BSV5-0008-447 01), the Institut National de la Santé et de la Recherche Médicale (Grant 2011-1-PL BIO-448 11-IC-1) and by the Centre National de la Recherche Scientifique ('Programme Emergence 2016').

## ORCID

Aurélien Gourrier https://orcid.org/0000-0001-9526-5746

## References

[1] Friedl P, Sahai E, Weiss S and Yamada K M 2012 New dimensions in cell migration *Nat. Rev. Mol. Cell Biol.* **13** 743–7
[2] Delarue M, Montel F, Caen O, Elgeti J, Siaugue J-M, Vignjevic D, Prost J, Joanny J-F and Cappello G 2013 Mechanical control of cell flow in multicellular spheroids *Phys. Rev. Lett.* **110** 138103
[3] Meijering E *et al* 2012 Methods for cell and particle tracking *Methods Enzymol.* **504** 183–200
[4] Fournet G and Guinier A 1955 *Small Angle Scattering of X-Rays* (New York: Wiley) pp 7–78 Translated by Walker C B and Yudowitch K L
[5] Glatter O and Kratky O 1982 *Small Angle X-Ray Scattering* (London: Academic)
[6] Feigin L A, Svergun D I and Taylor G W 1987 *Structure Analysis by Small-Angle X-Ray and Neutron Scattering* (Berlin: Springer)
[7] Steinkamp J A 1984 Flow cytometry *Rev. Sci. Instrum.* **55** 1375–400
[8] Xu M, Wu T T and Qu J Y 2008 Unified mie and fractal scattering by cells and experimental study on application in optical characterization of cellular and subcellular structures *J. Biomed. Opt.* **13** 024015
[9] Perelman L T 2006 Optical diagnostic technology based on light scattering spectroscopy for early cancer detection *Expert Rev. Med. Devices* **3** 787–803
[10] Wax A and Backman V 2015 *Biomedical Applications of Light Scattering IX* vol 9333 (Bellingham WA: SPIE Press) http://spie.org/Publications/Proceedings/Volume/9333
[11] Berne B J and Pecora R 1976 *Dynamic Light Scattering: With Applications to Chemistry, Biology, and Physics* (Mineola, NY: Dover)
[12] Conrad H, Lehmkühler F, Fischer B, Westermeier F, Schroer M A, Chushkin Y, Gutt C, Sprung M and Grübel G 2015 Correlated heterogeneous dynamics in glass-forming polymers *Phys. Rev.* E **91** 042309
[13] Tamborini E and Cipelletti L 2012 Multiangle static and dynamic light scattering in the intermediate scattering angle range *Rev. Sci. Instrum.* **83** 093106
[14] Li J, Dietsche G, Iftime D, Skipetrov S E, Maret G, Elbert T, Rockstroh B and Gisler T 2005 Noninvasive detection of functional brain activity with near-infrared diffusing-wave spectroscopy *J. Biomed. Opt.* **20** 044002
[15] Weber B, Burger C, Wyss M T, von Schulthess G K, Scheffold F and Buck A 2004 Optical imaging of the spatiotemporal dynamics of cerebral blood flow and oxidative metabolism in the rat barrel cortex *Eur. J. Neurosci.* **20** 2664

[16] Jaillon F, Skipetrov S E, Li J, Dietsche G, Maret G and Gisler T 2001 Diffusing-wave spectroscopy from head-like tissue phantoms: influence of a non-scattering layer *Opt. Express* **14** 10181
[17] Suissa M, Place C, Goillot E and Freyssingeas E 2008 Internal dynamics of a living cell nucleus investigated by dynamic light scattering *Eur. Phys. J.* E **26** 435–48
[18] Nolte D D, An R, Turek J and Jeong K 2011 Holographic tissue dynamics spectroscopy *J. Biomed. Opt.* **16** 087004
[19] Lee J, Radhakrishnan H, Wu W, Daneshmand A, Climov M, Ayata C and Boas D A 2013 Quantitative imaging of cerebral blood flow velocity and intracellular motility using dynamic light scattering-optical coherence tomography *J. Cereb. Blood Flow Metab.* **33** 819–25
[20] Martinez V A, Besseling R, Croze O A, Tailleur J, Reufer M, Schwarz-Linek J, Wilson L G, Bees M A and Poon W C K 2012 Differential dynamic microscopy: a high-throughput method for characterizing the motility of microorganisms *Biophys. J.* **103** 1637–47
[21] Mourant J R, Johnson T M, Doddi V and Freyer J P 2002 Angular dependent light scattering from multicellular spheroids *J. Biomed. Opt.* **7** 93–9
[22] Tseng Q, Wang I, Duchemin-Pelletier E, Azioune A, Carpi N, Gao J, Filhol O, Piel M, Théry M and Balland M 2011 A new micropatterning method of soft substrates reveals that different tumorigenic signals can promote or reduce cell contraction levels *Lab Chip* **11** 2231–40
[23] Cipelletti L and Weitz D A 1999 Ultralow-angle dynamic light scattering with a charge coupled device camera based multispeckle, multitau correlator *Rev. Sci. Instrum.* **70** 3214–21
[24] Lax M 1952 Multiple scattering of waves: II. The effective field in dense systems *Phys. Rev.* **85** 621
[25] Ferri F 1997 Use of a charge coupled device camera for low-angle elastic light scattering *Rev. Sci. Instrum.* **68** 2265–74
[26] Goodman J W 1976 Some fundamental properties of speckle *J. Opt. Soc. Am.* **66** 1145–50
[27] Ventsel H 1973 *Théorie des probabilités* (Moscou: Mir)
[28] Pine D J, Weitz D A, Zhu J X and Herbolzheimer E 1990 Diffusing-wave spectroscopy: dynamic light scattering in the multiple scattering limit *J. Phys.* **51** 2101–27

# Bibliography


[1] C. A. Klausmeier. Regular and Irregular Patterns in Semiarid Vegetation. *Science*, 284(5421):1826–1828, jun 1999.

[2] Gui Quan Sun, Juan Zhang, Li Peng Song, Zhen Jin, and Bai Lian Li. Pattern formation of a spatial predator-prey system. *Applied Mathematics and Computation*, 218(22):11151–11162, jul 2012.

[3] Iain D Couzin. Collective cognition in animal groups. *Trends in cognitive sciences*, 13(1):36–43, 2009.

[4] Johannes Jaeger. The gap gene network. *Cellular and Molecular Life Sciences*, 68(2):243–274, 2011.

[5] V. V. Isaeva. Self-organization in biological systems. *Biology Bulletin*, 39(2):110–118, apr 2012.

[6] A. M. Turing. The chemical basis of morphogenesis. *Philosophical Transactions of the Royal Society of London. Series B, Biological Sciences*, 237(641):37–72, aug 1952.

[7] K. J. Painter, G. S. Hunt, K. L. Wells, J. A. Johansson, and D. J. Headon. Towards an integrated experimental-theoretical approach for assessing the mechanistic basis of hair and feather morphogenesis. *Interface Focus*, 2(4):433–450, 2012.

[8] Damian Dalle Nogare and Ajay B. Chitnis. Self-organizing spots get under your skin. *PLOS Biology*, 15(12):e2004412, dec 2017.

[9] Hans Meinhardt and Alfred Gierer. Pattern formation by local self-activation and lateral inhibition. *BioEssays*, 22(8):753–760, 2000.

[10] J Raspopovic, L. Marcon, L. Russo, and J. Sharpe. Digit patterning is controlled by a Bmp-Sox9-Wnt Turing network modulated by morphogen gradients. *Science*, 345(6196):566–570, aug 2014.

[11] Darren Gilmour, Martina Rembold, and Maria Leptin. From morphogen to morphogenesis and back. *Nature*, 541(7637):311–320, 2017.

[12] Verena Ruprecht, Pascale Monzo, Andrea Ravasio, Zhang Yue, Ekta Makhija,

Pierre Olivier Strale, Nils Gauthier, G. V. Shivashankar, Vincent Studer, Corinne Albiges-Rizo, and Virgile Viasnoff. How cells respond to environmental cues – insights from bio-functionalized substrates. *Journal of Cell Science*, 130(1):51–61, 2016.

[13] William J Polacheck and Christopher S Chen. Measuring cell-generated forces: a guide to the available tools. *Nature Methods*, 13(5):415–423, 2016.

[14] Kaoru Sugimura, Pierre-François P.-F. Lenne, and François Graner. Measuring forces and stresses in situ in living tissues. *Development*, 143(2):186–196, jan 2016.

[15] Ruiguo Yang, Joshua A. Broussard, Kathleen J. Green, and Horacio D. Espinosa. Techniques to stimulate and interrogate cell–cell adhesion mechanics. *Extreme Mechanics Letters*, 20:125–139, apr 2018.

[16] Pere Roca-Cusachs, Vito Conte, and Xavier Trepat. Quantifying forces in cell biology. *Nature Cell Biology*, 19(7):742–751, jul 2017.

[17] Jason P. Gleghorn, Sriram Manivannan, and Celeste M. Nelson. Quantitative approaches to uncover physical mechanisms of tissue morphogenesis. *Current Opinion in Biotechnology*, 24(5):954–961, 2013.

[18] Benjamin L. Vaughan, Ruth E. Baker, David Kay, and Philip K. Maini. A Modified Oster–Murray–Harris Mechanical Model of Morphogenesis. *SIAM Journal on Applied Mathematics*, 73(6):2124–2142, jan 2013.

[19] G F Oster, J D Murray, and A K Harris. Mechanical aspects of mesenchymal morphogenesis. *Journal of embryology and experimental morphology*, 78:83–125, 1983.

[20] Kevin J. Painter, William Ho, and Denis J. Headon. A chemotaxis model of feather primordia pattern formation during avian development. *Journal of Theoretical Biology*, 437:225–238, 2018.

[21] H Meinhardt. Pattern formation in biology: a comparison of models and experiments. *Reports on Progress in Physics*, 55(6):797–849, jun 1992.

[22] James D. Murray. On the mechanochemical theory of biological pattern formation with application to vasculogenesis. *Comptes Rendus - Biologies*, 326(2):239–252, 2003.

[23] Nikolce Gjorevski and Celeste M. Nelson. The mechanics of development: Models and methods for tissue morphogenesis. *Birth Defects Research Part C - Embryo Today: Reviews*, 90(3):193–202, 2010.

[24] Nicolas Desprat, Willy Supatto, Philippe Alexandre Pouille, Emmanuel Beaurepaire, and Emmanuel Farge. Tissue Deformation Modulates Twist Expression to Determine Anterior Midgut Differentiation in Drosophila Embryos. *Developmental Cell*, 15(3):470–477, 2008.

[25] James D. Glover, Kirsty L. Wells, Franziska Matthäus, Kevin J. Painter, William Ho, Jon Riddell, Jeanette A. Johansson, Matthew J. Ford, Colin A. B. Jahoda, Vaclav Klika, Richard L. Mort, and Denis J. Headon. Hierarchical patterning modes orchestrate hair follicle morphogenesis. *PLOS Biology*, 15(7):e2002117, jul 2017.

[26] Amy E Shyer, Alan R Rodrigues, Grant G Schroeder, Elena Kassianidou, Sanjay Kumar, and Richard M Harland. Emergent cellular self-organization and mechanosensation initiate follicle pattern in the avian skin. *Science*, 357(6353):811–815, aug 2017.

[27] William K. W. Ho, Lucy Freem, Debiao Zhao, Kevin J. Painter, Thomas E. Woolley, Eamonn A. Gaffney, Michael J. McGrew, Athanasia Tzika, Michel C. Milinkovitch, Pascal Schneider, Armin Drusko, Franziska Matthäus, James D. Glover, Kirsty L. Wells, Jeanette A. Johansson, Megan G. Davey, Helen M. Sang, Michael Clinton, and Denis J. Headon. Feather arrays are patterned by interacting signalling and cell density waves. *PLOS Biology*, 17(2):e3000132, feb 2019.

[28] Tadanori Mammoto, Akiko Mammoto, Yu suke Torisawa, Tracy Tat, Ashley Gibbs, Ratmir Derda, Robert Mannix, Marlieke de Bruijn, Chong Wing Yung, Dongeun Huh, and Donald E. Ingber. Mechanochemical Control of Mesenchymal Condensation and Embryonic Tooth Organ Formation. *Developmental Cell*, 21(4):758–769, 2011.

[29] Peter Gross, K. Vijay Kumar, and Stephan W. Grill. How Active Mechanics and Regulatory Biochemistry Combine to Form Patterns in Development. *Annual Review of Biophysics*, 46(1):337–356, 2017.

[30] Eric Brouzés and Emmanuel Farge. Interplay of mechanical deformation and patterned gene expression in developing embryos. *Current Opinion in Genetics and Development*, 14(4):367–374, 2004.

[31] Otger Campàs, Tadanori Mammoto, Sean Hasso, Ralph A Sperling, Daniel O'Connell, Ashley G Bischof, Richard Maas, David A Weitz, L Mahadevan, and Donald E Ingber. Quantifying cell-generated mechanical forces within living embryonic tissues. *Nature methods*, 11(2):183–9, 2014.

[32] Kapil Bambardekar, Raphaël Clément, Olivier Blanc, Claire Chardès, and Pierre-

François Lenne. Direct laser manipulation reveals the mechanics of cell contacts in vivo. *Proceedings of the National Academy of Sciences*, 112(5):1416–1421, 2015.

[33] Christopher C DuFort, Matthew J Paszek, and Valerie M Weaver. Balancing forces: architectural control of mechanotransduction. *Nature reviews. Molecular cell biology*, 12(5):308–19, 2011.

[34] Daniel A Fletcher and R Dyche Mullins. Cell mechanics and the cytoskeleton. *Nature*, 463(7280):485–492, jan 2010.

[35] Tatyana Svitkina. The Actin Cytoskeleton and Actin-Based Motility. *Cold Spring Harbor Perspectives in Biology*, 10(1):a018267, jan 2018.

[36] J Thomas Parsons, Alan Rick Horwitz, and Martin A Schwartz. Cell adhesion: integrating cytoskeletal dynamics and cellular tension. *Nature reviews. Molecular cell biology*, 11(9):633–43, 2010.

[37] Michael Murrell, Patrick W. Oakes, Martin Lenz, and Margaret L. Gardel. Forcing cells into shape: The mechanics of actomyosin contractility. *Nature Reviews Molecular Cell Biology*, 16(8):486–498, 2015.

[38] Laurent Blanchoin, Rajaa Boujemaa-Paterski, Cécile Sykes, and Julie Plastino. Actin dynamics, architecture, and mechanics in cell motility. *Physiological Reviews*, 94(1):235–263, 2014.

[39] Richard O Hynes. The Extracellular Matrix: Not Just Pretty Fibrils. *Science*, 326(5957):1216–1219, nov 2009.

[40] Viola Vogel. Unraveling the Mechanobiology of Extracellular Matrix. *Annual Review of Physiology*, 80(1):353–387, feb 2018.

[41] Nico Strohmeyer, Mitasha Bharadwaj, Mercedes Costell, Reinhard Fässler, and Daniel J Müller. Fibronectin-bound $\alpha5\beta1$ integrins sense load and signal to reinforce adhesion in less than a second. *Nature Materials*, 16:1262, nov 2017.

[42] Pakorn Kanchanawong, Gleb Shtengel, Ana M Pasapera, Ericka B Ramko, Michael W Davidson, Harald F Hess, and Clare M Waterman. Nanoscale architecture of integrin-based cell adhesions. *Nature*, 468(7323):580–584, nov 2010.

[43] Benjamin Geiger, Joachim P. Spatz, and Alexander D. Bershadsky. Environmental sensing through focal adhesions. *Nature Reviews Molecular Cell Biology*, 10(1):21–33, jan 2009.

[44] S. Huveneers and E. H. J. Danen. Adhesion signaling - crosstalk between inte-

grins, Src and Rho. *Journal of Cell Science*, 122(8):1059–1069, 2009.

[45] Thomas Iskratsch, Haguy Wolfenson, and Michael P Sheetz. Appreciating force and shape - the rise of mechanotransduction in cell biology. *Nature reviews. Molecular cell biology*, 15(12):825–33, 2014.

[46] Fabiana Martino, Ana R Perestrelo, Vladimír Vinarský, Stefania Pagliari, and Giancarlo Forte. Cellular Mechanotransduction: From Tension to Function. *Frontiers in Physiology*, 9(July):1–21, jul 2018.

[47] Bernhard Wehrle-Haller. Structure and function of focal adhesions. *Current Opinion in Cell Biology*, 24(1):116–124, 2012.

[48] Jean-cheng Kuo. Mechanotransduction at focal adhesions: integrating cytoskeletal mechanics in migrating cells. *Journal of Cellular and Molecular Medicine*, 17(6):704–712, jun 2013.

[49] C. S. Chen. Mechanotransduction - a field pulling together? *Journal of Cell Science*, 121(20):3285–3292, 2008.

[50] Boris Martinac. The ion channels to cytoskeleton connection as potential mechanism of mechanosensitivity. *Biochimica et Biophysica Acta - Biomembranes*, 1838(2):682–691, 2014.

[51] Jóhanna Árnadóttir and Martin Chalfie. Eukaryotic mechanosensitive channels. *Annual review of biophysics*, 39:111–137, 2010.

[52] José Luis Alonso and Wolfgang H. Goldmann. Cellular mechanotransduction. *AIMS Biophysics*, 3(1):50–62, 2016.

[53] Lucas Smith, Sangkyun Cho, and Dennis E. Discher. Mechanosensing of matrix by stem cells: From matrix heterogeneity, contractility, and the nucleus in pore-migration to cardiogenesis and muscle stem cells in vivo. *Seminars in Cell & Developmental Biology*, 71(24):84–98, nov 2017.

[54] Meilang Xue and Christopher J Jackson. Extracellular matrix reorganization during wound healing and its impact on abnormal scarring. *Advances in wound care*, 4(3):119–136, 2015.

[55] Mariliis Klaas, Triin Kangur, Janeli Viil, Kristina Mäemets-Allas, Ave Minajeva, Krista Vadi, Mikk Antsov, Natalia Lapidus, Martin Järvekülg, and Viljar Jaks. The alterations in the extracellular matrix composition guide the repair of damaged liver tissue. *Scientific reports*, 6:27398, 2016.

[56] Kandice R. Levental, Hongmei Yu, Laura Kass, Johnathon N. Lakins, Mikala Egeblad, Janine T. Erler, Sheri F T Fong, Katalin Csiszar, Amato Giaccia, Wolfgang

Weninger, Mitsuo Yamauchi, David L. Gasser, and Valerie M. Weaver. Matrix Crosslinking Forces Tumor Progression by Enhancing Integrin Signaling. *Cell*, 139(5):891–906, 2009.

[57] Steven E Reid, Emily J Kay, Lisa J Neilson, Anne-Theres Henze, Jens Serneels, Ewan J McGhee, Sandeep Dhayade, Colin Nixon, John BG Mackey, Alice Santi, Karthic Swaminathan, Dimitris Athineos, Vasileios Papalazarou, Francesca Patella, Álvaro Román-Fernández, Yasmin ElMaghloob, Juan Ramon Hernandez-Fernaud, Ralf H Adams, Shehab Ismail, David M Bryant, Manuel Salmeron-Sanchez, Laura M Machesky, Leo M Carlin, Karen Blyth, Massimiliano Mazzone, and Sara Zanivan. Tumor matrix stiffness promotes metastatic cancer cell interaction with the endothelium. *The EMBO Journal*, 36(16):2373–2389, aug 2017.

[58] Herbert B Schiller and Reinhard Fässler. Mechanosensitivity and compositional dynamics of cell–matrix adhesions. *EMBO reports*, 14(6):509–519, 2013.

[59] Nathalie Q. Balaban, Ulrich S. Schwarz, Daniel Riveline, Polina Goichberg, Gila Tzur, Ilana Sabanay, Diana Mahalu, Sam Safran, Alexander Bershadsky, Lia Addadi, and Benjamin Geiger. Force and focal adhesion assembly: A close relationship studied using elastic micropatterned substrates. *Nature Cell Biology*, 3(5):466–472, 2001.

[60] Jasper Foolen, Tadahiro Yamashita, and Philip Kollmannsberger. Shaping tissues by balancing active forces and geometric constraints. *Journal of Physics D: Applied Physics*, 49(5):053001, 2016.

[61] Thomas Boudou, Tomas Andersen, and Martial Balland. On the spatiotemporal regulation of cell tensional state, may 2019.

[62] Tito Panciera, Luca Azzolin, Michelangelo Cordenonsi, and Stefano Piccolo. Mechanobiology of YAP and TAZ in physiology and disease. *Nature Reviews Molecular Cell Biology*, 18(12):758–770, 2017.

[63] Tsutomu Oka and Marius Sudol. Nuclear localization and pro-apoptotic signaling of YAP2 require intact PDZ-binding motif. *Genes to Cells*, 14(5):607–615, 2009.

[64] Jung Soon Mo, Fa Xing Yu, Rui Gong, Joan Heller Brown, and Kun Liang Guan. Regulation of the Hippo-YAP pathway by protease-activated receptors (PARs). *Genes and Development*, 26(19):2138–2143, 2012.

[65] Sirio Dupont, Leonardo Morsut, Mariaceleste Aragona, Elena Enzo, Stefano Giulitti, Michelangelo Cordenonsi, Francesca Zanconato, Jimmy Le Digabel, Mattia Forcato, Silvio Bicciato, Nicola Elvassore, and Stefano Piccolo. Role of YAP/-TAZ in mechanotransduction. *Nature*, 474(7350):179–83, 2011.

[66] Diogo Mosqueira, Stefania Pagliari, Koichiro Uto, Mitsuhiro Ebara, Sara Romanazzo, Carmen Escobedo-Lucea, Jun Nakanishi, Akiyoshi Taniguchi, Ornella Franzese, Paolo Di Nardo, Marie José Goumans, Enrico Traversa, Perpetua Pinto-do Ó, Takao Aoyagi, and Giancarlo Forte. Hippo Pathway Effectors Control Cardiac Progenitor Cell Fate by Acting as Dynamic Sensors of Substrate Mechanics and Nanostructure. *ACS Nano*, 8(3):2033–2047, mar 2014.

[67] N.-G. Kim, E. Koh, X. Chen, and B. M. Gumbiner. E-cadherin mediates contact inhibition of proliferation through Hippo signaling-pathway components. *Proceedings of the National Academy of Sciences*, 108(29):11930–11935, jul 2011.

[68] Giorgia Nardone, Jorge Oliver-De La Cruz, Jan Vrbsky, Cecilia Martini, Jan Pribyl, Petr Skládal, Martin Pešl, Guido Caluori, Stefania Pagliari, Fabiana Martino, Zuzana Maceckova, Marian Hajduch, Andres Sanz-Garcia, Nicola Maria Pugno, Gorazd Bernard Stokin, and Giancarlo Forte. YAP regulates cell mechanics by controlling focal adhesion assembly. *Nature Communications*, 8:15321, may 2017.

[69] Francesca Zanconato, Mattia Forcato, Giusy Battilana, Luca Azzolin, Erika Quaranta, Beatrice Bodega, Antonio Rosato, Silvio Bicciato, Michelangelo Cordenonsi, and Stefano Piccolo. Genome-wide association between YAP/TAZ/TEAD and AP-1 at enhancers drives oncogenic growth. *Nature Cell Biology*, 17(9):1218–1227, sep 2015.

[70] Yoichi Asaoka, Hiroshi Nishina, and Makoto Furutani-Seiki. YAP is essential for 3D organogenesis withstanding gravity. *Development, Growth & Differentiation*, 59(1):52–58, jan 2017.

[71] Georg Halder, Sirio Dupont, and Stefano Piccolo. Transduction of mechanical and cytoskeletal cues by YAP and TAZ, 2012.

[72] Sangkyun Cho, Jerome Irianto, and Dennis E Discher. Mechanosensing by the nucleus: From pathways to scaling relationships, feb 2017.

[73] Gunes Uzer, Clinton T. Rubin, and Janet Rubin. Cell Mechanosensitivity Is Enabled by the LINC Nuclear Complex. *Current Molecular Biology Reports*, 2(1):36–47, 2016.

[74] Srujana Neelam, T. J. Chancellor, Yuan Li, Jeffrey A. Nickerson, Kyle J. Roux, Richard B. Dickinson, and Tanmay P. Lele. Direct force probe reveals the mechanics of nuclear homeostasis in the mammalian cell. *Proceedings of the National Academy of Sciences*, 112(18):5720–5725, may 2015.

[75] Tristan P. Driscoll, Brian D. Cosgrove, Su-Jin Heo, Zach E. Shurden, and Robert L.

Mauck. Cytoskeletal to Nuclear Strain Transfer Regulates YAP Signaling in Mesenchymal Stem Cells. *Biophysical Journal*, 108(12):2783–2793, jun 2015.

[76] Meiyu Sun, Guangfan Chi, Pengdong Li, Shuang Lv, Juanjuan Xu, Ziran Xu, Yuhan Xia, Ye Tan, Jiayi Xu, Lisha Li, and Yulin Li. Effects of Matrix Stiffness on the Morphology, Adhesion, Proliferation and Osteogenic Differentiation of Mesenchymal Stem Cells. *International Journal of Medical Sciences*, 15(3):257–268, 2018.

[77] Adam J. Engler, Shamik Sen, H. Lee Sweeney, and Dennis E. Discher. Matrix Elasticity Directs Stem Cell Lineage Specification. *Cell*, 126(4):677–689, 2006.

[78] Rowena McBeath, Dana M. Pirone, Celeste M. Nelson, Kiran Bhadriraju, and Christopher S. Chen. Cell shape, cytoskeletal tension, and RhoA regulate stem cell lineage commitment. *Developmental Cell*, 6(4):483–495, 2004.

[79] Yi-Ting Yeh, Sung Sik Hur, Joann Chang, Kuei-Chun Wang, Jeng-Jiann Chiu, Yi-Shuan Li, and Shu Chien. Matrix Stiffness Regulates Endothelial Cell Proliferation through Septin 9. *PLoS ONE*, 7(10):e46889, oct 2012.

[80] Anh Tuan Nguyen, Sharvari R. Sathe, and Evelyn K.F. Yim. From nano to micro: Topographical scale and its impact on cell adhesion, morphology and contact guidance, 2016.

[81] G. Reig, E. Pulgar, and M. L. Concha. Cell migration: from tissue culture to embryos. *Development*, 141(10):1999–2013, 2014.

[82] Revathi Ananthakrishnan and Allen Ehrlicher. The Forces Behind Cell Movement. *International Journal of Biological Sciences*, 3(February 2007):303–317, 2007.

[83] Benoit Ladoux, René Marc Mège, and Xavier Trepat. Front-Rear Polarization by Mechanical Cues: From Single Cells to Tissues. *Trends in Cell Biology*, 26(6):420–433, 2016.

[84] Roberto Mayor and Sandrine Etienne-Manneville. The front and rear of collective cell migration. *Nature Reviews Molecular Cell Biology*, 17(2):97–109, 2016.

[85] Chun-Min M Lo, Hong-Bei B Wang, Micah Dembo, and Yu-li L Wang. Cell movement is guided by the rigidity of the substrate. *Biophysical journal*, 79(1):144–152, jul 2000.

[86] Sergey V Plotnikov and Clare M Waterman. Guiding cell migration by tugging. *Current Opinion in Cell Biology*, 25(5):619–626, oct 2013.

[87] Ewa K. Paluch, Celeste M. Nelson, Nicolas Biais, Ben Fabry, Jens Moeller, Beth L. Pruitt, Carina Wollnik, Galina Kudryasheva, Florian Rehfeldt, and Walter Federle.

Mechanotransduction: use the force(s). *BMC Biology*, 13(1):47, 2015.

[88] L. Trichet, J. Le Digabel, R. J. Hawkins, S. R. K. Vedula, M. Gupta, C. Ribrault, P. Hersen, R. Voituriez, and Benoit Ladoux. Evidence of a large-scale mechanosensing mechanism for cellular adaptation to substrate stiffness. *Proceedings of the National Academy of Sciences*, 109(18):6933–6938, 2012.

[89] Alexandre Saez, Axel Buguin, Pascal Silberzan, and Benoit Ladoux. Is the mechanical activity of epithelial cells controlled by deformations or forces? *Biophysical Journal*, 89(6):52–54, 2005.

[90] Mukund Gupta, Bibhu Ranjan Sarangi, Joran Deschamps, Yasaman Nematbakhsh, Andrew Callan-Jones, Felix Margadant, René Marc Mège, Chwee Teck Lim, Raphaël Voituriez, and Benoit Ladoux. Adaptive rheology and ordering of cell cytoskeleton govern matrix rigidity sensing. *Nature Communications*, 6(May), 2015.

[91] Xian Hu, Felix Martin Margadant, Mingxi Yao, and Michael Patrick Sheetz. Molecular stretching modulates mechanosensing pathways. *Protein Science*, 26(7):1337–1351, 2017.

[92] R. J. Pelham and Y.-l. Wang. Cell locomotion and focal adhesions are regulated by substrate flexibility. *Proceedings of the National Academy of Sciences*, 94(25):13661–13665, dec 1997.

[93] Guillaume Charras and Erik Sahai. Physical influences of the extracellular environment on cell migration. *Nature Reviews Molecular Cell Biology*, 15(12):813–824, 2014.

[94] P. Kollmannsberger, C. M. Bidan, J. W. C. Dunlop, and P. Fratzl. The physics of tissue patterning and extracellular matrix organisation: how cells join forces. *Soft Matter*, 7(20):9549, 2011.

[95] Enrique Rodriguez-Boulan and Ian G. Macara. Organization and execution of the epithelial polarity programme. *Nature Reviews Molecular Cell Biology*, 15(4):225–242, 2014.

[96] Miguel A Garcia, W James Nelson, and Natalie Chavez. Cell–Cell Junctions Organize Structural and Signaling Networks. *Cold Spring Harbor Perspectives in Biology*, 10(4):a029181, apr 2018.

[97] Andrew P Kowalczyk and Kathleen J Green. Structure, function, and regulation of desmosomes. *Progress in molecular biology and translational science*, 116:95–118, 2013.

[98] Andrew J Price, Anna Lena Cost, Hanna Ungewiß, Jens Waschke, Alexander R Dunn, and Carsten Grashoff. Mechanical loading of desmosomes depends on the magnitude and orientation of external stress. *Nature Communications*, 9(1):5284, dec 2018.

[99] Brett J. Roberts, Anjeza Pashaj, Keith R. Johnson, and James K. Wahl. Desmosome dynamics in migrating epithelial cells requires the actin cytoskeleton. *Experimental Cell Research*, 317(20):2814–2822, dec 2011.

[100] Tony J C Harris and Ulrich Tepass. Adherens junctions: from molecules to morphogenesis. *Nature Reviews Molecular Cell Biology*, 11(7):502–514, jul 2010.

[101] Andrea Hartsock and W James Nelson. Adherens and tight junctions: Structure, function and connections to the actin cytoskeleton, 2008.

[102] Wenxiang Meng and Masatoshi Takeichi. Adherens Junction: Molecular Architecture and Regulation. *Cold Spring Harbor Perspectives in Biology*, 1(6):a002899–a002899, dec 2009.

[103] Xavier Trepat, Zaozao Chen, and Ken Jacobson. Cell Migration. In *Comprehensive Physiology*, volume 2, pages 430–435. John Wiley & Sons, Inc., Hoboken, NJ, USA, oct 2012.

[104] James S Lowe and Peter G Anderson. *Stevens & Lowe's Human Histology*. Elsevier Health Sciences, 2014.

[105] Benoit Ladoux, Ester Anon, Mireille Lambert, Aleksandr Rabodzey, Pascal Hersen, Axel Buguin, Pascal Silberzan, and René Marc Mège. Strength dependence of cadherin-mediated adhesions. *Biophysical Journal*, 98(4):534–542, 2010.

[106] Brenton D Hoffman and Alpha S Yap. Towards a Dynamic Understanding of Cadherin-Based Mechanobiology, 2015.

[107] Bryan T MacDonald, Keiko Tamai, and Xi He. Wnt/$\beta$-catenin signaling: components, mechanisms, and diseases. *Developmental cell*, 17(1):9–26, 2009.

[108] Thibaut Brunet, Adrien Bouclet, Padra Ahmadi, Démosthène Mitrossilis, Benjamin Driquez, Anne Christine Brunet, Laurent Henry, Fanny Serman, Gaëlle Béalle, Christine Ménager, Frédéric Dumas-Bouchiat, Dominique Givord, Constantin Yanicostas, Damien Le-Roy, Nora M. Dempsey, Anne Plessis, and Emmanuel Farge. Evolutionary conservation of early mesoderm specification by mechanotransduction in Bilateria. *Nature Communications*, 4(February 2014), 2013.

[109] Hiroaki Hirata, Mikhail Samsonov, and Masahiro Sokabe. Actomyosin contractility provokes contact inhibition in E-cadherin-ligated keratinocytes. *Scientific Reports*, 7(1):46326, jun 2017.

[110] Blair W. Benham-Pyle, Beth L. Pruitt, and W. James Nelson. Mechanical strain induces E-cadherin-dependent Yap1 and $\beta$-catenin activation to drive cell cycle entry. *Science*, 348(6238):1024–1027, 2015.

[111] Ian G. Macara, Richard Guyer, Graham Richardson, Yongliang Huo, and Syed M. Ahmed. Epithelial homeostasis, sep 2014.

[112] Diana Pinheiro and Yohanns Bellaïche. Mechanical Force-Driven Adherens Junction Remodeling and Epithelial Dynamics, 2018.

[113] Benoit Ladoux and René-Marc Mège. Mechanobiology of collective cell behaviours. *Nature Reviews Molecular Cell Biology*, 18(12):743–757, nov 2017.

[114] Kyle H. Vining and David J. Mooney. Mechanical forces direct stem cell behaviour in development and regeneration. *Nature Reviews Molecular Cell Biology*, 18(12):728–742, 2017.

[115] Guillaume Charras and Alpha S. Yap. Tensile Forces and Mechanotransduction at Cell–Cell Junctions. *Current Biology*, 28(8):R445–R457, 2018.

[116] Gregory F Weber, Maureen A Bjerke, and D. W. DeSimone. Integrins and cadherins join forces to form adhesive networks. *Journal of Cell Science*, 124(8):1183–1193, 2011.

[117] Keeley L. Mui, Christopher S. Chen, and Richard K. Assoian. The mechanical regulation of integrin–cadherin crosstalk organizes cells, signaling and forces. *Journal of Cell Science*, 129(6):1093–1100, mar 2016.

[118] Y. Wang, G. Jin, H. Miao, J. Y.-S. Li, S. Usami, and S. Chien. Integrins regulate VE-cadherin and catenins: Dependence of this regulation on Src, but not on Ras. *Proceedings of the National Academy of Sciences*, 103(6):1774–1779, feb 2006.

[119] Wei-hui Guo, Margo T. Frey, Nancy A. Burnham, and Yu-li Wang. Substrate Rigidity Regulates the Formation and Maintenance of Tissues. *Biophysical Journal*, 90(6):2213–2220, mar 2006.

[120] M Playford, K Vadali, X CAI, K BURRIDGE, and M SCHALLER. Focal Adhesion Kinase regulates cell–cell contact formation in epithelial cells via modulation of Rho. *Experimental Cell Research*, 314(17):3187–3197, oct 2008.

[121] Hiroyuki Yamamoto, Manuel Ehling, Katsuhiro Kato, Kenichi Kanai, Max van Lessen, Maike Frye, Dagmar Zeuschner, Masanori Nakayama, Dietmar Vestweber,

and Ralf H. Adams. Integrin $\beta 1$ controls VE-cadherin localization and blood vessel stability. *Nature Communications*, 6(1):6429, may 2015.

[122] Céline Labouesse, Alexander B. Verkhovsky, Jean-Jacques Meister, Chiara Gabella, and Benoît Vianay. Cell Shape Dynamics Reveal Balance of Elasticity and Contractility in Peripheral Arcs. *Biophysical Journal*, 108(10):2437–2447, 2015.

[123] Thomas Lecuit and Pierre-François Lenne. Cell surface mechanics and the control of cell shape, tissue patterns and morphogenesis. *Nature reviews. Molecular cell biology*, 8(8):633–644, 2007.

[124] T Yamashita, P Kollmannsberger, K Mawatari, V Vogel, and T Kitamori. Curvature-Induced Spontaneous Detachment of Vascular Smooth Muscle Cell Sheets : Towards Vascular Self Assembly in Microchannels Abstract. *Microsystem Technology in Chemistry and Life Science*, 1(October):2022–2024, 2013.

[125] Cecile M. Bidan, Krishna P. Kommareddy, Monika Rumpler, Philip Kollmannsberger, Peter Fratzl, and John W C Dunlop. Geometry as a Factor for Tissue Growth: Towards Shape Optimization of Tissue Engineering Scaffolds. *Advanced Healthcare Materials*, 2(1):186–194, 2013.

[126] Celeste M Nelson, Ronald P Jean, John L Tan, Wendy F Liu, Nathan J Sniadecki, Alexander a Spector, and Christopher S Chen. Emergent patterns of growth controlled by multicellular form and mechanics. *Proceedings of the National Academy of Sciences of the United States of America*, 102(33):11594–11599, 2005.

[127] Sami Alom Ruiz and Christopher S. Chen. Emergence of Patterned Stem Cell Differentiation Within Multicellular Structures. *Stem Cells*, 26(11):2921–2927, nov 2008.

[128] M. Deforet, V Hakim, H.G. Yevick, G Duclos, and P Silberzan. Emergence of collective modes and tri-dimensional structures from epithelial confinement. *Nature Communications*, 5(1):3747, dec 2014.

[129] Celeste M. Nelson and Jason P. Gleghorn. Sculpting Organs: Mechanical Regulation of Tissue Development. *Annual Review of Biomedical Engineering*, 14(1):129–154, 2012.

[130] Carl Philipp Heisenberg and Yohanns Bellaïche. Forces in tissue morphogenesis and patterning. *Cell*, 153(5), 2013.

[131] Kevin S. Kolahi and Mohammad R.K. Mofrad. Mechanotransduction: a major regulator of homeostasis and development. *Wiley Interdisciplinary Reviews: Sys-*

*tems Biology and Medicine*, 2(6):625–639, nov 2010.

[132] Diana E. Jaalouk and Jan Lammerding. Mechanotransduction gone awry. *Nature Reviews Molecular Cell Biology*, 10(1):63–73, jan 2009.

[133] Xufeng Xue, Yubing Sun, Agnes M. Resto-Irizarry, Ye Yuan, Koh Meng Aw Yong, Yi Zheng, Shinuo Weng, Yue Shao, Yimin Chai, Lorenz Studer, and Jianping Fu. Mechanics-guided embryonic patterning of neuroectoderm tissue from human pluripotent stem cells. *Nature Materials*, 17(7):633–641, 2018.

[134] Celeste M. Nelson. Geometric control of tissue morphogenesis. *Biochimica et Biophysica Acta - Molecular Cell Research*, 1793(5):903–910, 2009.

[135] C. J. Weijer. Collective cell migration in development. *Journal of Cell Science*, 122(18):3215–3223, sep 2009.

[136] Carlos Carmona-Fontaine, Eric Theveneau, Apostolia Tzekou, Masazumi Tada, Mae Woods, Karen M. Page, Maddy Parsons, John D. Lambris, and Roberto Mayor. Complement Fragment C3a Controls Mutual Cell Attraction during Collective Cell Migration. *Developmental Cell*, 21(6):1026–1037, dec 2011.

[137] Peter Friedl and Darren Gilmour. Collective cell migration in morphogenesis, regeneration and cancer. *Nature reviews. Molecular cell biology*, 10(7):445–57, 2009.

[138] Peter Friedl and Stephanie Alexander. Cancer Invasion and the Microenvironment: Plasticity and Reciprocity. *Cell*, 147(5):992–1009, nov 2011.

[139] Veronika te Boekhorst, Luigi Preziosi, and Peter Friedl. Plasticity of Cell Migration In Vivo and In Silico. *Annual Review of Cell and Developmental Biology*, 32(1):491–526, 2016.

[140] Pernille Rorth. Fellow travellers: Emergent properties of collective cell migration. *EMBO Reports*, 13(11):984–991, 2012.

[141] Peter Friedl and Katarina Wolf. Plasticity of cell migration: A multiscale tuning model. *Journal of Cell Biology*, 188(1):11–19, 2010.

[142] Eliah R. Shamir and Andrew J. Ewald. Adhesion in Mammary Development. In *Current Topics in Developmental Biology*, pages 353–382. Elsevier, 2015.

[143] Guilherme Costa, Kyle I. Harrington, Holly E. Lovegrove, Donna J. Page, Shilpa Chakravartula, Katie Bentley, and Shane P. Herbert. Asymmetric division coordinates collective cell migration in angiogenesis. *Nature Cell Biology*, 18(12):1292–1301, dec 2016.

[144] Peran Hayes and Jérôme Solon. Drosophila dorsal closure: An orchestra of forces

to zip shut the embryo. *Mechanisms of Development*, 144:2–10, apr 2017.

[145] Denise J. Montell, Wan Hee Yoon, and Michelle Starz-Gaiano. Group choreography: mechanisms orchestrating the collective movement of border cells. *Nature Reviews Molecular Cell Biology*, 13(10):631–645, oct 2012.

[146] Alain Ghysen, Christine Dambly-Chaudière, and David Raible. Making sense of zebrafish neural development in the Minervois. *Neural Development*, 2(1):15, 2007.

[147] R. Mayor and E. Theveneau. The neural crest. *Development*, 140(11):2247–2251, jun 2013.

[148] Peter Friedl, Joseph Locker, Erik Sahai, and Jeffrey E. Segall. Classifying collective cancer cell invasion. *Nature Cell Biology*, 14(8):777–783, aug 2012.

[149] P. Martin. Parallels between tissue repair and embryo morphogenesis. *Development*, 131(13):3021–3034, jul 2004.

[150] Justin C Yarrow, Zachary E Perlman, Nicholas J Westwood, and Timothy J Mitchison. A high-throughput cell migration assay using scratch wound healing, a comparison of image-based readout methods. *BMC biotechnology*, 4(1):21, 2004.

[151] Emanuele Ostuni, Ravi Kane, Christopher S Chen, Donald E Ingber, and George M Whitesides. Patterning mammalian cells using elastomeric membranes. *Langmuir*, 16(20):7811–7819, 2000.

[152] M Poujade, E Grasland-Mongrain, A Hertzog, J Jouanneau, P Chavrier, Benoit Ladoux, A Buguin, and P Silberzan. Collective migration of an epithelial monolayer in response to a model wound. *Proceedings of the National Academy of Sciences of the United States of America*, 104(41):15988–93, 2007.

[153] Asha M. Das, Alexander M.M. Eggermont, and Timo L.M. Ten Hagen. A ring barrier-based migration assay to assess cell migration in vitro. *Nature Protocols*, 10(6):904–915, 2015.

[154] Claudio G. Rolli, Hidekazu Nakayama, Kazuo Yamaguchi, Joachim P. Spatz, Ralf Kemkemer, and Jun Nakanishi. Switchable adhesive substrates: Revealing geometry dependence in collective cell behavior. *Biomaterials*, 33(8):2409–2418, mar 2012.

[155] Dhananjay T Tambe, C Corey Hardin, Thomas E Angelini, Kavitha Rajendran, Chan Young Park, Xavier Serra-Picamal, Enhua H Zhou, Muhammad H Zaman, James P Butler, David A Weitz, Jeffrey J Fredberg, and Xavier Trepat. Collective cell guidance by cooperative intercellular forces. *Nature materials*, 10(6):469–

75, 2011.

[156] Monirosadat Sadati, Nader Taheri Qazvini, Ramaswamy Krishnan, Chan Young Park, and Jeffrey J. Fredberg. Collective migration and cell jamming. *Differentiation*, 86(3):121–125, oct 2013.

[157] Roberto Mayor and Carlos Carmona-Fontaine. Keeping in touch with contact inhibition of locomotion. *Trends in Cell Biology*, 20(6):319–328, jun 2010.

[158] L. Petitjean, M. Reffay, E. Grasland-Mongrain, M. Poujade, Benoit Ladoux, A. Buguin, and P. Silberzan. Velocity fields in a collectively migrating epithelium. *Biophysical Journal*, 98(9):1790–1800, 2010.

[159] A. Puliafito, L. Hufnagel, P. Neveu, S. Streichan, A. Sigal, D. K. Fygenson, and B. I. Shraiman. Collective and single cell behavior in epithelial contact inhibition. *Proceedings of the National Academy of Sciences*, 109(3):739–744, jan 2012.

[160] Simon Garcia, Edouard Hannezo, Jens Elgeti, Jean-François Joanny, Pascal Silberzan, and Nir S. Gov. Physics of active jamming during collective cellular motion in a monolayer. *Proceedings of the National Academy of Sciences*, 112(50):15314–15319, 2015.

[161] Thomas E. Angelini, Edouard Hannezo, Xavier Trepat, Jeffrey J. Fredberg, and David A. Weitz. Cell migration driven by cooperative substrate deformation patterns. *Physical Review Letters*, 104(16):1–4, 2010.

[162] Gary Wilk, Masatomo Iwasa, Patrick E. Fuller, Kristiana Kandere-Grzybowska, and Bartosz A. Grzybowski. Universal area distributions in the monolayers of confluent mammalian cells. *Physical Review Letters*, 2014.

[163] Leyla Kocgozlu, Thuan Beng Saw, Anh Phuong Le, Ivan Yow, Murat Shagirov, Eunice Wong, René Marc Mège, Chwee Teck Lim, Yusuke Toyama, and Benoit Ladoux. Epithelial Cell Packing Induces Distinct Modes of Cell Extrusions. *Current Biology*, 26(21):2942–2950, 2016.

[164] T. E. Angelini, E. Hannezo, Xavier Trepat, M. Marquez, J. J. Fredberg, and D. A. Weitz. Glass-like dynamics of collective cell migration. *Proceedings of the National Academy of Sciences*, 108(12):4714–4719, 2011.

[165] Kevin Doxzen, Sri Ram Krishna Vedula, Man Chun Leong, Hiroaki Hirata, Nir S. Gov, Alexandre J. Kabla, Benoit Ladoux, and Chwee Teck Lim. Guidance of collective cell migration by substrate geometry. *Integrative Biology*, 5(8):1026, 2013.

[166] Hisashi Haga, Chikako Irahara, Ryo Kobayashi, Toshiyuki Nakagaki, and

Kazushige Kawabata. Collective movement of epithelial cells on a collagen gel substrate. *Biophysical Journal*, 88(3):2250–2256, 2005.

[167] Guillaume Duclos, Christoph Erlenkämper, Jean François Joanny, and Pascal Silberzan. Topological defects in confined populations of spindle-shaped cells. *Nature Physics*, 13(1):58–62, 2017.

[168] Tamal Das, Kai Safferling, Sebastian Rausch, Niels Grabe, Heike Boehm, and Joachim P. Spatz. A molecular mechanotransduction pathway regulates collective migration of epithelial cells. *Nature Cell Biology*, 17(3):276–287, feb 2015.

[169] András Czirók, Katalin Varga, Előd Méhes, and András Szabó. Collective cell streams in epithelial monolayers depend on cell adhesion. *New Journal of Physics*, 15(7):075006, jul 2013.

[170] Mei Rosa Ng, Achim Besser, Gaudenz Danuser, and Joan S. Brugge. Substrate stiffness regulates cadherin-dependent collective migration through myosin-II contractility. *Journal of Cell Biology*, 199(3):545–563, 2012.

[171] M. Basan, J. Elgeti, E. Hannezo, W.-J. Rappel, and H. Levine. Alignment of cellular motility forces with tissue flow as a mechanism for efficient wound healing. *Proceedings of the National Academy of Sciences*, 110(7):2452–2459, 2013.

[172] Jacob Notbohm, Shiladitya Banerjee, Kazage J C Utuje, Bomi Gweon, Hwanseok Jang, Yongdoo Park, Jennifer Shin, James P. Butler, Jeffrey J. Fredberg, and M. Cristina Marchetti. Cellular Contraction and Polarization Drive Collective Cellular Motion. *Biophysical Journal*, 110(12):2729–2738, 2016.

[173] Jae Hun Kim, Xavier Serra-Picamal, Dhananjay T. Tambe, Enhua H. Zhou, Chan Young Park, Monirosadat Sadati, Jin Ah Park, Ramaswamy Krishnan, Bomi Gweon, Emil Millet, James P. Butler, Xavier Trepat, and Jeffrey J. Fredberg. Propulsion and navigation within the advancing monolayer sheet. *Nature Materials*, 12(9):856–863, 2013.

[174] Xavier Serra-Picamal, Vito Conte, Romaric Vincent, Ester Anon, Dhananjay T. Tambe, Elsa Bazellieres, James P. Butler, Jeffrey J. Fredberg, and Xavier Trepat. Mechanical waves during tissue expansion. *Nature Physics*, 8(8):628–634, 2012.

[175] Jin-Ah Park, Lior Atia, Jennifer A. Mitchel, Jeffrey J. Fredberg, and James P. Butler. Collective migration and cell jamming in asthma, cancer and development. *Journal of Cell Science*, 129(18):3375–3383, 2016.

[176] Xavier Trepat and Jeffrey J. Fredberg. Plithotaxis and emergent dynamics in collective cellular migration. *Trends in Cell Biology*, 21(11):638–646, 2011.

[177] Andrea J. Liu and Sidney R. Nagel. Jamming is not just cool any more. *Nature*, 396(6706):21–22, nov 1998.

[178] Vincent Hakim and Pascal Silberzan. Collective cell migration: a physics perspective. *Reports on Progress in Physics*, 80(7):076601, jul 2017.

[179] Ricard Alert and Xavier Trepat. Physical Models of Collective Cell Migration. *arXiv*, may 2019.

[180] Dapeng Bi, Xingbo Yang, M. Cristina Marchetti, and M. Lisa Manning. Motility-driven glass and jamming transitions in biological tissues. *Physical Review X*, 6(2):1–13, 2016.

[181] B. Szabó, G. J. Szöllösi, B. Gönci, Zs Jurányi, D. Selmeczi, and Tamás Vicsek. Phase transition in the collective migration of tissue cells: Experiment and model. *Physical Review E - Statistical, Nonlinear, and Soft Matter Physics*, 74(6):1–5, 2006.

[182] Kenechukwu David Nnetu, Melanie Knorr, Josef Käs, and Mareike Zink. The impact of jamming on boundaries of collectively moving weak-interacting cells. *New Journal of Physics*, 14, 2012.

[183] E.-M. Schotz, M. Lanio, J. A. Talbot, and M. L. Manning. Glassy dynamics in three-dimensional embryonic tissues. *Journal of The Royal Society Interface*, 10(89):20130726–20130726, sep 2013.

[184] Lior Atia, Dapeng Bi, Yasha Sharma, Jennifer A. Mitchel, Bomi Gweon, Stephan A. Koehler, Stephen J. DeCamp, Bo Lan, Jae Hun Kim, Rebecca Hirsch, Adrian F. Pegoraro, Kyu Ha Lee, Jacqueline R. Starr, David A. Weitz, Adam C. Martin, Jin-Ah Park, James P. Butler, and Jeffrey J. Fredberg. Geometric constraints during epithelial jamming. *Nature Physics*, 14(6):613–620, jun 2018.

[185] Dapeng Bi, J. H. Lopez, J. M. Schwarz, and M. Lisa Manning. A density-independent rigidity transition in biological tissues. *Nature Physics*, 11(12):1074–1079, 2015.

[186] Jin-Ah Park, Jae Hun Kim, Dapeng Bi, Jennifer A Mitchel, Nader Taheri Qazvini, Kelan Tantisira, Chan Young Park, Maureen McGill, Sae-Hoon Kim, Bomi Gweon, Jacob Notbohm, Robert Steward, Stephanie Burger, Scott H Randell, Alvin T Kho, Dhananjay T Tambe, Corey Hardin, Stephanie A Shore, Elliot Israel, David A Weitz, Daniel J Tschumperlin, Elizabeth P Henske, Scott T Weiss, M Lisa Manning, James P Butler, Jeffrey M Drazen, and Jeffrey J Fredberg. Unjamming and cell shape in the asthmatic airway epithelium. *Nature materials*, 14(10):1040–8, 2015.

[187] Juliane Zimmermann, Brian A. Camley, Wouter-Jan Rappel, and Herbert Levine. Contact inhibition of locomotion determines cell-cell and cell-substrate forces in tissues. *Proceedings of the National Academy of Sciences of the United States of America*, 113(10):2660–2665, 2016.

[188] P Rosen and D S Misfeldt. Cell density determines epithelial migration in culture. *Proceedings of the National Academy of Sciences of the United States of America*, 1980.

[189] Chiara Malinverno, Salvatore Corallino, Fabio Giavazzi, Martin Bergert, Qingsen Li, Marco Leoni, Andrea Disanza, Emanuela Frittoli, Amanda Oldani, Emanuele Martini, Tobias Lendenmann, Gianluca Deflorian, Galina V. Beznoussenko, Dimos Poulikakos, Kok Haur Ong, Marina Uroz, Xavier Trepat, Dario Parazzoli, Paolo Maiuri, Weimiao Yu, Aldo Ferrari, Roberto Cerbino, and Giorgio Scita. Endocytic reawakening of motility in jammed epithelia. *Nature Materials*, 16(5):587–596, 2017.

[190] S. A. Gudipaty, J. Lindblom, P. D. Loftus, M. J. Redd, K. Edes, C. F. Davey, V. Krishnegowda, and J. Rosenblatt. Mechanical stretch triggers rapid epithelial cell division through Piezo1. *Nature*, 543(7643):118–121, 2017.

[191] Sebastian J Streichan, Christian R Hoerner, Tatjana Schneidt, Daniela Holzer, and Lars Hufnagel. Spatial constraints control cell proliferation in tissues. *Proceedings of the National Academy of Sciences of the United States of America*, 111(15):5586–91, 2014.

[192] Anna Kristina Marel, Matthias Zorn, Christoph Klingner, Roland Wedlich-Söldner, Erwin Frey, and Joachim O. Rädler. Flow and diffusion in channel-guided cell migration. *Biophysical Journal*, 107(5):1054–1064, 2014.

[193] R. Sunyer, V. Conte, J. Escribano, A. Elosegui-Artola, A. Labernadie, L. Valon, D. Navajas, J. M. Garcia-Aznar, J. J. Munoz, P. Roca-Cusachs, and Xavier Trepat. Collective cell durotaxis emerges from long-range intercellular force transmission. *Science*, 353(6304):1157–1161, sep 2016.

[194] Pilar Rodríguez-Franco, Agustí Brugués, Ariadna Marín-Llauradó, Vito Conte, Guiomar Solanas, Eduard Batlle, Jeffrey J. Fredberg, Pere Roca-Cusachs, Raimon Sunyer, and Xavier Trepat. Long-lived force patterns and deformation waves at repulsive epithelial boundaries. *Nature Materials*, 16(10):1029–1037, oct 2017.

[195] Sham Tlili, Estelle Gauquelin, Brigitte Li, Olivier Cardoso, Benoit Ladoux, Hélène Delanoë-Ayari, and François Graner. Collective cell migration without proliferation: density determines cell velocity and wave velocity. *Royal Society Open*

*Science*, 5(5):172421, may 2018.

[196] Sri Ram Krishna Vedula, Grégoire Peyret, Ibrahim Cheddadi, Tianchi Chen, Agustí Brugués, Hiroaki Hirata, Horacio Lopez-Menendez, Yusuke Toyama, Luís Neves De Almeida, Xavier Trepat, Chwee Teck Lim, and Benoit Ladoux. Mechanics of epithelial closure over non-adherent environments. *Nature Communications*, 6:1–10, 2015.

[197] M. Bindschadler and J. L. McGrath. Sheet migration by wounded monolayers as an emergent property of single-cell dynamics. *Journal of Cell Science*, 120(5):876–884, 2007.

[198] Kazuhiro Aoki, Yohei Kondo, Honda Naoki, Toru Hiratsuka, Reina E. Itoh, and Michiyuki Matsuda. Propagating Wave of ERK Activation Orients Collective Cell Migration. *Developmental Cell*, 43(3):305–317.e5, 2017.

[199] S. Huang, C. P. Brangwynne, K. K. Parker, and Donald E. Ingber. Symmetry-breaking in mammalian cell cohort migration during tissue pattern formation: Role of random-walk persistence. *Cell Motility and the Cytoskeleton*, 61(4):201–213, 2005.

[200] M. Reffay, M. C. Parrini, O. Cochet-Escartin, Benoit Ladoux, A. Buguin, S. Coscoy, F. Amblard, J. Camonis, and P. Silberzan. Interplay of RhoA and mechanical forces in collective cell migration driven by leader cells. *Nature Cell Biology*, 16(3):217–223, 2014.

[201] Sho Yokoyama, Tsubasa S. Matsui, and Shinji Deguchi. New wrinkling substrate assay reveals traction force fields of leader and follower cells undergoing collective migration. *Biochemical and Biophysical Research Communications*, 482(4):975–979, 2017.

[202] D. A. Chapnick and X. Liu. Leader cell positioning drives wound-directed collective migration in TGF -stimulated epithelial sheets. *Molecular Biology of the Cell*, 25(10):1586–1593, 2014.

[203] Elsa Bazellières, Vito Conte, Alberto Elosegui-Artola, Xavier Serra-Picamal, María Bintanel-Morcillo, Pere Roca-Cusachs, José J Muñoz, Marta Sales-Pardo, Roger Guimerà, and Xavier Trepat. Control of cell-cell forces and collective cell dynamics by the intercellular adhesome. *Nature cell biology*, 17(4):409–420, 2015.

[204] Ravi A. Desai, Lin Gao, Srivatsan Raghavan, Wendy F. Liu, and Christopher S. Chen. Cell polarity triggered by cell-cell adhesion via E-cadherin. *Journal of Cell Science*, 122(Pt 7):905–911, 2009.

[205] H. Delanoë-Ayari, P. Lenz, J. Brevier, M. Weidenhaupt, M. Vallade, D. Gulino, J. F. Joanny, and D. Riveline. Periodic Adhesive Fingers between Contacting Cells. *Physical Review Letters*, 93(10):1–4, 2004.

[206] Arnold Hayer, Lin Shao, Mingyu Chung, Lydia Marie Joubert, Hee Won Yang, Feng Chiao Tsai, Anjali Bisaria, Eric Betzig, and Tobias Meyer. Engulfed cadherin fingers are polarized junctional structures between collectively migrating endothelial cells. *Nature Cell Biology*, 18(12):1311–1323, 2016.

[207] J. K. Klarlund. Dual modes of motility at the leading edge of migrating epithelial cell sheets. *Proceedings of the National Academy of Sciences*, 109(39):15799–15804, 2012.

[208] Brian Stramer and Roberto Mayor. Mechanisms and in vivo functions of contact inhibition of locomotion. *Nature Reviews Molecular Cell Biology*, 18(1):43–55, jan 2017.

[209] Ravi A. Desai, Smitha B. Gopal, Sophia Chen, and Christopher S. Chen. Contact inhibition of locomotion probabilities drive solitary versus collective cell migration. *Journal of the Royal Society Interface*, 10(88), 2013.

[210] R K Vedula, A Ravasio, C T Lim, and Benoit Ladoux. Collective Cell Migration: A Mechanistic Perspective. *Physiology*, 28(6):370–379, 2013.

[211] Chiara De Pascalis and Sandrine Etienne-Manneville. Single and collective cell migration: the mechanics of adhesions. *Molecular Biology of the Cell*, 28(14):1833–1846, 2017.

[212] Antoine A. Khalil and Peter Friedl. Determinants of leader cells in collective cell migration. *Integrative Biology*, 2(11-12):568–574, 2010.

[213] Xavier Trepat, Michael R. Wasserman, Thomas E. Angelini, Emil Millet, David A. Weitz, James P. Butler, and Jeffrey J. Fredberg. Physical forces during collective cell migration. *Nature Physics*, 5(6):426–430, 2009.

[214] Rizwan Farooqui and Gabriel Fenteany. Multiple rows of cells behind an epithelial wound edge extend cryptic lamellipodia to collectively drive cell-sheet movement. *Journal of Cell Science*, 118(1):51–63, jan 2005.

[215] Dhananjay T. Tambe, Ugo Croutelle, Xavier Trepat, Chan Young Park, Jae Hun Kim, Emil Millet, James P. Butler, and Jeffrey J. Fredberg. Monolayer Stress Microscopy: Limitations, Artifacts, and Accuracy of Recovered Intercellular Stresses. *PLoS ONE*, 8(2):12, 2013.

[216] Charlène Gayrard, Clément Bernaudin, Théophile Déjardin, Cynthia Seiler, and

Nicolas Borghi. Src- and confinement-dependent FAK activation causes E-cadherin relaxation and $\beta$-catenin activity. *Journal of Cell Biology*, 217(3):1063–1077, 2018.

[217] Manuel Théry. Wave of migration. *Nature Physics*, 8(8):583–584, aug 2012.

[218] A. R. Harris, L. Peter, J. Bellis, B. Baum, A. J. Kabla, and G. T. Charras. Characterizing the mechanics of cultured cell monolayers. *Proceedings of the National Academy of Sciences*, 109(41):16449–16454, 2012.

[219] Claire Bertet, Lawrence Sulak, and Thomas Lecuit. Myosin-dependent junction remodelling controls planar cell intercalation and axis elongation. *Nature*, 2004.

[220] Tom P J Wyatt, Andrew R Harris, Maxine Lam, Qian Cheng, Julien Bellis, Andrea Dimitracopoulos, Alexandre J Kabla, Guillaume T Charras, and Buzz Baum. Emergence of homeostatic epithelial packing and stress dissipation through divisions oriented along the long cell axis. *Proceedings of the National Academy of Sciences of the United States of America*, 112(18):5726–31, 2015.

[221] Romaric Vincent, Elsa Bazellières, Carlos Pérez-González, Marina Uroz, Xavier Serra-Picamal, and Xavier Trepat. Active Tensile Modulus of an Epithelial Monolayer. *Physical Review Letters*, 115(24):248103, dec 2015.

[222] Aaron F. Mertz, Shiladitya Banerjee, Yonglu Che, Guy K. German, Ye Xu, Callen Hyland, M. Cristina Marchetti, Valerie Horsley, and Eric. R. Dufresne. Scaling of Traction Forces with the Size of Cohesive Cell Colonies. *Physical Review Letters*, 108(19):198101, may 2012.

[223] Sri Ram Krishna Vedula, Hiroaki Hirata, Mui Hoon Nai, Agustı´ Brugués, Yusuke Toyama, Xavier Trepat, Chwee Teck Lim, and Benoit Ladoux. Epithelial bridges maintain tissue integrity during collective cell migration. *Nature Materials*, 13(1):87–96, jan 2014.

[224] Ernest Latorre, Sohan Kale, Laura Casares, Manuel Gómez-González, Marina Uroz, Léo Valon, Roshna V. Nair, Elena Garreta, Nuria Montserrat, Aránzazu del Campo, Benoit Ladoux, Marino Arroyo, and Xavier Trepat. Active superelasticity in three-dimensional epithelia of controlled shape. *Nature*, 563(7730):203–208, nov 2018.

[225] Ryan J. Petrie, Andrew D. Doyle, and Kenneth M. Yamada. Random versus directionally persistent cell migration. *Nature Reviews Molecular Cell Biology*, 10(8):538–549, aug 2009.

[226] Yoshiyuki Rikitake and Yoshimi Takai. Directional Cell Migration: Regulation by

Small G Proteins, Nectin-like Molecule-5, and Afadin. In *International review of cell and molecular biology*, volume 287, pages 97–143. Elsevier, 2011.

[227] Anna Haeger, Katarina Wolf, Mirjam M. Zegers, and Peter Friedl. Collective cell migration: Guidance principles and hierarchies. *Trends in Cell Biology*, 25(9):556–566, 2015.

[228] Gema Malet-Engra, Weimiao Yu, Amanda Oldani, Javier Rey-Barroso, Nir S. Gov, Giorgio Scita, and Loïc Dupré. Collective cell motility promotes chemotactic prowess and resistance to chemorepulsion. *Current Biology*, 25(2):242–250, 2015.

[229] Brian A. Camley, Juliane Zimmermann, Herbert Levine, and Wouter Jan Rappel. Emergent Collective Chemotaxis without Single-Cell Gradient Sensing. *Physical Review Letters*, 2016.

[230] Richard Nuccitelli. A Role for Endogenous Electric Fields in Wound Healing, 2003.

[231] Barbara Cortese, Ilaria Elena Palamà, Stefania D'Amone, and Giuseppe Gigli. Influence of electrotaxis on cell behaviour, 2014.

[232] Daniel J. Cohen, W. James Nelson, and Michel M. Maharbiz. Galvanotactic control of collective cell migration in epithelial monolayers. *Nature Materials*, 13(4):409–417, 2014.

[233] Qian Liu and Bing Song. Electric field regulated signaling pathways. *International Journal of Biochemistry and Cell Biology*, 2014.

[234] Amy L Bauer, Trachette L Jackson, and Yi Jiang. Topography of Extracellular Matrix Mediates Vascular Morphogenesis and Migration Speeds in Angiogenesis. *PLOS Computational Biology*, 5(7):1–18, 2009.

[235] Jessica S. Martinez, Joseph B. Schlenoff, and Thomas C.S. Keller. Collective epithelial cell sheet adhesion and migration on polyelectrolyte multilayers with uniform and gradients of compliance. *Experimental Cell Research*, 2016.

[236] Wang Xi, Thuan Beng Saw, Delphine Delacour, Chwee Teck Lim, and Benoit Ladoux. Material approaches to active tissue mechanics. *Nature Reviews Materials*, 4(1):23–44, jan 2019.

[237] Assaf Zaritsky, Erik S. Welf, Yun Yu Tseng, M. Angeles Rabadán, Xavier Serra-Picamal, Xavier Trepat, and Gaudenz Danuser. Seeds of Locally Aligned Motion and Stress Coordinate a Collective Cell Migration. *Biophysical Journal*, 109(12):2492–2600, 2015.

[238] L Chang and M Karin. Mammalian MAP kinase signalling cascades. *Nature*, 2001.

[239] Yu Sun, Wen Zhou Liu, Tao Liu, Xu Feng, Nuo Yang, and Hua Fu Zhou. Signaling pathway of MAPK/ERK in cell proliferation, differentiation, migration, senescence and apoptosis. *Journal of Receptors and Signal Transduction*, 35(6):600–604, 2015.

[240] Susumu Tanimura and Kohsuke Takeda. ERK signalling as a regulator of cell motility. *Journal of Biochemistry*, 162(3):145–154, 2017.

[241] Scott T. Eblen. *Extracellular-Regulated Kinases: Signaling From Ras to ERK Substrates to Control Biological Outcomes*, volume 138. Elsevier Inc., 1 edition, 2018.

[242] Yutaka Matsubayashi, Miki Ebisuya, Sakiko Honjoh, and Eisuke Nishida. ERK Activation Propagates in Epithelial Cell Sheets and Regulates Their Migration during Wound Healing. *Current Biology*, 14(8):731–735, apr 2004.

[243] L Djordje, Alistair N Boettiger, Dafna Bar-sagi, Jeffrey D Carbeck, and Stanislav Y Shvartsman. Role of boundary conditions in an experimental model of epithelial wound healing. *Am J Physiol Cell Physiol*, 08544:68–75, 2006.

[244] Toru Hiratsuka, Yoshihisa Fujita, Honda Naoki, Kazuhiro Aoki, Yuji Kamioka, and Michiyuki Matsuda. Intercellular propagation of extracellular signal-regulated kinase activation revealed by in vivo imaging of mouse skin. *eLife*, 4:1–18, 2015.

[245] Kazuhiro Aoki, Yuka Kumagai, Atsuro Sakurai, Naoki Komatsu, Yoshihisa Fujita, Clara Shionyu, and Michiyuki Matsuda. Stochastic ERK activation induced by noise and cell-to-cell propagation regulates cell density-dependent proliferation. *Molecular Cell*, 52(4):529–540, 2013.

[246] Simon Begnaud, Tianchi Chen, Delphine Delacour, René Marc Mège, and Benoît Ladoux. Mechanics of epithelial tissues during gap closure. *Current Opinion in Cell Biology*, 42:52–62, 2016.

[247] George T. Eisenhoffer, Patrick D. Loftus, Masaaki Yoshigi, Hideo Otsuna, Chi Bin Chien, Paul A. Morcos, and Jody Rosenblatt. Crowding induces live cell extrusion to maintain homeostatic cell numbers in epithelia. *Nature*, 2012.

[248] E. Anon, X. Serra-Picamal, P. Hersen, N. C. Gauthier, M. P. Sheetz, Xavier Trepat, and Benoit Ladoux. Cell crawling mediates collective cell migration to close undamaged epithelial gaps. *Proceedings of the National Academy of Sciences*, 109(27):10891–10896, 2012.

[249] Agustí Brugués, Ester Anon, Vito Conte, Jim H. Veldhuis, Mukund Gupta, Julien

Colombelli, José J. Muñoz, G. Wayne Brodland, Benoit Ladoux, and Xavier Trepat. Forces driving epithelial wound healing. *Nature Physics*, 10(9):683–690, sep 2014.

[250] Andrea Ravasio, Ibrahim Cheddadi, Tianchi Chen, Telmo Pereira, Hui Ting Ong, Cristina Bertocchi, Agusti Brugues, Antonio Jacinto, Alexandre J. Kabla, Yusuke Toyama, Xavier Trepat, Nir Gov, Luís Neves De Almeida, and Benoit Ladoux. Gap geometry dictates epithelial closure efficiency. *Nature Communications*, 6, 2015.

[251] Olivier Cochet-Escartin, Jonas Ranft, Pascal Silberzan, and Philippe Marcq. Border forces and friction control epithelial closure dynamics. *Biophysical Journal*, 106(1):65–73, 2014.

[252] Vincent Nier, Maxime Deforet, Guillaume Duclos, Hannah G. Yevick, Olivier Cochet-Escartin, Philippe Marcq, and Pascal Silberzan. Tissue fusion over nonadhering surfaces. *Proceedings of the National Academy of Sciences*, 112(31):9546–9551, 2015.

[253] G. Duclos, S. Garcia, H. G. Yevick, and P. Silberzan. Perfect nematic order in confined monolayers of spindle-shaped cells. *Soft Matter*, 10(14):2346–2353, 2014.

[254] G. Duclos, Carles Blanch Mercader, V Yashunsky, Guillaume Salbreux, J. Prost, Jean-François Joanny, and Pascal Silberzan. Spontaneous shear flow in confined cellular nematics. *Nature Physics*, in press, 2018.

[255] Thuan Beng Saw, Amin Doostmohammadi, Vincent Nier, Leyla Kocgozlu, Sumesh Thampi, Yusuke Toyama, Philippe Marcq, Chwee Teck Lim, Julia M. Yeomans, and Benoit Ladoux. Topological defects in epithelia govern cell death and extrusion. *Nature*, 544(7649):212–216, 2017.

[256] Michael J. Raymond, Poulomi Ray, Gurleen Kaur, Ajay V. Singh, and Leo Q. Wan. Cellular and Nuclear Alignment Analysis for Determining Epithelial Cell Chirality. *Annals of Biomedical Engineering*, 44(5):1475–1486, 2016.

[257] Sri Ram Krishna Vedula, Man Chun Leong, Tan Lei Lai, Pascal Hersen, Alexandre J Kabla, Chwee Teck Lim, and Benoit Ladoux. Emerging modes of collective cell migration induced by geometrical constraints. *Proceedings of the National Academy of Sciences of the United States of America*, 109(32):12974–9, 2012.

[258] C Brangwynne, S Huang, K K Parker, D E Ingber, and E Ostuni. Symmetry breaking in cultured mammalian cells. *In vitro cellular & developmental biology. Animal*, 2000.

[259] Wang Xi, Surabhi Sonam, Thuan Beng Saw, Benoit Ladoux, and Chwee Teck Lim. Emergent patterns of collective cell migration under tubular confinement. *Nature Communications*, 8(1):1517, dec 2017.

[260] Tianchi Chen, Thuan Beng Saw, René-Marc Mège, and Benoit Ladoux. Mechanical forces in cell monolayers. *Journal of Cell Science*, 131(24):jcs218156, 2018.

[261] Assaf Zaritsky, Doron Kaplan, Inbal Hecht, Sari Natan, Lior Wolf, Nir S. Gov, Eshel Ben-Jacob, and Ilan Tsarfaty. Propagating Waves of Directionality and Coordination Orchestrate Collective Cell Migration. *PLoS Computational Biology*, 10(7):15–19, 2014.

[262] Shiladitya Banerjee and M. Cristina Marchetti. Continuum models of collective cell migration. *arXiv*, pages 1–30, may 2018.

[263] Tams Vicsek, Andrs Czirk, Eshel Ben-Jacob, Inon Cohen, and Ofer Shochet. Novel type of phase transition in a system of self-driven particles. *Physical Review Letters*, 1995.

[264] Fabio Giavazzi, Matteo Paoluzzi, Marta Macchi, Dapeng Bi, Giorgio Scita, M. Lisa Manning, Roberto Cerbino, and M. Cristina Marchetti. Flocking transitions in confluent tissues. *Soft Matter*, 14(18):3471–3477, 2018.

[265] Shiladitya Banerjee, Kazage J.C. C Utuje, and M. Cristina Marchetti. Propagating Stress Waves during Epithelial Expansion. *Physical Review Letters*, 114(22), 2015.

[266] Grégoire Peyret, Romain Mueller, Joseph D'Alessandro, Simon Begnaud, Philippe Marcq, René-Marc Mège, Julia M. Yeomans, Amin Doostmohammadi, and Benoît Ladoux. Sustained Oscillations of Epithelial Cell Sheets. *Biophysical Journal*, 117(3):464–478, aug 2019.

[267] Loïc LeGoff and Thomas Lecuit. Mechanical Forces and Growth in Animal Tissues. *Cold Spring Harbor perspectives in biology*, pages 1–18, 2015.

[268] Alejo E. Rodríguez-Fraticelli, Muriel Auzan, Miguel A. Alonso, Michel Bornens, and Fernando Martín-Belmonte. Cell confinement controls centrosome positioning and lumen initiation during epithelial morphogenesis. *Journal of Cell Biology*, 198(6):1011–1023, 2012.

[269] Patrick W. Oakes, Shiladitya Banerjee, M. Cristina Marchetti, and Margaret L. Gardel. Geometry regulates traction stresses in adherent cells. *Biophysical Journal*, 107(4):825–833, 2014.

[270] Christopher S. Chen, Jose L. Alonso, Emanuele Ostuni, George M. Whitesides, and Donald E. Ingber. Cell shape provides global control of focal adhesion as-

sembly. *Biochemical and Biophysical Research Communications*, 307(2):355–361, 2003.

[271] Timothée Vignaud, Hajer Ennomani, and Manuel Théry. Polyacrylamide Hydrogel Micropatterning. *Methods in Cell Biology*, 120:93–116, 2014.

[272] Justin R. Tse and Adam J. Engler. Preparation of Hydrogel Substrates with Tunable Mechanical Properties. *Current Protocols in Cell Biology*, 47(1):10.16.1–10.16.16, jun 2010.

[273] James P Butler, Iva Marija Tolić-Nørrelykke, Ben Fabry, and Jeffrey J Fredberg. Traction fields, moments, and strain energy that cells exert on their surroundings. *American journal of physiology. Cell physiology*, 282(3):C595–605, 2002.

[274] Benedikt Sabass, Margaret L. Gardel, Clare M. Waterman, and Ulrich S. Schwarz. High resolution traction force microscopy based on experimental and computational advances. *Biophysical Journal*, 94(1):207–220, 2008.

[275] Aleksandra K. Denisin and Beth L. Pruitt. Tuning the Range of Polyacrylamide Gel Stiffness for Mechanobiology Applications. *ACS Applied Materials and Interfaces*, 8(34):21893–21902, 2016.

[276] Lionel Bureau and Martial Balland. 9 - Thermosensitive Micropatterned Substrates. *Methods in Cell Biology*, 120:145–154, 2014.

[277] Srikanth Vinjimore Kesavan, Fabrice P Navarro, Mathilde Menneteau, Frederique Mittler, Brigitte David-Watine, Nelly Dubrulle, Spencer L Shorte, Bernard Chalmond, Jean-marc Dinten, and Cedric P Allier. Real-time label-free detection of dividing cells by means of lensfree video-microscopy. *Journal of biomedical optics*, 19(3):36004, 2014.

[278] Onur Mudanyali, Euan McLeod, Wei Luo, Alon Greenbaum, Ahmet F Coskun, Yves Hennequin, Cédric P Allier, and Aydogan Ozcan. Wide-field optical detection of nanoparticles using on-chip microscopy and self-assembled nanolenses. *Nature photonics*, 7(3):240–247, 2013.

[279] Vanni Petrolli, Magali Le Goff, Monika Tadrous, Kirsten Martens, Cédric Allier, Ondrej Mandula, Lionel Hervé, Silke Henkes, Rastko Sknepnek, Thomas Boudou, Giovanni Cappello, and Martial Balland. Confinement-Induced Transition between Wavelike Collective Cell Migration Modes. *Physical Review Letters*, 122(16):168101, apr 2019.

[280] L. Herve, O. Cioni, P. Blandin, F. Navarro, M. Menneteau, T. Bordy, S. Morales, and C. Allier. Multispectral total-variation reconstruction applied to lens-free

microscopy. *Biomedical Optics Express*, 9(11):5828, nov 2018.

[281] Davide Heller, Andreas Hoppe, Simon Restrepo, Lorenzo Gatti, Alexander L Tournier, Nicolas Tapon, Konrad Basler, and Yanlan Mao. EpiTools: An Open-Source Image Analysis Toolkit for Quantifying Epithelial Growth Dynamics. *Developmental cell*, 36(1):103–116, 2016.

[282] Benoit Aigouy, Daiki Umetsu, and Suzanne Eaton. Segmentation and Quantitative Analysis of Epithelial Tissues. In *Drosophila: Methods and Protocols, Methods in Molecular Biology, vol. 1478*, volume 1478, pages 227–239. 2016.

[283] Markus Raffel, Christian E Willert, Steve T Wereley, and Jürgen Kompenhans. *Particle Image Velocimetry*. Experimental Fluid Mechanics. Springer Berlin Heidelberg, Berlin, Heidelberg, 2007.

[284] Maxime Deforet, Maria Carla Parrini, Laurence Petitjean, Marco Biondini, Axel Buguin, Jacques Camonis, and Pascal Silberzan. Automated velocity mapping of migrating cell populations (AVeMap). *Nature Methods*, 9(11):1081–1083, 2012.

[285] Sung Min Choi, Wi Han Kim, Daniel Côté, Cheol-Woo Park, and Ho Lee. Blood cell assisted in vivo Particle Image Velocimetry using the confocal laser scanning microscope. *Optics Express*, 19(5):4357, 2011.

[286] A. Harris, P Wild, and D Stopak. Silicone rubber substrata: a new wrinkle in the study of cell locomotion. *Science*, 208(4440):177–179, apr 1980.

[287] Mei R osa Ng, Achim Besser, Joan S. Brugge, and Gaudenz Danuser. Mapping the dynamics of force transduction at cell-cell junctions of epithelial clusters. *eLife*, 3:e03282, 2014.

[288] Yunfei Huang, Christoph Schell, Tobias B. Huber, Ahmet Nihat Şimşek, Nils Hersch, Rudolf Merkel, Gerhard Gompper, and Benedikt Sabass. Traction force microscopy with optimized regularization and automated Bayesian parameter selection for comparing cells. *Scientific Reports*, 9(1):1–16, 2019.

[289] James H-c Wang and Bin Li. The principles and biological applications of cell traction force microscopy. *World*, 29:449–458, 2010.

[290] James H.C. Wang and Jeen Shang Lin. Cell traction force and measurement methods. *Biomechanics and Modeling in Mechanobiology*, 6(6):361–371, 2007.

[291] John C. Crocker and David G. Grier. Methods of digital video microscopy for colloidal studies. *Journal of Colloid and Interface Science*, 1996.

[292] Yongxiang Gao and Maria L. Kilfoil. Accurate detection and complete tracking of large populations of features in three dimensions. *Optics Express*, 2009.

[293] Fabien Montel, Morgan Delarue, Jens Elgeti, Laurent Malaquin, Markus Basan, Thomas Risler, Bernard Cabane, Danijela Vignjevic, Jacques Prost, Giovanni Cappello, and Jean-François Joanny. Stress clamp experiments on multicellular tumor spheroids. *Physical Review Letters*, 107(18):1–4, 2011.

[294] Esther W Gomez, Qike K Chen, Nikolce Gjorevski, and Celeste M Nelson. Tissue geometry patterns epithelial-mesenchymal transition via intercellular mechanotransduction. *Journal of Cellular Biochemistry*, 110(1):n/a–n/a, 2010.

[295] Erik N. Schaumann, Michael F. Staddon, Margaret L. Gardel, and Shiladitya Banerjee. Force localization modes in dynamic epithelial colonies. *Molecular Biology of the Cell*, 29(23):2835–2847, 2018.

[296] Nikolce Gjorevski and Celeste M. Nelson. Mapping of mechanical strains and stresses around quiescent engineered three-dimensional epithelial tissues. *Biophysical Journal*, 103(1):152–162, 2012.

[297] Katharina Hennig, Irene Wang, Philippe Moreau, Leo Valon, Simon De Beco, Mathieu Coppey, Yekaterina Miroshnikova, Corinne Albiges Rizo, Cyril Favard, Raphael Voituriez, and Martial Balland. Stick-slip dynamics of cell adhesion triggers spontaneous symmetry breaking and directional migration. *bioRxiv*, 2018.

[298] Hsin Chih Lin, Ling Ling Wang, and Shi Nine Yang. Extracting periodicity of a regular texture based on autocorrelation functions. *Pattern Recognition Letters*, 1997.

[299] B A Camley and W-J Rappel. Physical models of collective cell motility: from cell to tissue. *Journal of Physics D: Applied Physics*, 50(11):113002, 2017.

[300] Xavier Trepat and Erik Sahai. Mesoscale physical principles of collective cell organization. *Nature Physics*, page 1, 2018.

[301] Daniel L. Barton, Silke Henkes, Cornelis J. Weijer, and Rastko Sknepnek. Active Vertex Model for cell-resolution description of epithelial tissue mechanics. *PLoS Computational Biology*, 13(6), 2017.

[302] Guo Chen and Xingming Deng. Cell Synchronization by Double Thymidine Block. *BIO-PROTOCOL*, 2018.

[303] Sean P. Palecek, Joseph C. Loftust, Mark H. Ginsberg, Douglas A. Lauffenburger, and Alan F. Horwitz. Integrin-ligand binding properties govern cell migration speed through cell-substratum adhesiveness, 1997.

[304] Mihály Kovács, Judit Tóth, Csaba Hetényi, András Málnási-Csizmadia, and James R. Seller. Mechanism of blebbistatin inhibition of myosin II. *Journal of*

*Biological Chemistry*, 279(34):35557–35563, 2004.

[305] J. Prost, F. Jülicher, and J. F. Joanny. Active gel physics. *Nature Physics*, 11(2):111–117, 2015.

[306] Pierre Recho, Thibaut Putelat, and Lev Truskinovsky. Force-induced repolarization of an active crawler. *New Journal of Physics*, 21(3), 2019.

[307] David B. Brückner, Alexandra Fink, Christoph Schreiber, Peter J.F. Röttgermann, Joachim O. Rädler, and Chase P. Broedersz. Stochastic nonlinear dynamics of confined cell migration in two-state systems. *Nature Physics*, 2019.

[308] Steven M. Zehnder, Melanie Suaris, Madisonclaire M. Bellaire, and Thomas E. Angelini. Cell volume fluctuations in MDCK monolayers. *Biophysical Journal*, 108(2):247–250, 2015.

[309] C. Cadart, E. Zlotek-Zlotkiewicz, L. Venkova, O. Thouvenin, V. Racine, M. Le Berre, S. Monnier, and M. Piel. Fluorescence eXclusion Measurement of volume in live cells. *Methods in Cell Biology*, 2017.

[310] Nicolas Perez Gonzalez, Nash D. Rochman, Evelyn Chiu, Denis Wirtz, Sean X. Sun, Jiaxiang Tao, and Dhruv Vig. Cell tension and mechanical regulation of cell volume. *Molecular Biology of the Cell*, 29(21):2591–2600, 2018.

[311] David E Clapham. Calcium Signaling. *Cell*, 131(6):1047–1058, dec 2007.

[312] Scott Boitano, Ellen R. Dirksen, and Michael J. Sanderson. Intercellular propagation of calcium waves mediated by inositol trisphosphate. *Science*, 1992.

[313] O. K. Nihei, A. C. Campos de Carvalho, D. C. Spray, W. Savino, and L. A. Alves. A novel form of cellular communication among thymic epithelial cells: Intercellular calcium wave propagation. *American Journal of Physiology - Cell Physiology*, 2003.

[314] Anne-Kathrin Classen, Alexander Hildebrand, Cornelia Stadler, Christina Bielmeier, Hartmann Harz, Jack Bates, and Ramya Balaji. Calcium spikes, waves and oscillations in a large, patterned epithelial tissue. *Scientific Reports*, 7(1):1–14, 2017.

[315] Panagiota A. Sotiropoulou and Cedric Blanpain. Development and homeostasis of the skin epidermis. *Cold Spring Harbor Perspectives in Biology*, 4(7):1–9, 2012.

[316] Shuang Liu, Huishan Zhang, and Enkui Duan. Epidermal development in mammals: Key regulators, signals from beneath, and stem cells. *International Journal of Molecular Sciences*, 14(6):10869–10895, 2013.

[317] Jonathan A. Nowak, Lisa Polak, H. Amalia Pasolli, and Elaine Fuchs. Hair follicle

stem cells are specified and function in early skin morphogenesis. *Cell Stem Cell*, 2008.

[318] Carlos Andrés Chacón-Martínez, Markus Klose, Catherin Niemann, Ingmar Glauche, and Sara A Wickström. Hair follicle stem cell cultures reveal self-organizing plasticity of stem cells and their progeny. *The EMBO Journal*, 36(2):151–164, 2017.

[319] M. Reffay, L. Petitjean, S. Coscoy, E. Grasland-Mongrain, F. Amblard, A. Buguin, and P Silberzan. Orientation and polarity in collectively migrating cell structures: Statics and dynamics. *Biophysical Journal*, 100(11):2566–2575, 2011.